Development of Electrocatalysts for Oxygen Electrodes in Alkaline Electrochemical Systems

Submitted by Adeline Loh,

to the University of Exeter as a thesis for the degree of

Doctor of Philosophy in Renewable Energy in April 2019

I certify that all material in this thesis which is not my own work has been identified and that no material has previously been submitted and approved for the award of a degree by this or any other University.

Signature: ……..

Abstract

In recent years as a larger proportion of our energy needs are being met by renewable energy sources, research and development in energy storage is becoming more significant. Oxygen electrodes, found in electrical energy storage applications such as fuel cells, water electrolysers and metal-air secondary batteries, face the demand for improved performance. In view of this, the research in this thesis focuses on the synthesis and development of oxygen reduction reaction (ORR) and oxygen evolution reaction (OER) catalysts to overcome the slow kinetics of the oxygen electrochemical reactions in alkaline media, followed by the investigation of their combined performance in a tri-electrode zinc-air secondary cell. The ORR performance of various transition metal oxides and carbonaceous materials was initially compared against benchmark catalyst Pt/C using rotating disc electrode measurements. Amorphous MnO_x combined with Vulcan XC-72R was found to demonstrate high ORR activity and good stability over the range of cathodic current densities tested. The influence of the synthesis parameters of amorphous MnO_x on its ORR activity was subsequently investigated and it was found that optimal amorphous MnO_x catalyst can be synthesised with a molar ratio of MnO_4^-/ Mn^{2+} of 2.67, by adding $KMnO_4$ to $Mn(CH_3COO)_2$ in a basic solution of pH 12 at 295 K. Similarly, the OER performance of transition metal oxides and hydroxides coated on metal mesh was compared and electrodeposited Ni-Fe hydroxide was reported to display high activity and durability when held at anodic potentials. Based on this, various compositions of Ni-based binary and Ni-Fe based ternary metal hydroxides were screened with a unique microelectrode set-up at high current densities up to 1 A cm^{-2}. Ni-Fe-Co hydroxide showed most improved OER performance. The effect of electrodeposition parameters on the electrocatalytic performance of Ni-Fe-Co hydroxide were examined and used to further optimise the catalyst. Ni-Fe-Co hydroxide cathodically deposited at 300 mA cm^{-2} for 240 s at 22 ºC, pH 3.9 was found to demonstrate best OER performance, giving an overpotential of 235 mV at 0.1 A cm^{-2}. The electrodes with optimised catalysts were tested in an in-house built zinc-air cycling set-up, demonstrating energy efficiencies of 58-61% up to 40 h at 20 mA cm^{-2} in 4 M NaOH + 0.3 M ZnO at 333 K.

Acknowledgements

First and foremost, I would like to thank my main supervisor Professor Xiaohong Li for giving me the opportunity to embark on this PhD project. Her constant support, endless advice and encouragement throughout the entire journey has been crucial to my achievements. I am truly grateful for the invaluable experience and knowledge she has shared with me during my time spent on the project.

I would like to thank the College of Engineering, Mathematics and Physical Sciences (CEMPS) at the University of Exeter for granting me a full scholarship for the PhD.

I am extremely grateful to Professor Derek Pletcher and Professor Andrea Russell from the University of Southampton for their kind generosity in the provision of facilities and support at the start of my journey, as well as Dave, Danai, Andy and Turgut for their friendship during my time in Southampton.

My sincerest thanks to the CSM laboratory staff Gavyn, Sharon, Malcolm and Joe for all their support in creating a good working environment without which the experimental work could not have taken place. Not forgetting Daniela, Joe and Rob for graciously lending me space in their labs in the beginning. Thanks also to Hong and Judith for training me to use the characterisation equipment and Brian and James for their technical support, time and patience.

I wish to express my gratitude to past and present members of my research group whom I've had the pleasure of spending many hours with in the lab, their advice and friendship is duly noted. Special thanks to David for sharing the responsibilities of building the group and for always making time for in-depth discussions on the research.

Last but not least, I would like to thank my parents for giving me a good foundation in life, my sisters, Shirin and Sheralyn, for always being there for me through thick and thin, and Sam for believing in me. Thank you.

Table of Contents

List of Tables

List of Figures

Figure B1 Chronopotentiometric measurements at 10, 20, 50 and 100 mA cm^{-2} of M2 and M4 MnO_x catalyst coated GDE (loading 2 mg cm^{-2}) on either GDS 1120 or TGP-H-60 carbon fibre paper in 1 M NaOH, 333 K, O_2 feed rate of 200 cm^3 min^{-1} to the back of the electrode. 231

List of Abbreviations

2D	Two-dimensional
3D	Three-dimensional
BET	Brunauer-Emmett-Teller
BJH	Barrett-Joyner-Halenda
CE	Counter electrode
CV	Cyclic voltammetry
DFT	Density functional theory
EDX	Energy dispersive x-ray spectroscopy
EES	Electrochemical energy storage
GC	Glassy carbon
GDE	Gas diffusion electrode
RDE	Rotating disc electrode
OER	Oxygen evolution reaction
ORR	Oxygen reduction reaction
LSV	Liner sweep voltammetry
MEA	Membrane electrode assembly
RE	Reference electrode
rpm	revolutions per minute
PTFE	Polytetrafluroethylene
SEM	Scanning electron microscope
SHE	Standard hydrogen electrode
SS	Stainless steel
TEM	Transmission electron microscope
URFC	Unitized regenerative fuel cell
WE	Working electrode
XAS	X-ray absorption spectroscopy
XPS	X-ray photoelectron spectroscopy
XRD	X-ray diffraction

List of Symbols

Symbol	Meaning	Units
ΔE	Difference in potential	mV
E^{θ}	Standard electrode potential	V
E_{cell}	Cell potential	V
E_p	Peak potential	V
E_{pa}	Anodic peak potential	V
E_{pc}	Cathodic peak potential	V
E_{eq}	Electrode equilibrium potential	V
$E_{1/2}$	Half-wave potential in voltammetry	V
$E_{1/4}$	Potential at which $j/ j_L = ¼$	V
$E_{3/4}$	Potential at which $j/ j_L = ¾$	V
F	Faraday's constant	C
ΔG	Change in Gibbs free energy	kJ
i_k	Kinetically limited current	A
i_L	Limiting current	A
i_{pa}	Anodic peak current	A
i_{pc}	Cathodic peak current	A
j	Current density	A cm^{-2}
k	Rate constant for homogeneous reaction	Dependent on order
Q	Charge passed	C
n	Stoichiometric number of electrons involved in electrode reaction	N/A
η	Overpotential, $E-E_{eq}$	V
⌀	Diameter	mm
R	Gas constant	J mol^{-1} K^{-1}
t	Time	s
V	Volume	cm^3
υ	Linear potential scan rate	V s^{-1}
ω	Rotational speed	rad s^{-1}

List of Publications

1. Adeline Loh, Ke Xu, Xiaohong Li, Baoguo Wang. *Influence of synthesis parameters on amorphous manganese dioxide catalyst electrocatalytic performance*. Electrochimica Acta. 2017, 245, p 615-624.
2. Ke Xu, Adeline Loh, Baoguo Wang, Xiaohong Li. *Enhancement of Oxygen Transfer by Design Nickel Foam Electrode for Zinc−Air Battery*. Journal of the Electrochemical Society. 2018, 165 (5): A809-A818.
3. L.F. Arenas, A. Loh, D.P. Trudgeon, X. Li, C. Ponce de León, F.C. Walsh. *The characteristics and performance of redox flow batteries having zinc negative electrodes for energy storage*. Renewable and Sustainable Energy Reviews. 2018, 90, p 992-1016
4. Bing Li, Junye Quan, Adeline Loh, Jianwei Chai, Ye Chen, Chaoliang Tan, Xiaoming Ge, T. S. Andy Hor, Zhaolin Liu, Hua Zhang, and Yun Zong. *A Robust Hybrid Zn-Battery with Ultralong Cycle Life*. Nano Letters., 2017, 17 (1), p 156–163.
5. Wei-Bin Zhang, Xue-Jing Ma, Adeline Loh, Xiaohong Li, Frank Walsh, Ling-Bin Kong. *High Volumetric Energy Densities Capacitors Based on New Electrode Material Lanthanum Nitride*. ACS Energy Letters. 2017 2 (2), p 336-341.
6. Adeline Loh, Xiaohong Li, Oluwadamilola O. Taiwo, Ke Xu, Farid Tariq, Nigel P. Brandon, Baoguo Wang. Selection and optimisation of Ni-Fe based ternary metal hydroxide catalyst for oxygen evolution. *In preparation.*
7. Adeline Loh, Xiaohong Li, Frank Walsh. A comparative study of oxygen reduction electrocatalysts under alkaline conditions. *In preparation.*
8. Adeline Loh, Xiaohong Li, David P. Trudgeon. Understanding the performance of a secondary zinc-air cell. *In preparation.*

Chapter 1 Introduction

1.1. The emergence of renewable energy

The implementation and use of renewable energy sources has been growing rapidly over recent decades due to the ever-increasing global demand for electricity and the concerns surrounding the environmental impact of conventional electricity generation from fossil fuels [1]. The capacity of global renewable power generation was reported to have increased by 8.3% (**Figure 1.1**) during 2017 [2].

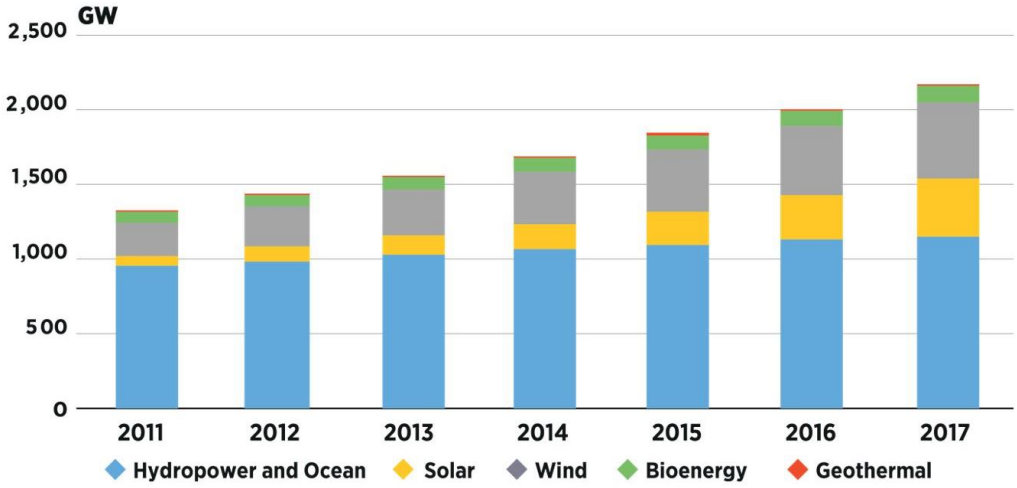

Figure 1.1 Total global renewable power generation capacity, 2011-17 [2].

These shifts have been encouraged by policies such as the EU Renewable Energy Directive for 2020 [3] initiated by the European Commission, which stated that renewable energy sources should provide 20% energy consumption in the EU by 2020 and more recently a future renewable energy target of 32% was set for 2030 [4]. Similarly, a long-term target set out in the 2008 Climate Change Act [5] specified that by 2050, the UK's net greenhouse gas emissions were expected to be reduced by at least 80% from 1990 baseline levels. New state and regional policies in the United States [6] particularly in California, New Jersey and Massachusetts reflect the promotion of increased clean energy or renewables generation by 2030 and onwards. In China, the China National Renewable Energy Centre (CNREC) laid out ambitious targets in its 2017 outlook report [7], to reduce the use of coal to half of the current level by 2050 whilst rapidly increasing the power capacity of renewables so that non-fossil fuel sources make up 60% of the energy supply. These targets were set to comply with the 'below 2 ºC by 2050' objective in the Paris Agreement.

Renewable energy sources such as wind, solar, tidal, biomass and geothermal power provide low-carbon alternatives to the more conventional sources of energy. In spite of this, energy generation from renewable sources can be problematic [8] as energy is directly harnessed from nature making it difficult to match power output to demand. The storage of electrical energy especially on a large-scale is crucial to overcoming the problems of intermittency and seasonal fluctuations of renewable energy, helping to absorb surplus generation capacity, smooth residual loads and provide flexibility for energy balancing [9]. This is demonstrated in **Figure 1.2** where the excess energy stored during low demand periods can be used to level out the load curve at higher demand periods. Some examples of energy storage technologies are pumped-hydro, compressed air, flywheel and rechargeable battery systems. The selection of a suitable energy storage technology depends on its efficiency, environmental impact, location, lifetime, capital and life cycle cost and spatial requirements.

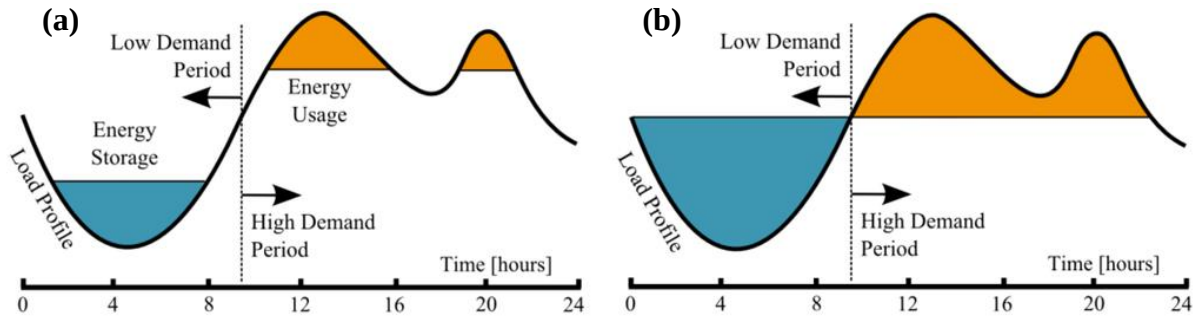

Figure 1.2 Load profiles over a 24 h period of an electricity storage system showing **a)** peak shaving and **b)** load levelling [10].

1.2. Electrochemical energy storage technology

Electrochemical energy storage (EES) is an attractive solution for intermittent renewable energy sources. EES covers electrochemical cells such as: secondary or rechargeable batteries, fuel cells, supercapacitors and flow batteries [11-13]. Secondary batteries are good candidates for stationary and portable energy storage applications, covering a wide range of capacities up to 100 MW with up to 80% energy efficiencies [14]. Some of the earliest EES chemistries are lead-acid and Ni-metal batteries, but both of these systems involve hazardous materials which raise concerns regarding safe disposal or recycling, especially if used on a large-scale. Lithium ion

and lithium polymer batteries which were originally developed for portable electronics and electric vehicles, have also been stacked to provide several MWs of power for grid energy storage demonstration projects [15].

More recently, renewed research efforts have been made on metal-air batteries as they demonstrate much greater theoretical specific energy densities since one of its electroactive materials, oxygen, does not require storage [16]. This is especially true for Li-air [17] compared to Li-ion batteries as seen in **Table 1.1**. These batteries can be electrically or mechanically recharged by physically replacing the spent anode and electrolyte after discharge [18, 19] giving them the potential to be developed for electric vehicles [20] . Although much progress has been made in this area, these systems are yet to be economically feasible due to safety concerns, low performance and high material costs.

Table 1.1 Comparison of cell voltages and theoretical specific energy densities of selected systems.

System	Thermodynamic cell voltage/ V	Theoretical specific energy density/ Wh kg^{-1}	Ref
Lead acid	2.10	30-50	[21]
Ni-Cd	1.20	45-80	[22]
Li-ion	3.80	250	[23]
Li-air	2.91	5200	[24]
Zn-air	1.65	1350	[20]
Fe-air	1.28	764	[25]
URFC	1.23	3660	[26]

Fuel cells and electrolysers have also attracted importance as energy conversion and storage devices. Hydrogen, as an energy carrier, is environmentally benign when generated from renewable energy sources via water electrolysis. Whilst pure hydrogen, as a fuel source, emits only water and heat as by-products [27, 28]. A unitized regenerative fuel cell (URFC) combines both of these into a single unit such that the same electrochemical cell operates as both a fuel cell and water electrolyser with the advantages of long-term energy storage and theoretically high specific energy density seen in **Table 1.1** [29, 30]. Further efforts are still required to handle issues of hydrogen storage and transportation, and to ultimately enhance the efficiencies of these systems whilst ensuring material costs are kept to a minimum in order to bring this technology to commercialisation.

1.3. The oxygen electrode and it's research challenges

In order for EES technologies to be coupled with renewable energy sources, they must first be improved to meet the economic requirements. The oxygen electrode plays a critical role in EES applications such as fuel cells, water electrolysers and metal-air batteries. In these EES systems, the electrochemical reactions involve oxygen through cathodic reduction found in both fuel cells and metal-air batteries and conversely, the production of oxygen via anodic oxidation in water electrolysis. In theory, these systems have high specific energy densities. In reality, however, it is the sluggish kinetics associated with the two electrochemical reactions that take place at the oxygen electrode, the overpotential of the oxygen reduction reaction (ORR) and the oxygen evolution reaction (OER) which hinders the performance of these devices. In response to this, precious metal-based electrocatalysts have been demonstrated to be the most effective catalysts for ORR and OER but are considered too expensive for commercialisation. The main research challenge is therefore to develop highly efficient, stable, yet inexpensive electrocatalysts to overcome these high reaction overpotentials.

It is known that the ORR and OER typically take place at triple-phase (solid-liquid-gaseous) boundaries [31]. These reaction environments lead to difficulties in the optimisation of porosity and hydrophobicity of the catalyst layer in a bifunctional secondary oxygen electrode. On top of this, the catalyst as well as any additional ancillary additives in the bifunctional catalyst layer must be stable at highly cathodic and anodic current densities. The design, construction and suitable arrangement of electrodes are therefore subsequent challenges which must be overcome for the development of a secondary cell.

Furthermore, the mechanical stability of the catalyst layer over time is a critical issue. For instance, the constant evolution of oxygen bubbles during OER can cause delamination of the catalyst layer whilst the prolonged absorption of carbon dioxide from the air in contact with the alkaline electrolyte results in the progressive formation of carbonates in the catalyst layer - leading to a loss in porosity and reduction in active surface area available. Adequate catalyst stability and durability over a longer period of time will contribute to EES systems with longer cycling lifetimes, which in turn leads to greater cost efficiencies.

1.4. Research objectives

The main aim of this project is to improve the overall performance of the ORR and OER electrochemical reactions in the oxygen electrode for secondary alkaline systems whilst keeping costs low. This was achieved through the research objectives given below.

- To carry out a comprehensive literature review on oxygen electrodes focusing on the challenges associated with catalyst development for the associated electrochemical reactions, construction of electrodes with suitable materials and incorporation of the catalysts into a secondary electrode.
- To develop, characterise and optimise stable, efficient, scalable reaction-specific oxygen electrocatalysts with high activity from low cost, environmentally abundant materials.
- To incorporate these electrocatalysts into optimal electrode structures.
- To design a suitable secondary cell set-up to test these electrodes in.
- To assess the stability of the electrodes over an extended period of time and demonstrate their ability to operate over a range of current densities.

1.5. Outline of thesis

This thesis has been structured as follows: review, methodology, experimental results followed by conclusions and recommendations for further work.

In Chapter 1, a brief introduction of energy storage technologies for renewable energy sources is given along with a concise background of the oxygen electrode and its applications. The scope of the research is defined and challenges of developing a secondary oxygen electrode for alkaline systems are highlighted which are linked to the objectives of the work carried out. Chapter 2 presents an extensive review of the separate ORR and OER electrochemical reactions, with details of the current research status of catalyst development for these reactions. In addition, the pros and cons of proposed designs of secondary oxygen electrodes are weighed up. Based on the

literature review and taking the research objectives into account, Chapter 3 describes the methodology of the selection, synthesis, characterisation and assessment of the activity of suitable catalysts for ORR and OER. The parameters chosen for the physical and electrochemical characterisation techniques including experimental set-up and materials used are presented and reasons for selecting these are discussed. The experimental results and analysis of the findings are given in Chapters 4 to 8.

Chapter 4 focuses on the selection of a suitable ORR catalyst from a range of non-precious metal oxides and carbonaceous materials. The catalysts' oxygen reduction activity are assessed in both rotating disc electrode and gas diffusion electrode set-ups. Following this, Chapter 5 reports on the further optimisation of the catalytic performance of the selected catalyst by varying its synthesis parameters as well as the improvement of the ORR catalyst layer composition on the gas diffusion electrode. In a similar manner, Chapter 6 focuses on the selection of a suitable OER catalyst from a choice of transition metal oxides and hydroxides. Attempts to increase OER activity of selected Ni-Fe based metal hydroxide catalysts by optimising catalyst composition and altering the electrodeposition parameters are discussed in Chapter 7. In Chapter 8, the construction of a tri-electrode secondary cell set-up for the assessment of activity of the optimised ORR and OER electrodes in an operational system is described in detail. Lastly, Chapter 9 gives a summary of the conclusions from the results in relation to the aims of the research and provides suggestions for further work.

1.6. References

1. IRENA, *Global Energy Transformation: A Roadmap to 2050*. 2018, International Renewable Energy Agency: Abu Dhabi.
2. IRENA, *Renewable capacity highlights* 2018, International Renewable Energy Agency.
3. E. Union, Directive 2009/28/EC of the European Parliament and of the Council on the promotion of the use of energy from renewable sources and amending and subsequently repealing Directives 2001/77/EC and 2003/30/EC., Official Journal of the European Union L 140 (2009) 16-47.
4. E. Commission, *Europe leads the global clean energy transition: Commission welcomes ambitious agreement on further renewable energy development in the EU*. 2018, European Commission: Strasbourg.
5. Department for Energy and Climate Change (DECC) & Department for Environment and Rural Affairs (Defra), *Climate Change Act 2008*. 2008, United Kingdom: Climate Change Unit.
6. U.S. Energy Information Administration, *Annual Energy Outlook 2019*. 2019, Washington, DC: U.S. Department of Energy.
7. Energy Research Institute of Academy of Macroeconomic Research, *China Renewable Energy Outlook 2017*. 2017, China: China National Renewable Energy Centre.
8. I. Hadjipaschalis, A. Poullikkas, V. Efthimiou, Overview of current and future energy storage technologies for electric power applications, Renew Sus Energy Rev 13 (2009) 1513-22.
9. G.E. Agency. *dena Grid Study II – Integration of Renewable Energy Sources in the German Power Supply System from 2015 – 2020 with an Outlook to 2025*. 2010, Germany 17 of 26.
10. S. Sabihuddin, A.E. Kiprakis, M. Mueller, A numerical and graphical review of energy storage technologies, Energies 8 (2015) 172-216.
11. P. Krivik, P. Baca, Energy Storage – Technologies and Applications,A.F. Zobaa (ed), InTechOpen, 2013
12. D.N. Buckley, C. O'Dwyer, N. Quill, R.P. Lynch, Energy Storage Options and Their Environmental Impact,R.E. Hester, R.M. Harrison (ed), 2018
13. B.K. Kim, S. Sy, A. Yu, J. Zhang, Handbook of Clean Energy Systems(ed), John Wiley & Sons, Ltd, 2015
14. Z. Yang, J. Zhang, M.C. Kintner-Meyer, X. Lu, D. Choi, J.P. Lemmon, J. Liu, Electrochemical energy storage for green grid, Chem. Rev. 111 (2011) 3577-613.
15. S. Bradbury, A. Laguna-Estopier, P. Papadopoulos, *Electricity storage in GB: Final evaluation of the Smarter Network Storage solution*, in *Smarter Network Storage*. 2016: London.
16. J. Pan, Y.Y. Xu, H. Yang, Z. Dong, H. Liu, B.Y. Xia, Advanced architectures and relatives of air electrodes in Zn–air batteries, Adv. Sci. 1700691 (2018) 1-30.
17. K.M. Abraham, Z. Jiang, A polymer electrolyte ‐ based rechargeable lithium/oxygen battery, J. Electrochem. Soc. 143 (1996) 1-5.
18. K. F.Blurton, A. F.Sammells, Metal/air batteries: Their status and potential — a review, J. Power Sources 4 (1979) 263-79.
19. J. Cooper, Powering future vehicles with the refuelable zinc/air battery, LLNL Sci. Technol. Rev. 1995) 7-13.
20. J. Goldstein, I. Brown, B. Koretz, New developments in the Electric Fuel Ltd. zinc/air system, J. Power Sources 80 (1999) 171-9.
21. J. Baker, New technology and possible advances in energy storage, Energy Policy 36 (2008) 4368-73.
22. X. Luo, J. Wang, M. Dooner, J. Clarke, Overview of current development in electrical energy storage technologies and the application potential in power system operation, Appl. Ener. 137 (2015) 511-36.

23. A. Manthiram, An outlook on lithium ion battery technology, ACS Cent. Sci. 3 (2017) 1063-9.
24. J.S. Lee, S.T. Kim, R. Cao, N.S. Choi, M. Liu, K.T. Lee, J. Cho, Metal–air batteries with high energy density: Li–air versus Zn–air, Adv. Energy Mater. 1 (2011) 34-50.
25. R.D. McKerracher, C.P.d. Leon, R.G.A. Wills, A.A. Shah, F.C. Walsh, A review of the iron–air secondary battery for energy storage, Chem Plus Chem 80 (2014) 323-35.
26. T. Sadhasivam, K. Dhanabalan, S.-H. Roh, T.-H. Kim, K.-W. Park, S. Jung, M.D. Kurkuri, H.-Y. Jung, A comprehensive review on unitized regenerative fuel cells: Crucial challenges and developments, Int. J. Hydrogen Energy 42 (2017) 4415-33.
27. K. Zeng, D. Zhang, Recent progress in alkaline water electrolysis for hydrogen production and applications, Prog. in Energy and Combustion Sci. 36 (2010) 307-326.
28. G. Chisholm, L. Cronin, Storing Energy,T.M. Letcher (ed), Elsevier, 2016
29. T. Ioroi, K. Yasuda, Z. Siroma, N. Fujiwara, Y. Miyazaki, Thin film electrocatalyst layer for unitized regenerative polymer electrolyte fuel cells, J. Power Sources 112 (2002) 583-7.
30. J. Pettersson, B. Ramsey, D. Harrison, A review of the latest developments in electrodes for unitised regenerative polymer electrolyte fuel cells, J. Power Sources 157 (2006) 28-34.
31. S.R. Narayan, A.K. Manohar, S. Mukerjee, *Bi-Functional oxygen electrodes – Challenges and prospects*, in *The Electrochem. Soc. Interface*. 2015.

Chapter 2 The Oxygen Electrode in Alkaline Media

The earliest recording of the oxygen electrode was in 1789, observed in the decomposition of water into its constituents: oxygen and hydrogen [1]. This was fully investigated and described in 1800 by Nicholson and Carlisle [2]. The invention and demonstration of the fuel cell by Grove followed in 1839 [3] and by 1878 the first zinc-air battery was designed and patented by Maiche [4], involving the replacement of the manganese dioxide electrode in the Lelanché cell with a porous air electrode, coated with a platinum on carbon catalyst. This eventually led to the commercialisation of primary alkaline zinc-air batteries in 1932 [5] which are still used today in hearing aids and railway signalling. Around the same time in 1939, Bacon developed the alkaline fuel cell with circulating electrolyte enabling the use of non-noble metals whilst achieving high performance [3]. This technology was adopted by NASA in the 1960s for the Apollo lunar missions, without which the landings could not have taken place [3]. More recently, there has been a growing interest in rechargeable oxygen electrode systems such as unitized regenerative fuel cells (URFC) and secondary alkaline Zn-air cells, sparked by their potential application in vehicles [6, 7].

In this chapter, the literature has been organised into three sections. The oxygen reduction reaction is examined first, followed by the oxygen evolution reaction and finally the secondary oxygen electrode is discussed

2.1. The oxygen reduction reaction

Oxygen reduction reaction (ORR) usually takes place via the direct 4 or indirect 2 electron pathways [8, 9] depending on the chemical environment. Although these reactions can occur in both acidic and alkaline aqueous solutions as well as non-aqueous aprotic solvents [10], an aqueous alkaline electrolyte is more favourable due to the lower reaction overpotential at basic pH [11] and reduced likelihood of metal electrode corrosion, thereby allowing the use of non-precious metal catalysts [12]. The scope of this review is therefore limited to ORR and OER in aqueous alkaline environments. Under alkaline conditions the direct 4 electron pathway presented in equation (2.1) takes place at 0.401 V versus standard hydrogen electrode (SHE).

$O_2 + 2H_2O + 4e^- \rightarrow 4OH^-$ 0.401 V vs SHE (2.1)

The indirect 2-electron pathway leads to the production of peroxide as an intermediate which is either further reduced or decomposed by catalytic disproportionation seen in equation (2.2) to (2.4).

$O_2 + H_2O + 2e^- \rightarrow HO_2^- + OH^-$ -0.065 V vs SHE (2.2)

$HO_2^- + H_2O + 2e^- \rightarrow 3OH^-$ 0.867 V vs SHE (2.3)

$2HO_2^- \rightarrow O_2 + 2OH^-$ (2.4)

Generally, the direct 4 electron pathway is preferred since the reaction has a greater equilibrium potential than the 2 electron reaction leading to greater potential energy storage capacity per mole of oxygen. The direct 4 electron pathway also avoids the production of peroxide which contributes to corrosion of electrode components such as the catalyst and supporting substrate. Regardless of the pathway, an ORR catalyst's main function is to facilitate O-O bond breakage (e.g. O_2, O_2H) and O-H bond formation [13, 14]. A surface with higher reactivity binds adsorbates more strongly whilst a surface with lower reactivity promotes the formation of bonds between the adsorbates. To prevent the build up of adsorbates on the surface of the catalyst, which in turn slows down the rate of adsorprtion, dissociation and hydrogenation, a balance is sought between the rate of hydrogenation and binding strength of oxygen-containing fragments. Trends in the surface activity of metals have been inferred from their binding energies for both the O and OH in **Figure 2.1** where Pt and Pd are seen to be the most active catalysts for ORR.

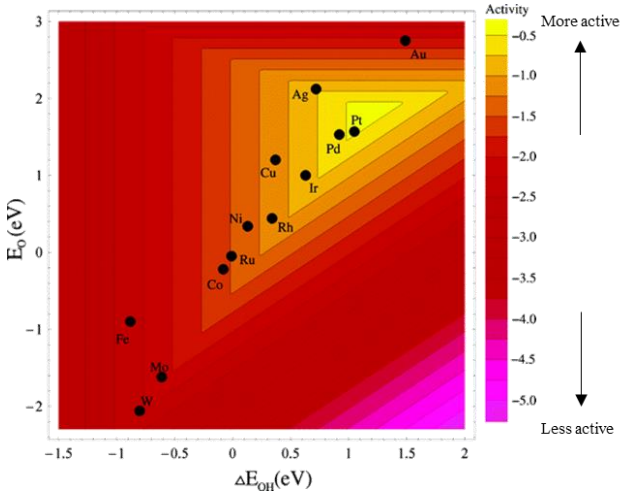

Figure 2.1 Relationship between binding energy of O and OH, and ORR catalytic activity [15].

There are several published reviews [6, 16, 17] on oxygen reduction reaction catalysts in aqueous alkaline electrolytes, these materials can be categorised into

- Precious metals and their alloys
- Non-precious metal oxides
- Non-metals
- Transition metal macrocycles

From a practical perspective, three aspects which must be taken into consideration when selecting materials for catalysts are elemental abundance, price, and supply risk. Seen in **Figure 2.2 a** [18], precious metals Ag, Au, Pt and Ru are least abundant as expected. On the other hand, rare earth elements (e.g. La, Ce, Pr etc.) appear to be on par with transition metals (e.g. Ni, Cu, Zn and Co) whilst transition metals Mn and Fe are ~1000 times more abundant than rare earth elements. As shown in **Figure 2.2 b** [19], the price of these metals has a negative relationship with their abundance. The more abundant the metal, the cheaper it is.

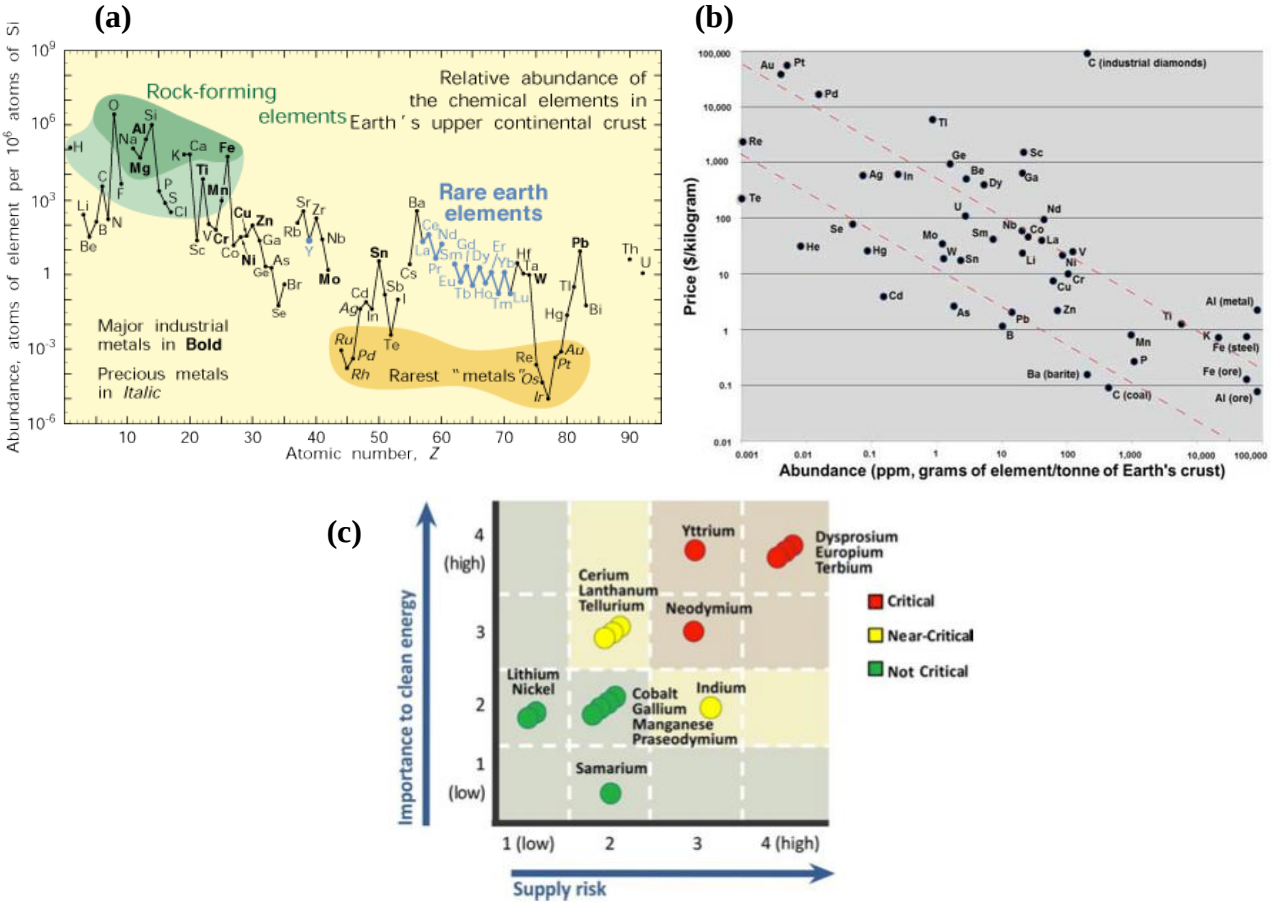

Figure 2.2 a) Plot of abundance of chemical elements in the Earth's upper continental crust versus atomic number [18], **b)** Price per kg of elements versus abundance in the Earth's crust [19], **c)** Projections of the demand and supply of rare earth elements [20].

Figure 2.2 c [20] illustrates a plot of the “importance to clean energy” versus “supply risk” of the material. Some rare earth elements e.g. Dy, Nd, Y etc. are defined as critical or near-critical as they are high in supply risk but equally high in importance to clean energy. The dependency on the geopolitics of the countries that these elements can be obtained from also make the supply unpredictable.

2.1.1. ORR catalysts

2.1.1.1. Precious metals and their alloys

Precious metals such as Pt, Pd, Au and Ag [21-25] are considered the most effective ORR catalysts due to their inert quality in aqueous electrolytes and their distinct preference for the direct 4 electron pathway. On noble metals, the ORR has been proven to be structure sensitive [26-28], such that catalyst structure is more important than that of the surface area available or degree of dispersion.

Large pieces or slabs of these noble metals can be employed in systems as electrodes but their high cost makes this option unattractive. Measures have been taken to avoid using bulk noble metal electrodes by dispersing nanoparticles of these noble metals, using methods such as electrodeposition, functional ion adsorption or vacuum sputtering, onto various conductive carbon supports [29-33] like charcoal, acetylene blacks, carbon blacks, and furnace blacks [34]. However, the size of the catalyst nanoparticles [35-38] was seen to have a complex effect on the ORR activity of the two reduction pathways as these pathways occur at different active sites on the catalyst. As such, further efforts have also been made to enhance the ORR electrolytic activity by increasing the selectivity for specific surface sites which are more active for the direct 4 electron pathway, such as the preferential growth of cubic Au with (100) domains [39].

More recent attempts to increase the catalytic activity of precious metals include alloying to create a variety of carbon supported binary, and ternary alloys such as PtCo, PtNi, AgCo, PdNi, Pd-Cu-Ni, Co-Au-Pd, Pt-Co-Ni etc. [40-44]. The combination of two or more noble metals such as PdAg, AuPt, PtRu, Ir-Pt-Au etc. [45-48] have also been reported to improve electrocatalytic activity. Nevertheless, although precious metals are excellent electrocatalysts for ORR in an alkaline environment, their high cost and

scarcity are cause for concern. In this study Pt on carbon has been employed solely as an activity benchmark.

2.1.1.2. Non-precious metals

Of the non-precious metals, a large proportion consists of transition metals. Transition metals or ions are an obvious choice for electrocatalysts due to their variable oxidation states which mean electronic energy levels for receiving electrons and cleaving bonds are more likely to be available [49, 50]. On top of that, they are typically more environmentally abundant, low in cost and are able to be prepared with a variety of methods. Two common families of transition metal oxide crystal structures are spinels and perovskites. Spinels are normally composed of divalent and trivalent transition metal ions whilst perovskites frequently consist of rare-earth metals in combination with a transition metal. Considering the abundance, cost and ease of access to rare earth metals, perovskites were not selected for comparison in this work and more emphasis has been placed on spinel transition metal oxides in this review as they are believed to be more cost-effective for future applications.

A screening study [51] of thirty transition metal oxides revealed that only oxides of manganese, iron, cobalt, and nickel displayed earlier onset potentials for ORR (marked in red in **Figure 2.3**) when compared to bare glassy carbon, signifying improved electrocatalytic activity towards ORR. As such, single and mixed oxides of these transition metals were further examined in the literature.

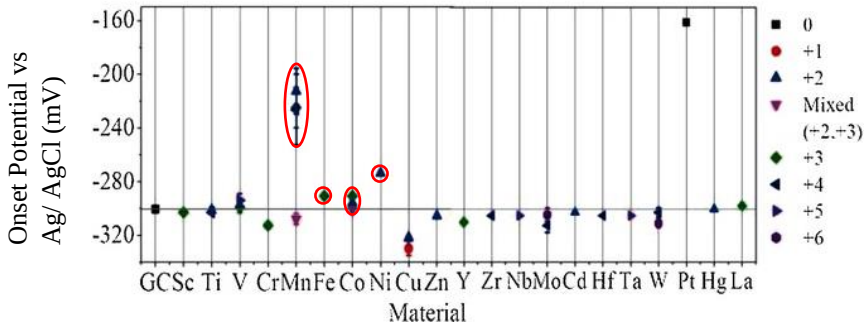

Figure 2.3 Plot of onset potential of various transition metal oxides extracted from linear sweep voltammograms of oxygen reduction in air-saturated 0.1 M KOH, scan rate 5 mV s^{-1} [51].

Single metal oxides

As a metal, manganese is inexpensive, much more widely available compared to precious metals and low in toxicity [52-54]. To date, manganese oxides are one of the most well investigated oxides, first proposed by Leclanché to be used in Zn-MnO_2 cells in 1868 [55]. An early technical review of the manganese dioxide electrode by Vosburgh [56] in 1959 summarised the vast amount of literature on properties of MnO_2 and the MnO_2 electrode discharge mechanism. More interest in the understanding of the cathodic reduction of manganese oxides in alkaline electrolytes followed in the 1960s [57-64] and later studies on the ability of Mn-based oxides and hydroxides to catalyse the decomposition of hydrogen peroxide [65, 66] eventually led to work being carried out on characterising manganese oxides as oxygen reduction electrocatalysts [67]. These studies highlighted the oxides and hydroxides of manganese which are active as oxygen reduction catalysts in alkaline media, namely MnO_2, Mn_2O_3, Mn_3O_4, Mn_5O_8 and MnOOH [68], as well as the properties of various crystalline phases and oxidation states of manganese (Mn^{2+}, Mn^{3+} and Mn^{4+}) which contribute towards its activity and selectivity as a catalyst.

The oxygen reduction mechanism on MnO_2 has long since been a subject of contention. Zoltowski *et al*. [69] first reported the application of redox couple Mn^{3+}/ Mn^{2+} in a carbon-air electrode for fuel cells and secondary cathodes in alkaline systems citing Kozawa and Yeager's [60] discharge mechanism. In this mechanism, a homogenous phase reaction (Mn^{4+} to Mn^{3+}) takes place via an electron-proton mechanism followed by a heterogeneous dissolution-precipitation (Mn^{3+} to Mn^{2+}) system. It was proposed by Cao *et al.* [70] that the electroreduction of MnO_2 occurred simultaneously with the reduction of oxygen. Following this, a study by Mao *et al.* [71] showed that MnO_x catalysts displayed high activity for the heterogeneous disproportionation of HO_2^- to O_2 and OH^- which led to an overall 4 electron pathway. Subsequently, Lima *et al.* [72, 73] confirmed that ORR activity was enhanced by the presence of MnO_2 for the initial reduction of Mn^{4+} to Mn^{3+}, which is associated with the reduction of O_2 to HO_2^-. More recent investigations by Roche *et al.* [74] and Valim *et al.* [75] demonstrated that ORR can take place on MnO_x supported on carbon via the complete 4 electron or indirect 2 electron pathway.

Although it was the intrinsically low conductivity of MnO_2 which prompted researchers to add a conductive carbon support, the carbon chosen for the composite was found to affect the structure of the catalyst layer as well [76]. A porous carbon material is more likely to provide efficient gas diffusion pathways creating more suitable three-phase interfaces for ORR to take place at, thereby increasing the rate of ORR. The ratio of Mn_yO_x to C was also seen to have an effect on the ORR reaction pathway [77]. With a lower concentration of Mn_yO_x, the 2 electron pathway was dominant resulting in the formation of HO_2^- ions. However with a higher concentration of Mn_yO_x to C, the 4 electron mechanism was detected as more disproportionation of HO_2^- took place.

The structural and electronic properties and consequently the catalytic activity of MnO_x are closely related to its composition, crystal phase and morphology [78]. Varying preparation conditions can help to control the thermodynamic growth of MnO_x to produce desired phases and morphologies. Common synthesis methods of metastable porous manganese oxides were described in detail in a review by Brock *et al.* [79], such as precipitation, hydrothermal, ion-exchange, sol-gel and high temperature solid-state. Additionally, other chemical and electrochemical methods for example thermal decomposition, electrodeposition and sonochemistry *etc.* [68, 77, 80, 81], have been illustrated as methods of synthesising amorphous and polymorphic structures of manganese dioxide (e.g. α-MnO_2, β-MnO_2, γ-MnO_2, δ-MnO_2). Amorphous structures, in particular, are attractive as they are likely to be energetically favourable for all oxygen adsorption surface configurations [76]. According to Yang and Xu [82], larger concentrations of lattice defects and active sites present within the bulk of the distorted structure of an amorphous nanoporous manganese oxide lead to greater catalytic activity. Other advantages of an amorphous material are that they are naturally more corrosion resistant and more variation in the catalyst composition can be achieved.

An early study by Bagotzky *et al*. [83] showed that oxides with spinel structures such as Co_3O_4 and $NiCo_2O_4$ obtained by thermal oxidation at temperatures greater than 300ºC displayed greater electrocatalytic activities compared to simple nickel oxides formed on the surface of pure Ni. This was suggested to be due to the presence of bi- and tri-valent cations in the spinels which act as donor-acceptor sites for the chemisorption of oxygen. Generally, cations of higher oxidation states on the surface

of the electrocatalyst such as Co^{3+} are considered active for ORR [84, 85], and tailoring the distribution and frequency of these sites across the catalyst surface, for example by altering the morphology of the catalyst [86, 87] is expected to improve ORR activity.

Similar to carbon composites of MnO_x, the inclusion of an electro-conductive carbon material to these spinels plays a complex role in the ORR process. As the $2e^-$ pathway is normally dominant on oxides and hydroxides of Co [88, 89], the physical addition of carbon was observed to not only enhance the ORR current by facilitating electron transfer, but also improve the likelihood of interaction between the intermediate products of HO_2^- and the electrode surface as described by the 'trapped effect' [90, 91]. Moreover, the combined ability of carbon materials such as graphene or N-doped graphene oxide [92, 93] to assist in the reduction of O_2 to HO_2^- and cobalt oxide to reduce HO_2 to OH^-, contributes to favourable increases in electron transfer number and ORR activity. In addition, as the efficiency of the catalytic reactions is influenced by the distribution of cobalt oxide catalysts over the carbon support [94], reducing the size of the catalyst particles on the carbon support serves to increase the interfacial area, thereby promoting the production of HO_2^- [95].

A benchmarking study [96] of first row transition metal oxides on CNTs concluded that MnO_x and CoO_x were most active for ORR, based on their earlier onset potentials (marked in red in **Figure 2.4**) and ability to reduce peroxide to hydroxide for the indirect $2e^-$ pathway even at low overpotentials. This in combination with reported ORR performance values in **Table 2.1** reaffirms the selection of metal oxides of Mn and Co as potential ORR catalyst candidates in Chapter 4. The presence of carbon in the catalyst layer of these single metal oxides is clearly beneficial and the effect of this will be investigated in Chapters 4 and 5.

(a)

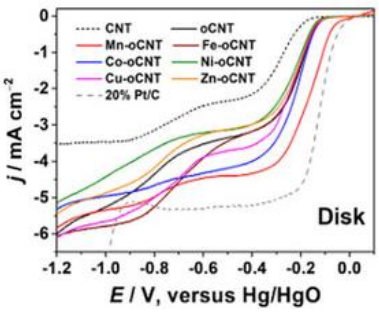

(b)

Table 2. A summary of ORR activity parameters and the behavior for M-oCNTs.

Sample	E_{onset} [V, Hg/HgO]	Tafel slope [mV dec^{-1}]	$j_0 \times 10^{-6}$ [a] [mA cm^{-2}]	j_{O2P}@−0.4 V [mA cm^{-2}]	j_{P2H}@−0.4 V [mA cm^{-2}]	n @−0.4 V	%HO_2^- [%] @−0.4 V	E_{onset} upshift? (vs. oCNT)	Capability to reduce peroxide
20% Pt/C	+0.00	62.7	42.2	−2.66[b]	−2.55[b]	3.91	4.3	n/a	strong
oCNT	−0.12	58.0	0.44	−2.30	−0.88	2.76	61.8	n/a	weak
Mn-oCNT	−0.05	61.7	17.3	−2.40	−1.94	3.62	19.0	yes	strong from −0.07 V
Fe-oCNT	−0.12	56.0	0.19	−2.28	−0.90	2.79	60.6	no	strong from −0.50 V
Co-oCNT	−0.11	62.2	1.92	−2.42	−1.59	3.32	34.1	no	moderate from −0.15 V
Ni-oCNT	−0.13	56.8	0.21	−2.20	−0.79	2.71	64.3	no	weak
Cu-oCNT	−0.12	67.3	6.41	−2.62	−0.95	2.73	63.6	no	strong from −0.60 V
Zn-oCNT	−0.12	67.3	4.60	−2.20	−0.78	2.71	64.5	no	weak

[a] Extrapolated to the thermodynamic potential in 0.1 M KOH; [b] denotes the equivalent $jO2P$ and $jP2H$ for 20% Pt/C.

Figure 2.4 a) RRDE linear sweep voltammograms of various M-oCNTs in O_2 saturated 0.1 M KOH, scan rate of 10 mV s^{-1} at 1600 rpm. **b)** Table summarising the activity parameters of the M-oCNTs tested [96].

Table 2.1 ORR performance of single metal oxides of Mn and Co.

Catalyst	Electrode substrate	Preparation method	Performance (onset potential and electron transfer number, *n*)	Stability	Ref
Amorphous manganese oxides	GC electrode	$KMnO_4$ soln + oxalic acid soln	-0.14 V vs SCE in 0.1 M KOH, 22 ºC +/- 2 ºC, (O_2 sat.) $n \approx 2.5$	-	[50]
α-MnO_2		Solid state method	-0.14 V vs SCE in 0.1 M KOH, 22 ºC +/- 2 ºC, (O_2 sat.) $n \approx 3.7$	-	
α-MnO_2 nanowires	GC electrode	Hydrothermal	0.1 V vs Ag/AgCl in 0.1 M KOH, (O_2 sat.) $n \approx 3.1$	-	[97]
β-MnO_2			-0.045 V vs Ag/AgCl in 0.1 M KOH, (O_2 sat.) $n \approx 2.7$	-	
α-MnO_2 nanowires + carbon black			0.06 V vs Ag/AgCl in 0.1 M KOH, (O_2 sat.) $n \approx 3.8$	-	
MnO-oCNT	GC electrode	Addition of mildly oxidised CNTs to metal sulphate soln with heating and stirring.	-0.05 V vs Hg/HgO, in 0.1 M KOH, (O_2 sat.) $n \approx 3.62$	-	[96]
CoO-oCNT			-0.11 V vs Hg/HgO, in 0.1 M KOH, (O_2 sat.) $n \approx 3.32$	-	
Amorphous MnO_x spheres	GC electrode	Reflux	-0.25 V vs Hg/HgO, in 0.1 M KOH, (O_2 sat.)	-	[76]
Amorphous MnOx nanowires/ketjen black			-0.05 V vs Hg/HgO in 0.1 M KOH, (O_2 sat.)	-	
Co_3O_4	GC electrode	Thermal decomposition	-0.149 V vs Hg/HgO in 1 M KOH, 298 K (O_2 sat.)	-	[98]
Co_3O_4 nanocrystals	GC electrode	Hydrothermal	0.83 V vs RHE, (≈-0.157 V vs SCE) in 0.1 M KOH, 25 ºC, (O_2 sat.) $n \approx 3.57$	-	[99]
Co_3O_4 nanocrystals + XC-72R			0.85 V vs RHE (≈-0.137 V vs SCE), in 0.1 M KOH, 25 ºC, (O_2 sat.)	-	
Co_3O_4 nano-octehedrons/ RGO	GC electrode	Chemical synthesis + hydrothermal	-0.06 V vs Hg/HgO in 0.1 M KOH, room temp, (O_2 sat.) $n \approx 4.0$	No current density decay after 2.8 h at -0.40 V at 2400rpm.	[100]
Co_3O_4 nanocrystals/ rmGO	GC electrode	Hydrolysis and oxidation	0.88 V vs RHE (≈-0.11 V vs SCE) in 0.1 M KOH, (O_2 sat.) $n \approx 3.9$	Teflon-treated carbon fibre paper GDE: No current density decay after 2.8 - 6.9 h at 0.7 V vs RHE in 0.1M, 1M and 6M KOH.	[92]

Mixed metal oxides

Mixed valence spinel oxides tend to possess better electrical conductivity allowing them to be used directly as catalyst materials. Due to the presence of cations of different valencies, pathways of low activation energies are available for electron transfer. The ORR mechanism at Co_3O_4 and $NiCo_2O_4$ without the inclusion of a carbon support was investigated by Sömnez *et al.* [98]. The 4 electron pathway was found to be dominant on $NiCo_2O_4$ whilst it appeared that the 2 electron pathway was more prevalent on Co_3O_4. It was also observed from reaction overpotentials and limiting current density, that $NiCo_2O_4$ is a better ORR electrocatalyst compared to Co_3O_4. The substitution of Co^{2+} and Co^{3+} for Ni in the Co_3O_4 structure was suggested to stabilise the Co^{3+} surface species [101] which is recognised as an active site for ORR for O_2 adsorption. Additionally, the stoichiometric composition of $NiCo_2O_4$ was proposed to have a higher surface concentration of Co^{3+} and Ni^{3+} species [102]. The ORR catalytic activity of mixed spinels of nickel and cobalt oxides prepared via co-precipitation, freeze drying and thermal decomposition of mixed nitrates were examined by King and Tseung [103]. It was acknowledged that the method of synthesis affected the chemical and physical properties of the resultant oxide, such as composition, electrical conductivity, crystal structure, ferromagnetism, and surface area. A follow-up study by the same group [104] noted that the availability of Co at the tetrahedral sites of the spinel was essential to ORR activity.

Although the addition of a carbon support to $NiCo_2O_4$ has not been researched specifically for its influence on the ORR mechanism it has been suggested to help with the dispersion of metal oxide particles, thereby increasing surface area, preventing agglomeration and acting as a highly conductive network for efficient electron transfer. More recently, further attempts have been made to increase activity of $NiCo_2O_4$ by fabricating three-dimensional morphologies for instance spheres, wires or flowers, macro-porous sheets and other hierarchical nanostructures [105-107]. Such morphologies and structures are likely to enhance conductivity, increase surface area and enrich the porosity – which improves gas diffusion pathways to facilitate the movement of O_2 [108].

An investigation [109] on the structural and electronic properties of $MnCo_2O_4$ showed that doping Co_3O_4 with Mn resulted in the occupation of the octahedral sites

with Mn^{3+}, whilst half of the Co were present as Co^{2+} at the tetrahedral sites and the other half as Co^{3+} at the octahedral sites. Rios *et al.* [110] proposed that ORR activity was correlated to the Mn content as the reaction was facilitated by the manganese Mn^{4+}/Mn^{3+} redox pairs present in the octahedral sites of the inverse spinel of $MnCo_2O_4$. However, a few studies [111, 112] have since suggested that both Mn^{3+} and Co^{3+} ions show activity for ORR. Regardless, it is clear that the Mn sites are considered to be more active than the Co sites for ORR [113] and the substitution of Mn^{3+} in the octahedral sites of the mixed Mn-Co spinel is beneficial to the ORR activity. Furthermore, the crystal phases of these Mn-Co mixed spinel oxides are closely related to the ratio of metal cations whereby a greater percentage of Mn results in a tetragonal crystal structure and conversely a lower quantity of Mn tends to form a cubic crystal structure [114]. These structures are noted to have an effect on the ORR mechanism with the cubic structure recognised as having better activity for ORR [111, 115, 116]. This is believed to be due to the surface of the cubic spinel having a higher proportion of catalytic sites available with greater oxygen adsorption binding energies at Co and Mn defect sites [117, 118] and a higher mean oxidation state for Mn as a result of the mixture of Mn^{3+}/Mn^{4+} cations.

The direct nucleation or covalent attachment of $MnCo_2O_4$ nanoparticles onto a conductive carbon support [119, 120], as opposed to the physical mixture of spinel and carbon material, has been shown to enhance ORR activity. This is due to the formation of C-O-metal bonds which assist in facilitating charge-transfer in the catalyst layer. Additionally, the dispersion of the metal oxide particles over the carbon support gives rise to a greater electrochemically active surface area.

Equally, the partial substitution of Co in Co_3O_4 with Fe or Cu was observed to incur different effects on catalytic activity. Systematic studies conducted by Cota *et al.* [121] on 14 different catalysts in potassium hydroxide concluded that cobalt ferrite, $Co_{1.1}Fe_{0.9}O_4$, showed considerable activity for the decomposition of hydrogen peroxide. As cobalt-iron oxides were subsequently shown to have negligible activity for oxygen reduction [122], it was necessary for these oxides to be combined with graphite, at which the two electron indirect reduction of O_2 to HO_2^- takes place. Marsan *et al.* [123] reported higher current densities for ORR at $CuCo_2O_4$ compared to Co_3O_4 due to the greater abundance of Co^{3+} and Cu^{2+} cations on the surface which acted as sites for O_2 adsorption. The significance of a suitable synthesis method to produce

phase pure $CuCo_2O_4$ was highlighted in an investigation where [124] the spinel prepared by a sacrificial support method displayed most active ORR performance due to the lower amount of CuO, which was found to have poor electrical conductivity and low catalytic activity for ORR. Similarly, when compared to other M^{2+} substituted $M_xFe_{3-x}O_4$, $Mn_xFe_{3-x}O_4$ spinels have shown promising activity for both ORR [125] and peroxide decomposition [126] ascribed to the presence of Mn^{3+}/Mn^{2+} which is crucial for both reactions.

Table 2.2 ORR performance of mixed transition metal oxides.

Catalyst	Electrode substrate	Preparation method	Performance (onset potential and electron transfer number, n)	Stability	Ref
$NiCo_2O_4$	GC electrode	Thermal decomposition	-0.06 V vs Hg/HgO in 1 M KOH, 298 K (O_2 sat.) $n \approx 4$	-	[98]
3D macroporous $NiCo_2O_4$	GC electrode	Hydrothermal	-0.1 V vs Ag/AgCl in 0.1 M KOH, 25 ºC +/- 1 ºC, (O_2 sat.) $n \approx 3.8$-4	Retained 70% current density after 100 h at -0.3 V.	[101]
$NiCo_2O_4$ urchin-like nanostructures	GC electrode	Hydrothermal	-0.1 V vs Ag/AgCl in 0.1 M KOH, room temp. (O_2 sat.) $n \approx 4.0$	Retained 87% current density after 1000 CV cycles.	[102]
$NiCo_2O_4$ hollow nanospheres	GC electrode	Hydrothermal	0.77 V vs RHE, in 0.1 M KOH, room temp. (O_2 sat.) $n \approx 3.0$-4.0	Retained 93.4% current density after 12 h at 0.61 V vs RHE.	[127]
$NiCo_2O_4$/ ordered mesoporous carbon, CMK-3	GC electrode	Hydrothermal	-0.09V vs Ag/AgCl in 0.1 M KOH (O_2 sat) $n \approx 3.8$-3.9	-	[128]
$Mn_{0.4}Co_{1.6}O_4$	GC electrode	Sonochemical	0.9 V vs RHE in 0.1 M KOH, (O_2 sat.) $n \approx 4.0$	Retained 85% current density after 2.8 h at 0.47 V vs RHE at 1600 rpm.	[111]
$CoMn_2O_4$/ C	GC electrode	Thermal annealing of carbonates	0.9 V vs RHE, 0.1 M KOH (O_2 sat.) $n \approx 3.68$	No current density decay after 8.3 h at 0.8 V vs RHE.	[112]
$MnCo_2O_4$/ C			0.87 V vs RHE, 0.1 M KOH (O_2 sat.) $n \approx 3.51$		
$MnCo_2O_4$	GC electrode	Spray pyrolysis	0.95 V vs RHE, 0.1 M KOH (O_2 sat.) $n \approx 3.94$	Retained 85% current density after 10 h at -0.3 V vs Ag/AgCl at 1600 rpm.	[113]
Cubic $CoMn_2O_4$	GC electrode	Oxidation-precipitation crystallisation	0.91 V vs RHE, 0.1 M KOH, (O_2 sat.) $n \approx 3.83$	-	[116]
Cubic $CoMn_2O_4$/C			0.95 V vs RHE, 0.1 M KOH (O_2 sat.) $n \approx 3.91$	Retained 91.5% current density after 50 h at 0.8 V vs RHE.	

2.1.1.3. Non-metals

As well as being another low-cost alternative to precious metals, carbonaceous materials are widely available with high electrical conductivity and large surface areas. The allotropes of carbon relevant to electrochemistry are graphite, diamond and fullerenes [129]. Graphite is composed of sp^2 hybridised carbon atoms in a structure consisting of stacks of two-dimensional graphene sheets, whilst diamond consists of sp^3 hybridised carbon atoms in a tetrahedral arrangement which results in low conductivity. Carbon nanotubes, the most commonly used fullerene electrode material, are made of one or several graphene layers rolled up to form tubes. Due to the favourable electrical conductivity of graphitic materials [130], these are usually more appropriate for electrode applications.

The electrochemical activity for oxygen reduction of these carbon materials was determined to be directly influenced by the surface area [131], morphology [132] and surface sites [133]. For instance, carbon nanotubes with corrugated walls performed better than carbon nanotubes with smooth walls due to the greater presence of edge and defect sites which are active for ORR. This was confirmed by a study [134] of ball-milled graphite and carbon which concluded that the edge atoms of graphene showed more ORR activity over the basal-plane atoms. In addition to this, the electroreduction of oxygen at carbon-based materials is also dependent on pH [135] with both unmodified and, in some cases, modified carbon materials displaying considerably better ORR performance in a basic than an acidic solution [136, 137].

To improve the ORR performance of these carbon materials, one or more heteroatoms with differing electron negativities such as nitrogen, boron, oxygen, phosphorus, sulphur, fluorine etc. [138] have been introduced into the carbon to vary its nanostructure. Based on experimental results and theoretical calculations, this is suggested to be due to the redistribution of charge on the carbon atoms from the electron movement between the heteroatoms and adjacent carbon atoms. A systematic study carried out by Jiao *et al.* [139] of five heteroatom B, N, P, O and S doped-graphene materials indicated that B and N-doped graphene were the most active ORR catalysts. In (**Figure 2.5 a**), the B and N-doped graphene catalysts have the smallest Tafel slope values from RDE experiments and which corresponds to the

volcano plots (**Figure 2.5 b**) obtained with DFT calculations these catalysts show closest performance to Pt.

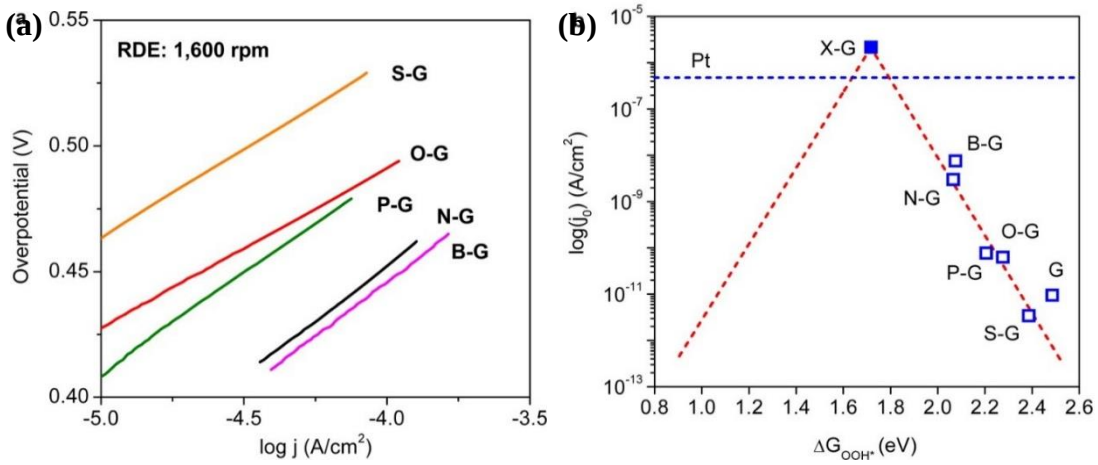

Figure 2.5 a) Tafel slope plots for the single-doped graphene catalysts from experimental ORR polarisation plots collected at 1600 rpm **b)** Volcano plot of DFT calculated ΔG_{OOH^*} against log j_0 theoretical values obtained. The blue squares are representative of the j_0 experimental values obtained from Tafel plots [139].

One of the first reports of the utilisation of an N-doped graphene electrocatalyst for ORR was by Dai *et al*. [140]. It has since become the most extensively utilised heteroatom for doping as it is of a similar size to carbon with one extra electron in its outer shell [141]. Owing to the high electronegativity of nitrogen, the doping of graphene with nitrogen is suggested to result in the formation of positively charged carbon atoms which facilitate the adsorption of oxygen molecules for ORR [142]. In addition, the nitrogen is suggested to create defects on the carbon surrounding it, causing greater exposure of the edge plane which promotes ORR activity. Other dopants such as boron, phosphorus and sulphur have a much lower electronegativity than carbon however, and are more inclined to donate electrons to the carbon atoms which results in the dopant becoming slightly positively charged instead. The active sites on B, P and S- doped carbons are therefore believed to be the charged B, P or S atoms [143, 144].

The incorporation of two or more heteroatoms into a carbon material results in greater ORR electrocatalytic activity than its corresponding single-heteroatom doped carbon counter-parts due to the synergistic effects on catalysis. For example as doping of multi-walled carbon nanotubes occurs at defect sites in the C-C structure, co-doping N with S was shown to enable more pyridinic N to be incorporated into the sp^2 carbon atom network [145, 146]. Equally, co-doping of multiple heteroatoms P, N and S into

mesoporous graphene [147] was proposed to lead to a combination of complementary effects such as the creation of P^+ and C^+ charge sites, more carbon edge site exposure and higher carbon spin density which enhanced ORR activity.

Table 2.3 ORR performance of doped and non-doped carbonaceous materials.

Catalyst	Electrode substrate	Preparation method	Performance (onset potential and electron transfer number, n)	Stability	Ref
N-doped graphene	GC electrode	CVD	-0.20 V vs. Ag/AgCl in 4 M KCI, in 0.1 M KOH, 25 ºC (O_2 sat.) $n \approx 3.6$ to 4	-	[140]
S-doped graphene	GC electrode	Thermal annealing	-0.14 V vs. Ag/AgCl, in 0.1 M KOH, room temp. (O_2 sat.) $n \approx 3.82$	Retained 91.1% of current density after 5.6 h at -0.3 V vs Ag/AgCl.	[148]
Graphene	GC electrode	Thermal annealing	-0.15 V vs. Ag/AgCl, in 0.1 M KOH, room temp. (O_2 sat.) $n \approx 2.59$	-	[144]
S-doped graphene			-0.11 V vs. Ag/AgCl, in 0.1 M KOH, room temp. (O_2 sat.) $n \approx 3.81$	Retained 70.3% of current density after 5.6 h at -0.3 V vs Ag/AgCl.	
N-doped graphene			-0.09 V vs. Ag/AgCl, in 0.1 M KOH, room temp. (O_2 sat.) $n \approx 3.99$	Retained 67.9% of current density after 5.6 h at -0.3 V vs Ag/AgCl.	
B-doped graphene	GC electrode	Thermal solid state reaction	-0.12 V Ag/AgCl, in 0.1 M KOH at room temp. (O_2 sat.) $n \approx 2.3$-2.7	-	[149]
N-doped graphene			-0.09 V vs Ag/AgCl, in 0.1 M KOH at room temp. (O_2 sat.) $n \approx 2.3$-2	-	
Ketjen black	-	Reflux	-0.13 V vs. Hg/HgO, in 0.1 M KOH, (O_2 sat) $n \approx 3.4$	-	[150]
N-doped ketjen black			-0.08 V vs. Hg/HgO, In 0.1 M KOH, (O_2 sat) $n \approx 3.6$		
N & S-doped GO	GC electrode	Reflux	~-0.015 V vs. Hg/HgO, in 0.1 M KOH (O_2 sat) $n \approx 3.5$	Retained 80% of current density after 2.8 h at -0.6 V vs Hg/HgO.	[146]
P, N & S-doped porous carbon	GC electrode	Electrostatic assembly method + carbonization	0.9 V vs RHE, in 0.1 M KOH, room temp (O_2 sat.) $n \approx 3.68$-3.96	Retained 86.6% of current density after 16.7 h at 0.7 V vs RHE.	[147]

2.1.1.4. Transition metal macrocycles

The application of transition metal macrocycles, in particular cobalt phthalocyanine, as a fuel cell cathode catalyst was pioneered by Jasinski [151, 152] in the mid-1960s. Since then, N_4 chelate macrocycle complexes such as porphyrins and phythalocyanines containing non-stoichiometric non-precious metals have been investigated for their oxygen reduction activity. The transition metal assigned as the central metal atom of the macrocycle has been proposed to function as the active sites for ORR [153, 154]. As such, both cobalt and iron phthalocyanines and porphyrins have been demonstrated to be most active for oxygen reduction in alkaline media [155, 156].

The monomeric form of these catalysts is prone to aggregation, and dispersion over a carbon support material is necessary to prevent agglomeration whilst enhancing electrical conductivity [157]. Alternatively, the polymeric forms of these catalysts exhibit better chemical and thermal stability, higher electrical conductivity and lower catalytic activity; however they are usually associated with more costly methods of synthesis, of which the key step is a high temperature pyrolysis step in the absence of oxygen. Although non-pyrolysing methods of synthesis exist, they are often more complex. Hence, owing to the limitations of the synthesis of macrocycles, it was decided that this category of catalysts would not be included in this work.

2.1.2. Summary

The review of the literature shows that a substantial amount of work has gone into synthesising and testing various groups of materials deemed to be active for oxygen reduction. The inclusion of a carbon support in the catalyst layer is frequently mentioned and demonstrated to be beneficial for ORR performance. In addition, a large number of catalyst studies tend to focus on defining the ORR reaction kinetics using RDE and RRDE set-ups, however fewer studies have incorporated these catalysts into gas diffusion electrodes (GDE) in order to establish the operational performances of these catalysts at practical current densities. These points will be addressed in the following research chapters.

2.2. The oxygen evolution reaction

The oxygen evolution reaction (OER) is a key reaction in several anodic processes such as water electrolysis or in a secondary oxygen electrode. The production of one molecule of water in either acidic or alkaline environment requires four electrons in total. Since the transfer of multiple electrons is not kinetically favourable, the mechanism of oxygen evolution comprises several intermediate states. This leads to a build-up of energy barriers which contributes to slow reaction kinetics. Under alkaline conditions, there are a number of proposed pathways suggested by Krasil'schchikov [158], Yeager [159, 160] and Bockris [161, 162].

In the potential region of the OER reaction, an oxide layer is always formed even if an inert metal is used. The growth of these metal oxide layers is inevitable as the reaction proceeds. Hence, the reaction either takes place on thin oxide films of noble metals such as Pt, Au, Ir, Rh and Ru or thicker oxide films of non-noble metals such as Ni, Co and Pb. In general, the OER mechanism which takes place at a metal oxide surface under alkaline conditions can be described by the following elementary steps [163, 164]. Firstly, water dissociates on the metal oxide surface to form OH_{ad}.

$$OH^- \rightarrow OH_{ad} + e^- \qquad (2.5)$$

OH_{ad} is considered to be further oxidised to O_{ad}.

$$OH_{ad} + OH^- \rightarrow O_{ad} + H_2O + e^- \qquad (2.6)$$

In some cases, it is suggested that two O_{ad} intermediates recombine to form a molecule of O_2.

$$O_{ad} + O_{ad} \rightarrow O_2 \qquad (2.7)$$

Alternatively, a superoxide intermediate OOH_{ad} is formed which acts as a precursor to the formation of O_2

$$O_{ad} + OH^- \rightarrow OOH_{ad} + e^- \qquad (2.8)$$

$$OOH_{ad} + OH^- \rightarrow O_2 + H_2O + e^- \qquad (2.9)$$

The OER intermediates are therefore OH_{ad}, O_{ad} and OOH_{ad}. These intermediates are important as the catalytic activity of a metal oxide surface for oxygen evolution can be predicted from their binding energies. According to the Sabatier principle [165, 166],

optimum catalysts should not bind to adsorbates too weakly as the reaction may not take place but also not too strongly or desorption will occur too slowly or not at all, poisoning the catalyst. Consequently, the binding energy of atomic oxygen $\Delta E_{O_{ad}}$ has been used as an activity descriptor for OER. Alternatively $\Delta G_{O_{ad}} - \Delta G_{OH_{ad}}$, which depends on the assumption that the pristine (001) surface is representative of the catalyst during OER, is seen to be a universal descriptor of OER activity for several classes of catalyst materials [163, 167, 168]. Examples of volcano plots based on these activity descriptors are given in **Figure 2.6.** The general trend in transition metal reactivity from these plots is Ni > Co > Fe > Mn > Cr. It should be mentioned that although perovskites are active for oxygen evolution [169, 170], they will not be discussed in this review.

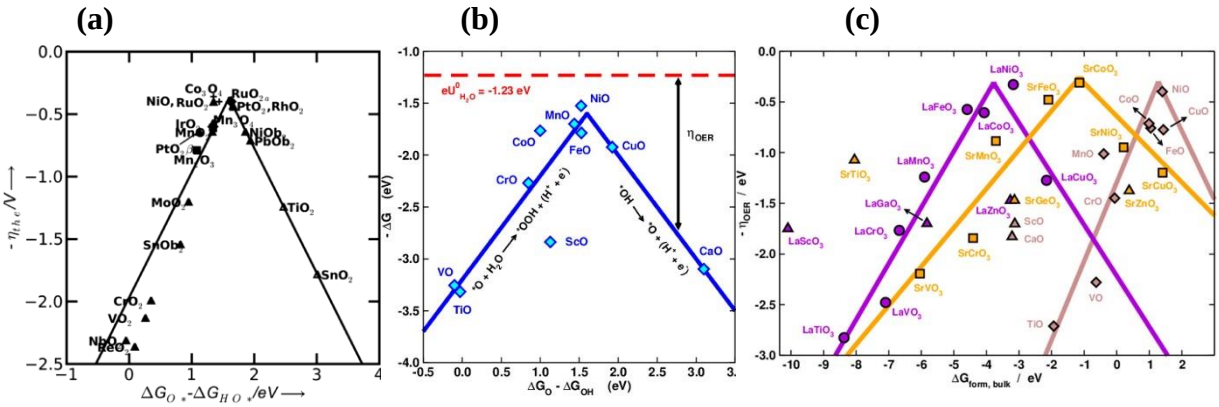

Figure 2.6 a) Theoretical volcano plot for pristine (001) surface of oxides based on the difference between adsorption energies of oxygen (*O) and hydroxyl (*OOH) intermediates as descriptor [168]. **b)** Volcano plot of theoretical overpotential against standard free energy of ΔG_{HO^*} - ΔG_{O^*} as descriptor [171]. **c)** Volcano plots of overpotentials for OER of $LaMO_3$, $SrMO_3$ and MO based on formation energy of oxide in bulk, $\Delta G_{form,\ bulk}$, as descriptor [172].

2.2.1. OER catalysts

2.2.1.1. Precious metals

Precious noble metal oxide catalysts RuO_2 and IrO_2 have been recognised as benchmark catalysts for OER under both acidic and alkaline conditions [173-175] however, their high cost, low elemental abundance and activity losses at high anodic potentials [176] make them impractical. RuO_2 is highly prone to corrosion or dissolution at oxidative potentials since the onset of corrosion occurs at similar potentials to oxygen evolution, therefore affecting its stability over time [177]. Under

similar conditions, IrO_2 demonstrates better corrosion stability but its OER catalytic activity is lower than RuO_2 [178]. In order to overcome these issues, various mixtures or composites [179, 180] of these catalysts have been tested and an example of a mixed IrO_2-RuO_2 catalyst is employed as an OER activity benchmark catalyst in Chapter 8.

2.2.1.2. Non-precious metals

Oxides

First row transition metal-based OER catalysts have been of particular interest as they demonstrate good catalytic activity for OER whilst remaining low in cost and resistant to corrosion in highly alkaline environments [181-183]. Among transition metal oxides, materials classed as spinels have attracted much interest and the method of preparation of such oxides is seen to affect the catalytic performance [184-186]. Based on the observations that the metal or metal oxide should be able to form a higher valence oxide at potentials lower than oxygen evolution [187], nickel and cobalt oxides are generally considered suitable catalysts for the reaction.

The electrocatalytic activity of spinel Co_3O_4 is correlated to the presence of Co valence states Co^{2+}/ Co^{3+} and Co^{3+}/ Co^{4+} [188] and it is largely accepted that cobaltites on the surface are oxidised to Co^{4+} state before oxygen evolution occurs. The partial substitution of Co by an additional metallic cation such as Ni, Li, or Mn into the lattice disrupts the homogenous distribution of these cations. In the case of $Li_xCo_{3-x}O_4$ [189], the introduction of Li was suggested to stabilise the Co^{3+} active sites, whilst in $Ni_xCo_{3-x}O_4$ [190] the number and binding energies of surface Co^{3+} and Ni^{3+} sites were altered, contributing to improved OER activity. Since it is primarily the top layer of the catalyst which is electrochemically active [191], the electrocatalytic activity can be further enhanced by increasing the surface roughness or electroactive surface area. Methods of synthesis or morphologies which maximise surface per unit area or promote better durability of the catalyst layer and gas management are therefore preferred [192] .

Hydroxides/ oxyhydroxides

Besides oxides, transition metal hydroxides and oxyhydroxides have also been investigated and activities for these catalysts have been benchmarked [193, 194]. These comparative studies propose nickel to be the most efficient catalyst for OER based on the adsorption energies or bond strengths of the reaction intermediates [195, 196] displayed in **Figure 2.6**. As marked in red on the Pourbaix diagram of Ni in **Figure 2.7**, at pH 14 and oxidative potentials, $Ni(OH)_2$ should be present.

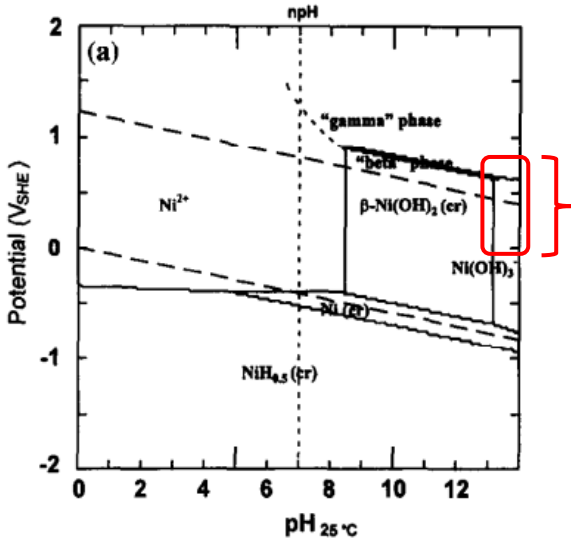

Figure 2.7 Pourbaix diagram of Ni [197].

The standard potential of the theoretical oxygen evolution reaction and oxidation of Ni^{2+} to Ni^{3+} in alkaline conditions occur around the same oxidative potentials, represented by equation (2.1) and (2.10) respectively [198]. However due to the sluggish kinetics of oxygen evolution the experimental onset potential of this reaction usually takes place at more positive potentials.

$$Ni(OH)_2 + OH^- \rightarrow NiOOH + H_2O + e^- \qquad 0.49\ V\ vs\ SHE \qquad (2.10)$$

Taking into account both experimental and theoretical benchmarking trends, Ni-based catalysts are an obvious choice. On top of that, in practical alkaline water electrolysis which is a mature technology, Ni is the best electrode material with good alkali resistance while not being too costly [199]. As a result, much work has been carried out to further enhance the activity of these hydroxides or oxyhydroxides – such as the incorporation of another transition metal which has been shown to have a significant effect on the electronic properties of $Ni(OH)_2$ [168, 200].

Ni-based binary metal oxide, hydroxide or oxyhydroxides

Fabrication and optimisation of mixed metal oxide composition is significant based on Brewer's theory of hypo-hyper-d-d-interelectronic bonding. It has been suggested in the literature that a stronger d-d-intermetallic bonding between the intermetallic phases means a weaker intermediate adsorptive bond (e.g. M-OH, M-H) during the rate determining step [201]. This allows for more rapid dissociation, faster reaction rate and better intrinsic catalyst activity overall. Synergism in mixed hypo-hyper-d electronic oxide catalysts depend on the composition ratio and the effect of the interaction results in a volcano plot or maximum [202]. Therefore, the introduction of 'impurities' into a Ni metal oxide can encourage increases in conductivity, change the intermediate bonding energy for better catalysis and possibly provide more favourable active sites for intermediates to bind to [203-206].

For instance the presence of Fe, which was discovered as an impurity in $Ni(OH)_2$ electrodes as early as the 1900s [207], helps to lower the overpotential of the reaction. NiFe-based oxide, hydroxide or oxyhydroxide materials have since been widely recognised to outperform other binary metal catalysts for OER [208]. Louie and Bell [209] proposed that the addition of Fe decreases the order of the crystal structure as well as the oxidation state of Ni. The same group carried out further investigation into the Ni-Fe-based oxyhydroxide catalyst using *in operando* XAS measurements and DFT calculations [210] on these catalysts. They deduced that in Fe-doped $Ni_{1-x}Fe_xOOH$, the OER activity increased up to a content of ~40% Fe as the Fe acted as active sites with optimal adsorption energies for intermediates [168]. Similarly, the overpotential for OER was observed to decrease with the substitution of cations of Ni with Co in hydrous oxide films of Ni-Co [211, 212]. The results from systematic studies screening the activities of binary Ni-based metal oxides, hydroxides and oxyhydroxides tested under different conditions are presented in **Figure 2.8** and ranked in **Table 2.4** with a general trend of Ni-Fe > Ni-Co > Ni-Cr for the performances of metal oxides, hydroxides and oxyhydroxides.

Table 2.4 Results of benchmarking studies of metal oxides, hydroxides and oxyhydroxides.

	Performance	**Testing conditions**	**Ref**
Metal oxides	NiFe > NiCo > CoFe > Ni > NiCu > NiCe > NiLa	Electrodeposited on GC electrode, tested at 1600 rpm in 1M NaOH.	[183]
Metal hydroxides	NiFe > NiCo > NiCr > Ni > NiMn > NiCu	Electrodeposited on Ni micro disc, tested at 1M NaOH, 353K.	[200]
Metal oxyhydroxides	NiFe > NiCr > NiMn > Ni > NiCu > NiCo > NiZn	Co-precipitated catalyst drop-cast on Au electrode, tested at 1500 rpm in 0.1M KOH.	[168]

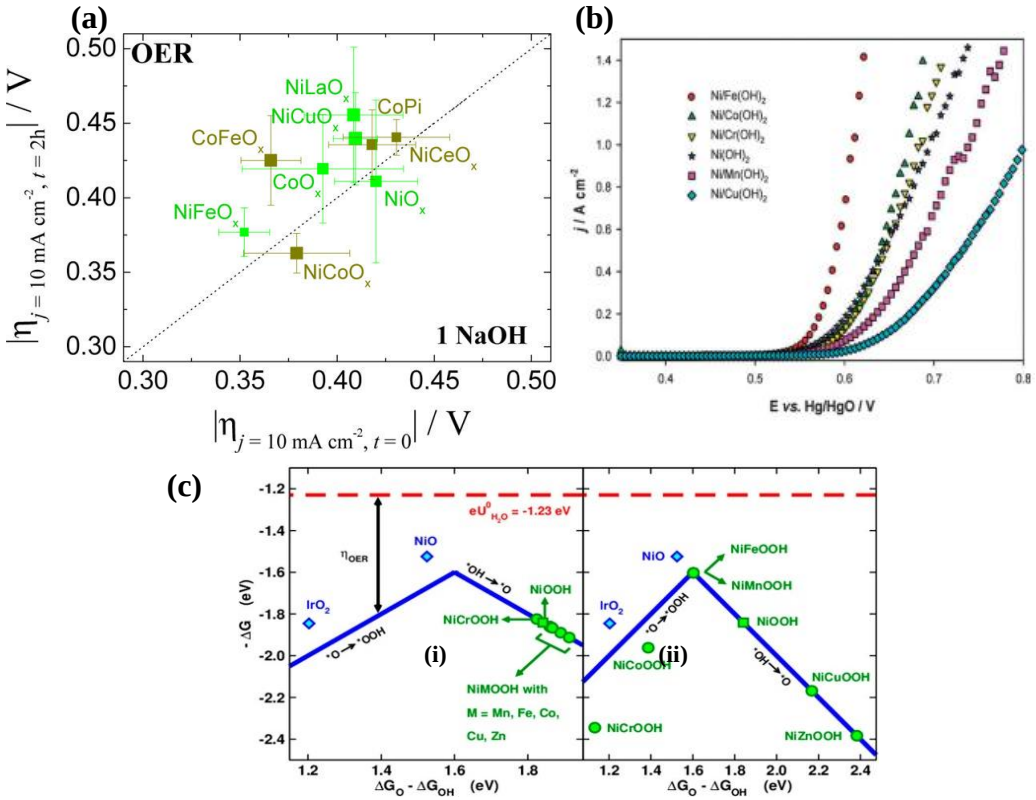

Figure 2.8 a) Plot of overpotential at 10 mA cm^{-2} at t = 0 h and 2 h for various metal oxides coated on GC electrode [183], **b)** Polarisation curves for Ni-based binary metal hydroxides coated on Ni microdisc [200], **c)** Volcano plot for Ni-based M-doped oxyhydroxides coated on Au RDE where (i) Ni; (ii) M; is active site based on $\Delta G_{O^*} - \Delta G_{OH^*}$ descriptor [168].

Ni-based ternary metal oxide, hydroxide or oxyhydroxide

Further still, the synergism of multiple first-row transition metals is suggested to provide the advantage of multiple oxidation states at the required range of potentials. An investigation [213] involving a quick, fluorescence-based, combinatorial assay of 3500 oxides in solution form reported that compositions containing Ni, Fe and a third metal show highest OER activity with good reproducibility (e.g. Ni-Fe-Ga, Ni-Fe-Cr,

and Ni-Fe-Al). From **Figure 2.9**, it is evident from the higher activity values that nickel-based oxides are much more active for OER than cobalt-based oxides. It is also apparent that the addition of a third transition metal to the oxides gives significantly higher activity than binary oxides As marked in red on **Figure 2.9**, the highest activities fall in the column and row of Ni-Fe ternary oxides. Whilst for the cobalt-based oxides, the highest activities are seen in the column and row of Ni-Co ternary oxides (marked in blue).

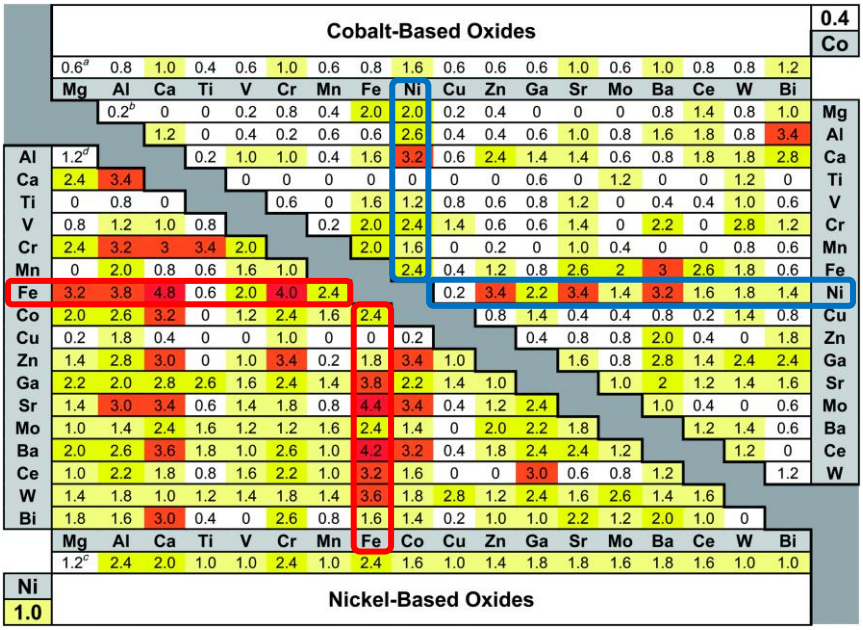

Figure 2.9 Diagram of highest observed activities of Ni and Co-based ternary metal oxides. Activities are colour coded and marked numerically from 0 to > 4 [213].

According to the activity numbers in **Figure 2.9**, potential ternary metal Ni-Fe based catalysts can be ranked NiCrFe (4.0) > NiAlFe (3.8) ≈ NiFeGa (3.8) > NiFeMo ≈ NiFeCo (2.4) > NiVFe (2.0). Correspondingly, **Table 2.5** summarises the reported experimental performances of ternary Ni-Fe based catalysts of Ni-Fe-Cr, Ni-Fe-Co, Ni-Fe-Mo and Ni-Fe-V at practical current densities. Based on these sources, Ni-Fe-Cr, Ni-Fe-Co and Ni-Fe-Mo ternary metal catalysts were seen as potential OER catalyst candidates for comparison and optimisation in Chapter 7.

Table 2.5 OER performance of ternary transition metal-based catalysts.

Catalyst		Electrode substrate	Preparation method	Performance	Stability	Ref
NiFeCr	$NiFe_{2-x}Cr_xO_4$ (x = 0.8-1.0)	Ni support	Hydroxide precipitation	0.587 V vs Hg/HgO at 100 mA cm^{-2} in 1 M KOH, 298 K; 0.2 mV s^{-1}, iR compensated	-	[214]
	NiFeCr hydroxide	Ni foam	Electrochemical deposition etching from nitrates	1.5 V vs RHE (≈ 0.452 V vs Ag/AgCl) at 100 mA cm^{-2} in 1 M KOH, 5 mV s^{-1}, 95% iR-compensation	1.58 V (≈ 0.532 vs Ag/AgCl) at 100 mA cm^{-2} for 11.1 h. (no iR correction)	[215]
NiFeCo	NiCoFe (5 or 6:2:1)	Ni foam	Electrodeposition from nitrates	1.59 V vs RHE (≈ 0.566 V vs Ag/AgCl) at 100 mA cm^{-2}, in 1 M KOH; 5mV s^{-1}, 85% iR compensation	1.85 V at 80 mA cm^{-2} for 8 h.	[216]
	$CoFeNiO_x$	Ni foam	Electrodeposition	1.495 V vs RHE at 100 mA cm^{-2} in 1 M KOH, 298 K;1 mV s^{-1}	-	[217]
NiFeMo	$Fe_{0.75}Ni_{0.25}MoO_4$ or $Fe_{0.5}Ni_{0.5}MoO_4$	Ni plate	Co-precipitation	0.641 V vs Hg/HgO at 100 mA cm^{-2} in 1 M KOH, 298 K; 0.2 mV s^{-1}, iR compensated	-	[218]
	MoFe:Ni$(OH)_2$/NiOOH	Ni foam	Hydrothermal and electrochemical oxidation	1.525 V vs RHE, in 1 M KOH, 298 K; 1mV s^{-1}, iR compensated	1.52 V at 100 mA cm^{-2} for 50 h (iR corrected)	[219]
NiFeV	$NiFeV_{0.5}O_4$	Ni support	Hydroxide precipitation	0.685 V vs Hg/HgO at 100 mA cm^{-2} in 1 M KOH, 298 K; 0.2 mV s^{-1}, iR compensated	-	[220]
	$Ni_{0.75}Fe_{0.125}V_{0.125}$ LDH	Ni foam	Hydrothermal	1.5 V vs RHE (≈ 0.583 V vs Hg/HgO) at 100 mA cm^{-2}, in 1 M KOH, room temp; 1mV s^{-1}, iR compensated	1.5 V (≈ 0.583 V vs Hg/HgO) at 30 mAcm^{-2} for 15 h	[221]

2.3. The secondary oxygen electrode

The rates of the electrochemical reactions involving the reduction and oxidation of oxygen are unfortunately slow and electrocatalysts are needed to provide lower activation energy pathways to help speed up these reaction rates to a practical level. It is desirable for the electrocatalysts chosen to be in abundant supply and as

inexpensive as possible, whilst still providing high activity. However, it is also important to keep in mind that the selection of electrocatalysts whether reaction-specific or bifunctional is merely an initial step to constructing a practical secondary oxygen electrode. The construction of the electrode and environment in which the reactions take place are also major influencing factors of the reaction pathway and reaction overpotential.

2.3.1. Bifunctional catalysts

A bifunctional electrocatalyst electrode simplifies the electrode construction and reduces mass transfer losses. The challenges in designing a truly bifunctional oxygen catalyst however, were highlighted by Rossmeisl *et al.* [222]. The difficulties originate from the scaling relation between the intermediate binding energy of the first and third proton/ electron transfer step (i.e. OH_{ad} and OOH_{ad} from equations (2.5) and (2.8)). According to the graphical representation of the elementary reactions of ORR and OER (**Figure 2.10**), not only do optimal catalysts still require ~0.37 V overpotential for OER and ORR [223] , the apexes of the volcano plots for ORR and OER do not meet at the same value suggesting that an optimal catalyst for ORR is not one for OER and vice versa.

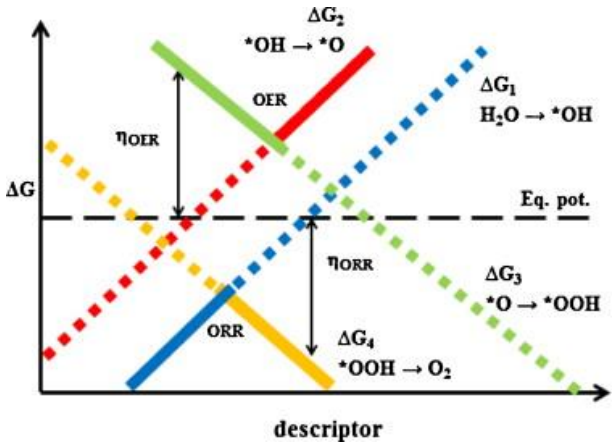

Figure 2.10 Plot of ΔG versus activity descriptor. Representative lines for Gibbs energies of reaction of proposed pathway ΔG_1, ΔG_2, ΔG_3 and ΔG_4. Theoretical η_{ORR} and η_{OER} are labelled as the vertical distances between equilibrium potential of 1.23 V and point on the line [223].

An ideal bifunctional catalyst operates at potentials close to the equilibrium potential, catalysing the ORR with a high reduction current just cathodic of the equilibrium potential and OER with a high oxidative current just anodic of the equilibrium potential [224]. Real catalysts however require large overpotentials and operate at significantly more cathodic

potentials and anodic potentials for ORR and OER respectively. This vast difference in operating potentials means that the surface of the catalyst faces different conditions over a wider potential range which may alter its surface structure over time. Due to the interdependence of intermediate binding energies, the active sites on the catalyst are also likely to be different for each reaction.

Electrocatalysts for oxygen electrochemical reactions are mainly a) metals, b) metal oxides and c) transition metal organic macrocycles [8]. Since both metallic particles and organic macrocycles may oxidise at high anodic potentials commonly used for oxygen electrochemical reactions, metal oxides are the most viable option for bifunctional catalysts. The conductivity and therefore, catalytic activity of the metal oxide can be adjusted by varying the composition and method of preparation. These are usually prepared by techniques such as co-precipitation, thermal decomposition, freeze-drying, pyrolysis of an organic precursor, hydrolysis, solid-state reactions etc. Metal oxides can be further broken down into perovskites, rutile-type structures, pyrochlores and spinel materials as seen in **Table 2.6**.

Table 2.6 General properties of different types of metal oxides [8].

Type	**General Formula**	**Shape**	**Examples**
Perovskite	ABO_3	Cubic crystal lattice	$LaNiO_3$, $LaCoO_3$
Rutile-type	AO_2	Tetragonal symmetry	MnO_2, PbO_2
Pyrochlore	$A_2B_2O_7$	Network of polyhedral linked on corners with interstices filled with A cations	$Bi_2Ru_2O_7$, Nd_3IrO_7
Spinel	AB_2O_4	Cubic crystal lattice	$NiCo_2O_4$, Co_3O_4

2.3.2. ORR and OER reaction requirements

Comparing the two reaction environments of the oxygen electrochemical reactions, the ORR occurs at a three-phase interface or boundary between the catalyst, binder and reactant found within the catalyst ink layer. These three-phase structures support the conversion of energy at the electrode and are vital since electrochemical reactions occur here [225]. These structures should permit the movement of reactants to, and products away from, the catalytic sites. If the transport of the reactant or product is limited, the percentage catalyst utilisation and consequent performance of the system

will be much lower for the given amount of catalyst. The significance of this three-dimensional boundary is described in detail in **Figure 2.11**.

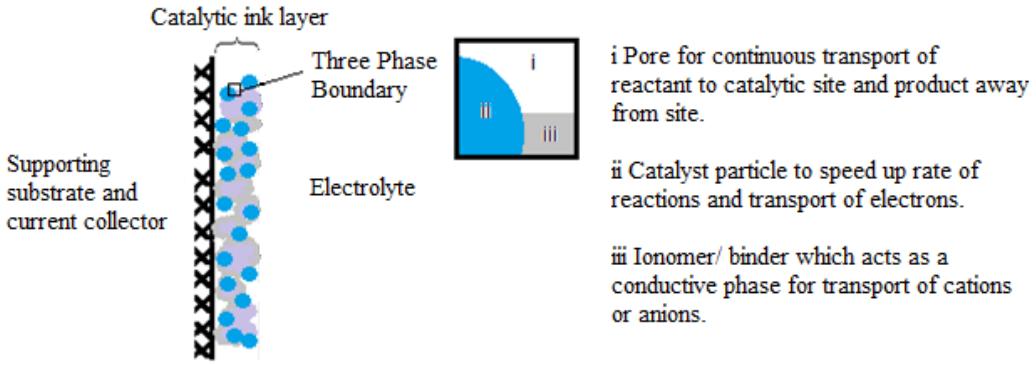

Figure 2.11 Schematic of three-phase interface found in porous catalyst ink structure adapted from Bladergröen *et al.* [226].

The ORR gas diffusion layer should be as hydrophobic as possible to prevent electrolyte or water flooding in the electrode which could cause blockages and prevent the gas from reaching the catalytic sites. The side of the electrode in contact with the electrolyte should also be hydrophobic but to a lesser extent with slightly smaller pores.

The OER reaction occurs between the liquid electrolyte and solid catalyst. As oxygen gas is evolved, the electrode surface or sites within the catalyst layer should be hydrophilic to facilitate the continuous replacement of oxygen bubbles with electrolyte. This helps to reduce the surface coverage of the electrode by bubbles.

2.3.3. Secondary oxygen electrode designs

In order to aid the commercialisation of secondary metal-air batteries and regenerative fuel cells, systems whereby both the oxygen reduction and evolution reactions can take place successively must be further developed. Factors that should be taken into consideration when designing a secondary oxygen electrode are [227] :

- Catalyst materials (bifunctional or separately optimised ORR and OER catalysts) must be chemically stable over the potential range that the electrode is cycled between
- The electrodes (2D or 3D) must be mechanically robust to overcome any shape or compositional changes that take place during cycling

- The movement of the products of ORR during cycling must be considered in regards to cycling stability
- The formation of carbonate ions in the pores of the oxygen electrode or in the electrolyte, from the interaction between carbon dioxide in the atmosphere and the electrolyte, which has a negative impact on both the ORR and OER
- Flow channels or structures which facilitate flow of O_2 towards and away from the electrode

There are three proposed secondary oxygen electrode designs given in **Figure 2.12** which are derived from Jörissen's review [12] of bifunctional oxygen electrodes. The first involves the use of a single layer of bifunctional catalyst which is able to catalyse both ORR and OER. At present, a large proportion of research focuses on developing bifunctional catalysts to reduce the number of steps required for catalyst synthesis. Some well-investigated bifunctional catalysts are precious metals (e.g. Ag [228], Pd [229]), metal oxides (e.g. Co_3O_4, $NiCo_2O_4$, $MnCo_2O_4$, MnO_2 etc), perovskites [230-233] and carbonaceous materials [234]. The second type of electrode design involves two (or more) layers of catalyst with different porosities and hydrophobicity to cope with the difference in reaction zones [235-237]. In some cases, the two catalyst layers are kept separate with the hydrophilic side for OER facing the electrolyte and semi-hydrophobic side for ORR facing the open end of the electrode [238-240]. The third electrode design requires decoupling the two reactions into two separate electrodes resulting in a supposed tri-electrode full-cell configuration [241, 242] with two reaction-specific oxygen counter electrodes and a working electrode. This design helps to minimise the degradation of the materials which are not stable over the full potential range, showing improved cycling stability for long-term performance. The advantages and disadvantages of each of these designs are summarised in **Table 2.7.**

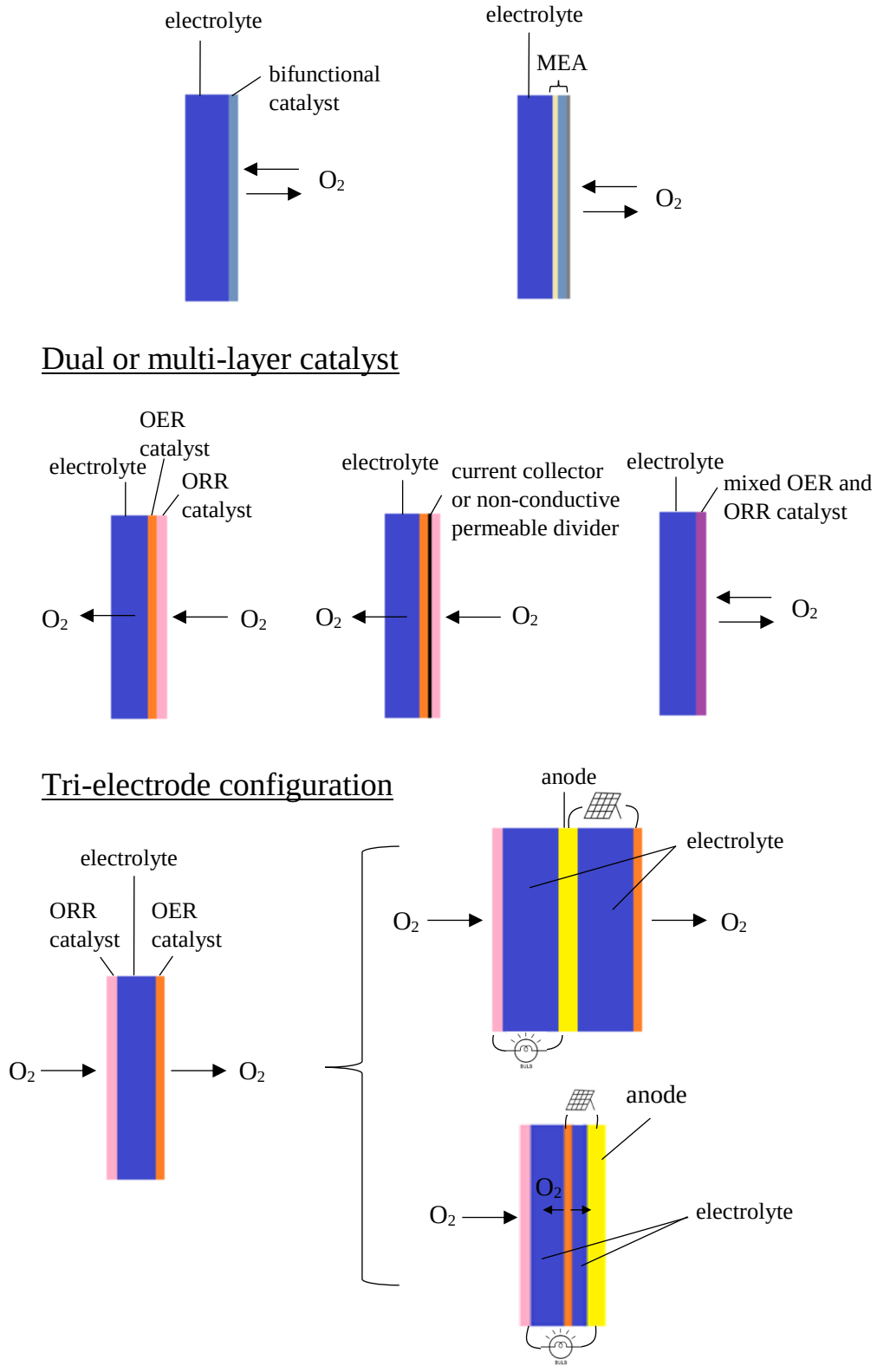

Figure 2.12 Schematic of secondary oxygen electrode designs.

Table 2.7 The advantages and disadvantages of the secondary oxygen electrode designs.

	Advantages	**Disadvantages**
Single-layer bifunctional catalyst	• Comparatively simple assembly • Cost-effective	• Bifunctional catalyst must be stable in full potential range • Ancillary additives (e.g. ionomers, carbon powders) may not be stable at oxidative potentials • Carbonate precipitation will affect the bifunctional catalyst layer
Dual or multi-layer catalyst	• Catalysts can be optimised for separate reactions • Suitable porosity can be achieved for ORR • Electrolytic contact between the two layers may be reduced during cycling	• Complex assembly • Potential mass transfer losses • Delamination or separation of layers by the pressure of the oxygen bubbles during evolution • Carbonate precipitation will affect both ORR and OER layers
Tri-electrode configuration	• Flexible design • Catalysts and electrodes can be optimised for separate reactions • Catalysts and ancillary additives need not be stable in full potential range • Oxygen evolved can be removed with flowing electrolyte during charge; oxygen required for reduction can be supplied during discharge	• Complex assembly which may add weight/ volume

Traditionally, ORR catalyst layers are constructed using a conventional slurry method with ancillary additives such as PTFE, ionomers and carbon powders. However the instability of these materials in a secondary electrode at highly oxidative potentials results in degradation of performance [243, 244] due to a decrease in hydrophobicity and hence loss of active surface area over time. To eliminate this issue, researchers have attempted to create binder-free and/ or carbon-free oxygen electrodes or by directly growing catalysts onto the surface of the electrode support such as stainless steel mesh [245-247] and nickel foam [248-251]. Whilst these studies show promising advancements, there is still insufficient demonstration of long-term performance.

Likewise, it is crucial for gas evolution from OER to be considered in the design of the oxygen electrode as physical processes such as the growth and attachment of the gas bubbles at the electrode have a significant impact on the chemical processes

taking place. The evolution of bubbles at the surface of the electrode can affect the voltage of the cell by increasing ohmic resistance and hence overpotential of the reaction. On top of this, the coalescence of bubbles at the electrode surface over time increases coverage which blocks or shields electroactive surface area. The growth of bubbles confined within the pores of gas evolving porous electrode structures, can result in mechanical degradation of the catalyst layer on the electrode. This is especially likely at high current densities, as more stress is applied at these layers during bubble growth or release [252]. Furthermore, the release of bubbles from the electrode surface creates turbulence in the electrode boundary layer which affects heat and mass transfer [253].

Thus the difference in reaction environments of ORR and OER makes constructing a porous electrode for a single bifunctional catalyst challenging. The stability of materials and the issue of gas management is of particular importance for the single bifunctional catalyst layer and dual or multi-layer catalyst design. In a tri-electrode configuration however, since ORR and OER take place at separate electrodes, catalysts and ancillary additives do not need to be stable in the full potential range and the evolution of gas is more easily managed. Comparing the advantages and disadvantages of the respective designs, a tri-electrode configuration appears to be the most ideal for long-term cycling performance and was therefore adopted in this work.

2.3.4. Tri-electrode designs in literature

A tri-electrode concept in a symmetrical configuration (**Figure 2.13 a**) [254] was implemented for an electrically rechargeable zinc-air cell. Tests were carried out in 7 M KOH with commercial oxygen reduction electrodes based on cobalt oxide or manganese dioxide catalysts, and 316 L stainless steel as oxygen evolution electrodes. Air supplied to the oxygen cathodes was bubbled through KOH solution to reduce the rate of carbonate formation. The full cell was cycled at low current densities of 5–15 mA cm^{-2}, 24-30 h cycle periods for ~120 cycles with a faradaic efficiency of ~90% and energy efficiency ~50%. The authors [254] reported that performance loss was mainly due to the degradation of the zinc electrode (i.e. shape change and

dendrite formation) especially at high current densities and partly due to the OER electrode although no details are given.

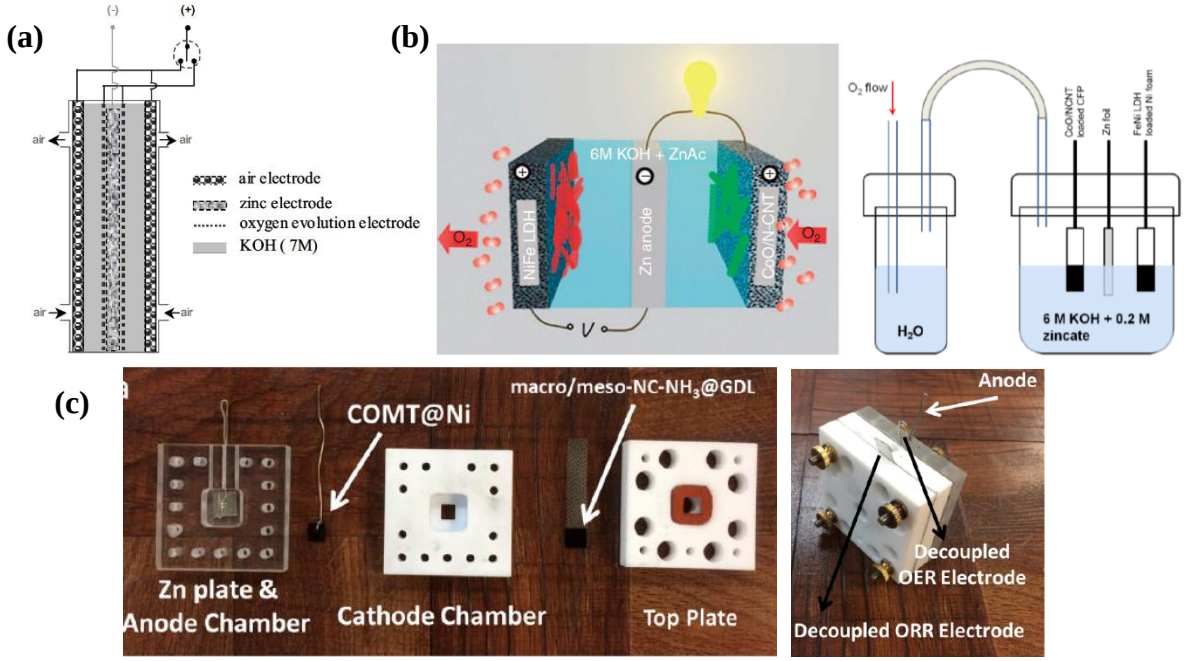

Figure 2.13 a) Diagram of zinc-air cell [254], **b)** Schematic of tri-electrode configuration of rechargeable zinc-air battery and schematic of home-built electrochemical cell for measurements [241], **c)** Zn-air battery cell parts and fully assembled cell with decoupled cathodes [238].

Similarly, a tri-electrode configuration concept [241] was tested in a beaker-type cell (**Figure 2.13 b**) with CoO/ N-CNT on carbon fibre paper as the ORR electrode, Ni-Fe LDH on Ni foam as the OER electrode and Zn foil as the anode. The full cell was cycled in 6 M KOH+ 0.2 M Zn acetate at 20-50 mA cm^{-2} at 4-20 h cycle periods for 10 cycles (~200 h) with energy efficiencies of 65% and 60% at 20 mA cm^{-2} at 50 mA cm^{-2} respectively. The electrolyte was saturated with O_2 before each measurement and humidified O_2 was fed continuously to the electrolyte during measurement. The authors remarked that atmospheric CO_2 management and dendritic growth of Zn metal during charge are still factors which must be considered for practical long term cycling performance.

A more recent study on novel electrocatalysts for ORR and OER, deemed suitable for both Li-air and Zn-air systems [238], were tested in the cell in **Figure 2.13 c**. The ORR catalyst was NH_3- activated N-doped macro/ mesoporous carbon and OER catalyst was Co_3O_4 microstructures on Ni foam. Humidified air was supplied to the cell to reduce the rate of water loss by evaporation. In the zinc-air configuration, the cell reported a voltaic efficiency of 60% when cycled at 10 mA cm^{-2} at 4 h cycle

periods for 200 cycles (800 h). The authors confirmed the formation of potassium bicarbonate, $KHCO_3$, on the surface of the ORR catalyst layer after cycling however the state of the Zn electrode after cycling was not discussed.

In contrast to the examples of vertically assembled secondary oxygen electrodes with the counter electrode and other components arranged adjacent to it, horizontally orientated secondary oxygen electrodes have been demonstrated by several studies to alleviate the issues of gas evolution at the oxygen electrode. For instance, this separator-free dual layer catalyst design (**Figure 2.14**) was patented in 2010 by Amendola *et al.* [255, 256]. The hydrophilic side of the air electrode was kept in contact with the electrolyte and hydrophobic side was facing the air tunnel. A third electrode, Zn metal, was introduced into the stack as an anode.

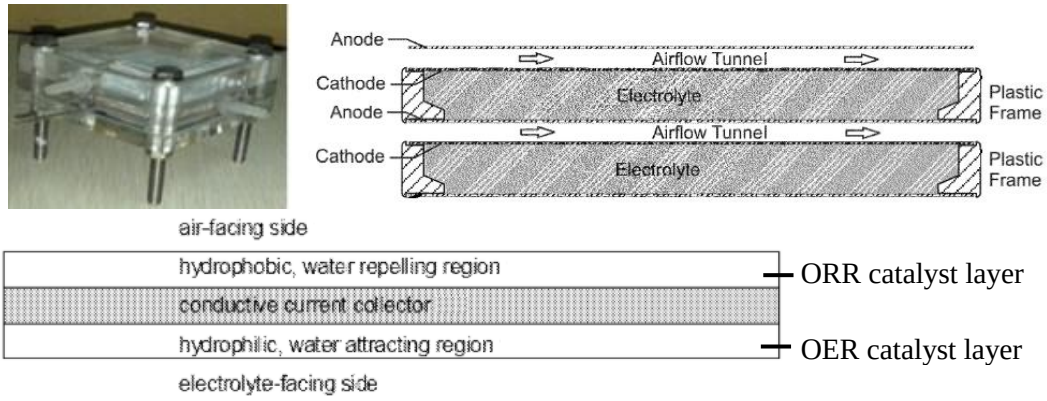

Figure 2.14 Photograph and corresponding schematic drawings of horizontal cell stack assembly [256].

A current collector was placed between the two layers in the air electrode as seen in **Figure 2.14**, however the authors also suggest that this can be removed and replaced by either an insulator or a gap. The advantages of this orientation are summarised:

- Controlled or consistent electrolyte resistance
- Ease of assembly and stacking of multiple cells to provide greater energy density, compression of multiple cells may help to keep cells in place
- Gravity can help to distribute any precipitate evenly and assist with flowing electrolyte through the cell stack

- Airflow tunnels assist in heat transfer to cool cells and transfer of oxygen to allow cell to operate at higher current densities

Other more recent examples of tri-electrode designs in horizontal configuration are given in **Figure 2.15**. In **Figure 2.15 a** [242], a tri-electrode horizontal cell assembly is described with an OER electrode (RuO_2 coated Ti mesh) on top to allow oxygen evolved to be released to the environment, an ORR electrode (MnO_2 on GDE) on the bottom and a Zn electrode between them. The cell had a static electrolyte volume of 45 mL and the authors claimed extended cycle life due to the lower chance of a short circuit between the Zn electrode and OER electrode. They recommended that performance could be further increased by reducing the distance between adjacent electrodes.

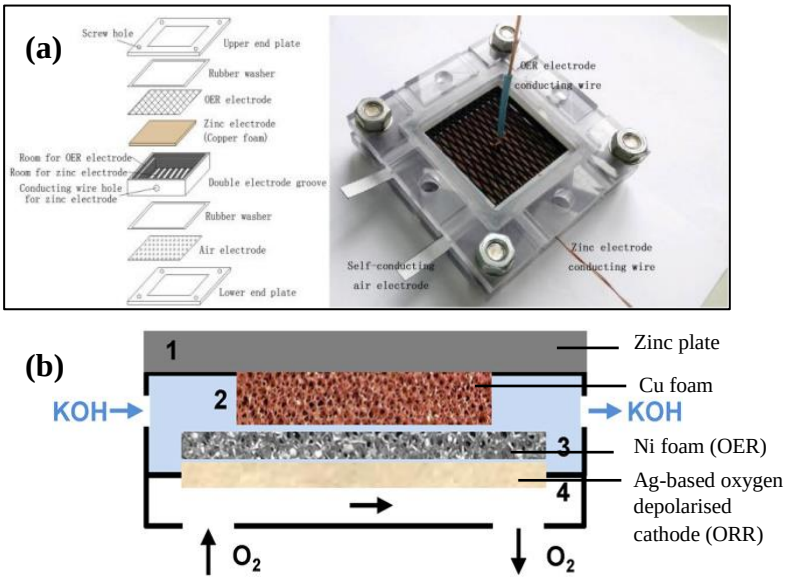

Figure 2.15 a) Schematic of a horizontal tri-electrode design Zn-air static battery cell assembly and photograph of the corresponding Zn-air cell [242], **b)** Schematic illustration of horizontal Zn-air testing cell [240].

Electrolyte was pumped through the cell in **Figure 2.15 b** [240] at a set volumetric rate of 0.4 L min^{-1} to remove the oxygen evolved at the Ni foam OER electrode whilst pure O_2 was supplied to the backside of the Ag-based ORR catalyst layer at a rate of 0.2 L min^{-1}. The authors reported greater voltage efficiency losses for the Ag-based ORR electrode than the Ni-foam OER electrode which they ascribed to the smaller surface area and longer diffusion paths within the porous structure. They

recommended positioning a separator between the anode and OER electrode or improving the flow distribution within the cell in order to prevent short circuiting of the cell from inhomogeneous zinc deposition, thereby extending the battery's lifetime and improving performance.

Based on these studies, recommendations for further improvement of oxygen electrodes are: good selection of electrode materials to avoid corrosion, consideration of width of inter-electrode gaps, even flow distribution and therefore current density distribution within the cell, consideration of carbonate precipitation and zinc dendrite formation. A summary of the cycling performances of these secondary Zn-air batteries is presented in **Table 2.8**. The reported performance values were used as points of reference for the constructed tri-electrode secondary system in Chapter 8.

Table 2.8 Examples of secondary tri-electrode Zn-air batteries.

Cathodes	Anode	Electrolyte	Cycling conditions and stability	Voltage polarisation	Ref
ORR: CoO or MnO_2 OER: 316L SS mesh	3D metal foam current collector filled with Zn, TiN and polymer binder	Commercial electrolyte mainly consisting of 7 M KOH, *static*	• 5-15 mA cm^{-2}, 24-30 h cycle periods for ~120 h (4 cycles) • 50% energy efficiency	>0.9 V at 5-15 mA cm^{-2}	[254]
ORR: CoO/ N-CNT on carbon fibre paper OER: NiFe LDH on Ni foam	Zn foil	6 M KOH + 0.2 M zincate, *static*	• 20-50 mA cm^{-2}, 4-20h cycle periods for > 200 h (10 cycles) • 65% energy efficiency at 20 mA cm^{-2}	0.70 V at 20 mA cm^{-2}	[241]
ORR: Macro/ meso-NC-NH_3 OER: Co_3O_4 on Ni foam	Zn foil	6 M KOH + 0.2 M $ZnCl_2$, *static*	• 10 mA cm^{-2}, 4h cycle periods for ~800 h (200 cycles) • 60-65% voltage efficiency at 10 mA cm^{-2}	~0.75 V at 10 mA cm^{-2}	[238]
ORR: Commercial GDE OER: RuO_2 on Ti net	Zn coated C felt on porous Cu foam	6 M KOH + 0.4 M ZnO, *static*	• 20 mA cm^{-2}, ~2 h cycle periods for 1917 h (1000 cycles) • 40% energy efficiency	~1.1 V to 1.4 V at 20 mA cm^{-2}	[242]
ORR: Ag-based catalyst OER: Ni foam	Cu foam soldered on Zn (not in contact with electrolyte)	30 wt% KOH + 2 wt% ZnO, 30ºC, *flowing* 0.4 L min^{-1}	• 50 mA cm^{-2}, ~8 min cycle periods, (>600 cycles) with short circuits • ~58% voltage efficiency at 20 mA cm^{-2}	~0.75 V at 20 mA cm^{-2} (~1.2 V at 50 mA cm^{-2})	[240]

2.4. References

1. V. Engelhardt, The Electrolysis of Water: Processes and Applications. Monographs on Applied Electrochemistry Vol. 1. 1904, Easton, PA: The Chemical Publishing Company
2. W. Nicholson, A Journal of Natural Philosophy, Chemistry and the Arts Vol. II. 1800, London
3. A.J. Appleby, From Sir William Grove to today: fuel cells and the future, J. Power Sources 29 (1990) 3-11.
4. L. Maiche, (1878) Patent: 127069.
5. S.F. Bender, J.W. Cretzmeyer, T.F. Reise, Handbook of Batteries Third Edition,D. Linden, T.B. Reddy (ed), McGraw-Hill, 2002
6. V. Neburchilov, H. Wang, J.J. Martin, W. Qu, A review on air cathodes for zinc–air fuel cells, J. Power Sources 195 (2010) 1271-91.
7. F. Mitlitsky, N.J. Colella, B. Myers. *Unitized regenerative fuel cells for solar rechargeable aircraft and zero emission vehicles*. in *Fuel Cell Seminar*. 1994. San Diego, CA.
8. K. Kinoshita, Electrochemical Oxygen Technology. 1992, New York: John Wiley & Sons, Inc
9. C. Song, J. Zhang, PEM Fuel Cell Electrocatalysts and Catalyst Layers: Fundamentals and Applications,J. Zhang (ed), Springer London, London, 2008
10. R.W. Verjulio, J. Santander, N. Sabaté, J.P. Esquivel, N. Torres-Herrero, A. Habrioux, N. Alonso-Vante, Fabrication and evaluation of a passive alkaline membrane micro direct methanol fuel cell, Int. J Hydrogen Energy 39 (2014) 5406-13.
11. B.B.Blizanac, P.N.Ross, N.M.Markovic, Oxygen electroreduction on Ag(1 1 1): The pH effect, Electrochim. Acta 52 (2007) 2264-71.
12. L. Jorissen, Bifunctional oxygen/air electrodes, J. Power Sources 155 (2006) 23-32.
13. J. Zhang, M.B. Vukmirovic, Y. Xu, M. Mavrikakis, R.R. Adzic, Controlling the catalytic activity of platinum-monolayer electrocatalysts for oxygen reduction with different substrates, Angew. Chem. 117 (2005) 2170–3.
14. A. Ignaczak, R. Nazmutdinov, A. Goduljan, L. Moreirade, C. Pinto, F. Juarez, P. Quaino, E. Santos, W. Schmickler, A scenario for oxygen reduction in alkaline media, Nano Energy 26 (2016) 558-64.
15. J.K. Nørskov, J. Rossmeisl, A. Logadottir, L. Lindqvist, Origin of the overpotential for oxygen reduction at a fuel-cell cathode, J. Phys. Chem. B 108 (2004) 17886-92.
16. R. Cao, J.S. Lee, M. Liu, J. Cho, Recent progress in non-precious catalysts for metal-air batteries, Adv. Energy Mater. 2 (2012) 816-29.
17. F. Cheng, J. Chen, Metal–air batteries: from oxygen reduction electrochemistry to cathode catalysts, Chem. Soc. Rev. 41 (2012) 2172-92.
18. J.B.H. Gordon B. Haxel, and Greta J. Orris, *Rare Earth Elements—Critical Resources for High Technology*, P.H. Stauffer, J.W. Hendley(II), Editors. 2002.
19. R. Jaffe, J. Price, M. Hitzman, F. Slakey, *Energy Critical Elements*. 2011, APS Physics. p. 10.
20. *The Process of Mining REEs and other Strategic Elements*. Mission 2016: The future of strategic natural resources 2016 04/03/19]; Available from: http://web.mit.edu/12.000/www/m2016/finalwebsite/solutions/newmines.html.
21. K.F. Blurton, E. McMullin, The cathodic reduction of oxygen on platinum in alkaline solutions, J. Electrochem. Soc. 116 (1969) 1476-80.
22. R.W. Zurilla, R.K. Sen, E. Yeager, The kinetics of the oxygen reduction reaction on gold in alkaline solution, J. Electrochem. Soc. 125 (1978) 1103-9.
23. N.A. Anastasijevic, Z.M. Dimitrijevic, R.R. Adzic, Oxygen reduction on a ruthenium electrode in alkaline electrolytes, J. Electroanal. Chem. 199 (1986) 351-64.
24. G.K.H. Wiberg, K.J.J. Mayrhofer, M. Arenz, Investigation of the oxygen reduction activity on silver – A rotating disc electrode study, Fuel Cells 10 (2010) 575-81.

25. J. Prakash, H. Joachin, Electrocatalytic activity of ruthenium for oxygen reduction in alkaline solution, Electrochim. Acta 45 (2000) 2289-96.
26. Y.-F. Yang, Y.-H. Zhou, Influence of carbon surface pre-oxidation on the properties of silver + carbon electrocatalysts, J. Electroanal. Chem. 415 (1996) 143-52.
27. S. Kondo, M. Nakamura, N. Maki, N. Hosh, Active sites for the oxygen reduction reaction on the low and high index planes of palladium, J. Phys. Chem. C 113 (2016) 12625-8.
28. N.M. Markovic, H.A. Gasteiger, P.N. Ross(Jr.), Oxygen reduction on platinum low-index single-crystal surfaces in alkaline solution: Rotating ring disk Pt(hkl) studies, J. Phys. Chem. 100 (1996) 6715-21.
29. Y.-F. Yang, Y.-H. Zhou, C.-S. Chat, Electrochemical reduction of oxygen on small palladium particles supported on carbon in alkaline solutions, Electrochim. Acta 40 (1995) 2579-86.
30. L. Demarconnay, C. Coutanceau, J.-M. Léger, Electroreduction of dioxygen (ORR) in alkaline medium on Ag/C and Pt/C nanostructured catalysts—effect of the presence of methanol, Electrochim. Acta 49 (2004) 4513-21.
31. H. Erikson, M. Liik, A. Sarapuu, J. Kozlova, V. Sammelselg, K. Tammeveski, Oxygen reduction on electrodeposited Pd coatings on glassy carbon, Electrochim. Acta 88 (2013) 513-8.
32. M. Lüsi, H. Erikson, A. Sarapuu, K. Tammeveski, J. Solla-Gullón, J.M. Feliu, Oxygen reduction reaction on carbon-supported palladium nanocubes in alkaline media, Electrochem. Commun. 64 (2016) 9-13.
33. C.-Y. Wu, P.-W. Wu, P. Lin, Y.-Y. Li, Y.-M. Lin, Silver-carbon nanocapsule electrocatalyst for oxygen reduction reaction, J. Electrochem. Soc. 154 (2007) 1059-62.
34. K. Kinoshita, Carbon: Electrochemical and Physicochemical Properties. 1988, New York: Wiley
35. M. Nesselberger, S. Ashton, J.C. Meier, I. Katsounaros, K.J.J. Mayrhofer, M. Arenz, The particle size effect on the oxygen reduction reaction activity of Pt catalysts: Influence of electrolyte and relation to single crystal models, J. Am. Chem. Soc. 133 (2011) 17428-33.
36. Y. Yang, Y. Zhou, Particle size effects for oxygen reduction on dispersed silver + carbon electrodes in alkaline solution, J. Electroanal. Chem. 397 (1995) 271-8.
37. J.-J. Han, N. Li, T.-Y. Zhang, Ag/C nanoparticles as an cathode catalyst for a zinc-air battery with a flowing alkaline electrolyte, J. Power Sources 193 (2009) 885-9.
38. W. Tang, H. Lin, A. Kleiman-Shwarsctein, G.D. Stucky, E.W. McFarland, Size-dependent activity of gold nanoparticles for oxygen electroreduction in alkaline electrolyte, J. Phys. Chem. C 112 (2008) 10515-9.
39. J. Hernandez, J. Solla-Gullon, E. Herrero, A. Aldaz, J.M. Feliu, Electrochemistry of shape-controlled catalysts: oxygen reduction reaction on cubic gold nanoparticles, J. Phys. Chem. C 111 (2007) 14078-83.
40. H.T. Duong, M.A. Rigsby, W.-P. Zhou, A. Wieckowski, Oxygen reduction catalysis of the Pt3Co alloy in alkaline and acidic media studied by x-ray photoelectron spectroscopy and electrochemical methods, J. Phys. Chem. C 111 (2007) 13460-5.
41. F.H.B. Lima, J.R.C. Salgado, E.R. Gonzalez, E.A. Ticianelli, Electrocatalytic properties of PtCo/C and PtNi/C alloys for the oxygen reduction reaction in alkaline solution, J. Electrochem. Soc. 154 (2007) A369-75.
42. F.H.B. Lima, J.F.R.d. Castro, E.A. Ticianelli, Silver-cobalt bimetallic particles for oxygen reduction in alkaline media, J. Power Sources 161 (2006) 806-12.
43. B. Li, J. Prakash, Oxygen reduction reaction on carbon supported Palladium–Nickel alloys in alkaline media, Electrochem. Commun. 11 (2009) 1162-5.
44. H. Wang, W. Luo, L. Zhu, Z. Zhao, B. E, W. Tu, X. Ke, M. Sui, C. Chen, Q. Chen, Y. Li, Y. Huang, Synergistically enhanced oxygen reduction electrocatalysis by subsurface atoms in ternary PdCuNi alloy catalysts, Adv. Func. Mater. 2018) 1707219.

45. J. Luo, P.N. Njoki, Y. Lin, L. Wang, C.J. Zhong, Activity-composition correlation of AuPt alloy nanoparticle catalysts in electrocatalytic reduction of oxygen, Electrochem. Commun. 8 (2006) 581-7.
46. L. Jiang, A. Hsu, D. Chu, R. Chen, A highly active Pd coated Ag electrocatalyst for oxygen reduction reactions in alkaline media, Electrochim. Acta 55 (2010) 4506-11.
47. Y.-J. Li, C.-C. Chang, T.-C. Wen, A mixture design approach to thermally prepared Ir-Pt-Au ternary electrodes for oxygen reduction in alkaline solution, J. Appl. Electrochem. 27 (1997) 227-34.
48. W. Tang, S. Jayaraman, T.F. Jaramillo, G.D. Stucky, E.W. McFarland, Electrocatalytic activity of gold-platinum clusters for low temperature fuel cell applications, J. Phys. Chem. C 113 (2009) 5014-24.
49. R.N. Singh, J.-F. Koenig, G. Poillerat, P. Chartier, Thin films of Co_3O_4 and $NiCo_2O_4$ prepared by the method of chemical spray pyrolysis for electrocatalysis J. Electroanal. Chem. 314 (1991) 241-57.
50. Y. Meng, W. Song, H. Huang, Z. Ren, S.-Y. Chen, S.L. Suib, Structure-property relationship of bifunctional MnO_2 nanostructures: highly efficient, ultra-stable electrochemical water oxidation and oxygen reduction reaction catalysts identified in alkaline media, J. Am Chem. Soc. 136 (2014) 11452–64.
51. R.J. Toh, Z.k. Sofer, M. Pumera, Transition metal oxides for the oxygen reduction reaction: Influence of the oxidation states of the metal and its position on the periodic table, ChemPhysChem 16 (2015) 3527-31.
52. K.A. Stoerzinger, M. Risch, B. Han, Y. Shao-Horn, Recent insights into manganese oxides in catalyzing oxygen reduction kinetics, ACS Catal. 5 (2015) 6021-31.
53. M. Fleischer, The abundance and distribution of the chemical elements in the earth's crust, J. Chem. Educ. 31 (1954) 446.
54. J.E. Post, Manganese oxide minerals: Crystal structures and economic and environmental significance, PNAS 96 (1999) 3447-54.
55. G. Leclanché, Quelques observations sur l'emploi des piles électriques. Pile constante au peroxyde de manganèse à un seul liquide, Les mondes 16 (1868) 532.
56. W.C. Vosburgh, The maganese dioxide electrode, J. Electrochem. Soc. 106 (1959) 839-45.
57. N.C. Cahoon, M.P. Korver, The cathodic reduction of manganese dioxide in alkaline electrolyte, J. Electrochem. Soc. 106 (1959) 745-750.
58. G.S. Bell, R. Huber, On the cathodic reduction of manganese dioxide in alkaline electrolyte, J. Electrochem. Soc. 111 (1964) 1-6.
59. G.S. Bell, R. Huber, The cathodic reduction of manganese dioxide in alkaline solution, Electrochim. Acta 10 (1965) 509-12.
60. A. Kozawa, J.F. Yeager, The cathodic reduction mechanism of electrolytic manganese dioxide in alkaline electrolyte, J. Electrochem. Soc. 112 (1965) 959-63.
61. A. Kozawa, R.A. Powers, The manganese dioxide electrode in alkaline electrolyte: The electron-proton mechanism for the discharge process from MnO_2 to $MnO_{1.5}$, J. Electrochem. Soc. 113 (1966) 870-8.
62. D. Boden, C.J. Venuto, D. Wisler, R.B. Wylie, The alkaline manganese dioxide electrode I. The discharge process, J. Electrochem. Soc. 114 (1967) 415-7.
63. D. Boden, C.J. Venuto, D. Wisler, R.B. Wylie, The alkaline manganese dioxide electrode II. The charge process, J. Electrochem. Soc. 115 (1968) 333-8.
64. A. Kozawa, J.F. Yeager, Cathodic reduction mechanism of MnOOH to $Mn(OH)_2$ in alkaline electrolyte, J. Electrochem. Soc. 115 (1968) 1003-7.
65. R.I.Razouk, G.M.Habashy, N.Ph.Kelada, Hydrated oxides of manganese supported on magnesium hydroxide as catalysts for hydrogen peroxide decomposition, J. Catal. 25 (1972) 183-93.
66. S.B.Kanungo, K.M.Parida, B.R.Sant, Studies on MnO_2—III. The kinetics and the mechanism for the catalytic decomposition of H_2O_2 over different crystalline modifications of MnO_2, Electrochim. Acta 26 (1981) 1157-67.

67. K.Matsuki, H.Kamada, Oxygen reduction electrocatalysis on some manganese oxides, Electrochim. Acta 31 (1986) 13-8.
68. L. Mao, T. Sotomura, K. Nakatsu, N. Koshiba, D. Zhang, T. Ohsaka, Electrochemical characterization of catalytic activities of manganese oxides to oxygen reduction in alkaline aqueous solution, J. Electrochem. Soc. 149 (2002) A504-7.
69. P. Żółtowski, D.M. Dražić, L. Vorkapić, Carbon-air electrode with regenerative short time overload capacity: Part 1. Effect of manganese dioxide, J. Appl. Electrochem. 3 (1973) 271-83.
70. Y.L. Cao, H.X. Yang, X.P. Ai, L.F. Xiao, The mechanism of oxygen reduction on MnO_2-catalyzed air cathode in alkaline solution, J. Electroanal. Chem. 557 (2003) 127-34.
71. L. Mao, D. Zhang, T. Sotomura, K. Nakatsu, N. Koshiba, T. Ohsaka, Mechanistic study of the reduction of oxygen in air electrode with manganese oxides as electrocatalysts, Electrochim. Acta 48 (2003) 1015-21.
72. F.H.B. Lima, M.L. Calegaro, E.A. Ticianelli, Electrocatalytic activity of manganese oxides prepared by thermal decomposition for oxygen reduction, Electrochim. Acta 52 (2007) 3732-8.
73. F.H.B. Lima, M.L. Calegaro, E.A. Ticianelli, Investigations of the catalytic properties of manganese oxides for the oxygen reduction reaction in alkaline medi, J. Electroanal. Chem. 590 (2006) 152-60.
74. I. Roche, E. Chaînet, M. Chatenet, J. Vondrák, Carbon-supported manganese oxide nanoparticles as electrocatalysts for the oxygen reduction reaction (ORR) in alkaline medium: physical characterizations and ORR mechanism, J. Phys. Chem. C 111 (2007) 1434-43.
75. R.B. Valim, M.C. Santos, M.R.V. Lanza, S.A.S. Machado, F.H.B. Lima, M.L. Calegaro, Oxygen reduction reaction catalyzed by ε-MnO_2: Influence of the crystalline structure on the reaction mechanism, Electrochim. Acta 85 (2012) 423-31.
76. J.-S. Lee, G.S. Park, H.I. Lee, S.T. Kim, R. Cao, M. Liu, J. Cho, Ketjenblack carbon supported amorphous manganese oxides nanowires as highly efficient electrocatalyst for oxygen reduction reaction in alkaline solutions, Nano Lett. 11 (2011) 5362-6.
77. M.L. Calegaro, F.H.B. Lima, E.A. Ticianelli, Oxygen reduction reaction on nanosized manganese oxide particles dispersed on carbon in alkaline solutions, J. Power Sources 158 (2006) 735-9.
78. F. Cheng, J. Shen, W. Ji, Z. Tao, J. Chen, Selective synthesis of manganese oxide nanostructures for electrocatalytic oxygen reduction, ACS Appl. Mater. Interfaces 1 (2009) 460-6.
79. S.L. Brock, N. Duan, Z.R. Tian, O. Giraldo, H. Zhou, S.L. Suib, A review of porous manganese oxide materials, Chem. Mater. 10 (1998) 2619-28.
80. A. Zolfaghari, F. Ataherian, M. Ghaemi, A. Gholami, Capacitive behavior of nanostructured MnO_2 prepared by sonochemistry method, Electrochim. Acta 52 (2007) 2806-14.
81. Y. Meng, W. Song, H. Huang, Z. Ren, S.-Y. Chen, S.L. Suib, Structure−property relationship of bifunctional MnO_2 nanostructures: Highly efficient, ultra-stable electrochemical water oxidation and oxygen reduction reaction catalysts identified in alkaline media, J. Am. Chem. Soc. 136 (2014) 11452-64.
82. J. Yang, J.J. Xu, Nanoporous amorphous manganese oxide as electrocatalyst for oxygen reduction in alkaline solutions, Electrochem. Commun. 5 (2003) 306-11.
83. V.S. Bagotzyky, N.A. Shumilova, E.I. Khrushcheva, Electrochemical oxygen reduction on oxide catalysts, Electrochim. Acta 21 (1976) 919-24.
84. E.J.M. O'Sullivan, E.J. Calvo, Comprehensive Chemical Kinetics. Electrode Kinetics: Reactions, ed. R.G. Compton. Vol. 27. 1989, Amsterdam, Oxford, New York, Tokyo Elsevier Science Publisher B. V.
85. X. Xie, Y. Li, Z.-Q. Liu, M. Haruta, W. Shen, Low-temperature oxidation of CO catalysed by Co_3O_4 nanorods, Nature 458 (2009) 746-9.

86. J. Xu, P. Gao, T.S. Zhao, Non-precious Co_3O_4 nano-rod electrocatalyst for oxygen reduction reaction in anion-exchange membrane fuel cells, Energy Environ. Sci. 5 (2012) 5333-9.
87. H. Qin, S. Lao, Z. Liu, J. Zhu, Z. Li, Effects of heat treatment on the structure, morphology and electrocatalytic activity of cobalt hydroxide electrocatalyst, Int. J Hydrogen Energy 35 (2010) 1872-8.
88. M. Savy, Oxygen reduction in alkaline solutions on semi-conducting cobalt oxide electrodes, Electrochim. Acta 13 (1968) 1359-76.
89. Y. Wang, D. Zhang, H. Liu, A study of the catalysis of cobalt hydroxide towards the oxygen reduction in alkaline media, J. Power Sources 195 (2010) 3135-9.
90. P.W. Menezes, A. Indra, D. González-Flores, N.R. Sahraie, I. Zaharieva, M. Schwarze, P. Strasser, H. Dau, M. Driess, High-performance oxygen redox catalysis with multifunctional cobalt oxide nanochains: morphology-dependent activity, ACS Catal. 5 (2015) 2017-27.
91. J. Liu, L. Jiang, Q. Tang, B. Zhang, D.S. Su, S. Wang, G. Sun, Coupling effect between cobalt oxides and carbon for oxygen reduction reaction, ChemSusChem 5 (2012) 2315-8.
92. Y. Liang, Y. Li, H. Wang, J. Zhou, J. Wang, T. Regier, H. Dai, Co_3O_4 nanocrystals on graphene as a synergistic catalyst for oxygen reduction reaction, Nat. Mater. 10 (2011) 780-6.
93. J. Wu, D. Zhang, Y. Wang, Y. Wan, B. Houa, Catalytic activity of graphene–cobalt hydroxide composite for oxygen reduction reaction in alkaline media, J. Power Sources 198 (2012) 122-6.
94. S.P. Jiang, Z.G. Lin, A.C.C. Tseung, Homogeneous and heterogeneous catalytic reactions in cobalt oxide/graphite air electrodes I. Chemical kinetics of peroxide decomposition by Co(ll) ions in alkaline solutions, J. Electrochem. Soc. 137 (1990) 759-64.
95. J. Liu, L. Jiang, B. Zhang, J. Jin, D.S. Su, J. Wang, G. Sun, Controllable synthesis of cobalt monoxide nanoparticles and the size-dependent activity for oxygen reduction reaction, ACS Catal. 4 (2014) 2998-3001.
96. K.-H. Wu, M. Allen-Ankins, Q. Zeng, B. Zhang, J. Pan, J. Zhang, D.-S. Su, I.R. Gentle, D.-W. Wang, Benchmarking the oxygen reduction electroactivity of first-row transition-metal oxide clusters on carbon nanotubes, ChemElectroChem 5 (2018) 1862-7.
97. F. Cheng, Y. Su, J. Liang, Z. Tao, J. Chen, MnO_2-based nanostructures as catalysts for electrochemical oxygen reduction in alkaline media, Chem. Mater. 22 (2010) 898-905.
98. T. Sonmez, S.J. Thompson, S.W.T. Price, D. Pletcher, A.E. Russella, Voltammetric studies of the mechanism of the oxygen reduction in alkaline media at the spinels Co_3O_4 and $NiCo_2O_4$, J. Electrochem. Soc. 163 (2016) H884-90.
99. Q. Liu, Z. Chen, Z. Yan, Y. Wang, E. Wang, S. Wang, S. Wang, G. Sun, Crystal-plane-dependent activity of spinel Co_3O_4 towards water splitting and the oxygen reduction reaction, ChemElectroChem 5 (2018) 1080-6.
100. J. Xiao, Q. Kuang, S. Yang, F. Xiao, S. Wang, L. Guo, Surface structure dependent electrocatalytic activity of Co_3O_4 anchored on graphene sheets toward oxygen reduction reaction, Sci. Rep. 3 (2013) 2300.
101. Y. Xiao, C. Hu, L. Qu, C. Hu, M. Cao, Three-dimensional macroporous $NiCo_2O_4$ sheets as a non-noble catalyst for efficient oxygen reduction reactions, Chem. Eur. J. 19 (2013) 14271-8.
102. P. Manivasakan, P. Ramasamy, J. Kim, Use of urchin-like $Ni_xCo_{3-x}O_4$ hierarchical nanostructures based on non-precious metals as bifunctional electrocatalysts for anion-exchange membrane alkaline alcohol fuel cells, Nanoscale 6 (2014) 9665-72.
103. W.J. King, A.C.C. Tseung, The reduction of oxygen on nickel-cobalt oxides - I The influence of composition and preparation method on the activity of nickel-cobalt oxides, Electrochim. Acta 19 (1974) 485-91.

104. W.J. King, A.C.C. Tseung, The reduction of oxygen on nickel-cobalt oxides - II Correlation between crystal structure and activity of Co_2NiO_4 and related oxides, Electrochim. Acta 19 (1974) 493-8.
105. S. Lin, X. Shi, H. Yang, D. Fan, Y. Wang, K. Bi, Reduced graphene oxide-$NiCo_2O_4$ nanoflowers as efficient electrocatalysts for the oxygen reduction reaction, J. Alloy Compd. 720 (2017) 147-55.
106. Y. Liu, C. Shu, Y. Fang, Y. Chen, Y. Liu, Two 3D structured Co-Ni bimetallic oxides as cathode catalysts for high-performance alkaline direct methanol fuel cells, J. Power Sources 361 (2017) 160-9.
107. Z.-Q. Liu, Q.-Z. Xu, J.-Y. Wang, N. Li, S.-H. Guo, Y.-Z. Su, H.-J. Wang, J.-H. Zhang, S. Chen, Facile hydrothermal synthesis of urchin-like $NiCo_2O_4$ spheres as efficient electrocatalysts for oxygen reduction reaction, Int. J Hydrogen Energy 38 (2013) 6657-62.
108. R.N. Singh, J.-F. Koenig, G. Poillerat, P. Chattier, Thin films of Co_3O_4 and $NiCo_2O_4$ prepared by the method of chemical spray pyrolysis for electrocatalysis Part IV. The electrocatalysis of oxygen reduction, J. Electroanal. Chem. 314 (1991) 241-57.
109. Y. Li, M.S. Wu, C.Y. Ouyang, The structural and electronic properties of spinel $MnCo_2O_4$ bulk and low-index surfaces: From first principles studies, Appl. Surf. Sci. 349 (2015) 510-5.
110. E. Rios, J.-L. Gautier, G. Poillerat, P. Chartier, Mixed valency spinel oxides of transition metals and electrocatalysis: case of the $Mn_xCo_{3-x}O_4$ system, Electrochim. Acta 44 (1998) 1491-7.
111. E. Lee, J.-H. Jang, Y.-U. Kwon, Composition effects of spinel $Mn_xCo_{3-x}O_4$ nanoparticles on their electrocatalytic properties in oxygen reduction reaction in alkaline media, J. Power Sources 273 (2015) 735-41.
112. P.W. Menezes, A. Indra, N.R. Sahraie, A. Bergmann, P. Strasser, M. Driess, Cobalt–manganese-based spinels as multifunctional materials that unify catalytic water oxidation and oxygen reduction reactions, ChemSusChem 8 (2015) 164-71.
113. W. Wang, L. Kuai, W. Cao, M. Huttula, S. Ollikkala, T. Ahopelto, A.-P. Honkanen, S. Huotari, M. Yu, B. Geng, Mass-production of mesoporous $MnCo_2O_4$ spinels with manganese(IV)- and cobalt(II)-rich surfaces for superior bifunctional oxygen electrocatalysis, Angew. Chem. Int. Ed. 56 (2017) 14977 –81.
114. E. Vila, R.M. Rojas, J.L.M.d. Vidales, O. Garcia-Martinez, Structural and thermal properties of the tetragonal cobalt manganese spinels $Mn_xCo_{3-x}O_4$ ($1.4 < x < 2.0$), Chem. Mater. 8 (1996) 1078-83.
115. J. Li, N. Zhou, H. Wang, H. Li, Z. Xie, H. Chu, Y. Tang, L. Sun, Z. Peng, Three-dimensional $MnCo_2O_{4.5}$ mesoporous networks as an electrocatalyst for oxygen reduction reaction, J. Electrochem. Soc. 162 (2015) A2302-7.
116. C. Li, X. Han, F. Cheng, Y. Hu, C. Chen, J. Chen, Phase and composition controllable synthesis of cobalt manganese spinel nanoparticles towards efficient oxygen electrocatalysis, Nat. Commun. 6 (2015) 7345.
117. M. Zhang, M.d. Respinis, H. Frei, Time-resolved observations of water oxidation intermediates on a cobalt oxide nanoparticle catalyst, Nat. Chem. 6 (2014) 362-7.
118. F. Cheng, J. Shen, B. Peng, Y. Pan, Z. Tao, J. Chen, Rapid room-temperature synthesis of nanocrystalline spinels as oxygen reduction and evolution electrocatalysts. , Nat. Chem. 3 (2010) 79-84.
119. Y. Liang, H. Wang, J. Zhou, Y. Li, J. Wang, T. Regier, H. Dai, Covalent hybrid of spinel manganese−cobalt oxide and graphene as advanced oxygen reduction electrocatalysts, J. Am. Chem. Soc. 134 (2012) 3517-23.
120. X. Yan, Y. Jia, J. Chen, Z. Zhu, X. Yao, Defective-activated-carbon-supported Mn–Co nanoparticles as a highly efficient electrocatalyst for oxygen reduction, Adv. Mater. 28 (2016) 8771-8.
121. H.M. Cota, T. Katan, M. Chin, F.J. Schoenweis, Decomposition of dilute hydrogen peroxide in alkaline solutions, Nature 4951 (1964) 1281.

122. J.R. Goldstein, A.C.C. Tseung, Kinetics of oxygen reduction on graphite | cobalt-iron oxide electrodes with coupled heterogeneous chemical decomposition of H_2O_2, J. Phys. Chem. 76 (1978) 3646-56.
123. M.D. Koninck, S.-C. Poirier, B. Marsan, $Cu_xCo_{3-x}O_4$ used as bifunctional electrocatalyst II. Electrochemical characterization for the oxygen reduction reaction, J. Electrochem. Soc. 154 (2007) A381-8.
124. A. Serov, N.I. Andersen, A.J. Roy, I. Matanovic, K. Artyushkova, P. Atanassov, $CuCo_2O_4$ ORR/OER bi-functional catalyst: Influence of synthetic approach on performance, J. Electrochem. Soc. 162 (2015) F449-54.
125. H. Zhu, S. Zhang, Y.-X. Huang, L. Wu, S. Sun, Monodisperse $M_xFe_{3-x}O_4$ (M = Fe, Cu, Co, Mn) nanoparticles and their electrocatalysis for oxygen reduction reaction, Nano Lett. 13 (2013) 2947-51.
126. P. Lahiri, S.K. Sengupta, Physico-chemical properties and catalytic activities of the spinel series $Mn_xFe_{3-x}O_4$ towards peroxide decomposition, J. Chem. Soc. Faraday Trans. 91 (1995) 3489-94.
127. J. Wang, Y. Fu, Y. Xu, J. Wu, J.-H. Tian, R. Yang, Hierarchical $NiCo_2O_4$ hollow nanospheres as high efficient bi-functional catalysts for oxygen reduction and evolution reactions, Int. J Hydrogen Energy 41 (2016) 8847-54.
128. X. Bo, Y. Zhang, M. Li, A. Nsabimana, L. Guo, $NiCo_2O_4$ spinel/ordered mesoporous carbons as noble-metal free electrocatalysts for oxygen reduction reaction and the influence of structure of catalyst support on the electrochemical activity of $NiCo_2O_4$, J. Power Sources 288 (2015) 1-8.
129. R.L. McCreery, Advanced carbon electrode materials for molecular electrochemistry, Chem. Rev. 108 (2008) 2646-87.
130. J. Wu, W. Pisula, K. Müllen, Graphenes as potential material for electronics, Chem. Rev. 107 (2007) 718-47.
131. A.J. Appleby, J.Marie, Kinetics of oxygen reduction on carbon materials in alkaline solution, Electrochim. Acta 24 (1978) 195-202.
132. M.D. Obradovic, G.D. Vukovic, S.I. Stevanovic, V.V. Panic, P.S. Uskokovic, A. Kowal, S.L. Gojkovic, A comparative study of the electrochemical properties of carbon nanotubes and carbon black, J. Electroanal. Chem. 634 (2009) 22-30.
133. Y. Li, W. Zhou, H. Wang, L. Xie, Y. Liang, F. Wei, J.-C. Idrobo, S.J. Pennycook, H. Dai, An oxygen reduction electrocatalyst based on carbon nanotube–graphene complexes, Nat. Nanotechnol. 7 (2012) 394-400.
134. A. Shen, Y. Zou, Q. Wang, R.A.W. Dryfe, X. Huang, S. Dou, L. Dai, S. Wang, Oxygen reduction reaction in a droplet on graphite: direct evidence that the edge Is more active than the basal plane, Angew. Chem. Int. Ed. 53 (2014) 10804-8.
135. I. Kruusenberg, N. Alexeyeva, K. Tammeveski, The pH-dependence of oxygen reduction on multi-walled carbon nanotube modified glassy carbon electrodes, Carbon 47 (2009) 651-8.
136. I. Kruusenberg, L. Matisen, H. Jiang, M. Huuppola, K. Kontturi, K. Tammeveski, Electrochemical reduction of oxygen on double-walled carbon nanotube modified glassy carbon electrodes in acid and alkaline solutions, Electrochem. Commun. 12 (2010) 920-3.
137. A.A. Gewirth, M.S. Thorum, Electroreduction of dioxygen for fuel-cell applications: Materials and challenges, Inorg. Chem. 49 (2010) 3557–66.
138. X.-K. Kong, C.-L. Chen, Q.-W. Chen, Doped graphene for metal-free catalysis, Chem. Soc. Rev. 43 (2014) 2841-57.
139. Y. Jiao, Y. Zheng, M. Jaroniec, S.Z. Qiao, Origin of the electrocatalytic oxygen reduction activity of graphene-based catalysts: A roadmap to achieve the best performance, J. Am. Chem. Soc. 136 (2014) 4394-403.
140. L. Qu, Y. Liu, J.-B. Baek, L. Dai, Nitrogen-doped graphene as efficient metal-free electrocatalyst for oxygen reduction in fuel cells, ACS Nano 4 (2010) 1321-6.

141. N. Daems, X. Sheng, I.F.J. Vankelecom, P.P. Pescarmona, Metal-free doped carbon materials as electrocatalysts for the oxygen reduction reaction, J. Mater. Chem. A 2 (2014) 4085-110.
142. R.I. Jafri, N. Rajalakshmi, S. Ramaprabhu, Nitrogen doped graphene nanoplatelets as catalyst support for oxygen reduction reaction in proton exchange membrane fuel cell, J. Mater. Chem 20 (2010) 7114-7.
143. Z.-H. Sheng, H.-L. Gao, W.-J. Bao, F.-B. Wang, X.-H. Xia, Synthesis of boron doped graphene for oxygen reduction reaction in fuel cells, J. Mater. Chem. 22 (2012) 390-5.
144. J.-e. Park, Y.J. Jang, Y.J. Kim, M.-s. Song, S. Yoon, D.H. Kim, S.-J. Kim, Sulfur-doped graphene as a potential alternative metal-free electrocatalyst and Pt-catalyst supporting material for oxygen reduction reaction, Phys. Chem. Chem. Phys. 16 (2014) 103-9.
145. C. Domínguez, F.J. Pérez-Alonso, S.A. Al-Thabaiti, S.N. Basahel, A.Y. Obaid, A.O. Alyoubi, J.L.G.d.l. Fuente, S. Rojas, Effect of N and S co-doping of multiwalled carbon nanotubes for the oxygen reduction, Electrochim. Acta 157 (2015) 158-65.
146. S. Bag, B. Mondal, A. Kumar, D.R. Raj, Nitrogen and sulfur dual-doped reduced graphene oxide: Synergistic effect of dopants towards oxygen reduction reaction, Electrochim. Acta 163 (2015) 16-23.
147. J. Wu, X. Zheng, C. Jin, J. Tian, R. Yang, Ternary doping of phosphorus, nitrogen, and sulfur into porous carbon for enhancing electrocatalytic oxygen reduction, Carbon 92 (2015) 327-38.
148. Z. Yang, Z. Yao, G. Li, G. Fang, H. Nie, Z. Liu, X. Zhou, X.-a. Chen, S. Huang, Sulfur-doped graphene as an efficient metal-free cathode catalyst for oxygen reduction, ACS Nano 6 (2012) 205-11.
149. X. Xu, T. Yuan, Y. Zhou, Y. Li, J. Lu, X. Tian, D. Wang, J. Wang, Facile synthesis of boron and nitrogen-doped graphene as efficient electrocatalyst for the oxygen reduction reaction in alkaline media, Int. J Hydrogen Energy 39 (2014) 16043-52.
150. A. Zahoor, M. Christy, Y.J. Hwang, Y.R. Lim, P. Kim, K.S. Nahm, Improved electrocatalytic activity of carbon materials by nitrogen doping, Appl. Catal. B: Environ. 147 (2014) 633-41.
151. R. Jasinski, A new fuel cell cathode catalyst, Nature 201 (1964) 1212-3.
152. R. Jasinski, Cobalt phthalocyanine as a fuel cell cathode, J. Electrochem. Soc. 112 (1965) 526-8.
153. I. Kruusenberg, L. Matisen, Q. Shah, A.M. Kannan, K. Tammeveski, Non-platinum cathode catalysts for alkaline membrane fuel cells, Int. J Hydrogen Energy 37 (2012) 4406-12.
154. D.-H. Kim, D.-H. Kwak, S.-B. Han, M.-C. Kim, H.-S. Park, J.-Y. Park, J.-E. Won, K.-B. Ma, K.-W. Park, Electrochemical catalytic contribution of transition metals at the center of porphyrin macrocycle structures as catalysts for oxygen reduction reaction, J. Ind. Eng. Chem. 54 (2017) 200-4.
155. J. Zagal, M. Paez, Electrocatalytic activity of metal phthalocyanines for oxygen reduction, J. Electroanal. Chem. 339 (1992) 13-30.
156. R. Chen, H. Li, D. Chu, G. Wang, Unraveling oxygen reduction reaction mechanisms on carbon-supported Fe-phthalocyanine and Co-phthalocyanine catalysts in alkaline solutions, J. Phys. Chem. C 113 (2009) 20689-97.
157. H.-J. Choi, N.A. Kumar, J.-B. Baek, Graphene supported non-precious metalmacrocycle catalysts for oxygen reduction reaction in fuel cells, Nanoscale 7 (2015) 6991-8.
158. A.I. Krasil'shckov, On the intermediate stages of anodic oxygen evolution., Zh. Fiz. Khim. 37 (1963) 273.
159. W. O'Grady, J.H. C. Iwakura, E. Yeager,M.W. Breiter (ed), The Electrochemical Society, Princeton, 1974
160. W. E. O'Grady, C. Iwakura, E. Yeager, *Oxygen electrocatalysts for life support systems.*, in *Intersociety Conference on Environmental Systems*. 1976: San Diego, CA.

161. T.O. J. O'M. Bockris, The electrocatalysis of oxygen evolution on perovskites, J. Electrochem. Soc. 131 (1984) 290.
162. J.O.M. Bockris, Kinetics of activation controlled consecutive electrochemical reactions: anodic evolution of oxygen, J. Chem. Phys. 24 (1956) 817.
163. M. Bajdich, M.n. García-Mota, A. Vojvodic, J.K. Nørskov, A.T. Bell, Theoretical investigation of the activity of cobalt oxides for the electrochemical oxidation of water, J. Am. Chem. Soc. 135 (2013) 13521-30.
164. M.T.M. Koper, Thermodynamic theory of multi-electron transfer reactions: Implications for electrocatalysis, J. Electroanal. Chem. 660 (2011) 254-60.
165. M. Che, Nobel Prize in chemistry 1912 to Sabatier: Organic chemistry or catalysis?, Catal. Today 218-9 (2013) 162-71.
166. P. Sabatier, La Catalyse en chimie organique. 1913, University of California, USA: C. Béranger
167. I.C. Man, H.-Y. Su, F. Calle-Vallejo, H.A. Hansen, J.I. Martinez, N.G. Inoglu, J. Kitchin, T.F. Jaramillo, J.K. Nørskov, J. Rossmeisl, Universality in oxygen evolution electrocatalysis on oxide surfaces, Chem. Cat. Chem. 3 (2011) 1159-65.
168. O. Diaz-Morales, I. Ledezma-Yanez, M.T.M. Koper, F. Calle-Vallejo, Guidelines for the rational design of Ni-based double hydroxide electrocatalysts for the oxygen evolution reaction, ACS Catalysis 5 (2015) 5380-5387.
169. J.O.M. Bockris, T. Otagawa, The electrocatalysis of oxygen evolution on perovskites, J. Electrochem. Soc. 131 (1984) 290-302.
170. J.O.M. Bockris, T. Otagawa, Mechanism of oxygen evolution on perovskites, J. Phys. Chem. 87 (1983) 2960-71.
171. E. Fabbri, A. Habereder, K. Waltar, R. Kötz, T.J. Schmidt, Developments and perspectives of oxide-based catalysts for the oxygen evolution reaction, Catal. Sci. Technol. 4 (2014) 3800-21.
172. Federico Calle-Vallejo, Oscar A. Díaz-Morales, Manuel J. Kolb, M.T.M. Koper, Why Is bulk thermochemistry a good descriptor for the electrocatalytic activity of transition metal oxides?, ACS Catalysis 5 (2015) 869-73.
173. Y. Lee, J. Suntivich, K.J. May, E.E. Perry, Y. Shao-Horn, Synthesis and activities of rutile IrO_2 and RuO_2 nanoparticles for oxygen evolution in acid and alkaline solutions, Phys. Chem. Lett. 3 (2012) 399-404.
174. S. Jung, C.C.L. McCrory, I.M. Ferrer, J.C. Peters, T.F. Jaramillo, Benchmarking nanoparticulate metal oxide electrocatalysts for the alkaline water oxidation reaction, J. Mater. Chem. A 4 (2016) 3068-3076.
175. T. Reier, M. Oezaslan, P. Strasser, Electrocatalytic oxygen evolution reaction (OER) on Ru, Ir, and Pt catalysts: a comparative study of nanoparticles and bulk materials, ACS Catal. 2 (2012) 1765-72.
176. S.M. Alia, B. Rasimick, C. Ngo, K.C. Neyerlin, S.S. Kocha, S. Pylypenko, H. Xu, B.S. Pivovar, Activity and durability of iridium nanoparticles in the oxygen evolution reaction, ECS Trans. 69 (2015) 883-92.
177. R. Kotz, H.J. Lewerenz, S. Stucki, XPS studies of oxygen evolution on Ru and RuO_2 anodes J. Electrochem. Soc. 130 (1983) 825-9.
178. S. Cherevko, S. Geiger, O. Kasian, N. Kulyk, J.-P. Grote, A. Savan, B.R. Shrestha, S. Merzlikin, B. Breitbach, A. Ludwig, K.J.J. Mayrhofer, Oxygen and hydrogen evolution reactions on Ru, RuO_2, Ir, and IrO_2 thin film electrodes in acidic and alkaline electrolytes: A comparative study on activity and stability, Catal. Today 262 (2016) 170-80.
179. L.-E. Owe, M. Tsypkin, K.S. Wallwork, R.G. Haverkamp, S. Sunde, Iridium–ruthenium single phase mixed oxides for oxygen evolution: composition dependence of electrocatalytic activity, Electrochim. Acta 70 (2012) 158-64.
180. T. Audichon, T.W. Napporn, C. Canaff, C. Morais, C. Comminges, K.B. Kokoh, IrO_2 coated on RuO_2 as efficient and stable electroactive nanocatalysts for electrochemical water splitting, J. Phys. Chem. C 120 (2016) 2562-73.

181. S. Matsumoto, Electrocatalytic properties of transition metal oxides for oxygen evolution reaction, Mater. Chem. Phys. 14 (1986) 397-426.
182. F. Lu, M. Zhou, Y. Zhou, X. Zeng, First-row transition metal based catalysts for the oxygen evolution reaction under alkaline conditions: basic principles and recent advances, Small 13 (2017) 1-18.
183. S.J. Charles C. L. McCrory, Jonas C. Peters and Thomas F. Jaramillo, Benchmarking heterogeneous electrocatalysts for the oxygen evolution reaction, J. Am. Chem. Soc. 135 (2013) 16977−87.
184. M.R.G.d. Chilvo, A.C. Chialvo, Oxygen evolution reaction on $Ni_xCo_{3-x}O_4$ electrodes with spinel structure, Electrochim. Acta 38 (1993) 2247-52.
185. P. Nkeng, G. Poillerat, J.F. Koenig, P. Charfier, B. Lefez, J. Lopitaux, M. Lenglet, Characterization of spinel-type cobalt and nickel oxide thin films by x-ray near grazing diffraction, transmission and reflectance spectroscopies, and cyclic voltammetry, J. Electrochem. Soc. 142 (1995) 1777-83.
186. C. Bocca, A. Barbucci, M. Delucchi, G. Cerisola, Nickel-cobalt oxide-coated electrodes: influence of the preparation technique on oxygen evolution reaction (OER) in an alkaline solution, Int. J. Hydrogen Energy 24 (1999) 21-6.
187. A.C.C. Tseung, S. Jasem, Oxygen evolution on semiconducting oxides, Electrochim. Acta 22 (1977) 31-4.
188. H. Wendt, V. Plzak, Electrocatalytic and thermal activation of anodic oxygen- and cathodic hydrogen evolution in alkaline water electrolysis, Electrochim. Acta 28 (1983) 27-34.
189. P. Rasiyah, A.C.C. Tseung, A mechanistic study of oxygen evolution on Li - doped Co_3O_4, J. Electrochem. Soc. 130 (1983) 365-8.
190. E.B. Castro, C.A. Gervasi, Electrodeposited Ni-Co-oxide electrodes:characterization and kinetics of the oxygen evolution reaction, Int. J Hydrogen Energy 25 (2000) 1163-70.
191. J.G.D. Haenen, W. Visscher, E. Barendrecht, Oxygen evolution on $NiCo_2O_4$ electrodes, J. Appl. Electrochem. 15 (1985) 29-38.
192. F.J. Perez-Alonso, C. Adan, S. Rojas, M.A. Pena, J.L.G. Fierro, Ni/Fe electrodes prepared by electrodeposition method over different substrates for oxygen evolution reaction in alkaline medium, Int. J. Hydrogen Energy 39 (2014) 5204-12.
193. M.S. Burke, S. Zou, L.J. Enman, J.E. Kellon, C.A. Gabor, E. Pledger, S.W. Boettcher, Revised oxygen evolution reaction activity trends for first-row transition-metal (oxy)hydroxides in alkaline media, Phys. Chem. Lett. 6 (2015) 3737-42.
194. D.T. Ram Subbaraman, Kee-Chul Chang, Dusan Strmcnik, Arvydas P. Paulikas, Pussana Hirunsit, Maria Chan, Jeff Greeley, Vojislav Stamenkovic, Nenad M. Markovic, Trends in activity for the water electrolyser reactions on 3d M(Ni, Co, Fe, Mn) hydr(oxy)oxide catalysts, Nat. Mater. 11 (2012) 550-557.
195. P. Olivia, J. Leonardi, J.F. Laurent, C. Delmas, J.J. Braconnier, M. Figlarz, F. Fievet, A.d. Guibert, Review of the structure and the electrochemistry of nickel hydroxides and oxy-hydroxides, J. Power Sources 8 (1982) 229-55.
196. M.E.G. Lyons, M.P. Brandon, A comparative study of the oxygen evolution reaction on oxidised nickel, cobalt and iron electrodes in base, J. Electroanal. Chem. 641 (2010) 119-130.
197. B. Beverskog, I. Puigdomenech, Revised Pourbaix diagrams for nickel at 25–300 °C, Corr. Sci. 39 (1997) 969-80.
198. A.J. Bard, R. Parsons, J. Jordan, Standard Potentials in Aqueous Solutions, ed. M. Dekker. 1985, New York
199. Foteini M. Sapountzi, Jose M. Gracia, C.J. (Kees-Jan)Weststrate, Hans O.A. Fredriksson, J.W.H. Niemantsverdriet, Electrocatalysts for the generation of hydrogen, oxygen and synthesis gas, Progress in Energy and Combustion Science 58 (2017) 1-35.

200. X. Li, F.C. Walsh, D. Pletcher, Nickel based electrocatalysts for oxygen evolution in high current density, alkaline water electrolysers, Phys. Chem. Chem. Phys. 13 (2010) 1162-7.
201. S.L. Suib, New and Future Developments in Catalysis: Hybrid Materials, Composites, and Organocatalysts. 2013, Newnes: Elsevier
202. M.M. Jaksic, Interionic nature of synergism in catalysis and electrocatalysis, Solid State Ion. 136-137 (2000) 733-46.
203. D.A. Corrigan, R.M. Bendert, Effect of coprecipitated metal ions on the electrochemistry of nickel hydroxide thin films: cyclic voltammetry in 1M KOH J. Electrochem. Soc. 136 (1989) 723-8.
204. S.I. Cordoba, R.E. Carbonio, M.L. Teijelo, V.A. Macagno, The electrochemical response of binary mixtures of hydrous transition metal hydroxides co-precipitated on conducting substrates with reference to the oxygen evolution reaction, Electrochim. Acta 31 (1986) 1321-32.
205. D.A. Corrigan, The catalysis of the oxygen evolution reaction by iron impurities in thin film nickel oxide electrodes, J. Electrochem. Soc. 134 (1987) 377-84.
206. D.A. Corrigan, S.L. Knight, Electrochemical and spectroscopic evidence on the participation of quadrivalent nickel in the nickel hydroxide redox reaction, J. Electrochem. Soc. 136 (1989) 613-619.
207. R.L. Tichenor, Nickel oxides - relation between electrochemical reactivity and foreign ion content, Ind. Eng. Chem. 44 (1952) 973-7.
208. M. Gong, H. Dai, A mini review of NiFe-based materials as highly active oxygen evolution reaction electrocatalysts, Nano Res. 8 (2015) 23-39.
209. M.W. Louie, A.T. Bell, An investigation of thin-film Ni–Fe oxide catalysts for the electrochemical evolution of oxygen, J. Am. Chem. Soc. 135 (2013) 12329-37.
210. D. Friebel, M.W. Louie, M. Bajdich, K.E. Sanwald, Y. Cai, A.M. Wise, M.-J. Cheng, D. Sokaras, T.-C. Weng, R. Alonso-Mori, R.C. Davis, J.R. Bargar, J.K. Nørskov, A. Nilsson, A.T. Bell, Identification of highly active Fe sites in (Ni,Fe)OOH for electrocatalytic water splitting, J. Am. Chem. Soc. 137 (2015) 1305-13.
211. S. Kim, D.A. Tryk, M.R. Antonio, R. Cam, D. Scherson, In situ x-ray absorption fine structure studies of foreign metal ions in nickel hydrous oxide electrodes in alkaline electrolytes, J. Phys. Chem. 98 (1994) 10269-76.
212. L. Trotochaud, J.K. Ranney, K.N. Williams, S.W. Boettcher, Solution-cast metal oxide thin film electrocatalysts for oxygen evolution, J. Am. Chem. Soc. 134 (2012) 17253-61.
213. James B. Gerken, Sarah E. Shaner, Robert C. Mass´e, Nicholas J. Porubsky, S.S. Stahl, A survey of diverse earth abundant oxygen evolution electrocatalysts showing enhanced activity from Ni–Fe oxides containing a third metal, Energy Environ. Sci. 7 (2014) 2376-82.
214. R.N. Singh, J.P. Singh, B. Lala, M.J.K. Thomas, S. Bera, New $NiFe_{2-x}Cr_xO_4$ spinel films for O_2 evolution in alkaline solutions, Electrochim. Acta 51 (2006) 5515-23.
215. X. Bo, Y. Li, R.K. Hocking, C. Zhao, NiFeCr hydroxide holey nanosheet as advanced electrocatalyst for water oxidation, ACS Appl. Mater. Interfaces 9 (2017) 41239-45.
216. Yuangang Li, Shuli Yang, Huajing Li, Gang Li, Min Li, Lihua Shen, Zhiyuan Yang, A. Zhou, Electrodeposited ternary iron-cobalt-nickel catalyst on nickel foam for efficient water electrolysis at high current density, Colloids Surf. A 506 (2016) 694-702.
217. C.G. Morales-Guio, L. Liardet, X. Hu, Oxidatively electrodeposited thin-film transition metal (oxy)hydroxides as oxygen evolution catalysts, J. Am. Chem. Soc. 138 (2016) 8946-57.
218. M. Kumar, R. Awasthi, A.K. Pramanick, R.N. Singh, New ternary mixed oxides of Fe, Ni and Mo for enhanced oxygen evolution, Int. J. Hydrogen Energy 36 (2011) 12698-12705.
219. Y. Jin, S. Huang, X. Yue, H. Du, P.K. Shen, Mo- and Fe-modified $Ni(OH)_2$/NiOOH nanosheets as highly active and stable electrocatalysts for oxygen evolution reaction, ACS Catal. 8 (2018) 2359-63.

220. A.A. Singh, R.N. Singh, Effect of V substitution at B-site on the physicochemical and electrocatalytic properties of spinel-type $NiFe_2O_4$ towards O_2 evolution in alkaline solutions, Int. J. Hydrogen Energy 35 (2010) 3243-8.
221. K.N. Dinh, P. Zheng, Z. Dai, Y. Zhang, R. Dangol, Yun Zheng, B. Li, Y. Zong, Q. Yan, Ultrathin porous NiFeV ternary layer hydroxide nanosheets as a highly efficient bifunctional electrocatalyst for overall water splitting, Small 2018) 1703257.
222. M. Busch, N.B. Halck, U.I. Kramm, S. Siahrostami, P. Krtil, J. Rossmeisl, Beyond the top of the volcano? – A unified approach to electrocatalytic oxygen reduction and oxygen evolution, Nano Energy 29 (2016) 126-35.
223. F. Calle-Vallejo, M.T.M. Koper, First-principles computational electrochemistry: Achievements and challenges, Electrochim. Acta 84 (2012) 3-11.
224. H.-Y. Su, Y. Gorlin, I.C. Man, F. Calle-Vallejo, J.K. Nørskov, T.F. Jaramillo, J. Rossmeisl, Identifying active surface phases for metal oxide electrocatalysts: a study of manganese oxide bi-functional catalysts for oxygen reduction and water oxidation catalysis, Phys. Chem. Chem. Phys. 14 (2012) 14010-22.
225. C. Song, J. Zhang, PEM Fuel Cell Electrocatalysts and Catalyst Layers,J. Zhang (ed), Springer London, 2008
226. H.S. Bernard Bladergroen, Sivakumar Pasupathi and Vladimir Linkov, Overview of Membrane Electrode Assembly Preparation Methods for Solid Polymer Electrolyte Electrolyzer(ed), InTech, SAIAMC, University of the Western Cape, South Africa, 2012
227. S.R. Narayan, A.K. Manohar, S. Mukerjee, *Bi-Functional oxygen electrodes – Challenges and prospects*, in *The Electrochem. Soc. Interface*. 2015.
228. N. Sasikala, K. Ramya, K.S. Dhathathreyan, Bifunctional electrocatalyst for oxygen/air electrodes, Energy Conver. Manag. 77 (2014) 545-9.
229. R. Thacker, On the use of palladium-catalyzed air cathodes in a secondary zinc-air cell, Energy Conver. 12 (1971) 17-20.
230. J.-I. Jung, M. Risch, S. Park, M.G. Kim, G. Nam, H.-Y. Jeong, Y. Shao-Horn, J. Cho, Optimizing nanoparticle perovskite for bifunctional oxygen electrocatalysis, Energy Environ. Sci. 9 (2016) 176-83.
231. S. Ahn, K. Kim, H. Kim, S. Nam, S. Eom, Synthesis and electrochemical performance of $La_{0.7}Sr_{0.3}Co_{1-x}Fe_xO_3$ catalysts for zinc air secondary batteries, Phys. Scr. T139 (2010) 014014.
232. A.M. Kannan, A.K. Shukla, S. Sathayanarayana, Oxide-based bifunctional oxygen electrode for rechargeable metal/ air batteries, J. Power Sources 25 (1989) 141-50.
233. S. Muller, K. Striebel, O. Haas, $La_{0.6}Ca_{0.4}CoO_3$: A stable and power catalyst for bifunctional air electrodes, Electrochim. Acta 39 (1994) 1661-8.
234. H.B. Yang, J. Miao, S.-F. Hung, J. Chen, H.B. Tao, X. Wang, L. Zhang, R. Chen, J. Gao, H.M. Chen, L. Dai, B. Liu, Identification of catalytic sites for oxygen reduction and oxygen evolution in N-doped graphene materials: Development of highly efficient metal-free bifunctional electrocatalyst, Sci. Adv. 2 (2016) e1501122.
235. L. Carlsson, L. Ojefors, Bifunctional air electrode for metal-air batteries J. Electrochem. Soc. 127 (1980) 525-8.
236. L. Swette, N. Kackley, S.A. McCatty, Oxygen electrodes for rechargeable alkaline fuel cells. III, J. Power Sources 36 (1991) 323-39.
237. X. Liu, M. Park, M.G. Kim, S. Gupta, X. Wang, G. Wu, J. Cho, High-performance non-spinel cobalt–manganese mixed oxide-based bifunctional electrocatalysts for rechargeable zinc–air batteries, Nano Energy 20 (2016) 315-25.
238. L. Li, C. Liu, G. He, D. Fan, A. Manthiram, Hierarchical pore-in-pore and wire-in-wire catalysts for rechargeable Zn– and Li–air batteries with ultra-long cycle life and high cell efficiency, Energy Environ. Sci. 8 (2015) 3274-82.
239. J.J. Postula, R. Thacker, On the use of third electrodes in a secondary zinc-air battery, Energy Conver. 10 (1970) 45-9.
240. M. Bockelmann, U. Kunz, T. Turek, Electrically rechargeable zinc-oxygen flow battery with high power density, Electrochem. Commun. 69 (2016) 24-7.

241. Y. Li, M. Gong, Y. Liang, J. Feng, J.-E. Kim, H. Wang, G. Hong, B. Zhang, H. Dai, Advanced zinc-air batteries based on high-performance hybrid electrocatalysts, Nat. Commun. 4 (2013) 1805.
242. W. Hong, H. Li, B. Wang, A horizontal three-electrode structure for zinc-air batteries with long-term cycle life and high performance, Int. J. Electrochem. Sci. 11 (2016) 3843-51.
243. H. Arai, S. Müller, O. Haas, AC impedance analysis of bifunctional air electrodes for metal-air batteries, J. Electrochem. Soc. 147 (2000) 3584-91.
244. Y. Takeshita, S. Fujimoto, M. Sudoh, Design of rechargeable air diffusion cathode for metal-air battery using alkaline solution, ECS Trans. 50 (2013) 3-12.
245. D.U. Lee, J.-Y. Choi, K. Feng, H.W. Park, Z. Chen, Advanced extremely durable 3D bifunctional air electrodes for rechargeable zinc-air batteries Adv. Energy Mater. 4 (2014) 1301389.
246. J. Fu, F.M. Hassan, J. Li, D.U. Lee, A.R. Ghannoum, G. Lui, M.A. Hoque, Z. Chen, Flexible rechargeable zinc-air batteries through morphological emulation of human hair array, Adv. Mater. 28 (2016) 6421-8.
247. J.W.D. Ng, M. Tang, T.F. Jaramillo, A carbon-free, precious-metal-free, high performance O_2 electrode for regenerative fuel cells and metal–air batteries, Energy Environ. Sci. 7 (2014) 2017–24.
248. X. Li, D. Pletcher, A.E. Russell, F.C. Walsh, R.G.A. Wills, S.F. Gorman, S.W.T. Price, S.J. Thompson, A novel bifunctional oxygen GDE for alkaline secondary batteries, Electrochem. Commun. 34 (2013) 228-30.
249. B. Li, X. Ge, F.W.T. Goh, T.S.A. Hor, D. Geng, G. Du, Z. Liu, J. Zhang, X. Liu, Y. Zong, Co_3O_4 nanoparticles decorated carbon nanofiber mat as binder-free air-cathode for high performance rechargeable zinc-air batteries, Nanoscale 7 (2015) 1830-8.
250. F. Meng, H. Zhong, D. Bao, J. Yan, X. Zhang, In situ coupling of strung Co_4N and intertwined N−C fibers toward free-standing bifunctional cathode for robust, efficient, and flexible Zn−air batteries, J. Am. Chem. Soc. 138 (2016) 10226-31.
251. Z. Wang, S. Xiao, Z. Zhu, X. Long, X. Zheng, X. Lu, S. Yang, Cobalt-embedded nitrogen doped carbon nanotubes: A bifunctional catalyst for oxygen electrode reactions in a wide pH range, ACS Appl. Mater. Interfaces 7 (2015) 4048-55.
252. P.R. Vassie, A.C.C. Tseung, A study of gas evolution in teflon bonded porous electrodes - I. The mechanical and chemical stability of teflon bonded graphite electrodes, Electrochim. Acta 20 (1975) 759-61.
253. J. Eigeldinger, H. Vogt, The bubble coverage of gas-evolving electrodes in a flowing electrolyte, Electrochim. Acta 45 (2000) 4449-56.
254. G. Toussaint, P. Stevens, L. Akrour, F. Rouget, F. Fourgeot, Development of a rechargeable zinc-air battery, ECS Trans. 28 (2010) 25-34.
255. S. Amendola, M. Binder, P.J. Black, S. Sharp-Goldman, L. Johnson, M. Kunz, M. Oster, T. Chciuk, R. Johnson, Bifunctional (rechargeable) air electrodes comprising a corrosion-resistant outer layer and conductive inner layer, (2010) Patent: US8802304B2.
256. S. Amendola, M. Binder, P.J. Black, S. Sharp-Goldman, L. Johnson, M. Kunz, M. Oster, T. Chciuk, R. Johnson, Electrically rechargeable, metal-air battery systems and methods, (2010) Patent: US20120021303A1.

Chapter 3 Methodology

3.1. Research tasks

The research was divided into four main research tasks, based on the objectives of this research project stated in Section 1.4 and review of the literature in Chapter 2: (1) Oxygen reduction reaction (ORR) catalyst selection and optimisation, (2) Oxygen evolution reaction (OER) catalyst selection and optimisation, (3) Secondary cell design, and (4) Electrode stability test. These tasks were then addressed in the respective research chapters as presented in **Table 3.1**. The selection process and optimisation of the oxygen reaction-specific ORR and OER catalysts are presented in chronological order in Chapters 4, 5, 6 and 7. The design and construction of a secondary cell testing set-up for assessing the stability of optimal ORR and OER electrodes is given in the final research chapter, Chapter 8.

Table 3.1 Research tasks and corresponding chapters.

Research Tasks	**Chapter**
Oxygen reduction reaction (ORR)	
• Selection of ORR catalyst	Chapter 4
• Optimisation of ORR catalyst	Chapter 5
• Investigation of effects of catalyst synthesis parameters on ORR and optimisation of ORR electrode	Chapter 5
Oxygen evolution reaction (OER)	
• Selection of OER catalyst	Chapter 6
• Optimisation of OER catalyst composition	Chapter 7
• Investigation of effects of catalyst synthesis parameters and optimisation of OER catalyst layer	Chapter 7
Secondary cell design	
• Construction and assembly of secondary cell design and testing set-up	Chapter 8
Electrode stability test	
• Evaluation of the effects of varying testing parameters on ORR and OER performance	Chapter 8
• Assessment of ORR and OER electrode performance in a long-term stability test	Chapter 8

3.2. Catalyst selection

3.2.1. Oxygen reduction reaction

3.2.1.1. Transition metal oxides

Aside from demonstrating high stability, conductivity and activity for ORR [1], the main motivation behind selecting transition metal oxides as potential ORR candidates are that they are more environmentally abundant in the earth and therefore lower in cost compared to precious metals which makes them suitable for large-scale production. have demonstrated. For example, the change in oxidation state of Mn between +2, +3 and +4 in manganese oxides coincides with the ORR equilibrium potential [2] thereby indicating that it has the ability to facilitate the exchange of oxygen atoms. Cobalt oxides and cobalt-based mixed oxides such as $NiCo_2O_4$ and $MnCo_2O_4$ have also previously demonstrated promising ORR performance under alkaline conditions due to the availability of cations with variable oxidation states.

3.2.1.2. Functional carbon materials

Functional carbon materials, and more specifically graphene-based carbon materials, were picked as prospective ORR electrocatalyst candidates as they have a potentially low production cost, are highly abundant and have high electrical conductivity and surface area to volume ratio [3]. Furthermore, since doping graphene with heteroatoms such as nitrogen, boron, phosphorus or sulphur has been shown to enhance ORR performance [4, 5], this led to the further selection of N-doped graphene for comparison.

3.2.2. Oxygen evolution reaction

3.2.2.1. Transition metal oxides & hydroxides

Transition metal oxides and hydroxides were selected as potential OER candidates for similar reasons given previously; low cost and environmentally abundant compared to noble metals. In addition, oxides and hydroxides of transition metals are favoured over metals as catalysts for OER as they are not able to be further oxidised and are therefore more stable for the reaction [6]. From the literature in

Chapter 2, Section 2.2.1, the general trend in transition metal reactivity was Ni > Co > Fe [7-10]. Hence, Ni-based catalysts were shown a preference although several other transition metal based catalysts were synthesised for comparison.

3.3. Catalyst synthesis and optimisation

The selection of a suitable synthesis method and preparation conditions is especially important as the catalysts' composition, morphology and crystal structure as well as their activity for ORR or OER are a direct result of this. Equally important as an objective of the work, was considering the ease with which the synthesis method of the selected catalysts could be scaled up for large-scale production in the future. Methods were therefore shown a preference over others if they required minimal processing steps, less time, materials and space or, resources which would add to the cost of production. This ensured higher product yield and limited variation in purity and crystal structure of the product.

In Chapters 4 and 5, a chemical redox method [11] was chosen for the production of ORR catalyst MnO_x. The advantages of the method were its simplicity and ability to produce catalysts at room temperature with comparable activity to manganese oxides made at higher temperatures. On top of this, the pH and temperature of the mixture, drop feed rate, stir rate, precursors and solution concentration could be well-controlled for better catalyst morphology, crystal structure and porosity.

In Chapters 6 and 7, a cathodic electrodeposition method [12] was used for the synthesis of Ni-based hydroxides as OER catalysts, which enabled the catalyst compositions to be controlled by simply varying the ratio of transition metal sulphates in the electrodeposition solution. This method of electrodeposition was also very versatile, producing diverse deposit morphologies with properties which were a function of the electrodeposition conditions such as electrodeposition potential and/or current, electrolyte pH, composition and additives etc.

A thermal decomposition method [13] was used to prepare transition metal spinel oxides of Co_3O_4 and $NiCo_2O_4$ in Chapter 4 and 6 because this method produces oxides of good mechanical stability and can be considered a rapid and easily reproducible technique. Using this technique, the spinel oxides of Co_3O_4 and $NiCo_2O_4$

could be synthesised as powders in Chapter 4 or directly coated onto metal mesh via dip-coating [14] in Chapter 6. Certain chemicals used in the synthesis method could also be substituted with others to reduce hazards associated with the procedure, for example, isopropanol was used as a solvent in place of methanol for the preparation of metal oxides on metal mesh.

3.4. Electrochemical methods

3.4.1. Electrochemical characterisation of catalysts

Electrochemical measurements were carried out with Biologic potentiostat/ galvanostats using EC-lab software. The SP-150 potentiostat model operated within a current range of 10 µA to 800 mA with a ±20 V compliance range and this potentiostat model was used for most experiments as this current range was sufficient. The SP-300 potentiostat model had an additional 10 A, ±5 V booster and was used for the stability experiments in Chapter 6 and 7, which required much higher currents.

3.4.1.1. Cyclic and linear sweep voltammetry

In this work, cyclic voltammetry and linear sweep voltammetry were used to study the performance of selected catalysts and effects of altering the synthesis and testing parameters on the kinetics of the oxygen reactions. Cyclic voltammetry (CV) is one of the most widely used techniques for acquiring qualitative knowledge on the mechanisms and potentials of electrode processes. Due to the processes that take place at the electrode, the current measured is a combination of faradaic current (oxidation/ reduction of the electroactive species at the electrode) and capacitive current (double layer charging). Appropriate potential ranges were selected to study the reactions of interest and multiple CVs were carried out in these ranges to determine the chemical changes that take place over time at the catalyst material and also to allow the system to reach an equilibrium. Other information gathered from CVs were characteristics of reversible and irreversible electron transfer reactions.

Linear sweep voltammetry (LSV) is similar to CV and potential ranges were usually chosen based on a prior CV scan. This technique is particularly useful for determining the effect of voltage on the equilibrium at the electrode surface. As

performance values obtained from this are affected by capacitive current effect and depend on conditions of measurement such as scan rate and potential sweep direction, very slow scan rates < 5 mV s^{-1} were chosen to increase accuracy of the measurements. The chemical reactivity and electron transfer kinetics of the catalyst samples were compared using this technique.

3.4.1.2. Overpotential

The performance of the catalysts were evaluated based on activity parameters such as overpotential at a constant current density. The current measured was normalised against geometrical electrode area or catalyst mass or loading to determine a current density value. Catalyst loading on the electrode was kept as consistent as possible to overcome the inaccuracy of normalising the current value against the electrode geometrical area for three dimensional electrodes. In general, the expression used to determine overpotential can be written as

$$\eta = E_{measured} - E_{rev} - iR_u$$

Where $E_{measured}$ is the recorded experimental potential, E_{rev} is the potential at which OER is expected to take place at, this is taken to be 0.303 V vs Hg/ HgO in 1 M NaOH [15] and R_u is the uncompensated series resistance.

Due to the discrepancies surrounding the methods of obtaining the iR_u value however, alternative methods to reduce iR in the system were used instead and these are mentioned in Section 3.6.

3.4.1.3. Tafel plot

Another activity parameter selected for assessing catalyst performance was the Tafel slope which relies on the reaction mechanism. This activity parameter was used to compare the activity of OER catalysts in Chapters 6 and 7. In general, the Tafel slope gives an indication of the reaction's rate of change of current density with overpotential. The values of the Tafel plot are hugely dependent on the measurement conditions such as scan rate and scan direction, therefore to ensure steady-state conditions were maintained, slow scan voltammetry at scan rate of 1 mV s^{-1} was used to measure current for Tafel slope analysis.

3.4.1.4. Chronopotentiometry

Chronopotentiometry is a constant current electrochemical technique whereby a fixed current is applied to an electrode in an environment of excess supporting electrolyte for a period of time. This electrochemical method was used in the cathodic electrodeposition synthesis method of catalyst in Chapters 6 and 7. Additionally, this technique was used to determine the stability of catalyst materials over prolonged periods of time at constant operating conditions. A plot of potential as a function of time is commonly obtained and this is used to demonstrate the catalyst durability at oxidising or reducing conditions. Cyclic chronopoteniometry or galvanostatic cycling, whereby the current is reversed after a period of time and this is repeated as required, was carried out in Chapter 8 to verify the stability of both oxygen electrodes in the same system over long periods of time.

3.4.2. Rotating disc electrode (RDE)

By combining the use of LSV with the RDE, the kinetic parameters and the ORR reaction pathway of the catalysed reaction under steady state conditions were able to be studied in Chapters 4 and 5, in order to provide a better understanding of the system's performance in non-steady state conditions. The rate of the electrochemical reaction is given by the current density which varies with potential; and the Levich and Koutecky-Levich equations were also employed to determine the mass transfer parameters in this study.

This method was chosen as it is very well-developed. Results from this tool are usually accurate and reproducible. To immobilise the catalyst powders onto the glassy carbon electrode surface, catalyst inks of samples were formulated by mixing the catalyst with 5 wt% Nafion solution to increase ionic conductivity and solvent of IPA and deionised H_2O. These inks were ultrasonicated and homogenised before being applied to electrode surface with a micropipette to prevent aggregation of the catalyst particles in the ink and ensure that the particles were evenly dispersed throughout. Since the same RDE tip was used for multiple experiments, the glassy carbon electrode surface was wet polished with alumina powders of two particle sizes 1.0 mm and 0.5 mm (MicroPolish, Buehler) and MicroCloth (Buehler), and then ultrasonicated in deionised water between each use.

3.4.3. Microelectrode

A unique microelectrode set-up in a custom-made glass cell was chosen for rapid synthesis and screening of OER catalyst performance in Chapter 7. The microelectrode was fabricated by sealing a stainless steel microwire (⌀ ~ 25 μm) in glass. This microelectrode set-up is considered advantageous in this work since less time is required for the system to reach steady state due to convergent diffusion to the working microelectrode tip, the charging effect of double-layer capacitance is reduced due to the smaller area and ohmic losses from solution resistance are reduced since a smaller current is used. As the microelectrode was reused for different samples, the surface of the microdisc was wet polished with 1.0 mm and 0.5 mm (MicroPolish, Buehler) alumina powders and MicroCloth (Buehler), and then ultrasonicated in deionised water in between each use.

The condition of the surface of the microelectrode was examined with SEM before and after screening all OER catalysts to determine if any severe wear had been sustained. SEM micrographs in **Figure 3.1 a & b** confirm the surface of the microdisc was intact after use with fewer scratches, possibly from incessant polishing.

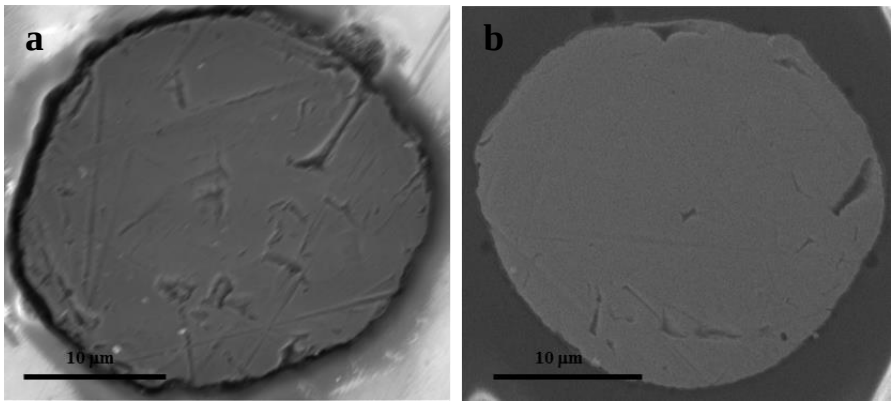

Figure 3.1 SEM micrographs of stainless steel microdisc **a)** before and **b)** after screening OER catalysts.

3.4.4. Selection of electrode material

The selection of electrode materials and methods of incorporating the synthesised catalysts into an electrode were based on the specific requirements of the oxygen electrochemical reaction environments and ensuring the electrode material would be mechanically robust, whilst keeping material costs low.

3.4.4.1. Gas diffusion electrode (GDE)

After suitable ORR catalysts were selected using the RDE setup as described in Section 3.4.2., carbon fibre paper was selected as an ORR electrode material for ORR catalyst to be coated onto. A custom-made GDE cell was used to test ORR electrode performances in Chapter 4 and 5 at different current densities. The ORR electrode displaying the best overall performance was then selected for further optimisation.

Carbon fibre paper is a well-developed material for fuel cells and was therefore seen as a suitable electrode material for the GDE cell. The advantages that it has as a material are that it is light, porous, has a high conductivity, large surface area, sufficient resistance to chemical corrosion, hydrophobic but still highly permeable to gas. This allowed the catalyst coated side to be immersed in electrolyte whilst oxygen gas was supplied as a reactant to the back of the GDE. Carbon paper was initially purchased from Alfa Aesar (TGP-H-60, Baselayered) however the production and supply of this product was discontinued. Subsequently, an alternative brand of carbon paper from AvCarb (GDS 1120) was sourced and purchased instead. Both brands of carbon paper were selected for their microporous coating layered on one side which was composed of a slurry of carbon and PTFE dispersion. The average PTFE content of the carbon paper from Alfa Aesar was ~ 25% whilst the PTFE content in the AvCarb carbon paper was between 10-13%. The microporous coating helps to reduce the contact resistance between the catalyst and gas diffusion layers, prevent the catalyst from being trapped in the gas diffusion layer as well as assist in the transport of electrolyte through the GDL. The properties of these brands of carbon paper, as reported by the companies, are compared side-by-side in the table below. The comparison of the performances of these two types of carbon paper are given in Appendix B.

Table 3.2 Specifications of the two brands of carbon paper.

	TGP-H-60	**GDS 1120**
Nominal thickness/ mm	0.190	0.184
Bulk density/ g cm^{-3}	0.44	0.40
Through-plane resistivity/ mΩ cm^{-2}	80	<14.5

3.4.4.2. Metal mesh electrode

Metal mesh electrodes were coated with selected and optimised OER catalysts for stability testing in a custom-designed water electrolyser unit cell (ITM power, plc UK). Expanded metal mesh (DeXmet Corporation, 4SS 5-050, 0.004″ nominal thickness, 0.005″ strand width, 0.050″ long diagonal of the diamond) was selected as an OER electrode substrate as it is highly conductive, light, and porous to facilitate the escape of bubbles from the surface of the electrode whilst avoiding the complexity of a three-dimensional electrode structure.

3.4.5. Secondary cell design and assembly

In order to evaluate the performance of both oxygen reduction and evolution electrodes in a secondary cell, a Zn-air system was selected as it has a high theoretical energy density and can be considered safer than other systems since Zn is not reactive or flammable in air. Considering the difficulties associated with a bifunctional oxygen electrode, a tri-electrode configuration was adopted for this system to avoid the issue of the instability of electrocatalysts and ancillary additives used to fabricate electrodes over the full cycling potential range. This meant that the oxygen reactions were decoupled into two separate reaction-specific cathodes on either side of the Zn anode, which helped to minimise the degradation of materials at oxidative potentials. During discharge, the ORR electrode was connected to the Zn anode and subsequently during charge, the OER electrode was connected to the Zn anode.

As the potentiostat was unable to differentiate between the ORR and OER oxygen cathodes, an automated set-up was constructed specially for these experiments with a Raspberry Pi as a microcontroller of a relay module to ensure the ORR and OER electrode could be connected to the Zn anode during discharge and charge respectively. The advantages of using a Raspberry Pi as a microcontroller in this set-up were that it is small, cheap, requires simple programming skills, is practical as it has digital IO pins for on/ off states and has sufficient voltage to control the relay module. An EC-lab galvanostatic cycling technique designed for a three-electrode cell setup was used to allow the electrode potentials to be monitored and recorded separately against an Hg/HgO reference electrode positioned in the cell.

3.5. Physical characterisation of catalysts

The physical properties of the synthesised catalyst materials were examined using techniques described in this section. This was necessary as the surface morphology, structure and composition of these materials are closely linked to their catalytic activity. These techniques were chosen based on the information that they could provide and most were non-destructive towards the samples which meant the same sample could be characterised by several techniques so different types of information of the same material could be gathered.

3.5.1. Scanning Electron Microscopy (SEM) - Energy Dispersive X-ray Spectroscopy (EDX)

SEM-EDX measurements were used to characterise the catalyst sample morphology at microscales and determine elemental composition at different points over the sample area. These techniques allowed rapid, high-resolution non-destructive assessment of the interfaces or surfaces that were involved in the reactions. Samples were mounted onto small aluminium stubs with carbon or copper tape to ensure good conductive contact. These stubs were then placed in specimen holders specific to the microscope. Measurements for catalyst samples were carried out using a FEI Quanta 650 FEG-SEM with Bruker EDX system. Typically, accelerating voltages of 1-5 kV were used to reduce the penetration depth of the electrons into the sample and allow the surface structures and morphology of the catalyst and electrode structures to be studied in better quality. ‘Charging’ artefacts, particularly from samples with higher resistivity such as metal oxides, were also able to be avoided by using lower accelerating voltages.

3.5.2. Transmission Electron Microscopy (TEM)

TEM was used to determine the morphology of the catalyst samples at nano-scale as well as identify the chemical composition of the different phases. Samples for TEM were prepared by directly electrodepositing samples onto the TEM Cu grids (AGG 2100C, Agar Scientific). Areas for electrodeposition were masked off with Kapton® polyimide tape (DuPont). A JEM-2100 LaB6 TEM was used at accelerating voltage of 200 kV to capture the micrographs for samples in Chapter 7. Diffraction

patterns of the samples were analysed using ImageJ software and compared against reflections of known patterns.

3.5.3. X-ray diffraction (XRD)

Diffraction was used to determine the crystal phrases present in the samples and the quantity of the phase since the intensity of the reflections are greater in an area of high electron density, and conversely in areas of low electron density, the planes are more weakly reflected. Powder diffraction measurements were carried out on a Bruker D8 Advance X-ray diffractometer for powder in Chapters 4 and 5. For powder samples, small amounts of powder samples were pressed firmly between two glass slides to create a uniformly flat surface and equipment was calibrated before each measurement was taken. A Siemens D5000 X-ray diffractometer was used for thin film diffraction of catalyst coated electrode samples in Chapter 6. Both systems were configured with a Cu tube source (λ= 1.5418 Å) and measurements were carried out with a step size of 0.02 degrees held for 1 to 4 s to ensure good resolution. XRD results were analysed using Bruker Diffraction Suite EVA software.

3.5.4. X-ray Photoelectron Spectroscopy (XPS)

XPS was used to determine elemental composition, chemical and electronic state of the catalyst materials up to depths of 1-10 nm. Elements present as well as bonding-specific information of the sample were gathered from the XPS spectra. XPS samples were prepared by cathodic electrodeposition in a three electrode half-cell onto polymer carbon plate (BMA5, Eisenhuth). This substrate material was chosen as it is conductive but can also be easily distinguished from the catalyst sample material and therefore not have any effect on the results. Measurements were carried out with Thermo Fisher, ESCALAB 250Xi XPS system with a monochromatic Al Kα source over energy range of 0 to 1350 eV with pass energy of 30.0 eV, step size of 0.05 eV and X-ray spot size of 500 μm. All spectra was analysed with XPSPEAK 4.1 software and XPS database http://srdata.nist.gov/xps/.

3.5.5. Surface adsorption and desorption measurements

Nitrogen gas sorptions of powder catalyst samples in Chapters 4 and 5 were carried out on Quantachrome Autosorb-iQ gas sorptometer or Belsorp max (MicrotracBEL Corp.) via the conventional volumetric technique. The catalyst powder samples were evacuated for 2-3 h at 200 ºC under vacuum before gas analysis. The textural properties of the samples were determined via N_2 sorption at 77 K. The sorption data was analysed with Braunner-Emmett-Teller (BET), Barrett-Joyner-Halenda (BJH) and Density Functional Theory (DFT) methods for comparison as each method has its limitations. Analysis of specific surface areas of the materials was based on adsorption data in partial pressure, P/P_o range of 0.02-0.22 and total pore volume was obtained from the amount of N_2 adsorbed at P/P_o ca. 0.99.

3.6. Experimental limitations

As the measurement of catalyst reaction kinetics is dependent on ohmic resistance through the electrolyte and cell components, a three-electrode set-up consisting of a working, counter and reference electrode was employed in this work to minimise this resistance. The reliability of the experiments was maintained by keeping the distances between these electrodes constant with the help of polymer lids and using Luggin capillaries wherever possible. The condition of the reference and counter electrodes were checked regularly and the same electrodes were used for the same sets of experiments to ensure consistency. Furthermore, resistances through connecting wires were tested and deemed negligible. Care was taken to ensure that glassware was free from contaminants before use. Fresh electrolyte was used for each experiment and glassware had inbuilt water jackets which were used in conjunction with recirculating water baths to maintain the temperature of the electrolyte solutions. Lastly, each experiment was repeated at least twice to ensure that results were reproducible.

3.7. References

1. V. Neburchilov, H. Wang, J. J.Martin, W. Qu, A review on air cathodes for zinc–air fuel cells, J. Power Sources 195 (2010) 1271-91.
2. H.-Y. Su, Y. Gorlin, I.C. Man, F. Calle-Vallejo, J.K. Norskov, T.F. Jaramillo, J. Rossmeisl, Identifying active surface phases for metal oxide electrocatalysts: a study of manganese oxide bi-functional catalysts for oxygen reduction and water oxidation catalysis, Phys. Chem. Chem. Phys. 14 (2012) 14010-22.
3. A.K. Geim, K.S. Novoselov, The rise of graphene, Nat. Mater. 6 (2007) 183-91.
4. X. Wang, G. Sun, P. Routh, D.-H. Kim, W. Huang, P. Chen, Heteroatom-doped graphene materials: syntheses, properties and applications, Chem. Soc. Rev. 43 (2014) 7067-98.
5. C.H. Choi, S.H. Park, S.I. Woo, Binary and ternary doping of nitrogen, boron, and phosphorus into carbon for enhancing electrochemical oxygen reduction activity, ACS Nano. 6 (2012) 7084-91.
6. S. Matsumoto, Electrocatalytic properties of transition metal oxides for oxygen evolution reaction, Mater. Chem. Phys. 14 (1986) 397-426.
7. D.T. Ram Subbaraman, Kee-Chul Chang, Dusan Strmcnik, Arvydas P. Paulikas, Pussana Hirunsit, Maria Chan, Jeff Greeley, Vojislav Stamenkovic, Nenad M. Markovic, Trends in activity for the water electrolyser reactions on 3d M(Ni, Co, Fe, Mn) hydr(oxy)oxide catalysts, Nat. Mater. 11 (2012) 550-557.
8. M.E.G. Lyons, M.P. Brandon, The oxygen evolution reaction on passive oxide covered transition metal electrodes in aqueous alkaline solution. Part 1-Nickel, Inter. J. Electrochem. Sci 3 (2008) 1386-424.
9. L. Trotochaud, J.K. Ranney, K.N. Williams, S.W. Boettcher, Solution-cast metal oxide thin film electrocatalysts for oxygen evolution, J. Am. Chem. Soc. 134 (2012) 17253-61.
10. M.P.B. Michael E.G. Lyons, A comparative study of the oxygen evolution reaction on oxidised nickel, cobalt and iron electrodes in base, J. Electroanal. Chem. 641 (2010) 119-130.
11. F. Cheng, J. Shen, B. Peng, Y. Pan, Z. Tao, J. Chen, Rapid room-temperature synthesis of nanocrystalline spinels as oxygen reduction and evolution electrocatalysts, Nat. Chem. 3 (2010) 79-84.
12. X. Li, F.C. Walsh, D. Pletcherb, Nickel based electrocatalysts for oxygen evolution in high current density, alkaline water electrolysers, Phys. Chem. Chem. Phys. 13 (2010) 1162-7.
13. S. W.T.Price, S. J.Thompson, X. Li, S. F.Gorman, D. Pletcher, A. E.Russell, F. C.Walsh, R. G.A.Wills, The fabrication of a bifunctional oxygen electrode without carbon components for alkaline secondary batteries, J. Power Sources 259 (2014) 43-9.
14. X. Li, D. Pletcher, A. E.Russell, F. C.Walsh, R. G.A.Wills, S. F.Gorman, S. W.T.Price, S. J.Thompson, A novel bifunctional oxygen GDE for alkaline secondary batteries, Electrochem. Commun. 34 (2013) 228-30.
15. M.E.G. Lyons, M.P. Brandon, The oxygen evolution reaction on passive oxide covered transition metal electrodes in aqueous alkaline solution. Part 1-Nickel Int. J. Electrochem. Sci. 3 (2008) 1386-424.

Chapter 4 Selection of Catalyst for Oxygen Reduction Reaction

This chapter presents the results of the characterisation and performances of different groups of ORR electrocatalysts under identical conditions. Non-precious metal oxides and non-metals were selected for comparison because of their good activity and high abundance in the environment. The ORR activity of metal oxide catalysts amorphous MnO_x, MnO_2, Co_3O_4, $NiCo_2O_4$ and $MnCo_2O_4$ were compared against graphene nanoplatelets and N-doped graphene as well as benchmark catalysts 5 wt% Pt/C and Vulcan XC-72R in alkaline media in a rotating disk electrode (RDE) set-up.

From previous studies, the addition of a carbon support to the catalyst layer was observed to not only increase conductivity and assist in catalyst dispersion but also to have an effect on the ORR pathway (Chapter 2, Section 2.1.1.2).Therefore, the effect on ORR performance of mixing Vulcan XC-72R carbon black with these catalysts was investigated in this chapter.

As highlighted in the literature review, much of the published work on catalysts tends to focus on determining ORR reaction kinetics with rotating disc and ring-disc electrode (RRDE) set-ups, whilst few studies have incorporated these catalysts into gas diffusion electrodes (GDE) in order to establish the operational performances of these catalysts at practical current densities. In this chapter, selected catalysts were incorporated into gas diffusion electrodes and tested at various current densities.

4.1. Experimental section

4.1.1. Synthesis of catalysts

The synthesis of Co_3O_4, $NiCo_2O_4$ and $MnCo_2O_4$ were carried out via a thermal decomposition method. $NiCo_2O_4$ and $MnCo_2O_4$ were prepared by adding 0.5 M (14.5 g) of nickel (II) nitrate hexahydrate, $Ni(NO_3)_2.6H_2O$ (Fisher Scientific, 99.9%) or 0.5 M (12.6 g) manganese (II) nitrate tetrahydrate $Mn(NO_3)_2.4H_2O$ (Sigma Aldrich, ≥ 97%), respectively and 1 M (29.1 g) cobalt (II) nitrate hexahydrate, $Co(NO_3)_2.6H_2O$ (Fisher Scientific, 98+%, ACS reagent) to methanol (Fisher Scientific, 99.9%) in a 100 mL

dilution flask. The methanol was added to the transition metal nitrates in small amounts and stirred continuously to obtain a homogenous solution. The solution was then transferred to a crucible and evaporated to dryness on a hotplate leaving a dark red solid. The solid was calcined in air at 648 K for 20 h. The resulting solid was then ground down to a fine black powder. The addition of $Ni(NO_3)_2.6H_2O$ or $Mn(NO_3)_2.4H_2O$ was omitted for the synthesis of Co_3O_4.

A chemical redox method was used to prepare amorphous MnO_x. In general, 50 mL of 0.04 M $KMnO_4$ (Fisher Scientific, 99%) was added into 100 mL of 0.03 M $Mn(CH_3COO)_2$ (Fisher Scientific, 98%) to from a brown precipitate. The mixture was adjusted to a pH of 12 with dilute sodium hydroxide before being centrifuged at 2500 rpm 3-5 times for 20 mins each time to collect the precipitate. The deposit was then rinsed with deionised H_2O to remove the purple colour of the permanganate ions. Finally, the deposit was dried overnight in air at 333 K and then ground into a powder.

Functional carbon catalysts such as graphene nanoplatelets of 300 m^2 g^{-1} surface area (Sigma Aldrich), N-doped graphene (Sigma Aldrich), carbon black powder (Vulcan XC-72R, Cabot Corp., 100%), commercial MnO_2 (Sigma Aldrich) and 5 wt% Pt/C (Acros Organics) were used as received.

4.1.2. Preparation of RDE samples

Rotating disc electrode (RDE) (Pine Research Instrumentation) measurements were used to characterise the catalytic activity of the various samples in 1 M NaOH. The catalyst ink consisted of 1 mg of catalyst + 1 mL deionised H_2O + 0.5 mL isopropanol + 5 µL of 5 wt% Nafion 117 (Sigma-Aldrich), used as received. If Vulcan XC-72R was added, the catalyst ink was composed of 0.50 mg catalyst + 0.50 mg Vulcan XC-72R + 1 mL deionised H_2O + 0.5 mL isopropanol + 5 µL of 5 wt% Nafion 117. This was to keep the loading of material on the surface of the glassy carbon (GC) tip consistent. To ensure a well-dispersed mixture, the ink was ultrasonicated for at least 20 mins and then homogenised at 28 000 rpm for 4 mins with a Cole-Parmer LabGen 7 series homogeniser. The catalyst ink was loaded with a micropipette onto the surface of a glassy carbon electrode (Pine Instrument Company) of 4 mm diameter (working area ≈ 0.126 cm^2) in three aliquots of 8 µL with drying in between each layer to give a loading of ~120 µg cm^{-2}. The catalyst layers were fully dried in air before the

electrode was attached to the rotating disc electrode shaft. The glassy carbon electrode surface was consecutively wet polished with MicroCloth (Buehler) and alumina powders, 1.0 mm and 0.5 mm (MicroPolish, Buehler) and ultrasonicated in deionised H_2O before use.

4.1.3. Preparation of GDE samples

Catalyst ink for GDE samples were prepared by adding catalyst powder to Vulcan XC-72R (Cabot Corp) in a 1:1 weight ratio. A mixture of polytetrafluoroethylene (PTFE) solution (60 wt% in H_2O) and solvent of 1:1 wt% IPA/ H_2O was then introduced to the powders, in which, the PTFE solution was combined with deionised H_2O first before isopropanol was added. This helped to prevent the particles from aggregating and forming a suspension. A catalyst to PTFE weight ratio of 10:2 was chosen as this was optimised previously [1]. To ensure homogeneity, the catalyst ink was ultrasonicated for 20 mins and homogenised at 28 000 rpm for 3-4 mins. Thin layers of the catalyst ink were then applied to carbon paper (AvCarb GDS 1120) of diameter 13 mm using a stainless steel spatula with drying and weighing in between. This was carried out until a loading of 2 mg cm^{-2} of catalyst was achieved.

4.1.4. Physical characterisation

The surface morphology and composition of the catalysts were characterized using a SEM-EDS (FEI Quanta 650 FEG) operated at accelerating voltage of 5 kV. Powder X-ray diffraction results were collected on a Bruker D8 Advance X-ray diffractometer with Cu tube source (λ= 1.5418 Å) and analysed using Bruker Diffraction Suite EVA software. Surface area measurements were carried out with a gas adsorption measurement instrument Belsorp max (MicrotracBEL Corp.) and results analysed with BELMaster. The samples were under vacuum at 200 ºC for 2 h before measurement and N_2 adsorption was done at 77 K. Specific surface areas of the samples were determined using the Brunauer-Emmett-Teller (BET) method and further analysis on the pore volume and pore size distribution within the samples were carried out with the Barrett-Joyner-Halenda (BJH) method and non-local density functional theory (NLDFT) method.

4.1.5. Electrochemical characterisation

All electrochemical measurements were carried out using Biologic potentiostatic instrumentation with the EC-Lab software package. Both RDE and GDE samples were tested in conventional three electrode cells consisting of a 200 cm^3 jacketed glass cell with a Luggin capillary for the reference electrode. Pt mesh and Hg/ HgO in 1 M NaOH were used as counter and reference electrodes respectively.

The RDE glass cell shown in **Figure 4.1** was designed with three inlets, one for each of the electrodes. A Luggin capillary helped to minimise the distance between the reference and working electrodes as the working electrode was orientated downwards in the cell. For the RDE electrochemical measurements, fresh electrolyte was used for each experiment and the temperature of the electrolyte was kept constant at 298 K by connecting the inbuilt water jacket to a recirculating water bath (TC120, Grant). A glass frit (Sigma Aldrich) of porosity 25-50 µm was used to saturate the electrolyte with oxygen (BOC) for a minimum of 30 mins before each experiment. To obtain ORR polarisation curves, the potential was swept from 0.1 to -0.5 V (*vs.* Hg/ HgO) at a scan rate of 5 mV s^{-1} at controlled rotation speeds – 100 rpm, 400 rpm, 900 rpm, 1600 rpm and 2500 rpm. Cyclic voltammograms were obtained by linearly scanning the potential at a rate of 50 mV s^{-1} between 0 V and -1.0 V then back to 0 V *vs.* Hg/ HgO.

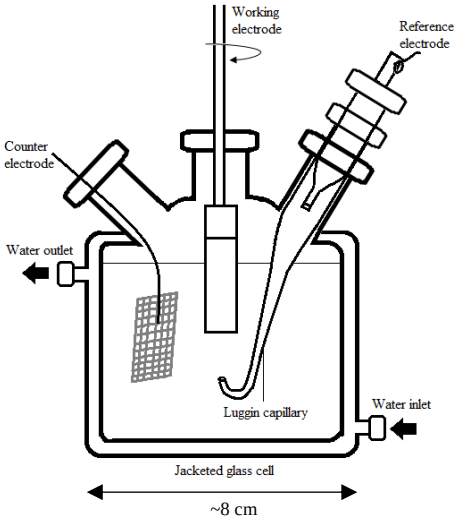

Figure 4.1 Labelled cross-section of jacketed RDE glass cell with Luggin capillary.

The GDE glass cell (200 cm^3) seen in **Figure 4.2** included a cylindrical PTFE insert for the oxygen or working electrode, held in place with a screw cap and an O-ring to prevent any leakages. The inbuilt jacket ensured the temperature of the cell

environment could be maintained when connected to a recirculating water bath (TC120, Grant). Special glass fittings allowed the reference electrode to be connected to a Luggin capillary positioned at a fixed distance of 10 mm from working electrode and a polymer lid (not pictured here) fitted onto the GDE cell held the working electrode at a distance of 13–15 mm from the counter electrode.

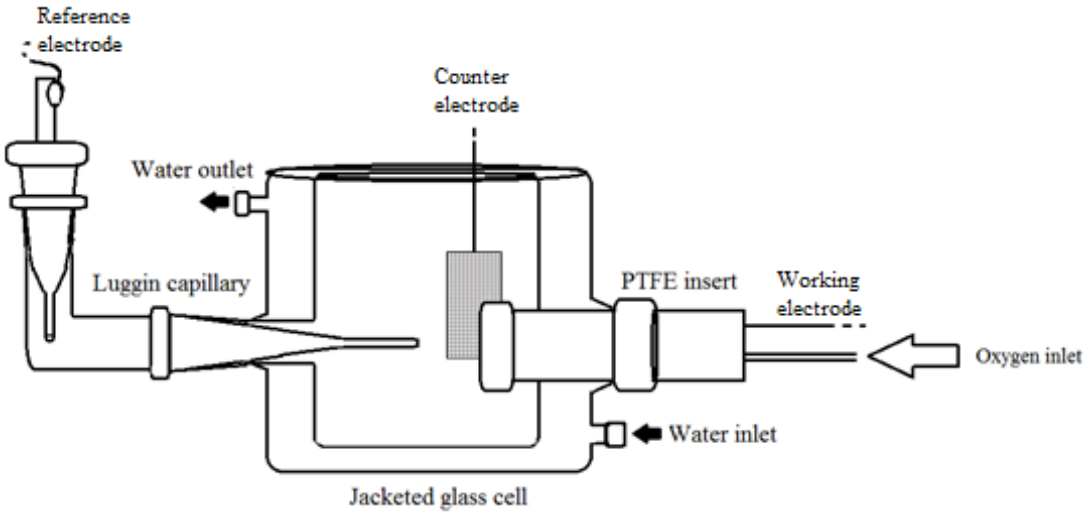

Figure 4.2 Labelled cross-section of jacketed GDE glass cell with Luggin capillary fitting and PTFE insert.

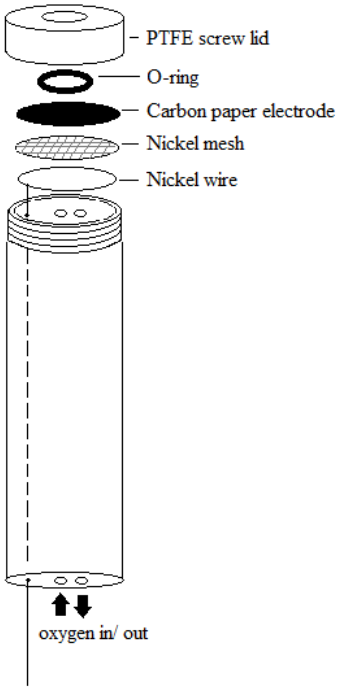

Figure 4.3 Illustration of the assembly of the PTFE insert with labelled components.

The cylindrical insert (**Figure 4.3**) was constructed of PTFE as it is non-reactive and maintains good corrosion resistance to hydroxides. The electrodes were of

circular discs of catalyst coated carbon paper, 1.3 cm in diameter with working area of 0.8 cm^2 based on the inner diameter of the O-ring. The electrodes were positioned with the catalyst coated side exposed to the electrolyte and uncoated side exposed to the oxygen inlet. A constant supply of oxygen was fed in from the rear of the working electrode holder and controlled at a flowrate of 200 cm^3 min^{-1} with a flowmeter. Nickel wire and mesh provided electrical contact from the gas side. For the GDE electrochemical measurements, the temperature of the electrolyte 1 M NaOH was controlled to 333 K with a recirculating water bath. Chronopotentiometric measurements were carried out at 10, 20, 50 and 100 mA cm^{-2} to evaluate the stability and performance of the electrodes.

4.2. Results and discussion

4.2.1. Sample characterisation

The SEM micrographs of the various catalysts are given in **Figure 4.4**. The morphology of commercial MnO_2 in **Figure 4.4 a** is composed of agglomerated particles with rough angular surfaces. In contrast, the surface of the amorphous MnO_x in **Figure 4.4 b** is uneven and 'fluffy' in texture. Cobalt based oxides Co_3O_4, $NiCo_2O_4$ and $MnCo_2O_4$ in **Figure 4.4 c, d and e** respectively are composed of clusters of particles. The sizes of the particles within the clusters appear more irregular in $NiCo_2O_4$ and $MnCo_2O_4$ probably due to the presence of two different transition metals. Based on these micrographs, as a greater availability of electrochemically active surface sites per volume ratio yields higher ORR activity for metal oxides, it is likely that amorphous MnO_x, $NiCo_2O_4$ and $MnCo_2O_4$ in (**Figure 4.4 b, d** and **e** respectively) may exhibit better performance.

The SEM micrograph of Vulcan XC-72R carbon black in **Figure 4.4 f** reveals an uneven surface composed of tightly packed nanoparticles. The appearance of graphene in **Figure 4.4 g** is that of highly disordered platelets with some agglomeration which could have an effect on its performance as surface area and the availability of edge or defect sites is especially important for carbonaceous materials (Chapter 2, Section 2.1.1.3). In comparison, nitrogen-doped graphene (**Figure 4.4 h**) appears to be composed of a structure of thin layered sheets, likely graphene.

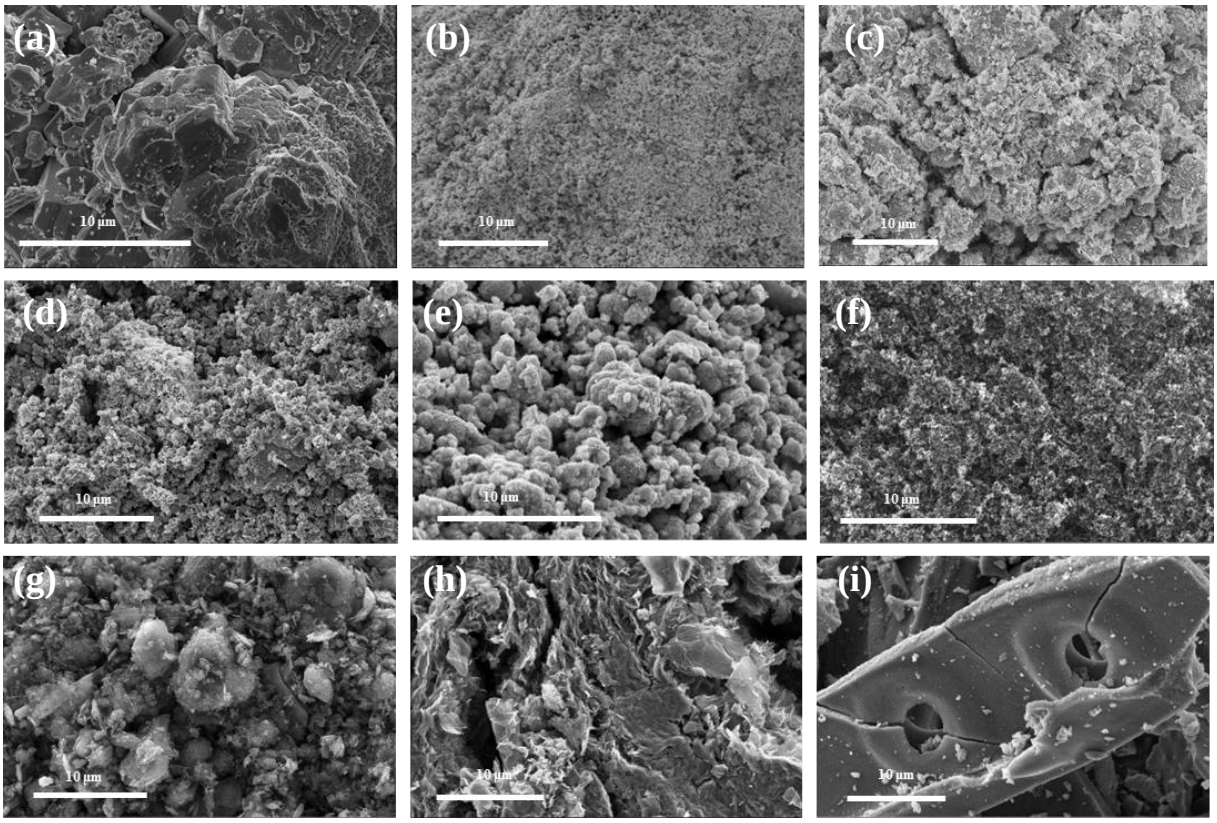

Figure 4.4 SEM micrographs of **a)** commercial MnO_2, **b)** amorphous MnO_x, **c)** Co_3O_4, **d)** $NiCo_2O_4$, **e)** $MnCo_2O_4$, **f)** Vulcan XC-72R, **g)** graphene, **h)** N-doped graphene, and **i)** 5 wt% Pt/C.

In **Figure 4.4 i**, SEM micrographs of 5 wt% Pt/C reveal rod-like fragments of carbon with circular voids filled with small amounts of platinum. EDX analysis on the percentage content of Pt to C demonstrated that ≈5% Pt is present which corresponds well with the supplier's reported specifications. Although the surface area of the 5 wt% Pt/C does not appear to be as high as the metal oxide or carbon-based catalysts, as shown in Section 2.1.1.1 in Chapter 2, the activity of the precious metal catalyst is expected to be more reliant on its structure rather than surface area.

The crystal structures of the various catalysts were confirmed by X-ray powder diffraction. The diffraction patterns are given in **Figure 4.5** and structural parameters are reported in **Table 4.1**. The transition metal oxides Co_3O_4, $NiCo_2O_4$ and $MnCo_2O_4$ in **Figure 4.5 a, b, c** have spinel structures with cubic crystal systems which match JCPDS 001-1152, JCPDS 020-0781 and JCPDS 23-1237 patterns, respectively. The synthesised MnO_x powder diffraction in **Figure 4.5 d** exhibits weak broad peaks which is characteristic of a non-crystalline nature. The peaks at 13.3 °, 37 °, and 66 ° match the (110), (211) and (541) peaks of tetragonal body-centred α-MnO_2 hydrate, JCPDS

44-0140. In contrast, the diffraction pattern of the commercially obtained MnO_2 in **Figure 4.5 e** matches that of JCPDS 24-0735 for tetragonal β-MnO_2.

Table 4.1 Summary of XRD structures of the patterns given in Figure 4.5.

Catalyst	**Crystal system**	**Space group**	**Lattice constant / Å**	**Cell volume / Å³**
Co_3O_4	Cubic	Fd3m	a=b=c=8.09	529.5
Amorphous MnO_x	Amorphous	n/a	n/a	n/a
Commercial MnO_2	Tetragonal	P42/mnm	a=b=4.4 c=2.87	55.6
$NiCo_2O_4$	Cubic	Fd3m	a=b=c=8.11	533.4
$MnCo_2O_4$	Cubic	Fd3m	a=b=c=8.28	567.7
XC-72R	Hexagonal	P 63/m m c	a=b=2.41 c=7.26	42.2
Graphene	Hexagonal	P 63/m m c	a=b=2.38 c=6.72	38.1
N-doped graphene	Hexagonal	P 63/m m c	a=b=2.41 c=6.68	38.8
5 wt% Pt/C	Cubic Pt	Fm3m	a=b=c=3.92	60.2

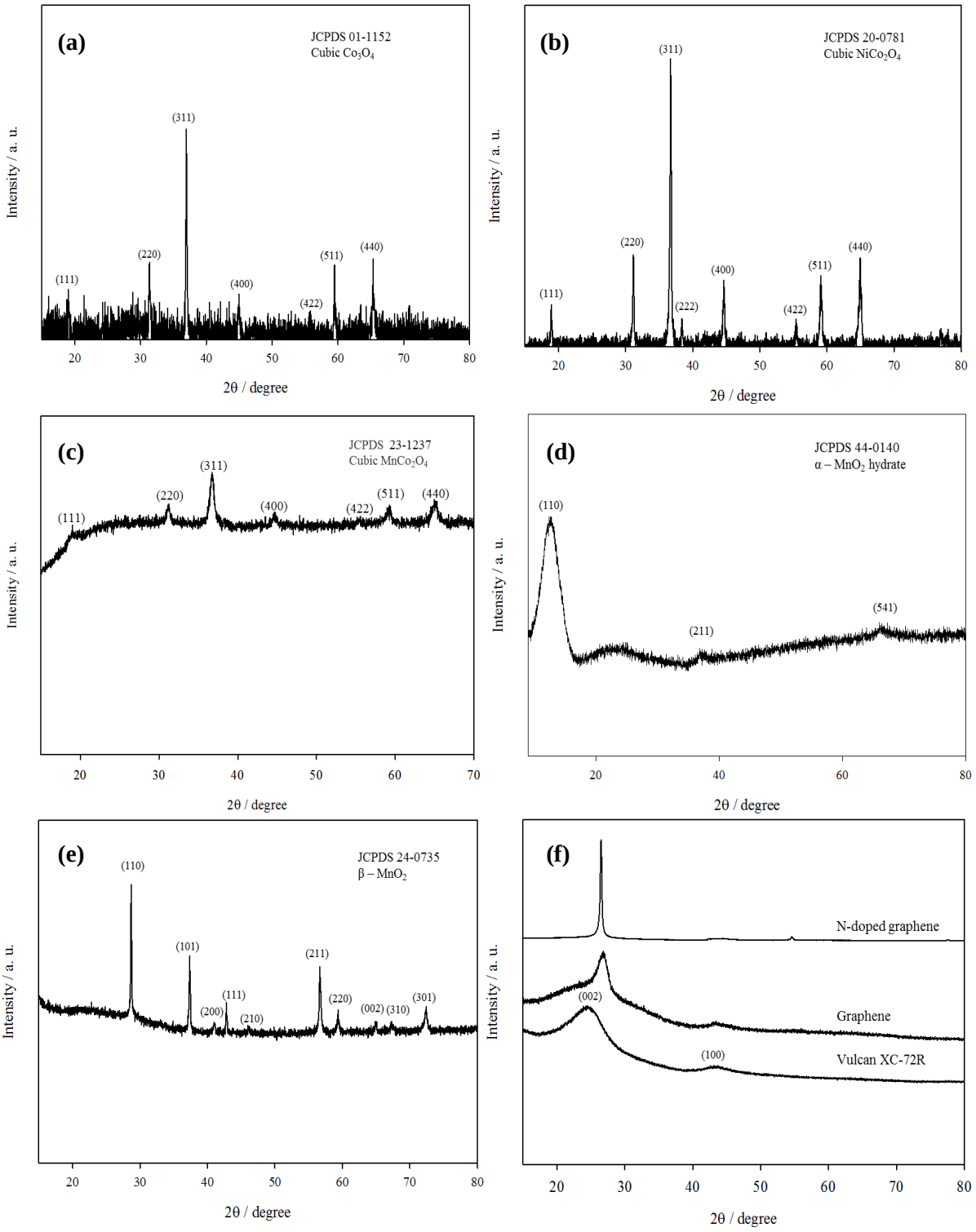
(a)
JCPDS 01-1152
Cubic Co_3O_4
(111)
(220)
(311)
(400)
(422)
(511)
(440)
(b)
JCPDS 20-0781
Cubic $NiCo_2O_4$
(111)
(220)
(311)
(222)
(400)
(422)
(511)
(440)
(c)
JCPDS 23-1237
Cubic $MnCo_2O_4$
(111)
(220)
(311)
(400)
(422)
(511)
(440)
(d)
JCPDS 44-0140
α – MnO_2 hydrate
(110)
(211)
(541)
(e)
JCPDS 24-0735
β – MnO_2
(110)
(101)
(200)
(111)
(210)
(211)
(220)
(002)
(310)
(301)
(f)
N-doped graphene
Graphene
Vulcan XC-72R
(002)
(100)
Intensity / a. u.
2θ / degree

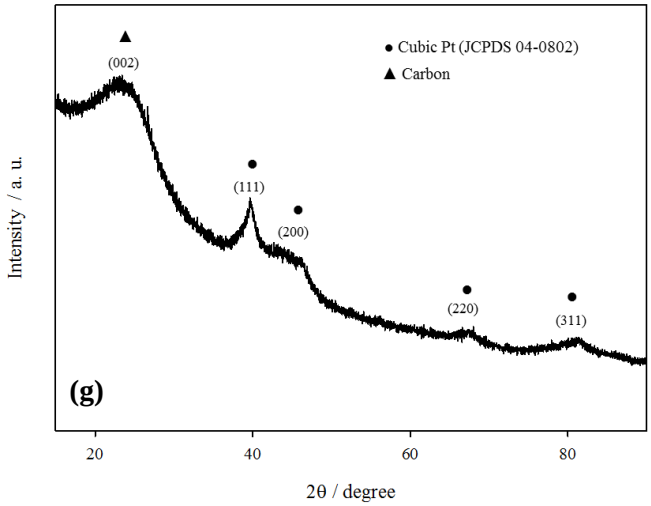

Figure 4.5 X-ray diffraction patterns of **a)** Co_3O_4, **b)** $NiCo_2O_4$, **c)** $MnCo_2O_4$, **d)** amorphous MnO_x, **e)** commercial MnO_2, **f)** Vulcan XC-72R, graphene and N-doped graphene; and **g)** 5 wt% Pt/C.

Figure 4.5 f shows a comparison of the diffraction patterns including Vulcan XC-72R, commercial graphene nanoplatelets and N-doped graphene, the (002) and (100) peaks of carbon are observed in all three materials at slightly varying 2θ values. Vulcan XC-72R is identified to be hexagonal graphite from JCPDS 41-1487 with (002) and (100) peaks present at 24.5 º and 43.2 º respectively. Similarly, the (002) and (100) peaks of N-doped graphene are present at 26.7 º and at 43.3 º, respectively. The diffraction pattern of commercial graphene nanoplatelets displays a sharp, intense (002) peak at 26.5 º and a small broad (100) peak at 44 º which indicates that the sample is highly crystalline. In contrast, the background intensity observed in diffraction patterns of Vulcan XC-72R and N-doped graphene is attributed to the highly disordered nature of these materials. The diffraction pattern of commercial Pt on carbon in **Figure 4.5 g** clearly indicates that cubic Pt is present and the peak at 23 ° is attributed to the (002) peak of the carbon support.

4.2.2. RDE results

Cyclic voltammograms of the catalysts inks in O_2 saturated 1 M NaOH electrolyte on glassy carbon RDE tip without electrode rotation are shown in **Figure 4.6 a & b**. Thin uniform catalyst ink coatings were applied to the surface of the GC tip to reduce the influence of mass transfer effects on the data and ensure reliable results.

Voltammograms of the uncoated glassy carbon tip and Vulcan XC-72R ink were also collected under the same conditions and plotted for comparison.

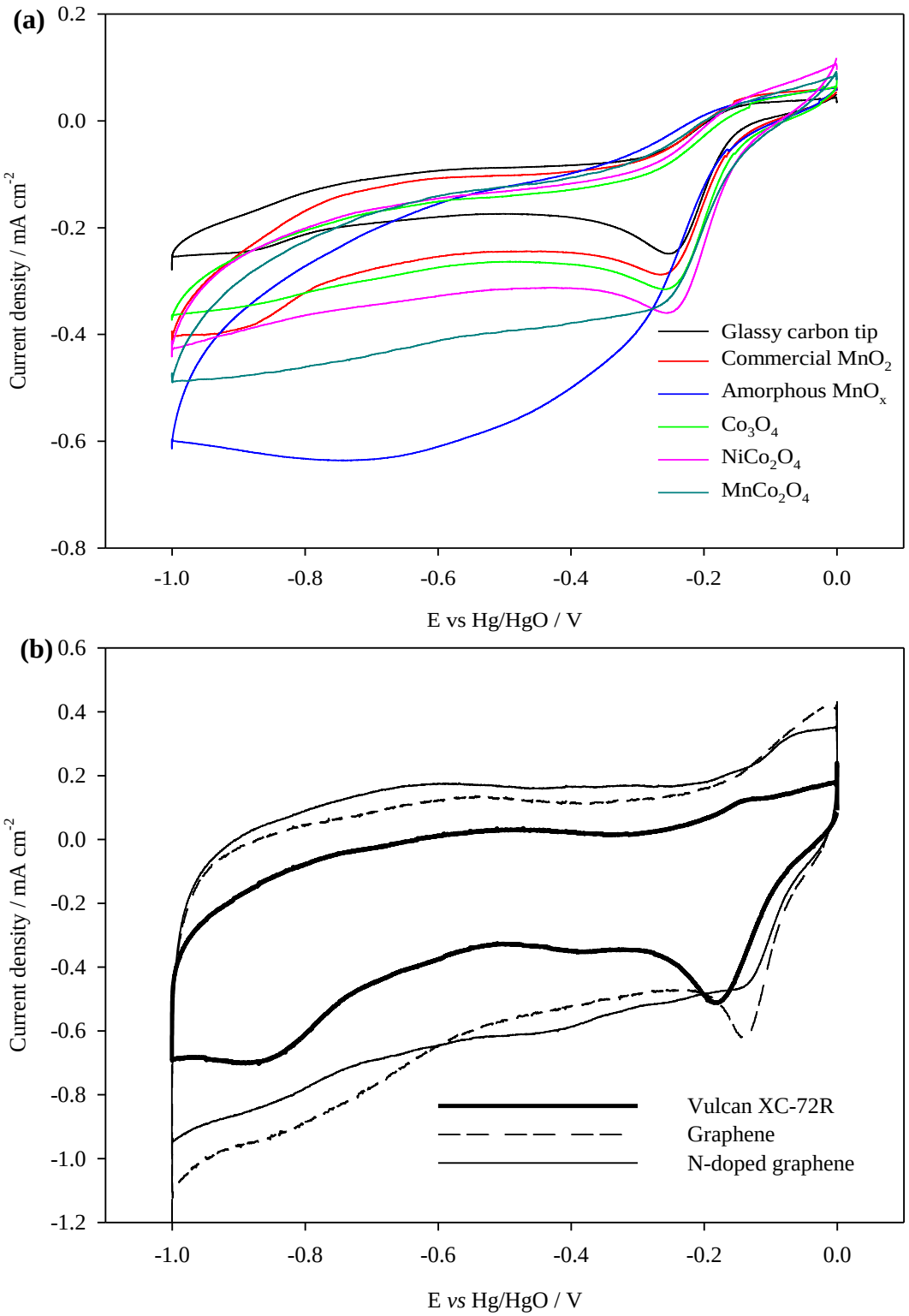

Figure 4.6 Cyclic voltammograms of thin films of **a)** metal oxides and **b)** functional carbon catalysts measured on glassy carbon RDE tip between cathodic potentials 0 V and -1.0 V at a scan rate of 50 mV s^{-1} in O_2 saturated 1 M NaOH solution at 298 K.

In **Figure 4.6 a**, all the voltammograms of metal oxide catalyst coated GC display earlier onset potentials and greater current densities for oxygen reduction in contrast to uncoated GC indicating that these materials are active for ORR. The cathodic peaks seen at ~-0.25 V for these catalysts is representative of the formation of OH^- from oxygen reduction reaction. Voltammograms of $MnCo_2O_4$ and amorphous MnO_x have much greater peak currents compared to the other metal oxide catalysts tested. The onset of oxygen reduction occurs at a slightly more positive potential at $MnCo_2O_4$ than at amorphous MnO_x and this was shown to be due to the presence of Co in the mixed metal oxide leading to enhanced conductivity [2].

From **Figure 4.6 b** the cathodic peak of benchmark Vulcan XC-72R carbon is found at -0.2 V whilst the voltammograms of both graphene-based catalysts have cathodic peaks at -0.14 V displaying improvements in onset potentials and current densities. These peaks signify the reduction of O_2 to HO_2^- via the indirect peroxide pathway as described in equation (4.1) commonly seen on graphite and carbon [3].

$$O_2 + H_2O + 2e^- \rightarrow HO_2^- + OH^- \qquad -0.165 \text{ V vs Hg/ HgO} \qquad (4.1)$$

The shape of the voltammograms for the graphene catalysts is typical of carbon materials, generally featureless, indicative of the double layer capacitance effect [4]. The onset potential for ORR at these carbon-based materials is slightly less negative than that seen for the catalysts in **Figure 4.6 a** which is representative of better catalytic activity. This is due to the higher electrical conductivity of these materials (up to 10^8 S m^{-1}) [5, 6] which helps to facilitate the rate of electron transfer for electrocatalysis. The peak currents at ~ -0.2 V in the voltammograms relate to the electrochemically active sites available. Compared to graphene, N-doped graphene has a slightly more negative onset potential for oxygen reduction, but the voltammogram of graphene has a greater peak current at more reductive potentials suggesting a trade-off between conductivity and electrochemically active sites available.

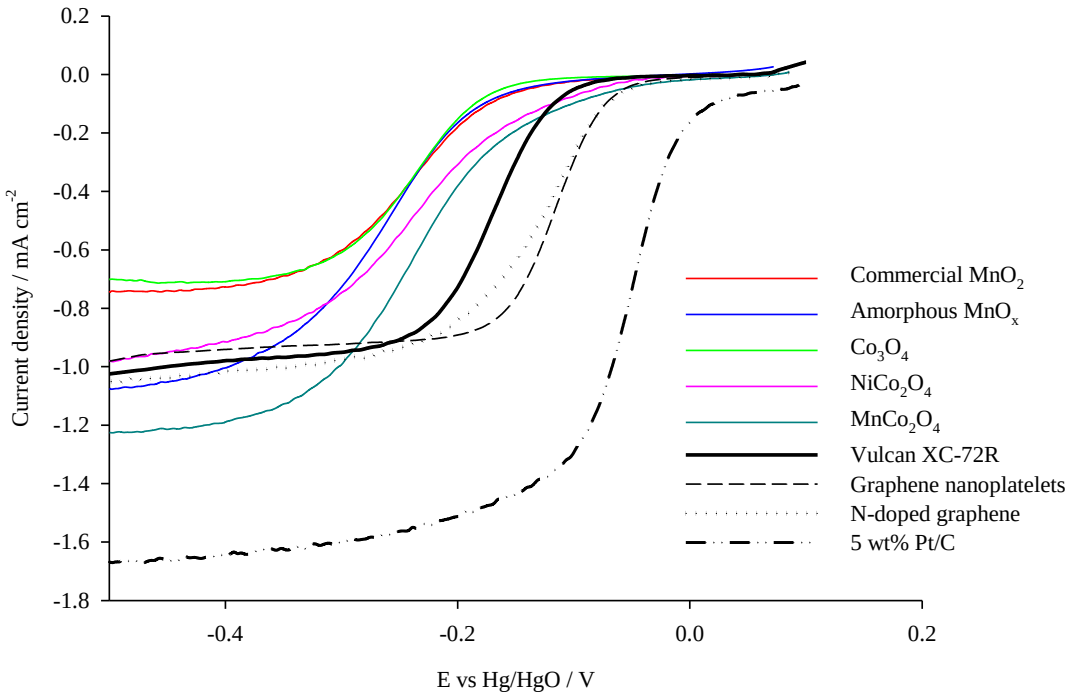

Figure 4.7 Linear sweep voltammograms of thin films of catalysts measured on glassy carbon RDE tip at 400 rpm rotation rate, scan rate of 5 mV s^{-1} in O_2 saturated 1 M NaOH at 298 K.

The linear sweep voltammograms of the synthesised catalysts were recorded at a rotating speed of 400 rpm using a scan rate of 5 mV s^{-1} in oxygen saturated 1 M NaOH at 298 K and presented in **Figure 4.7** against Vulcan XC-72R and 5 wt% Pt/C for reference. Generally, the linear sweep voltammogram plots are observed to be sigmoidal in shape extending into plateaus at higher potentials. Within the defined ORR potential range, three distinct sections are identified: (1) electron or charge transfer controlled, (2) mixture of electron transfer and mass transport controlled and (3) mass transport controlled. The limiting current densities and $E_{1/4}$, $E_{1/2}$ and $E_{3/4}$ potentials (potentials at which j/j_L = ¼, ½ and ¾ respectively) were extracted from these plots for all samples as reasonable estimates of the reaction potentials for these three regions (**Table 4.2**). On top of this, the potential at current density of -0.1 mA cm^{-2} was used as an indicator of the onset potential for ORR.

It is apparent from **Figure 4.7** that the catalysts can be divided according to their onset potentials into three groups: 1) Metal oxides, 2) Carbon materials and, 3) Precious metals. Within the first group of metal oxides, single metal oxides of Mn and Co display the most negative onset potentials for ORR at ~-0.17 V and -0.19 V respectively as well as $E_{1/2}$ values between -0.24 V and -0.26 V. The reduction

reactions of these metal oxides described in equations (4.2) and (4.3) occur around the onset potentials of these plots in **Figure 4.7** and also coincides with the standard potential of the first $2e^-$ step of the indirect pathway of ORR given in equation (4.1).

$Co_3O_4 + 4H_2O + 2e^- \rightarrow 3Co(OH)_2 + 2OH^-$ -0.19 V vs Hg/ HgO (4.2)

$MnO_2 + H_2O + e^- \rightarrow MnOOH + 2OH-$ -0.15 V vs Hg/ HgO (4.3)

It can be seen clearly from Fig 4.7 that the value of limiting current density of commercial MnO_2 and Co_3O_4 are approximately half of that of Pt/C, this corresponds to the two electron indirect pathway [7] because limiting current density is dependent on the number of electrons transferred in the ORR pathway. The amorphous MnO_x on the other hand, has a slightly higher current density which is suggestive of a mixture of $2e^-$ and $4e^-$ pathway. In the same category, mixed metal oxides of $MnCo_2O_4$ and $NiCo_2O_4$ display slightly more positive ORR onset potentials of -0.10 and -0.12 V respectively but retain similar $E_{1/2}$ values of ~-0.23 V. These positive shifts in onset potential are likely to be due to the substitution of Co for Mn or Ni. As indicated in Section 2.1.1.2 in Chapter 2, $MnCo_2O_4$ cationic sites of higher oxidation states namely, Co^{3+} and Mn^{3+}, are active sites for ORR [8, 9]. The presence of these cations and the interaction between them leads to increased conductivity which also contributes to the improvement in activity [10]. The four electron direct pathway of ORR has been reported to be favoured on $NiCo_2O_4$ and this was also observed for $MnCo_2O_4$ [11-14]. This explains why the limiting current densities for these mixed metal oxides, especially $MnCo_2O_4$, are greater.

Graphene and N-doped graphene in the second group display much more positive ORR onset potentials at ~-0.07 V and $E_{1/2}$ values of ~-0.11 V which is almost half that of the values seen for metal oxides. In contrast, the ORR onset potential for Vulcan XC-72R carbon black is ~-0.12 V with an $E_{1/2}$ value of -0.17 V. This variation in performance is due to the difference in conductivities and the mixture of $2e^-$ and $4e^-$ pathways which occur in parallel at these graphene materials [15, 16]. From the voltammograms in **Figure 4.7**, the ORR appears to occur predominately via the two electron pathway as the limiting current density is observed to be approximately half that of Pt/C [17].

In the last group, noble metal catalyst Pt/C has the most positive onset potential at 0.02 V, an $E_{1/2}$ value of -0.055 V and greatest limiting current density at -0.4 V as

expected since oxygen reduction proceeds via the four electron pathway [17]. As expected, Pt/C also has the smallest $E_{1/2}$ value due to its high electrical conductivity and reversible kinetics for the ORR reaction. The shift in half wave potential towards more negative potentials for the functional carbon materials, mixed metal and metal oxide catalysts indicates a decrease in catalytic performance in comparison to the benchmark catalysts Pt/C and XC-72R.

Table 4.2 Summary of kinetic parameters from Figure 4.7 of the various catalysts at 400 rpm rotation rate.

Catalyst	**$I_{Lat\ 0.4\ v}$/ mA cm^{-2}**	**$E_{-0.1\ mA\ cm^{-2}}$ vs Hg/ HgO / V**	**$E_{¼}$ vs Hg/ HgO / V**	**$E_{½}$ vs Hg/ HgO / V**	**$E_{¾}$ vs Hg/ HgO / V**	**$E_{¾} - E_{¼}$ vs Hg/ HgO / V**
Commercial MnO_2	-0.73	-0.174	-0.196	-0.236	-0.272	0.076
Amorphous MnO_x	-1.01	-0.177	-0.221	-0.261	-0.307	0.086
Co_3O_4	-0.71	-0.186	-0.202	-0.236	-0.270	0.068
$NiCo_2O_4$	-0.92	-0.119	-0.174	-0.229	-0.273	0.099
$MnCo_2O_4$	-1.19	-0.102	-0.181	-0.228	-0.280	0.099
XC-72R	-0.98	-0.117	-0.144	-0.173	-0.205	0.061
Graphene	-0.95	-0.073	-0.094	-0.116	-0.142	0.048
N-doped graphene	-1.01	-0.074	-0.097	-0.129	-0.177	0.080
5 wt% Pt/C	-1.65	+0.020	-0.029	-0.055	-0.089	0.060

The ($E_{3/4}$ - $E_{1/4}$) values in **Table 4.2** describe the region of mixed control of the LSV voltammograms in **Figure 4.7**. A low value of ≈60 mV is observed for Pt/C and XC-72R which suggests that the rate of electron transfer is fast for these benchmark catalysts. Graphene has an $E_{3/4}$ - $E_{1/4}$ value of 48 mV which is characteristic of a reversible system however N-doped graphene has an $E_{3/4}$ - $E_{1/4}$ value nearly twice that of 80 mV. Numerically greater $E_{3/4}$ - $E_{1/4}$ values of 99 mV are also recorded for the mixed metal oxides compared to the metal oxides which have $E_{3/4}$ - $E_{1/4}$ values in the range of 70 to 86 mV, indicating that electron transfer for ORR is slower at these catalysts or that a greater number of chemical steps are involved.

Linear sweep voltammograms for rotating speeds of 100, 400, 900, 1600 and 2500 rpm were collected for the various catalyst samples to determine reaction kinetic parameters using the Koutecky-Levich (K-L) equation (4.4), which is an extension of

the Levich equation (4.6). The K-L equation is valid in the mass transfer limiting region of the voltammograms, where the total measured current density, j, is the sum of the current density from electron transfer and mass transfer.

$$\frac{1}{j} = \frac{1}{j_k} + \frac{1}{j_L} \qquad (4.4)$$

j, j_k and j_L are the total measured, kinetic and limiting current density respectively.

The electron transfer or kinetic current density, j_k is expressed as

$$j_k = nFAkC \qquad (4.5)$$

Where k is the rate constant for electron transfer
n is the overall electron transfer number
F is Faraday's constant (96 485 C mol^{-1})
A is the area of the electrode
C is the concentration of oxygen in the bulk solution (8.4 x 10^{-7} mol cm^{-3} [18])

$$j_L = 0.201\, nFAD^{\frac{2}{3}}\upsilon^{-\frac{1}{6}}C\omega^{\frac{1}{2}} \qquad (4.6)$$

The limiting current density, j_L is seen to be proportional to the square root of rotation speed. As such, the K-L equation can be written as in (4.7) to describe a linear plot of j^{-1} vs $\omega^{-\frac{1}{2}}$, where the intercept is j_k and the slope of the plot is K.

$$\frac{1}{j} = \frac{1}{j_k} + \frac{1}{K\omega^{\frac{1}{2}}} \qquad (4.7)$$

$$\text{Hence, } K = \frac{\upsilon^{\frac{1}{6}}}{0.201\, nFD^{\frac{2}{3}}C} \qquad (4.8)$$

Where *υ* is the kinematic viscosity of electrolyte 1 M NaOH (1.1 x 10^{-2} cm^2 s^{-1} [19]) , D is the diffusion coefficient of O_2 in 1 M NaOH (1.89 x 10^{-5} cm^2 s^{-1} [18]) and ω is the rotation speed in rpm.

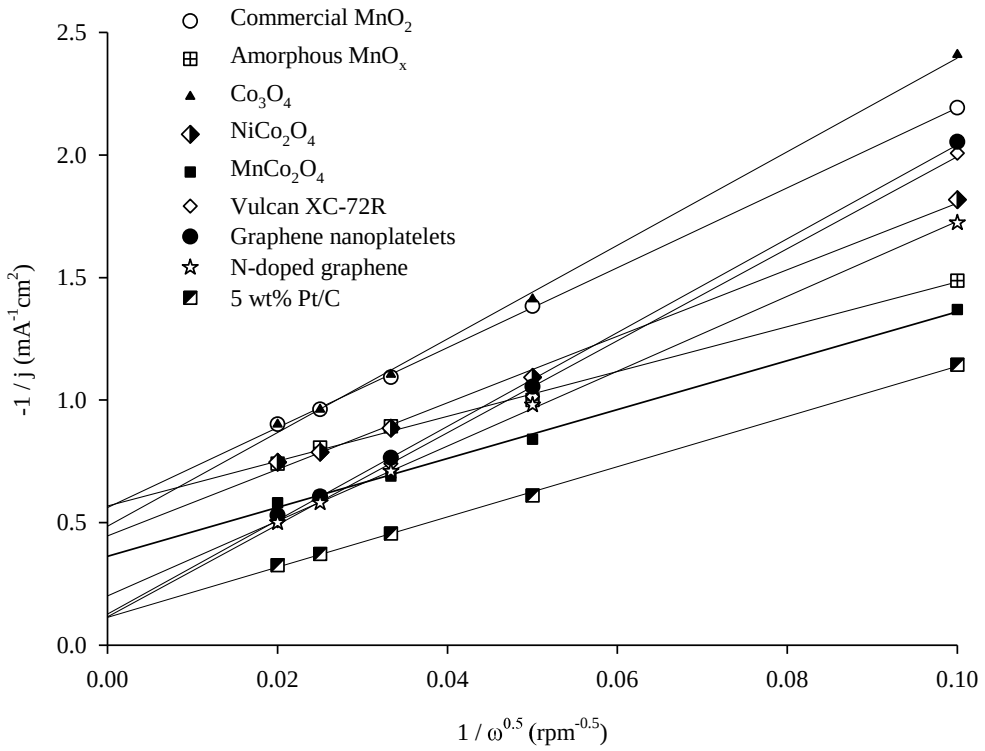

Figure 4.8 Koutecky-Levich plot j^{-1} versus $\omega^{-1/2}$ for catalysts taken from the mass transfer controlled region of -0.4 V for rotation rates 100, 400, 900, 1600 and 2500 rpm.

Koutecky-Levich plots of $-j^{-1}$ vs $\omega^{-1//2}$ for the various catalysts are given in **Figure 4.8** using values taken from a fixed potential at –0.4 V in the mass transfer limited region for rotation rates of 100, 400, 900, 1600 and 2500 rpm. Using the RDE, indicators of catalyst performance such as the kinetic current density without mass-transfer effects can be determined from the intercept and the electron transfer number, from the slope of the plot. Using equation (4.4) the slope of the plots, K is determined and the best fit line is extrapolated to obtain the y-intercept, kinetic current density j_k. The values of K and j_k for the catalyst samples are tabulated in **Table 4.3**.

Table 4.3 Intercept, slope values and apparent electron transfer numbers derived from the Koutecky-Levich plots given in Figure 4.8 for various catalyst samples.

Catalyst	Slope, K / mA^{-1} cm^2 $rpm^{-1/2}$	Intercept, j_k /mA^{-1} cm^2	Apparent electron transfer number, n_{app}
Commercial MnO_2	-16.3	-0.56	2.55
Amorphous MnO_x	-9.1	-0.57	4.56
Co_3O_4	-19.1	-0.48	2.18
$NiCo_2O_4$	-13.6	-0.45	3.05
$MnCo_2O_4$	-9.9	-0.36	4.20
XC-72R	-18.8	-0.12	2.21
N-doped graphene	-15.3	-0.20	2.71
Graphene	-19.2	-0.13	2.17
5 wt% Pt/C	-10.3	-0.11	4.04

The limiting current density is dependent on both kinetic and diffusion current densities, hence a lower absolute value of kinetic current density indicates a smaller limitation to the ORR kinetics. Under infinite mass transport conditions a zero intercept will be observed on the K-L plot that suggests electron transfer kinetics of the catalyst is very fast or reversible and current density is not dependent on voltage. From the intercept, j_k values in **Table 4.3**, Pt/C and XC-72R are observed to have the lowest absolute intercept values suggesting faster kinetics for these catalysts, due to their high electrical conductivity. The numerical value of the slope of the plot for XC-72R is almost double that for Pt/C which is expected as the value of slope, *K* is an indicator of the number of electrons involved in the oxygen reduction reaction. Theoretically the K-L plot for Pt/C should pass through the origin under mass transport limiting conditions [20] however this was not observed in **Figure 4.8**, suggesting that there were kinetic or diffusional limitations which affected the results. This could be due to a slight inconsistency in topology and morphology of the Pt/C catalyst film which has been shown by Garsany *et al.* [21] to affect the accuracy of ORR activity values. However, since all catalyst films were prepared in the same manner any effect on the results should be similar for all catalyst samples. The intercept of graphene, ≈ -0.13 mA^{-1} cm^2, is very close to that of XC-72R whereas the intercept of N-doped graphene, -0.20 mA^{-1} cm^2, indicates that the current density is more dependent on voltage for this catalyst. This can be explained that although the doping of graphene with nitrogen tends to reduce the overall conductivity which contributes to the slower electron

transfer kinetics, the presence of nitrogen helps to create more active sites for the ORR reaction [22, 23]. The effect of this can be seen in the smaller absolute slope value of the best fit line for N-doped graphene compared to graphene.

On the other hand, the intercepts with greatest absolute values come from the two forms of MnO_2 which have nearly identical intercept values of -0.57 mA^{-1} cm^2. These numerically large intercept values are attributed to the low electrical conductivity of MnO_2 [24] (10^{-5} to 10^{-6} S cm^{-1}) which hinders electron transport. Despite this, the slope of the best fit line for amorphous MnO_x is much lower than that of the commercial MnO_2 and is close to the value of the slope for 5 wt% Pt/C suggesting that the ORR pathway for this catalyst is similar to that of Pt/C. It has been reported that the number of electrons exchanged in the ORR pathway of α-MnO_2 is close to 4 whilst for β-MnO_2, the commercial MnO_2 in this case, the number of electrons tends to be less than 4 [25]. The ORR pathway therefore appears to be affected by the polymorphic form of the MnO_2 catalyst although the rate of the chemical step remains approximately the same.

The intercept for Co_3O_4, ≈ -0.48 mA^{-1} cm^2, is less negative compared to both forms of MnO_2 since it is more electrically conductive, however the absolute value of the slope of the plot is twice that for Pt/C reaffirming that oxygen reduction takes place via the two electron pathway on Co_3O_4. Substituting Co for transition metals Ni and Mn in $NiCo_2O_4$ reduces the absolute intercept value signifying the improvement in the electron transfer kinetics at mixed metal oxides. Furthermore, the presence of Mn in the Co_3O_4 is observed to alter the slope of the plot significantly to a value similar to the slope of amorphous MnO_x and Pt/C suggesting that oxygen reduction favours the four electron pathway at $MnCo_2O_4$.

Finally, comparing the absolute slope values for the various catalysts, amorphous MnO_x and $MnCo_2O_4$ have a slope value close to that of Pt/C signifying a preference for the $4e^-$ pathway; this is followed by $NiCo_2O_4$ > N-doped graphene > XC-72R > commercial MnO_2 > Co_3O_4 ≈ graphene.

4.2.3. Influence of carbon on electrochemical performance

The use of carbon as a support material for catalysts originates in fuel cells [26] due to its properties such as high specific surface area, high electrical conductivity, good pore structure, suitable surface chemistry and low cost [27]. A carbon support material is normally added to the catalyst ink to enhance conductivity and assist in forming a suitable three-phase boundary in the gas diffusion electrode for ORR. Vulcan-XC-72R was selected in this case as it is inexpensive, has a high surface area of 250 m^2 g^{-1} and low electrical resistivity of 0.08 to 1 Ω cm [28, 29]. The effect of the presence of Vulcan XC-72R on electrochemical activity was investigated using the RDE set-up. A catalyst to carbon ratio of 1:1 was used in ink preparation whilst maintaining the total catalyst loading at 1 mg (i.e. 0.5 mg catalyst + 0.5 mg carbon powder). This ratio was selected as it was previously optimised from a range of different catalyst to carbon ratios [1] and it was found that a catalyst to carbon ratio of 1:1 was optimal at both low and high current densities.

Figure 4.9 shows the electrochemical activities of catalyst samples with the addition of Vulcan XC-72R compared against benchmark catalyst Pt/C at rotation speed 400 rpm. The limiting current densities, onset potentials and $E_{1/4}$, $E_{1/2}$ and $E_{3/4}$ values of these plots are tabulated in **Table 4.4**.

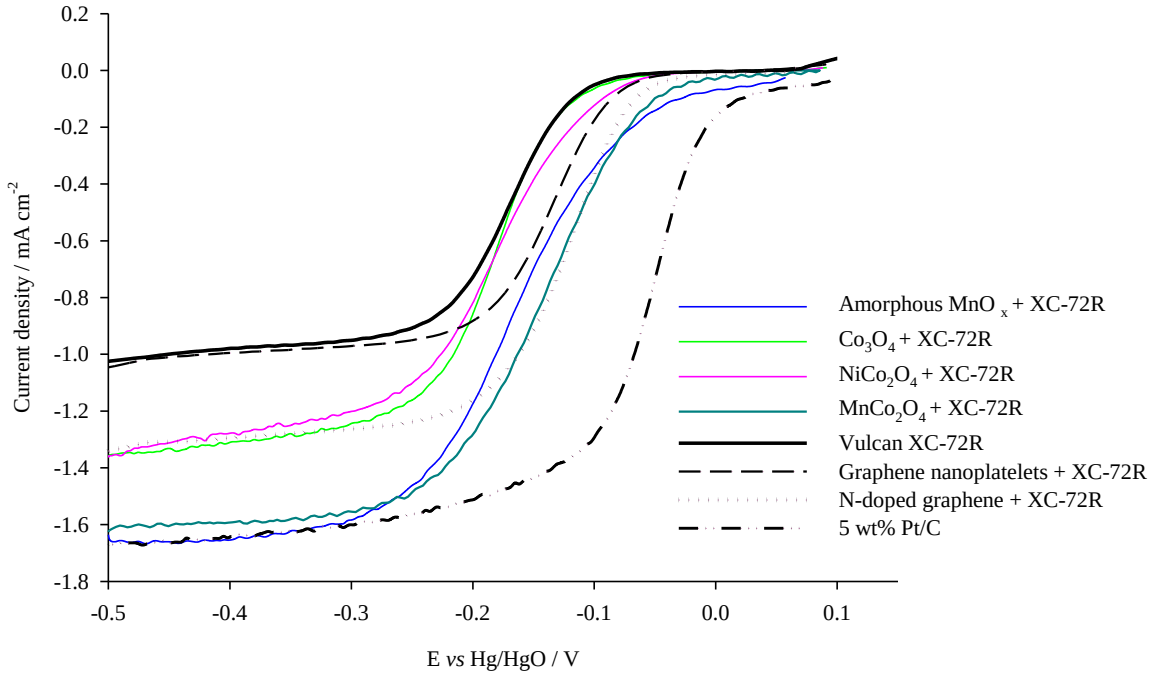

Figure 4.9 Linear sweep voltammograms of thin films of catalyst with Vulcan XC-72R measured on glassy carbon RDE tip at 400 rpm rotation rate, 5 mV s^{-1} scan rate in O_2 saturated 1 M NaOH at 298 K.

Table 4.4 Summary of kinetic parameters taken from Figure 4.9 of the various catalysts with addition of Vulcan XC-72R.

Catalyst	**$I_{L\ at\ 0.4\ V}$/ mA cm^{-2}**	**$E_{-0.1\ mA\ cm^{-2}}$ vs Hg/ HgO/ V**	**$E_{¼}$ vs Hg/ HgO/ V**	**$E_{½}$ vs Hg/ HgO/ V**	**$E_{¾}$ vs Hg/ HgO/ V**	**$E_{¾}$ - $E_{¼}$ vs Hg/ HgO/ V**
Amorphous MnO_x + XC-72R	-1.65	-0.029	-0.106	-0.163	-0.209	0.103
Co_3O_4 + XC-72R	-1.32	-0.114	-0.153	-0.183	-0.213	0.060
$NiCo_2O_4$ + XC-72R	-1.28	-0.093	-0.138	-0.180	-0.220	0.082
$MnCo_2O_4$ + XC-72R	-1.59	-0.049	-0.100	-0.141	-0.186	0.086
Graphene + XC-72R	-1.00	-0.086	-0.110	-0.137	-0.166	0.056
N-doped graphene + XC-72R	-1.29	-0.066	-0.097	-0.122	-0.156	0.059

One of the most visible effects of the addition of Vulcan XC-72R was the increase in limiting current density for all catalysts. This was noted to be an additional ~0.60 mA cm^{-2} for single metal oxides and ~0.40 mA cm^{-2} for mixed metal oxides. A 0.28 mA cm^{-2} increase was recorded for N-doped graphene, however only a 4 mA cm^{-2} increase was observed for graphene. Besides this, the inclusion of Vulcan XC-72R in the catalyst ink resulted in shifts to more positive onset potentials and half wave potentials, $E_{1/2}$ for all catalysts with the exception of graphene. These changes were a probable outcome of the increase in utilisation of electrochemical surface area [30] and improvement in contact between catalyst particles [31] on Vulcan XC-72R supported catalysts.

The greatest reduction in onset potential and $E_{1/2}$ value was observed at amorphous MnO_x with a decrease of 148 mV and 98 mV respectively, due to the enhancement of conductivity of MnO_x by the addition of Vulcan XC-72R. Conversely, N-doped graphene displayed the smallest reduction in onset potential and $E_{1/2}$ value of 8 mV and 7 mV respectively. This implies that the effect of the addition of Vulcan XC-72R is not as significant for N-doped graphene as it initially displayed high conductivity. Graphene is the only catalyst which displayed an increase in onset potential and $E_{1/2}$ values of 13 mV and 21 mV respectively with the addition of Vulcan XC-72R. This is likely to be due to the added Vulcan XC-72R filling the voids in between the graphene nanoplatelets which could contribute to slower ion transfer through the catalyst layer. This was supported by the decrease in specific surface area of the mixture based on BET analysis (**Table 4.5**) of the nitrogen sorption plots in

Figure 4.10 of graphene + XC-72R as opposed to just graphene. It is also likely that the graphene nanoplatelets, which have a tendency to self-agglomerate due to the strong Van der Waal forces between sp^2-hybridised carbon atoms, form larger clusters with the addition of Vulcan XC-72R thereby decreasing the electrochemically active surface area.

Table 4.5 Summary of surface area analysis from sorption plots given in Figure 4.10 and 4.11.

Sample	Brunauer Emmett Teller (BET)		Density Functional Theory (DFT)
	$a_{s,\,BET}$/ $m^2\ g^{-1}$	V_p / $cm^3\ g^{-1}$	V_p / $cm^3\ g^{-1}$
Graphene	349.3	-	-
Graphene + XC-72R (1:1)	313.3	-	-
Vulcan XC-72R	286.1	0.551	0.727
MnO_x + XC-72R (1:1)	185.0	0.408	0.487

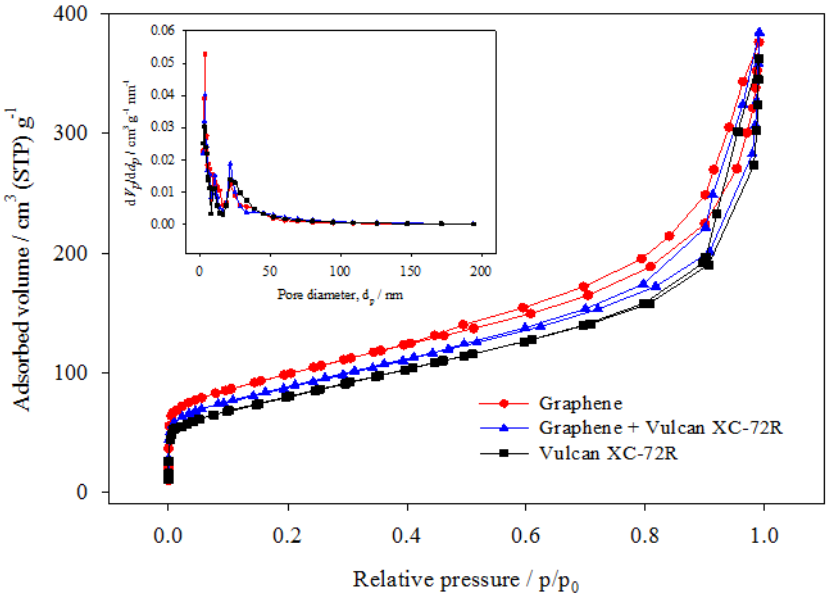

Figure 4.10 Nitrogen sorption isotherms of graphene (●), graphene and Vulcan XC-72R combined **(▲)** and Vulcan XC-72R (■). The inset is the corresponding graph of pore size distribution.

The values of $E_{3/4}$ - $E_{1/4}$ in **Table 4.4** decreased to different extents for metal oxides Co_3O_4, $NiCo_2O_4$ and $MnCo_2O_4$ with the addition of Vulcan XC-72R indicating that the region of mixed control is smaller, facilitated by the presence of carbon. In contrast however, the addition of Vulcan XC-72R to amorphous MnO_x appears to

increase the $E_{3/4}$ - $E_{1/4}$ value by 17 mV suggesting a greater dependency on mass transport of reactants to and products away from the catalyst.

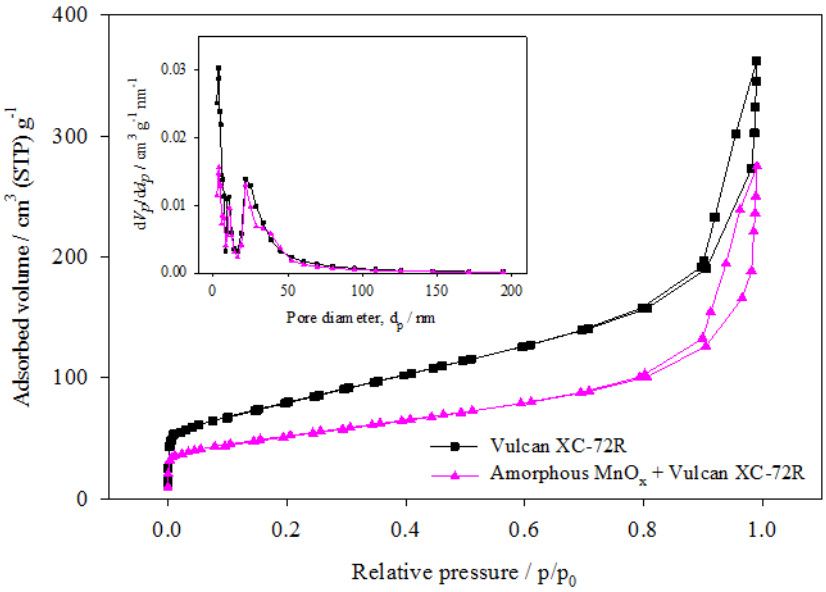

Figure 4.11 Nitrogen sorption isotherms of Vulcan XC-72R (■) and amorphous MnO_x and Vulcan XC-72R combined (▲). The inset is the corresponding graph of pore size distribution.

Based on the non-local density functional theory analysis of the pore size distribution (**Table 4.5**), the pore volume of the combined powder mixture of MnO_x and Vulcan XC-72R was significantly lower than that of Vulcan XC-72R. The BET analysis of nitrogen sorption plots (**Figure 4.11**) also show a decrease in specific surface area and pore volume with the addition of MnO_x to Vulcan XC-72R. These results support the electrochemical data and imply that MnO_x particles are located in the mesopores of the carbon support when mixed with Vulcan XC-72R which greatly reduces the porosity of the carbon support and therefore hinders the mass transport of oxygen and electrolyte through the catalyst film. Nevertheless, at high overpotentials in the mass transport controlled region, the limiting current density for amorphous MnO_x with addition of carbon is seen to be comparable to that of 5 wt% Pt/C.

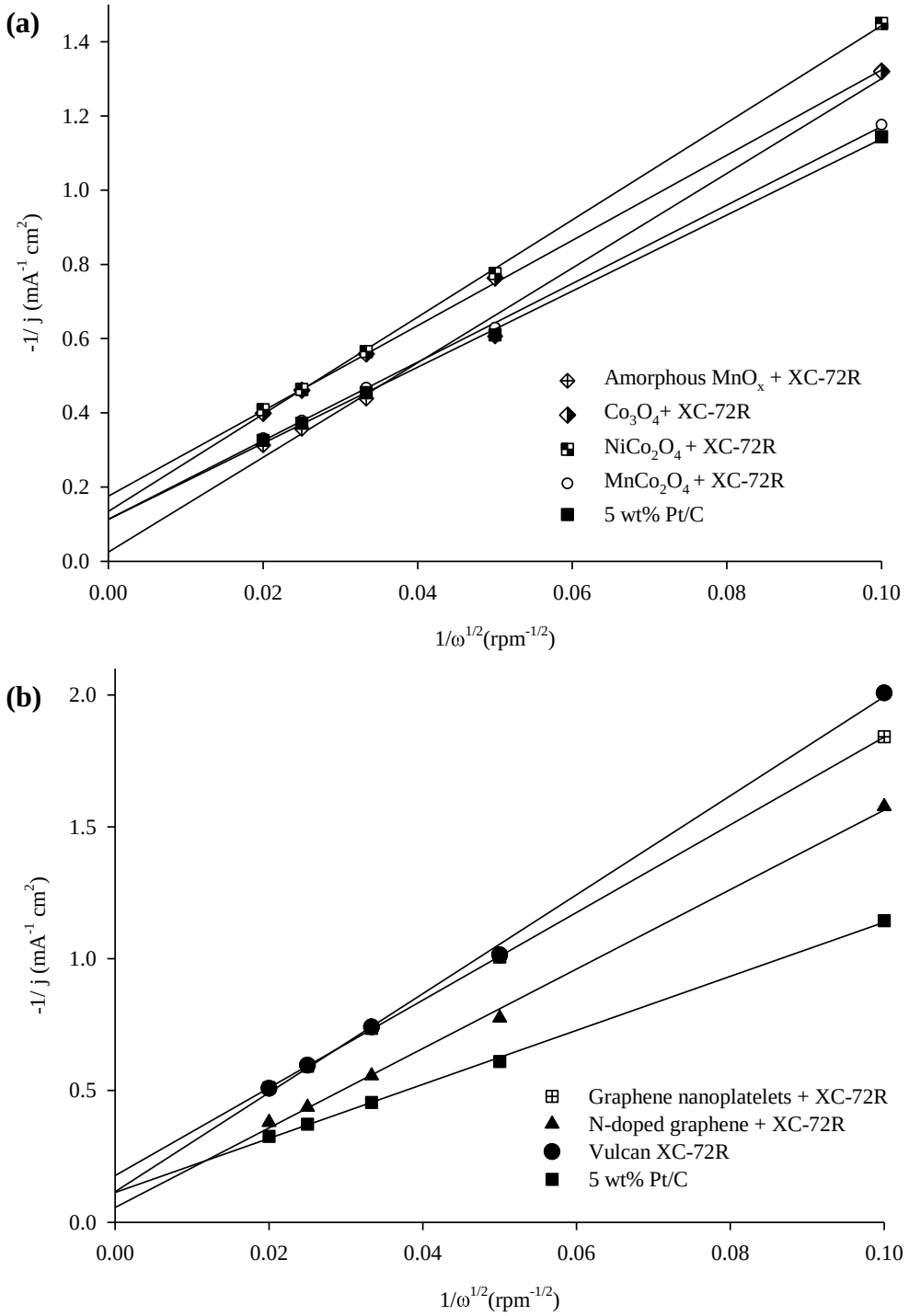

Figure 4.12 Koutecky-Levich plots j^{-1} versus $\omega^{-1/2}$ for **a)** metal oxide **b)** functional carbon catalysts combined with Vulcan XC-72R taken from the mass transfer controlled region of -0.4 V for rotation rates 100, 400, 900, 1600 and 2500 rpm.

K-L plots in **Figure 4.12 a & b** for the metal oxide catalysts and functional carbon materials combined with Vulcan XC-72R compared against 5 wt% Pt/C give an indication of how the catalyst performance has been affected. The values of slope, *K* and intercept, j_k of these plots are summarised in **Table 4.6**. Comparing the absolute

intercept values of the plots, the addition of Vulcan XC-72R results in a decrease in the absolute intercept values of all catalysts. In general, the metal oxide catalysts show a greater increase in electron transfer kinetics due to the addition of Vulcan XC-72R compared to functional carbon materials with amorphous MnO_x showing the greatest decrease in absolute intercept value of 55 mA^{-1} cm^2 followed by $NiCo_2O_4$ with a decrease of 32 mA^{-1} cm^{-2} and graphene showing the smallest decrease of 5 mA^{-1} cm^2. This suggests that the effect of addition of Vulcan XC-72R to various catalysts is subject to the initial conductivity and ORR activity of the catalyst.

Table 4.6 Intercept, slope values and apparent electron transfer numbers derived from the Koutecky-Levich plots in Figure 4.12 for various catalyst samples with addition of Vulcan XC-72R.

Catalyst	Slope, K / mA^{-1} cm^2 $rpm^{-1/2}$	Intercept, j_k /mA^{-1} cm^2	Apparent electron transfer number, n_{app}
Amorphous MnO_x + XC-72R	-12.8	-0.02	3.25
Co_3O_4 + XC-72R	-11.5	-0.18	3.62
$NiCo_2O_4$ + XC-72R	-13.1	-0.13	3.17
$MnCo_2O_4$ + XC-72R	-10.7	-0.11	3.89
Graphene + XC-72R	-16.6	-0.18	2.50
N-doped graphene + XC-72R	-15.1	-0.06	2.75

The absolute slope values obtained from the K-L plots (**Table 4.6**) are representative of the ORR electron transfer number. The slope values for mixed metal oxides $NiCo_2O_4$, $MnCo_2O_4$ graphene and N-doped graphene do not appear to be significantly affected by the presence of Vulcan XC-72R. However, the K-L slope value for Co_3O_4 decreased considerably with the addition of Vulcan XC-72R, indicating an increase in electron transfer number of the ORR pathway. This synergetic coupling of Co_3O_4 with a carbon component has been reported by several other studies [32, 33]. Without a carbon support, Co_3O_4 is proposed to favour the disproportionation of HO_2^- into O_2 and OH^- [12, 34] which agrees well with the slope value for Co_3O_4 in **Table 4.3**. Therefore it is expected that the physical adsorption of Co_3O_4 onto a carbon support yields a 2 + 2, four electron ORR pathway [35] that begins with the electroreduction of O_2 to HO_2^- (equation 4.1) at the Co_3O_4 catalyst and Vulcan XC-72R interface followed

by rapid disproportionation of the HO_2^- at the metal oxide surface into O_2 which is then further electroreduced.

In contrast, the absolute slope value of the K-L plot of amorphous MnO_x is observed to increase with the addition of Vulcan XC-72R, representative of a decrease in the electron transfer number. This has been suggested to be a result of the presence of two sites on the carbon-catalyst composite for the two step electron pathway. The initial reduction of O_2 into HO_2^- takes place at the carbon support more readily, causing a small increase in preference for the two electron ORR pathway [36].

4.2.4. GDE stability test

The stability of the catalysts was evaluated by chronopotentiometric measurements over a range of current densities. **Figure 4.13** shows the potential versus time plots for gas diffusion electrodes of amorphous MnO_x, $MnCo_2O_4$, $NiCo_2O_4$, graphene and N-doped graphene catalysts.

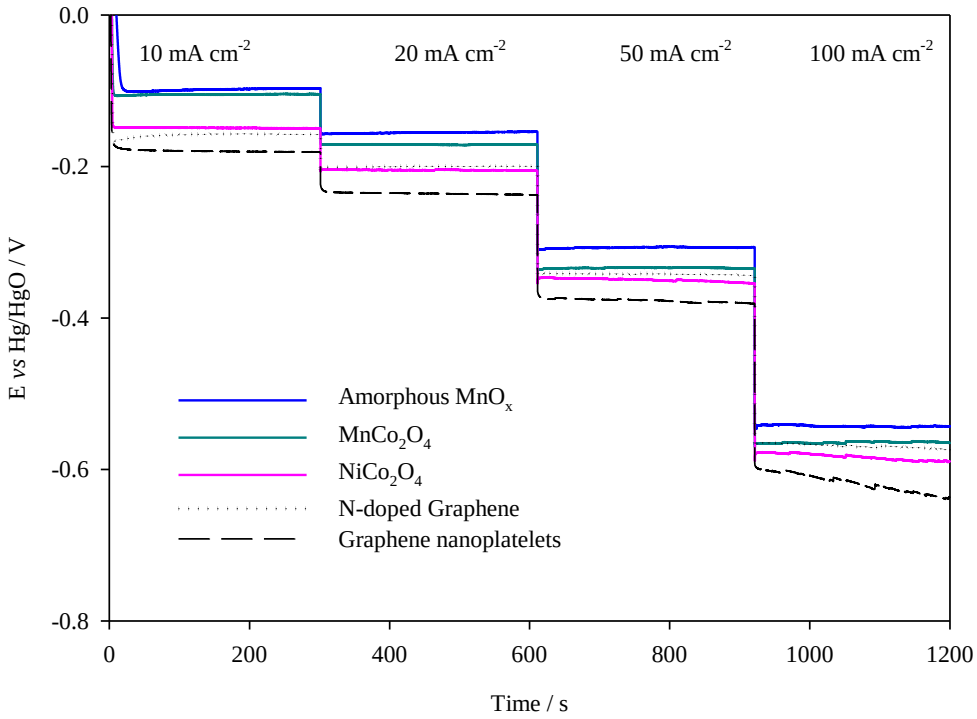

Figure 4.13 Chronopotentiometric measurements at various cathodic current densities of gas diffusion electrode (GDE) samples of various catalysts (catalyst loading 2 mg cm^{-2}) in electrolyte of 1 M NaOH at 333 K with O_2 feed rate of 200 cm^3 min^{-1} to the rear of the electrode.

Amorphous MnO_x showed good stability and performance for ORR at low and high current densities signifying its suitability for further optimisation. $MnCo_2O_4$ also appears to retain good stability for ORR over the range of current densities however at higher current densities of 50 and 100 mA cm^{-2}, a more pronounced potential difference between amorphous MnO_x and $MnCo_2O_4$ was observed indicating that $MnCo_2O_4$ does not perform as well as amorphous MnO_x at high current densities. At low current densities of 10 and 20 mA cm^{-2}, both mixed metal oxide $NiCo_2O_4$ and N-doped graphene demonstrated comparable stability; at higher current densities however, the N-doped graphene electrode presented lower ORR overpotentials compared to $NiCo_2O_4$.

The GDE sample of graphene nanoplatelets displayed the lowest ORR performance over the range of current densities tested, seen in **Figure 4.13**. Although the RDE data measurements showed rapid electron transfer for the graphene catalyst, when the graphene nanoplatelets were incorporated into a GDE and tested at 100 mA cm^{-2} it exhibited a rapid deterioration in performance, possibly due to flooding of the electrode. Hence, graphene is not a suitable catalyst for ORR.

4.3. Conclusion

In this chapter, several transition metal oxide catalysts Co_3O_4, MnO_2, MnO_x, $NiCo_2O_4$, and $MnCo_2O_4$ as well as graphene and N-doped graphene materials were tested for ORR performance using RDE measurements and compared against benchmark catalysts 5 wt% Pt/C and Vulcan XC-72R. All catalyst-coated glassy carbon voltammograms showed earlier onset potentials and greater current densities compared to bare glassy carbon. From the voltammograms recorded at 400 rpm and scan rate of 5 mV s^{-1} in **Figure 4.7**, the ORR catalysts were divided into three groups 1) metal oxides, 2) carbon materials and 3) precious metals, based on their onset potentials. Single and mixed metal oxides in the first group had the most negative onset potentials for ORR and $E_{1/2}$ values of ~-0.24 to -0.26 V. In the second group, graphene and N-doped graphene exhibited more positive onset potentials for ORR and displayed $E_{1/2}$ values of ~-0.11 V. Lastly in the third group, precious metal Pt/C showed the most positive onset potential for ORR and $E_{1/2}$ value of -0.055 V.

Further analysis of the data using the K-L equation gave an indication of the catalysts preference for the two or four electron pathway. From the K-L plot in **Figure 4.8**, the slope values for amorphous MnO_x and $MnCo_2O_4$ were close to that of Pt/C signifying that the $4e^-$ pathway is dominant for these catalysts. The remaining catalysts ranked according to their absolute slope values were $NiCo_2O_4$ > N-doped graphene > XC-72R > commercial MnO_2 > Co_3O_4 ≈ graphene.

The effect of the addition of Vulcan XC-72R on the catalysts' kinetic parameters was investigated, and observed to be dependent on the initial conductivity and ORR activity. Amorphous MnO_x combined with Vulcan XC-72R displayed the greatest reduction in ORR onset potential and $E_{1/2}$ value, due to the enhancement of the conductivity of MnO_x. Conversely, graphene was the only catalyst which displayed an increase in onset potential and $E_{1/2}$ value with the addition of Vulcan XC-72R, due to the reduction in electrochemically active surface area from agglomeration of the particles. More importantly, from the K-L plots in **Figure 4.12** the introduction of Vulcan XC-72R to the catalyst layer resulted in an increase in electron transfer number at Co_3O_4 and a slight increase in preference for the indirect two electron pathway at amorphous MnO_x.

Finally, the stability test at low and high current densities showed that amorphous MnO_x demonstrated the highest ORR activity, with good stability over the range of current densities indicating its suitability for further optimisation.

4.4. References

1. A. Loh, K. Xu, X. Li, B. Wang, Influence of synthesis parameters on amorphous manganese dioxide catalyst electrocatalytic performance, Electrochim. Acta 245 (2017) 615-624.
2. P.K. Sharma, G.J. Moore, F. Zhang, P. Zavalij, M.S. Whittingham, Electrical properties of the layered manganese dioxides $M_xMn_{1-y}Co_yO_2$, M = Na, K, Electrochem. Solid State Lett. 2 (1999) 494-6.
3. J.P. Hoare, Standard Potentials in Aqueous Solution,A.J. Bard (ed), Routledge, 2017
4. A. Ambrosi, C.K. Chua, N.M. Latiff, A.H. Loo, C.H.A. Wong, A.Y.S. Eng, A. Bonanni, M. Pumera, Graphene and its electrochemistry – an update, Chem. Soc. Rev. 45 (2016) 2458-93.
5. B. Marinho, M. Ghislandi, E. Tkalya, C.E. Koning, G.d. With, Electrical conductivity of compacts of graphene, multi-wall carbon nanotubes, carbon black, and graphite powder, Powder Tech. 221 (2012) 351-8.
6. J.-H. Chen, C. Jang, S. Xiao, M. Ishigami, M.S. Fuhrer, Intrinsic and extrinsic performance limits of graphene devices on SiO_2, Nat. Nanotechnol. 3 (2008) 206-9.
7. S.P. Jiang, Z.G. Lin, A.C.C. Tseung, Homogeneous and heterogeneous catalytic reactions in cobalt oxide/graphite air electrodes, J. Electrochem. Soc. 137 (1990) 759-64.
8. F. Cheng, J. Shen, B. Peng, Y. Pan, Z. Tao, J. Chen, Rapid room-temperature synthesis of nanocrystalline spinels as oxygen reduction and evolution electrocatalysts, Nat. Chem. 3 (2011) 79-84.
9. X. Ge, Y. Liu, F.W.T. Goh, T.S.A. Hor, Y. Zong, P. Xiao, Z. Zhang, S.H. Lim, B. Li, X. Wang, Z. Liu, Dual-phase spinel MnCo2O4 and spinel $MnCo_2O_4$/nanocarbon hybrids for electrocatalytic oxygen reduction and evolution, ACS Appl. Mater. Interfaces 6 (2014) 12684-91.
10. E. Lee, J.-H. Jang, Y.-U. Kwon, Composition effects of spinel $Mn_xCo_{3-x}O_4$ nanoparticles on their electrocatalytic properties in oxygen reduction reaction in alkaline media, J. Power Sources 273 (2015) 735-41.
11. D. Pletcher, X. Li, S.W.T. Price, A.E. Russell, T. Sönmez, S.J. Thompson, Comparison of the spinels Co_3O_4 and $NiCo_2O_4$ as bifunctional oxygen catalysts in alkaline media, Electrochim. Acta 188 (2016) 286-93.
12. T. Sönmez, S.J. Thompson, S.W.T. Price, D. Pletcher, A.E. Russell, Voltammetric studies of the mechanism of the oxygen reduction in alkaline media at the spinels Co_3O_4 and $NiCo_2O_4$, J. Electrochem. Soc. 163 (2016) H884-90.
13. C. Jin, F. Lu, X. Cao, Z. Yang, R. Yang, Facile synthesis and excellent electrochemical properties of $NiCo_2O_4$ spinel nanowire arrays as a bifunctional catalyst for the oxygen reduction and evolution reaction, J. Mater. Chem. A 1 (2013) 12170-7.
14. X. Cao, C. Jin, F. Lu, Z. Yang, M. Shen, R. Yang, Electrochemical properties of $MnCo_2O_4$ spinel bifunctional catalyst for oxygen reduction and evolution reaction, J. Electrochem. Soc. 161 (2014) 296-300.
15. Y. Jiao, Y. Zheng, M. Jaroniec, S.Z. Qiao, Origin of the electrocatalytic oxygen reduction activity of graphene-based catalysts: A roadmap to achieve the best performance, J. Am Chem. Soc. 136 (2014) 4394-403.
16. L. Yu, X. Pan, X. Cao, P. Hub, X. Bao, Oxygen reduction reaction mechanism on nitrogen-doped graphene: A density functional theory study, J. Catal. 282 (2011) 183-90.
17. E. Yeager, Dioxygen electrocatalysis: Mechanisms in relation to catalyst structure, J. Mol. Catal. 38 (1986) 5-25.
18. C. Paliteiro, A. Hamnett, J.B. Goodenough, The electroreduction of oxygen on pyrolytic graphite, J. Electroanal. Chem. Interfac. Electrochem. 233 (1987) 147-59.

19. P.M. Sipos, G. Hefter, P.M. May, Viscosities and densities of highly concentrated aqueous MOH solutions ($M^+ = Na^+, K^+, Li^+, Cs^+, (CH_3)4N^+$) at 25.0 °C, J. Chem. Eng. Data 45 (2000) 613-7.
20. K. Ke, K. Hiroshima, Y. Kamitaka, T. Hatanaka, Y. Morimoto, An accurate evaluation for the activity of nano-sized electrocatalysts by a thin-film rotating disk electrode: Oxygen reduction on Pt/C, Electrochim. Acta 72 (2012) 120-8.
21. Y. Garsany, I.L. Singer, K.E. Swider-Lyons, Impact of film drying procedures on RDE characterization of Pt/VC electrocatalysts, J. Electroanal. Chem. 662 (2011) 396-406.
22. L. Zhang, Z. Xia, Mechanisms of oxygen reduction reaction on nitrogen-doped graphene for fuel cells, J. Phys. Chem. C 115 (2011) 11170-6.
23. L. Lai, J.R. Potts, D. Zhan, L. Wang, C.K. Poh, C. Tang, H. Gong, Z. Shen, J. Linc, R.S. Ruoff, Exploration of the active center structure of nitrogen-doped graphene-based catalysts for oxygen reduction reaction, Energy Environ. Sci. 5 (2012) 7936-42.
24. O. Ghodbane, J.-L. Pascal, F. Favier, Microstructural effects on charge-storage properties in MnO_2-based electrochemical supercapacitors, ACS Appl. Mater. Interfaces 1 (2009) 1130-9.
25. K.A. Stoerzinger, M. Risch, B. Han, Y. Shao-Horn, Recent insights into manganese oxides in catalyzing oxygen reduction kinetics, ACS Catal. 5 (2015) 6021-31.
26. A.L. Dicks, The role of carbon in fuel cells, J. Power Sources 156 (2006) 128-41.
27. P. Trogadas, T.F. Fuller, P. Strasser, Carbon as catalyst and support for electrochemical energy conversion, Carbon 75 (2014) 5-42.
28. S. Sharma, B. G.Pollet, Support materials for PEMFC and DMFC electrocatalysts—A review, J. Power Sources 208 (2012) 96-119.
29. E.L. Wolf, Applications of Graphene: An Overview(ed), Springer International Publishing, 2014
30. E. Antolini, Carbon supports for low-temperature fuel cell catalysts, Appl. Catal. B 88 (2009) 1-24.
31. T. Poux, F.S. Napolskiy, T. Dintzer, G. Kéranguéven, S.Y. Istomin, G.A. Tsirlina, E.V. Antipov, E.R. Savinova, Dual role of carbon in the catalytic layers of perovskite/carbon composites for the electrocatalytic oxygen reduction reaction, Catal. Today 189 (2012) 83-92.
32. Y. Liang, Y. Li, H. Wang, J. Zhou, J. Wang, T. Regier, H. Dai, Co_3O_4 nanocrystals on graphene as a synergistic catalyst for oxygen reduction reaction, Nat. Mater. 10 (2011) 780-6.
33. S.K. Singh, V.M. Dhavale, S. Kurungot, Surface-tuned Co_3O_4 nanoparticles dispersed on nitrogen-doped graphene as an efficient cathode electrocatalyst for mechanical rechargeable zinc−air battery application, ACS Appl. Mater. Interfaces 7 (2015) 21138-49.
34. S.P. Jiang, Z.G. Lin, A.C.C. Tseung, Homogeneous and heterogeneous catalytic reactions in cobalt oxide/graphite air electrodes, J. Electrochem. Soc. 137 (1990) 764-9.
35. J. Liu, L. Jiang, Q. Tang, B. Zhang, D.S. Su, S. Wang, G. Sun, Coupling effect between cobalt oxides and carbon for oxygen reduction reaction, ChemSusChem 5 (2012) 2315-8.
36. K.-H. Wu, Q. Zeng, B. Zhang, X. Leng, D.-S. Su, I.R. Gentle, D.-W. Wang, Structural origin of the activity in Mn_3O_4–graphene oxide hybrid electrocatalysts for the oxygen reduction reaction, ChemSusChem 8 (2015) 3331-9.

Chapter 5 Optimisation of Selected ORR Catalyst

Amorphous MnO_x has demonstrated good activity and stability as a potential candidate for ORR in the previous chapter. The catalytic activity of manganese oxides is dependent on its composition, crystal phase and morphology, therefore altering the preparation conditions can be an effective way of controlling the structural and surface properties of the resultant MnO_x. However, the influence of preparation parameters on their ORR activity has not been systematically studied yet. In this chapter, a series of amorphous MnO_x catalysts were prepared by varying the parameters of the catalyst preparation method including molar ratio of MnO_4^-/ Mn^{2+}, addition order of reactants, synthesis pH, and temperature. The influence of the MnO_4^-/ Mn^{2+} molar ratios of the precursor solutions on the catalysts' ORR performance is discussed in more detail using a rotating disc electrode (RDE) set-up to assess improved activity. In addition, the electroreduction of Mn and reduction of O_2 at the amorphous MnO_x were investigated in O_2 and N_2 saturated environments. Finally, the performance and stability of the optimal amorphous MnO_x was tested in a gas diffusion electrode cell set-up.

5.1. Experimental section

5.1.1. Synthesis of catalysts

A series of amorphous MnO_x was prepared by chemical redox method by varying selected preparation conditions. In this experiment, a volume ratio is defined as volume of 0.04 M $KMnO_4$ vs that of 0.03 M $Mn(CH_3COO)_2$. The mixed solutions were made by different volume ratios at room temperature with stirring. Several MnO_x catalysts were prepared over a range of MnO_4^-/Mn^{2+} molar ratios presented in **Table 5.1** and these have been labelled in increasing order from M1 to M5 in **Table 5.2**. As shown in the synthesis reaction [1, 2] in equation (5.1), the theoretical molar ratio of MnO_4^-/Mn^{2+} for the synthesis of MnO_2 is 2:3.

$$2Mn^{7+} + 3\ Mn^{2+} \rightarrow 5\ Mn^{4+} \qquad (5.1)$$

The order in which these solutions were added to each other was also varied. For instance, when $KMnO_4$ was added dropwise to $Mn(CH_3COO)_2$ with stirring, this order

is represented by 'A'. Alternatively, when $Mn(CH_3COO)_2$ was added to $KMnO_4$, this order is represented by 'B'. The pH of the mixture at this stage was measured to be pH 5. This was increased to pH of 8, 10 or 12 with sodium hydroxide added slowly with continuous stirring. In some cases, the temperature of the solution during mixing was heated to 333 K.

Table 5.1 Volume ratios of 0.04 M $KMnO_4$ and 0.03 M $Mn(CH_3COO)_2$ and their respective MnO_4^-:Mn^{2+} molar ratios.

Volume ratio of 0.04 M $KMnO_4$: 0.03 M $Mn(CH_3COO)_2$	Molar ratio of MnO_4^-:Mn^{2+}
1:4	0.33
1:2	0.67
1:1	1.33
2:1	2.67
4:1	5.33

The precipitate which formed when the two solutions were added together was collected from the mixture using a bench-top centrifuge. The mixture was initially centrifuged at 2500 rpm for 20 mins at a time to remove the excess liquid. The deposit was then rinsed with deionised H_2O and centrifuged another 2 times to remove the purple colour of excess permanganate ions. The sediment was collected and dried at 333 K overnight in an oven to remove any moisture present. Finally, the dried sediment was ground with a pestle to a fine powder. The series of MnO_x synthesised is displayed in **Table 5.2**. Additional samples of stoichiometric sample M2 annealed in air at 873 K for 3 h and M2 without basic pH adjustment were prepared as well.

Table 5.2 Series of MnO_x catalyst prepared with different parameters.

Sample	Molar ratio of MnO_4^-:Mn^{2+}	Order of reactants	pH	Temperature
M1	0.33	A or B	8, 10 or 12	295 K or 333 K
M2	0.67			
M3	1.33			
M4	2.67			
M5	5.33			

5.1.2. Preparation of RDE samples

The glassy carbon RDE tip was initially cleaned by polishing with 1.0 mm and 0.5 mm alumina powders (MicroPolish, Buehler) on MicroCloth (Buehler). The tip was then sonicated in deionised H_2O to remove any excess polishing powder and dried in air before use. Catalyst inks were prepared as described in Chapter 4, 1 mg of catalyst was added to solvent of 1 mL deionised H_2O + 0.5 mL isopropanol and 5 µL of 5 wt% Nafion 117. With the inclusion of Vulcan XC-72R, 1 mg catalyst in the ink was replaced by 0.5 mg of catalyst + 0.5 mg of Vulcan XC-72R. The mixture was ultrasonicated for ~20 mins and then homogenised with a hand held homogeniser (LabGen 7 mixer, Cole-Parmer) for 3-4 mins at 28 000 rpm. Finally, the ink was applied to the surface of the glassy carbon RDE tip ⌀ = 4 mm. Aliquots of 8 µL of catalyst ink was loaded onto the surface three times with drying in air in between, for a loading of ~120 µg cm^{-2}.

5.1.3. Preparation of GDE samples

Carbon paper (Alfa Aesar, TGP-H-60, base-layered) was initially pre-cut with hand-held ⌀ =13 mm hole punch. Catalyst ink for GDE catalyst layer was prepared by adding catalyst, Vulcan XC-72R carbon powder (Cabot Corp.) and a polymeric binder, PTFE (Sigma Aldrich, 60 wt% dispersion in H_2O) in a 10:10:2 weight ratio. The PTFE solution was firstly mixed with solvent of 1:1 weight ratio of deionised H_2O to IPA before being added to the solid catalyst and carbon powders. The ink was sonicated for ~20 mins and homogenised for 3-4 mins. This well-mixed ink was carefully applied with a stainless steel spatula to the pre-cut carbon paper with drying in between until a loading of 2 mg cm^{-2} was reached.

5.1.4. Physical characterisation

The series of catalysts were characterised with SEM-EDS (FEI Quanta 650 FEG) at accelerating voltage of 1 kV to obtain surface morphology of the catalysts. A Bruker D8 Advance X-ray diffractometer with Cu tube source (λ= 1.5418 Å) was used to collect powder X-ray diffraction results which were then analysed using Bruker Diffraction Suite EVA software.

5.1.5. Electrochemical characterisation

The same RDE and GDE set-ups described in Chapter 4 were used and electrochemical measurements were performed with Biologic SP-150 potentiostat and recorded with EC-lab software package. Similar to RDE experiments carried out in Chapter 4, cyclic voltammograms were collected without electrode rotation by scanning in the reduction region between 0.0 V and -1.0 V (*vs* Hg/ HgO) at a scan rate of 50 mV s^{-1}. Polarisation curves were collected at electrode rotation speeds of 100, 400, 900, 1600 and 2500 rpm between potentials of 0.1 and -0.5 V (*vs* Hg/ HgO) using a slower scan rate of 5 mV s^{-1}. The 1 M NaOH electrolyte was replaced before each experiment and electrolyte temperature was maintained at 298 K by recirculating water bath (TC120, Grant) connected to the glass cell's inbuilt water jacket. The electrolyte was saturated with oxygen (BOC) or nitrogen (BOC) for at least 30 mins before each experiment using a glass frit (Sigma Aldrich, 25-50 µm porosity).

For measurements using the GDE set-up, cathodic current densities of 10, 20, 50 and 100 mA cm^{-2} were chosen to validate the performance of the electrodes as they are representative of a working system. The electrodes were exposed consecutively to each current density in increasing order from 10 to 100 mA cm^{-2} for a relatively short period of time. This was to allow rapid evaluation of the electrode performance over a wide range of current densities. The MnO_x catalyst coated GDEs were assessed based on their activation potential or potential above open circuit potential to maintain the required current density as well as stability. The temperature of the 1 M NaOH electrolyte was regulated to 333 K using a recirculating water bath connected to inbuilt water jacket and O_2 was supplied at a flowrate of 200 cm^3 min^{-1} to the back of the GDE.

5.2. Results and discussion

5.2.1. Sample characterisation

SEM micrographs of selected MnO_x samples are given in **Figure 5.1**. A low accelerating voltage of 1 kV was used as the MnO_x samples were found to be very non-conductive. This helped to minimise unwanted charging effects from the

accumulation of electrons on the surface of these samples such as image distortion and reduction in image quality.

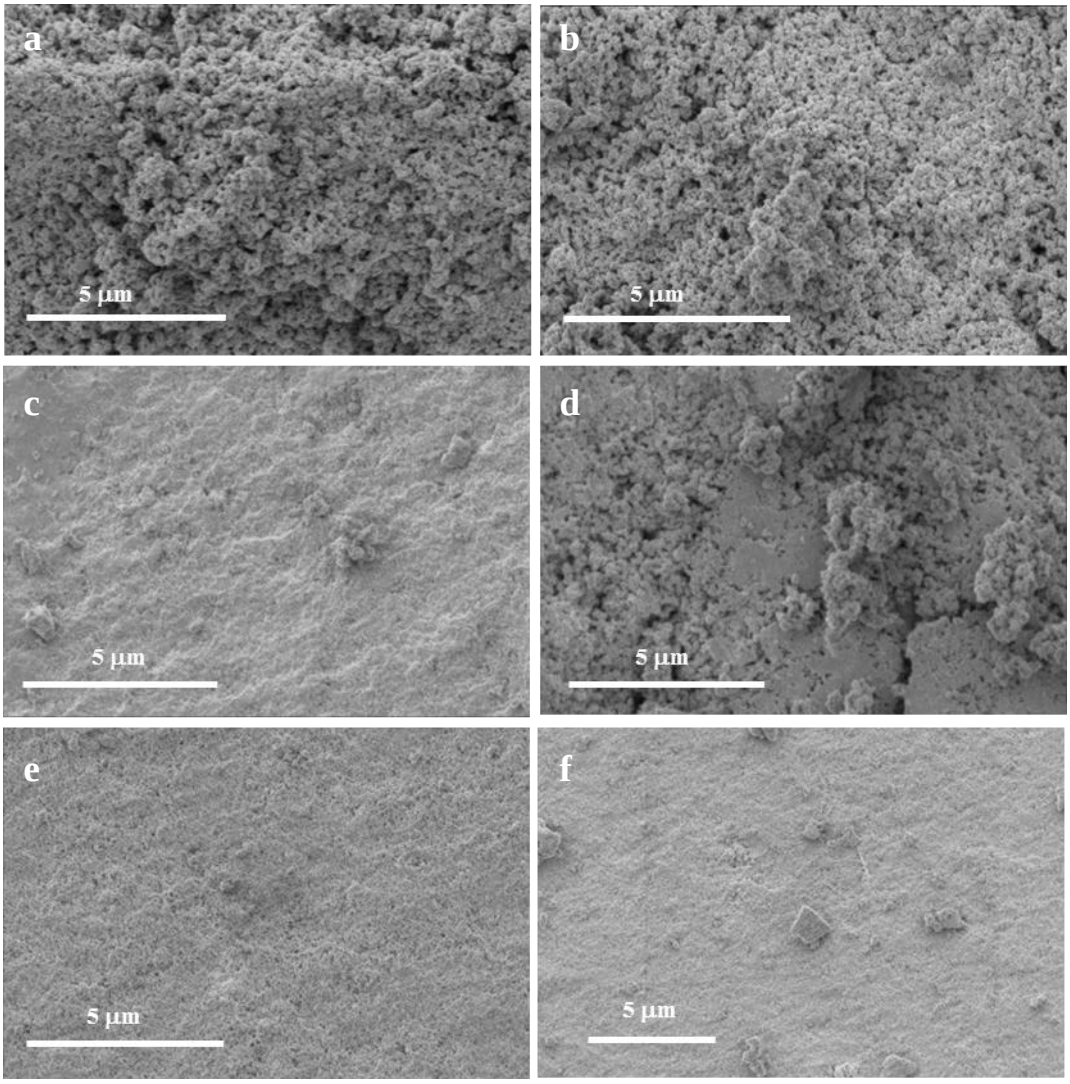

Figure 5.1 SEM micrographs of **a)** M3-A pH 12, 295 K, **b)** M3-A pH 10, 295 K, **c)** M3-A pH 12, 333 K, **d)** M3-A pH 10, 333 K, **e)** M3-B pH 12, 295 K and **f)** M4-B pH 12, 295 K.

The catalyst sample in **Figure. 5.1 a** was prepared with molar ratio MnO_4^-:MnO_2 of 1.33 and presents a morphology which is composed of small particles loosely grouped together. Samples prepared at different MnO_4^-:MnO_2 molar ratios (given in Appendix A) did not show any appreciative differences in morphology and this is likely because changing the molar ratio only affects the bulk elemental composition. Similarly, basic pH adjustment to pH 10 in **Figure 5.1 b** instead of pH 12 does not appear to affect the morphology of the catalyst surface either. The increase in synthesis temperature from 295 K to 333 K causes aggregation of the particles resulting in a smoother, cohesive surface as seen in **Figure 5.1 c**. The effect of

aggregation occurs to a lesser extent in **Figure 5.1 d**. as the M3 catalyst only experienced basic pH adjustment to pH 10. Using order B instead of A to add the reactant solutions of $KMnO_4$ and $Mn(CH_3COO)_2$ together produced a similar effect for M3 and M4 in **Figure 5.1 e & f** respectively, regardless of their different molar ratios. This is proposed to be due to the excess of oxidising agent $KMnO_4$ which causes rapid nucleation and affects the degree of crystallisation of the product [3, 4].

No apparent differences in morphology were observed in SEM micrographs of M2 with and without basic pH adjustment (**Figure 5.2 a & b**) as well. Annealing the M2 sample, however, results in the growth of needle-like structures as displayed in **Figure 5.2 c**.

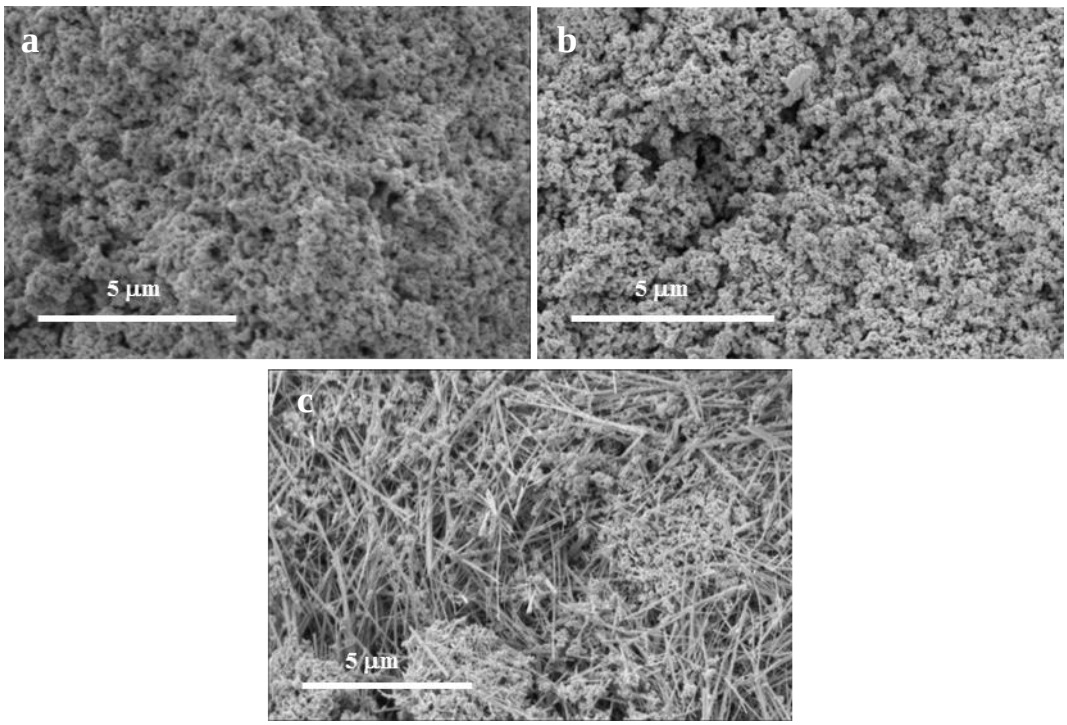

Figure 5.2 SEM micrographs of **a)** M2-A pH 12, 295 K, **b)** M2-A 295 K, without basic pH adjustment and **c)** annealed M2-A pH 12, 295 K.

X-ray diffraction of various samples were carried out and displayed in **Figure 5.3**. In **Figure 5.3 a**, diffractograms of samples M1 to M5 displayed broad weakly defined peaks which suggested that the catalyst samples were amorphous in nature. Due to this, not much variation was seen between diffractograms of different samples. The diffractogram of the annealed M2 sample in **Figure 5.3 b** exhibited peaks which matched that of tetragonal α-MnO_2 hydrate (JCPDS 44-0140).

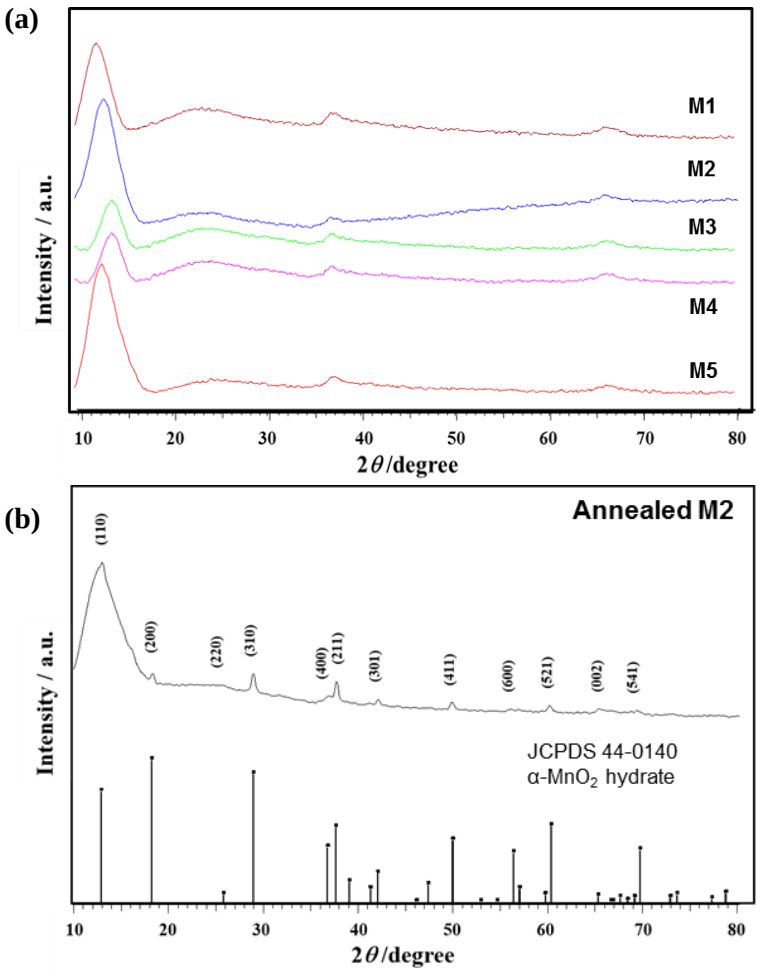

Figure 5.3 XRD diffractograms of **a)** MnO_x samples synthesised with various MnO_4^-:Mn^{2+} molar ratios and **b)** Annealed M2 MnO_x sample and standard pattern of tetragonal α-MnO_2 hydrate (JCPDS 44-0140).

Further XPS measurements of the surface composition and BET analysis of specific surface area for these catalyst samples were also previously reported [5]. A substantial amount of hydrated trivalent MnOOH and structural H_2O was found to be present in the amorphous MnO_x. The oxidation states of the MnO_x samples were in the range of 3.5 to 4.0 from the XPS data and specific surface areas of the catalyst samples were generally between 93 and 130 $m^2\ g^{-1}$. The M2 sample synthesised with stoichiometric molar ratio of 0.67 at 333 K with pH adjustment to pH 12 however presented the greatest oxidation state closest to the value of 4.0 with a correspondingly small specific surface area of 61 $m^2\ g^{-1}$ indicating that the product was most pure and crystalline.

5.2.2. RDE results

Cyclic voltammograms of catalysts M1 to M5 prepared with order A at 295 K with basic pH adjustment to 12 were made into inks and coated onto glassy carbon tips. These tips were then cycled between 0 V and 1.0 V in O_2 saturated 1M NaOH to give the plots shown in **Figure 5.4**. The voltammogram of the glassy carbon (GC) tip yields two cathodic peaks. The first cathodic peak at ~-0.26 V is representative of the $1e^-$ reduction of O_2 to superoxide anion $O_2\bullet^-$ [6] and the second broader cathodic peak at -0.85 V is characteristic of the reduction of HO_2^- to OH^- given in equation (5.2) [7].

$$HO_2^- + H_2O + 2e^- \rightarrow 3OH^- \qquad (5.2)$$

The shape of the voltammograms of various MnO_x catalysts are similar indicating that all catalyst variations have a common redox couple and they all exhibit greater peak currents compared to the GC tip. Voltammograms of M3 and M4 MnO_x samples yield higher currents and have slightly more positive onset potentials as compared to the other variations of MnO_x. This shows that altering the MnO_4^-/ Mn^{2+} molar ratio during catalyst preparation affects the specific capacitance of the catalyst which is related to the voltammetric charge, Q [8-10]. This is a consequence of changes in surface properties such as hydration, surface area and pore structure.

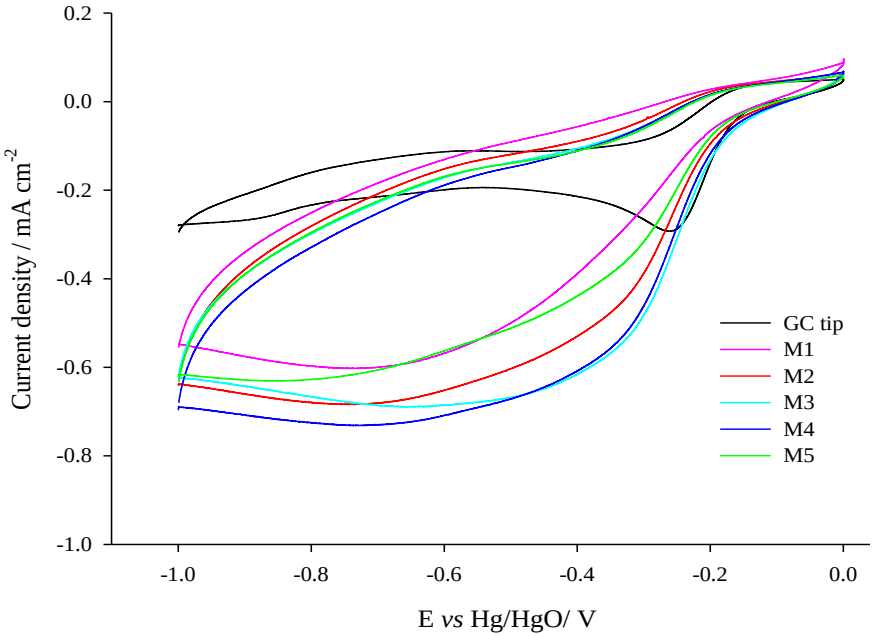

Figure 5.4 Cyclic voltammograms of thin films of MnO_x catalysts synthesised with different MnO_4^-/Mn^{2+} ratios coated on glassy carbon RDE tip and swept between potentials 0 to -1.0 V at a scan rate of 50 mV s^{-1} in O_2 saturated 1 M NaOH solution at 298 K.

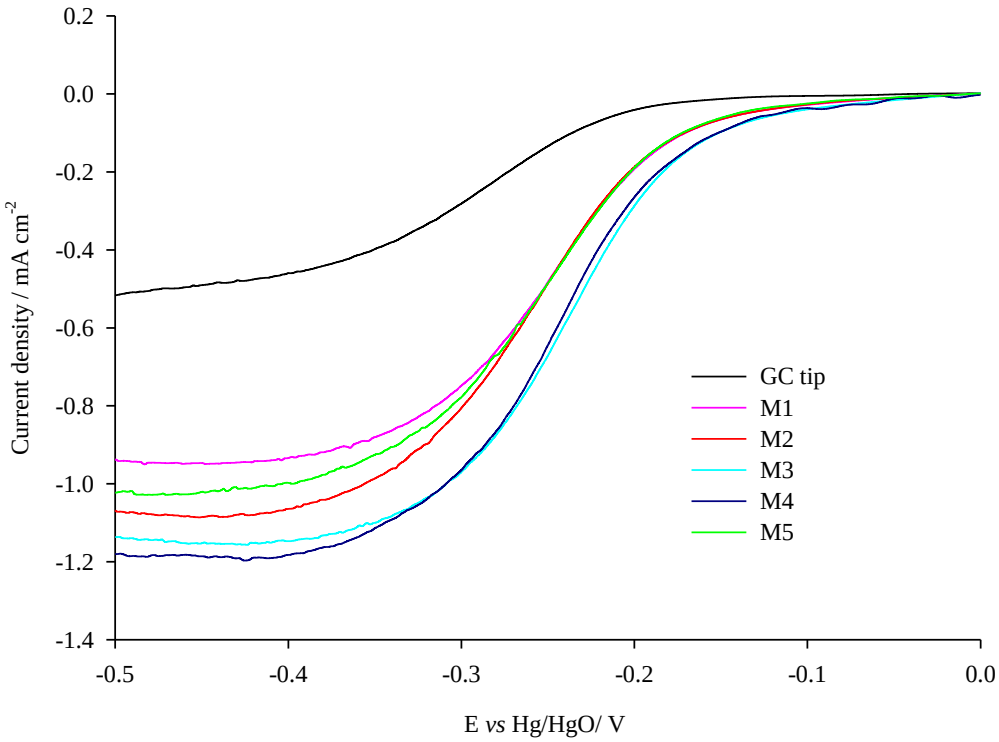

Figure 5.5 Linear sweep voltammograms of MnO_x samples synthesised with different MnO_4^-/ Mn^{2+} molar ratios coated on a glassy carbon RDE tip at 400 rpm rotation rate swept between 0 and -0.5 V at a scan rate of 5 mV s^{-1} in O_2 saturated 1 M NaOH at 298 K.

Table 5.3 Summary of kinetic parameters extracted from Figure 5.4 of the series of catalysts at 400 rpm rotation rate.

Catalyst	**$I_{Lat\ 0.4\ V}$/ mA cm^{-2}**	**E $_{-0.1\ mA\ cm^{-2}}$ vs Hg/ HgO / V**	**$E_{¼}$ vs Hg/ HgO / V**	**$E_{½}$ vs Hg/ HgO / V**	**$E_{¾}$ vs Hg/ HgO / V**	**$E_{¾}$ - $E_{¼}$ vs Hg/ HgO / V**
GC tip	-0.46	-0.237	-0.243	-0.283	-0.325	-0.082
M1	-0.95	-0.172	-0.210	-0.250	-0.292	-0.082
M2	-1.07	-0.171	-0.217	-0.257	-0.300	-0.083
M3	-1.15	-0.153	-0.200	-0.238	-0.278	-0.078
M4	-1.18	-0.151	-0.206	-0.244	-0.283	-0.077
M5	-1.00	-0.174	-0.213	-0.245	-0.294	-0.081

From the linear sweep voltammograms in **Figure 5.5** of these catalysts at 400 rpm, the GC tip presents the most negative ORR onset potential at ~ -0.24 V and least negative limiting current. Coating the GC tip with MnO_x catalyst ink clearly improves ORR activity. Catalysts M1, M2 and M5 display ORR onset potentials of approximately -0.17 V, whilst the onset potentials of M3 and M4 are more positive at ~-0.15 V. The limiting current densities of M3 and M4 recorded in **Table 5.3** are also more negative than that of M1, M2 and M5 indicating that these catalysts have a greater preference

for the $4e^-$ pathway over the $2e^-$ pathway. In addition, catalysts M3 and M4 have numerically smaller $E_{1/2}$ values compared to the other catalysts in the series indicative of a slightly faster rate of electron transfer for ORR. These results are consistent with the cyclic voltammogram data. Since the reduction of O_2 to HO_2^- is expected to proceed alongside the electroreduction of MnO_2 to MnOOH [11] via reactions (5.3), (5.4) and (5.5), the rate of reaction relies on how easily the M-O bond in MnO_2 can be broken [12].

$$MnO_2 + H_2O + e^- \rightarrow MnOOH + OH^- \quad (5.3)$$

$$2MnOOH + O_2 \rightarrow 2MnOOH(O_2)_{ads} \quad (5.4)$$

$$MnOOH(O_2)_{ads} + e^- \rightarrow MnO_2 + OH^- \quad (5.5)$$

The different catalytic activities of the series of MnO_x are therefore expected to be due to the varying content of MnO_2 with suitable M-O bond strength, which can give rise to a greater production of MnOOH [13].The catalysts can be ranked based on their kinetic parameters from most active for ORR to least M4 > M3 > M2 > M5 > M1. The same trend in performance was observed when this series of catalysts were incorporated into GDEs and tested at different current densities [5]. Further work on the influence of synthesis pH, temperature and addition sequence of reactants on ORR catalyst performance was also reported [5], and it was found that the catalysts which demonstrated the best ORR performance were M3 and M4-A 295 K with basic pH adjustment to pH 12. The reduction of O_2 at either of these two catalysts is therefore investigated in the rest of this chapter.

5.2.3. Importance of carbon in the catalyst layer

In **Figure 5.6**, catalyst inks of M2 and M4 with and without the inclusion of a carbon component were compared against catalyst inks of Vulcan XC-72R and 5 wt% Pt/C tested at the same conditions. Positive shifts of ~ 98 mV in the mixed control region represented by the $E_{1/2}$ value seen in **Table 5.4** indicates that the catalysts M2 and M4 were both limited by low conductivity and low utilisation of the MnO_x electrochemically active sites. Hence, Vulcan XC-72R acts as an electrically conductive support with high surface area for the MnO_x powder to be distributed across. With the inclusion of Vulcan XC-72R, an increase of ~ 0.60 mA cm^{-2} in limiting

currents as well as an increase of ~ 150 mV in ORR onset potentials of both M2 and M4 was observed. The $E_{3/4\text{-}1/4}$ values were equally observed to increase with the addition of carbon which has been explained in Chapter 4 to be due to the greater influence of transport of reactants to and products away from the catalyst. The similar effect of carbon on both M2 and M4 implies that the ORR reaction mechanism is the same for both variations of catalyst.

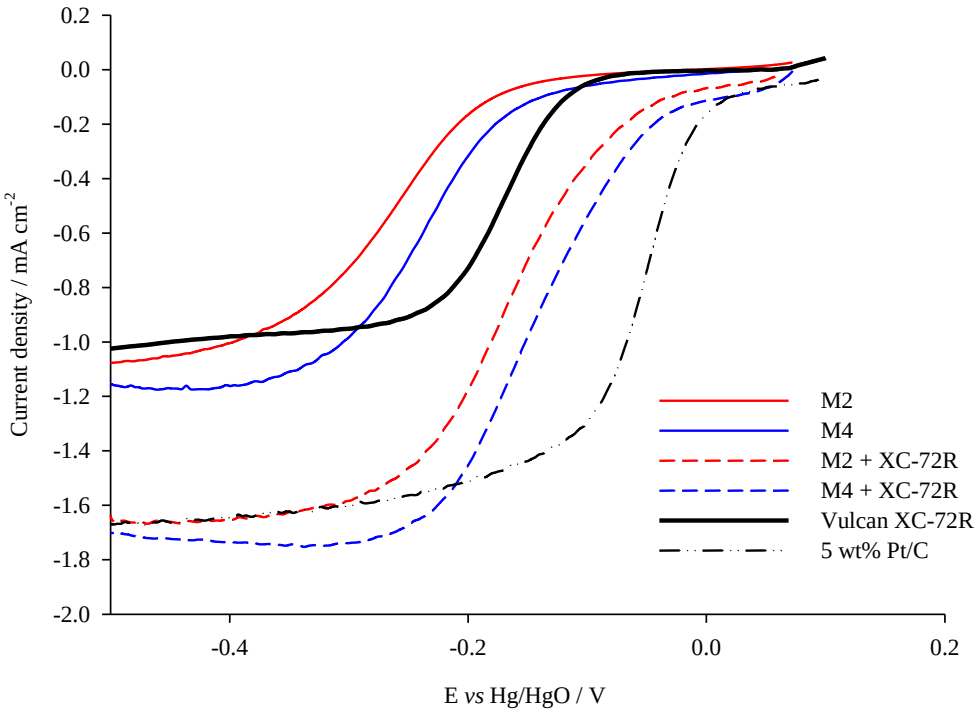

Figure 5.6 Linear sweep voltammograms of MnO_x samples M2 and M4 with and without Vulcan XC-72R coated on a glassy carbon RDE tip at 400 rpm rotation rate swept between 0 and -0.5 V at a scan rate of 5 mV s^{-1} in O_2 saturated 1 M NaOH at 298 K.

Table 5.4 Summary of kinetic parameters extracted from plots in Figure 5.5.

Catalyst	**$I_{Lat\ 0.4\ V}$/ mA cm^{-2}**	**$E_{-0.1\ mA\ cm^{-2}}$ vs Hg/ HgO / V**	**$E_{¼}$ vs Hg/ HgO / V**	**$E_{½}$ vs Hg/ HgO / V**	**$E_{¾}$ vs Hg/ HgO / V**	**$E_{¾}$ - $E_{¼}$ vs Hg/ HgO / V**
M2	-1.01	-0.177	-0.221	-0.261	-0.307	0.086
M4	-1.16	-0.138	-0.196	-0.235	-0.276	0.080
M2 + XC-72R	-1.65	-0.029	-0.106	-0.163	-0.209	0.103
M4 + XC-72R	-1.73	+0.011	-0.084	-0.138	-0.181	0.097
XC-72R	-0.98	-0.117	-0.144	-0.173	-0.205	0.061
5 wt% Pt/C	-1.65	+0.020	-0.029	-0.055	-0.089	0.060

Based on the K-L plot in **Figure 5.7**, after the inclusion of Vulcan XC-72R the value of the slope (**Table 5.5**) is seen to increase which suggests a preference for the

two electron pathway. As previously explained in Chapter 4, this is because in the mixture of catalyst and carbon, the reduction of O_2 to HO_2^- occurs at the carbon support and the MnO_x assists in catalysing the further reduction of HO_2^- to OH^- and O_2. However, between M2 and M4 the slope value of M4 + XC-72R is smaller, indicating that it still has a greater preference for the $4e^-$ pathway compared to M2. This agrees well with the results seen in Section 5.2.2. Lastly, the intercept of the plots of M2 and M4 with XC-72R are very close to zero, which suggests that this combination of catalyst and carbon gives rapid electron transfer without mass transfer effects comparable to benchmark Pt/C.

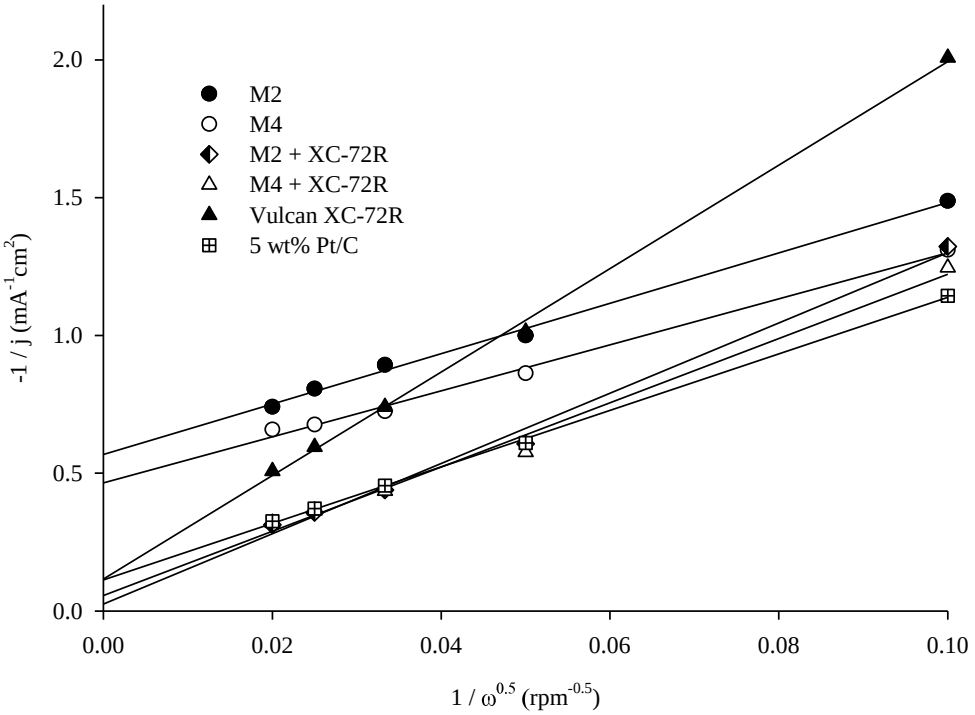

Figure 5.7 Koutecky-Levich plot j^{-1} versus $\omega^{-1/2}$ for various catalysts taken from the mass transfer controlled region of -0.4 V for rotation rates 100, 400, 900, 1600 and 2500 rpm.

Table 5.5 Intercept and slope values derived from the Koutecky-Levich plots given in Figure 5.6 for various catalyst samples.

Catalyst	Slope, K / mA^{-1} cm^2 $rpm^{-1/2}$	Intercept, i_k /mA^{-1} cm^2
M2	-9.1	-0.57
M4	-8.4	-0.47
M2 + XC-72R	-12.8	-0.02
M4 + XC-72R	-11.7	-0.06
Vulcan XC-72R	-18.8	-0.12
5 wt% Pt/C	-10.3	-0.11

5.2.4. Cyclic voltammetry of O_2 reduction on MnO_x catalyst

To understand the reduction of O_2 at the amorphous MnO_x catalyst, CVs were carried out over a wide range of scan rates from 5 up to 200 mV s^{-1} in both N_2 and O_2 saturated electrolyte. From **Figure 5.8**, the electroreduction of the Mn species is investigated at this range of scan rates in N_2-saturated electrolyte. The inset graph of cathodic current at -1.0 V *vs* Hg/ HgO versus scan rate was derived from the voltammograms. The cathodic currents increase linearly with scan rate signifying that the electroreduction of Mn^{4+} to Mn^{3+} and then Mn^{2+} occurs as a surface reaction.

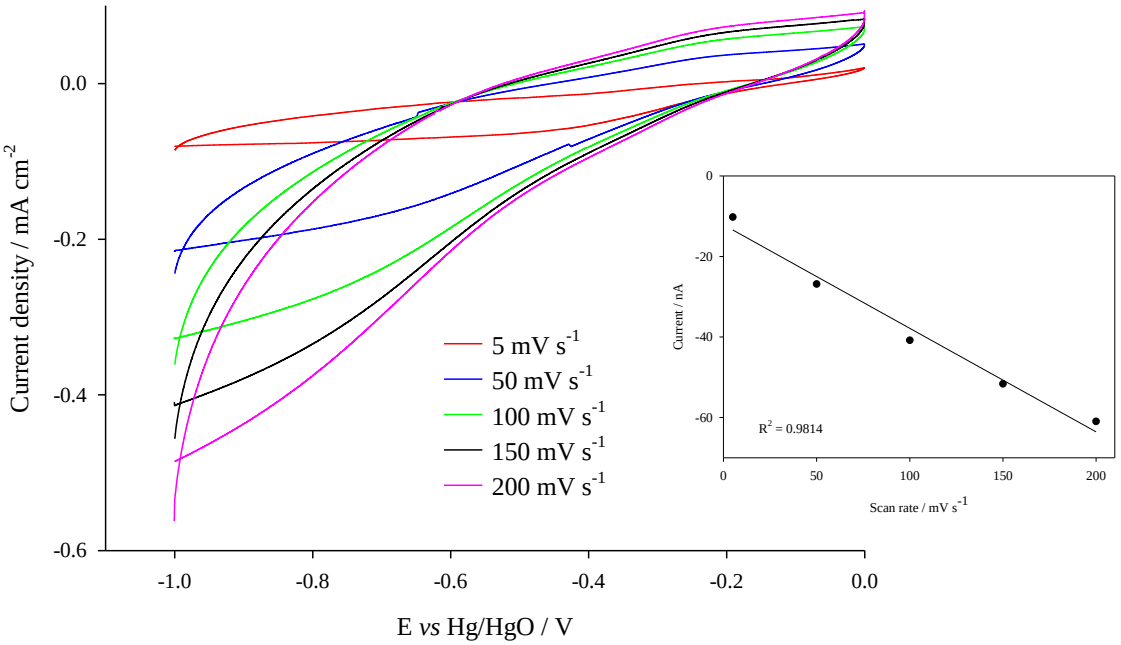

Figure 5.8 Cyclic voltammograms of MnO_x M4 catalyst sample prepared with MnO_4^-/ Mn^{2+} molar ratio 2.67, measured on a glassy carbon RDE tip at various scan rates in N_2 saturated 1 M NaOH solution at 298 K. Inset: Graph of cathodic current versus scan rate.

Likewise, cyclic voltammograms of MnO_x M4 catalyst cycled at different scan rates in O_2 saturated electrolyte were collected and presented in **Figure 5.9**. The relationship between the O_2 reduction peak current and scan rate (inset) is observed to be linear as well which suggests that the electroactive species is confined to the surface of the electrode, indicating that the reduction of oxygen which takes place alongside the electroreduction of Mn^{4+} is also a surface reaction.

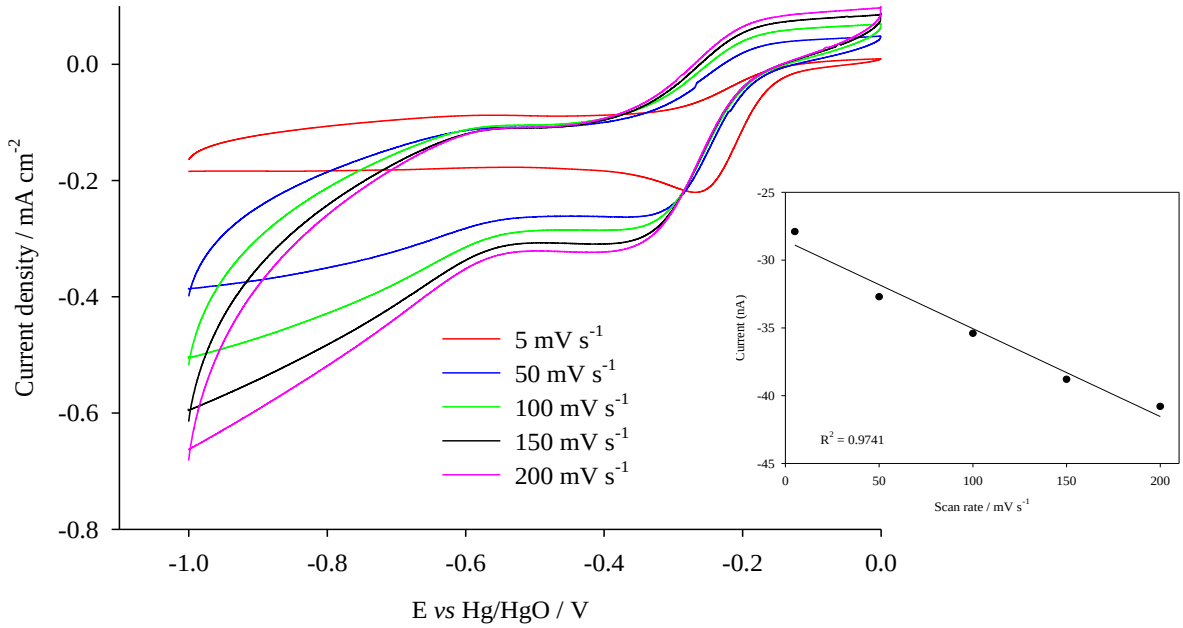

Figure 5.9 Cyclic voltammograms of MnO_x M4 catalyst sample prepared with MnO_4^-/ Mn^{2+} molar ratio 2.67, measured on a glassy carbon RDE tip at various scan rates in O_2 saturated 1 M NaOH solution at 298 K. Inset: Graph of cathodic current versus scan rate.

Since it was established that both the electroreduction of Mn^{4+} and oxygen reduction reactions occur at the surface, the effect of the order of cycling the same MnO_x sample consecutively in an O_2 or N_2 environment first was investigated. The same catalyst sample was cycled in an N_2 saturated electrolyte first (**Figure 5.10 a**) before being cycled in the same potential range at the same scan rate in an O_2 saturated electrolyte (**Figure 5.10 b**). Fresh electrolyte was used for each experiment and purged with O_2 or N_2 for the same amount of time. From **Figure 5.10 a**, the currents are much greater in the first cycle and a broad cathodic peak at ~-0.4 V is seen. In the following cycles, the electroreduction of Mn^{4+} appears to occur over a wide range of potentials as no distinct cathodic peaks are observed. This suggests that the appearance of the cathodic peak in the first cycle was due to the reduction of

oxygen initially trapped in the catalyst layer which took place alongside the electroreduction of Mn^{4+}.

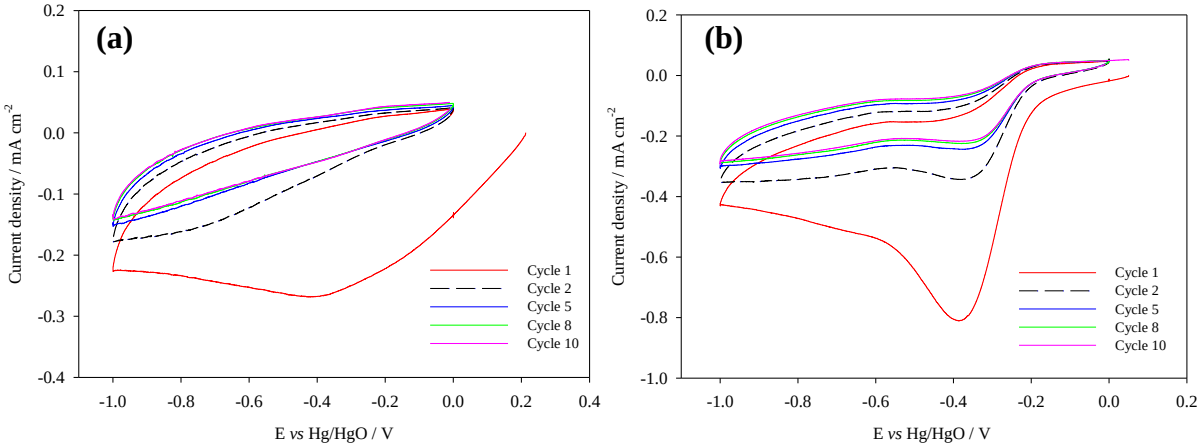

Figure 5.10 Progression of cyclic voltammograms from cycle 1 to 10 of MnO_x M4 catalyst sample prepared with MnO_4^-/ Mn^{2+} molar ratio 2.67, measured on a glassy carbon RDE tip at 50 mV s^{-1} in **a)** N_2 saturated 1 M NaOH followed by **b)** O_2 saturated 1 M NaOH at 298 K.

Subsequently, when cycled in the O_2 environment (**Figure 5.10 b**), a cathodic peak at ~0.4 V and onset potential at ~-0.17 indicative of the first step of the $2e^-$ ORR pathway is observed for all cycles. The peak current in cycle 1 is more than double that of the peak current of cycle 1 in N_2 environment. The current gradually decreases with increasing cycle number as the O_2 in the electrolyte is used up over time since cycle number is a function of time. The electrolyte was not able to be continuously replenished with O_2 as the design of the RDE cell did not permit constant bubbling of O_2 into the electrolyte whilst the experiment was running. Over time the cathodic peak shifted to slightly more positive potentials possibly as more electrochemically active sites on the catalyst are exposed to electrolyte. The return scan in the anodic direction reveals small broad peaks at -0.6 V and -0.2 which likely represents the oxidation of Mn^{2+} to Mn^{3+} [13].

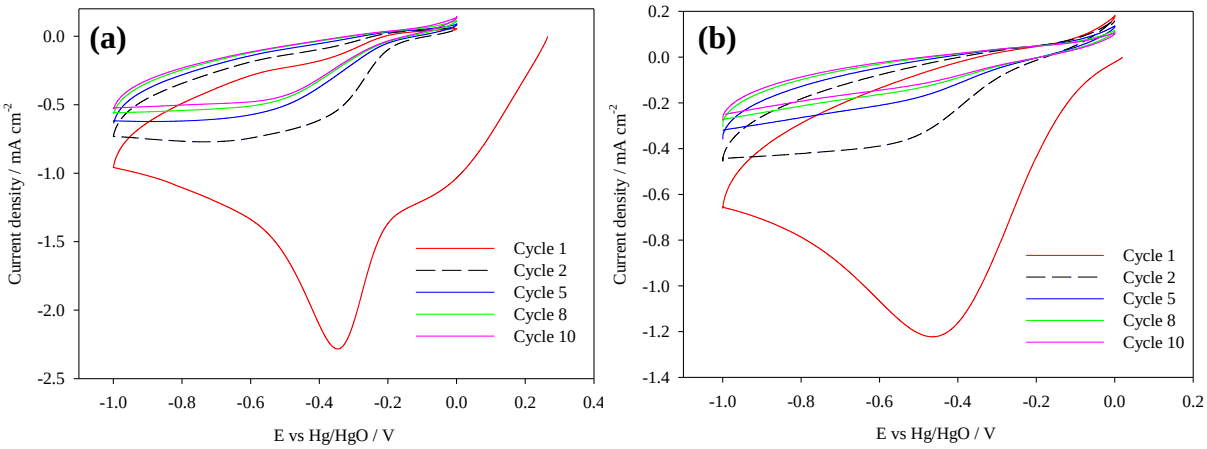

Figure 5.11 Progression of cyclic voltammograms from cycle 1 to 10 of MnO_x M4 catalyst sample prepared with MnO_4^-/ Mn^{2+} molar ratio 2.67, measured on a glassy carbon RDE tip at 50 mV s^{-1} in **a)** O_2 saturated 1 M NaOH followed by **b)** N_2 saturated 1 M NaOH at 298 K.

In comparison, a MnO_x M4 sample was cycled in O_2 saturated electrolyte first (**Figure 5.11 a**) before being cycled in N_2 saturated electrolyte (**Figure 5.11 b**). When the sample was initially cycled in O_2 saturated electrolyte, the first cycle presents a prominent cathodic peak at ~0.4 V with a peak current 2-3 times of that seen in **Figure 5.10 b**. This cathodic peak which is characteristic of oxygen reduction becomes broader in the following cycles and anodic peaks on the reverse scan are also less noticeable unlike the voltammograms in **Figure 5.10 b**. In general, the currents gradually decrease with increasing cycle number analogous to **Figure 5.10 b** as the oxygen in the electrolyte is depleted over time.

Subsequent cycling in a N_2 saturated electrolyte (**Figure 5.11 b**) produces voltammograms of a similar shape to **Figure 5.11 a**. The first cycle displays a peak at ~ -0.4 V which can be attributed to the reduction of the remaining O_2 at the electrochemically active sites. The current of this peak is gradually seen to decrease with cycling as well likely due to residual oxygen being reduced.

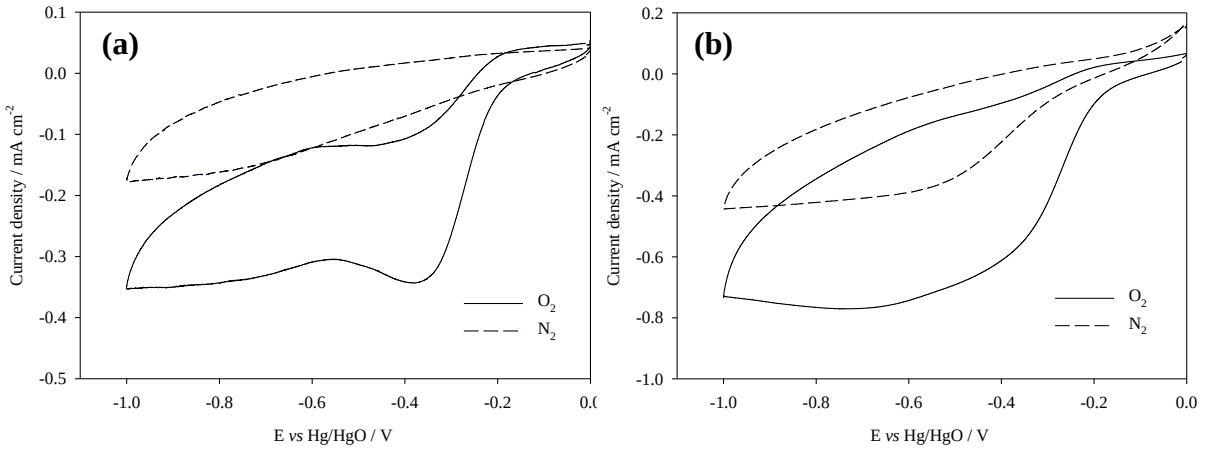

Figure 5.12 Cyclic voltammograms of the same MnO_x catalyst sample M4 prepared with MnO_4^-/ Mn^{2+} molar ratio 2.67, measured on a glassy carbon RDE tip in **a)** N_2 followed by O_2 saturated environment and **b)** O_2 followed by N_2 saturated environment.

The voltammograms from **Figure 5.10** and **5.11** were overlaid in **Figure 5.12 a & b**. The differences between these two graphs are suggested to be due to the surface sites of the catalyst being affected by the cycling environment. When cycled in a N_2 saturated electrolyte first, the catalyst surface may be occupied by Mn^{3+} species [14] hence peak current or charge is lower when cycled in O_2 saturated environment after compared to when the same sample is cycled in an O_2 saturated electrolyte first in **Figure 5.12 b**. Conversely when cycling in an O_2 saturated electrolyte first, the catalyst surface sites may be altered by the oxygen reduction reaction. For instance, the oxygen intermediates which adsorb to the surface sites of amorphous MnO_x may cause the expansion of the surface structure since the ionic radius of O^{2-} (1.40 Å) is approximately twice that of Mn^{2+} (0.83 Å), Mn^{3+} (0.645 Å) or Mn^{4+}(0.53 Å) [15], thereby helping to increase access to more electrochemically active sites. This explains the greater peak currents and broad cathodic peak observed and therefore the same voltammogram shape is seen for the sample when cycled in N_2 saturated electrolyte after. Overall, more cycles are recommended to determine if these changes are reversible over a longer period of time.

Regardless of the order of cycling in O_2 or N_2 saturated electrolyte first however, it is clear that the peak current density for the oxygen reduction reaction is greater in O_2 saturated electrolyte than in N_2 saturated electrolyte. This indicates that the MnO_x catalyst assists in catalysing the oxygen reduction reaction alongside the electroreduction of Mn^{4+}.

5.2.5. Effect of electrolyte concentration on GDE performance

MnO_x M3 catalyst was incorporated into GDEs using an optimised catalyst layer composition [5] and the effect of electrolyte concentration on this was studied at different current densities. Typically when varying the electrolyte concentration, the solubility and diffusivity of oxygen in the various electrolyte concentrations are considered significant factors. The solubility of oxygen has been shown previously [16, 17] to decrease as NaOH electrolyte concentration increases. In this set-up, although gaseous oxygen is supplied to the backside of the electrode, these factors are still seen to be equally important. In a basic environment, the four electron or direct pathway of ORR takes place via reaction (5.6) and OH^- is produced as the reaction is occurring. A higher concentration of OH^- in the electrolyte can therefore slow down the rate of the protonation of O_2^- to HO_2^- resulting in a change in the ORR mechanism.

$$O_2 + 2H_2O + 4e^- \rightarrow 4OH^- \qquad (5.6)$$

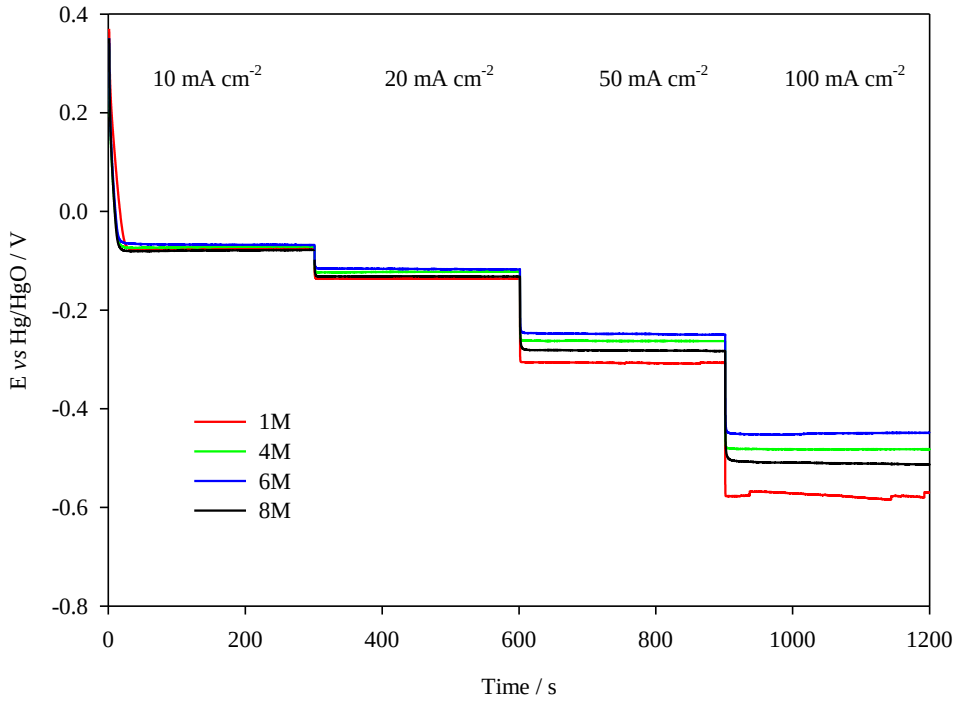

Figure 5.13 Chronopotentiometric measurements of GDEs coated with catalyst ink containing MnO_x M3 tested at different current densities in various NaOH electrolyte concentrations of at temperature 333 K with O_2 feed rate of 200 $cm^3\ min^{-1}$.

The effect of the OH^- concentration on the electrochemical performance of the GDE is displayed in the chronopotentiometric data at various current densities in

Figure 5.13. From the graph, no linear trend between the electrolyte concentration and the ORR performance is seen, likely due to the complex relationship between the ORR kinetics on the MnO_x catalyst and properties of the electrolyte. Of all the electrolyte concentrations, the performance of the GDE in 1 M NaOH is the worst, since the conductivity of 1 M NaOH is the lowest. Increasing the concentration of the electrolyte to 4 M and 6M is observed to increase the catalytic performance of the GDE and at this concentration, the GDE shows the best performance of all the electrolyte concentrations tested. However, further increasing the concentration to 8 M is seen to reduce the activity for ORR. This negative effect of high electrolyte concentrations on ORR performance is due to lower oxygen solubility, diffusivity and higher solution viscosity [18] which contributes to a lower concentration of oxygen at the three phase boundary within the GDE. Based on this GDE, the concentrations suitable for ORR performance are ranked as 6 M > 4 M > 8 M > 1 M. An electrolyte concentration of 4 M or 6 M NaOH is therefore suitable for obtaining good catalytic performance for the optimised MnO_x catalyst.

5.3. Conclusion

SEM micrographs of the catalysts indicated that changing the MnO_4^-:MnO_2 molar ratio and adjusting the pH of the synthesis solution did not bring about obvious changes in morphology. On the contrary, noticeable morphological differences were seen with changes in the synthesis temperature and order of addition of the reactants.

The results from RDE and GDE have shown that the catalysts were ordered according to their kinetic parameters M4 > M3 > M2 > M5 > M1. The catalysts which gave the most promising ORR performance were M3 and M4-A-295 K with basic pH adjustment to 12. The inclusion of carbon component of Vulcan XC-72R to the catalyst layer was found to be proportionate for both M2 and M4. However, M4 + XC-72R showed a greater preference for the $4e^-$ pathway compared to M2 + XC-72R.

In an N_2-saturated electrolyte, the electroreduction of Mn was determined to be a surface reaction as the cathodic peak current increased linearly with scan rate. In an O_2-saturated electrolyte, it was established that the reduction of oxygen was also a surface reaction which therefore occurred alongside the electroreduction of Mn. The

differences of the same MnO_x sample cycled consecutively in an O_2 or N_2 saturated electrolyte first were suggested to be due to changes in the surface sites of the catalyst over time. Longer cycling periods are suggested to determine if these changes in surface structure are reversible.

Finally, the effect of electrolyte concentration on the ORR performance of the optimised GDE catalyst layer was examined. 4 M and 6 M NaOH were found to be most suitable for obtaining good ORR performance. This was proposed to be due to a trade-off between an increase in conductivity and a decrease in the solubility and diffusivity of oxygen at these concentrations.

5.4. References

1. Y.F. Shen, R.P. Zerger, R.N. DeGuzman, S.L. Suib, L. McCurdy, D.I. Potter, C.L. O'Young, Manganese oxide octahedral molecular sieves: preparation, characterization, and applications, Science 260 (1993) 511-5.
2. M. Toupin, T. Brousse, D. Belanger, Influence of microstucture on the charge storage properties of chemically synthesized manganese, Chem. Mater. 14 (2002) 3946-52.
3. Y. Ma, J. Luo, S.L. Suib, Syntheses of birnessites using alcohols as reducing reagents: effects of synthesis parameters on the formation of birnessites, Chem. Mater. 11 (1999) 1972-9.
4. N. Subramanian, B. Viswanathan, T.K. Varadarajan, A facile, morphology-controlled synthesis of potassium-containing manganese oxide nanostructures for electrochemical supercapacitor application, RSC Adv. 4 (2014) 33911-22.
5. A. Loh, K. Xu, X. Li, B. Wang, Influence of synthesis parameters on amorphous manganese dioxide catalyst electrocatalytic performance, Electrochim. Acta 245 (2017) 615-624.
6. T. Ohsaka, L. Mao, K. Arihara, T. Sotomura, Bifunctional catalytic activity of manganese oxide toward O_2 reduction: novel insight into the mechanism of alkaline air electrode, Electrochem. Commun. 6 (2004) 273-277.
7. L. Mao, D. Zhang, T. Sotomura, K. Nakatsu, N. Koshiba, T. Ohsaka, Mechanistic study of the reduction of oxygen in air electrode with manganese oxides as electrocatalysts, Electrochim. Acta 48 (2003) 1015-1021.
8. W. Wei, X. Cui, W. Chen, D.G. Ivey, Manganese oxide-based materials as electrochemical supercapacitor electrodes, Chem. Soc. Rev. 40 (2011) 1697-1721.
9. P. Ragupathy, D.H. Park, G. Campet, H.N. Vasan, S.-J. Hwang, J.-H. Choy, N. Munichandraiah, Remarkable capacity retention of nanostructured manganese oxide upon cycling as an electrode material for supercapacitor, J. Phys. Chem. C 113 (2009) 6303-9.
10. M. Toupin, T. Brousse, D. Bélange, Charge storage mechanism of MnO_2 electrode used in aqueous electrochemical capacitor, Chem. Mater. 16 (2004) 3184-90.
11. J.C. Hunter, A. Kozawa, Standard Potentials in Aqueous Solution,A.J. Bard (ed), Routledge, 2017
12. W. Xiao, D. Wang, X.W. Lou, Shape-controlled synthesis of MnO_2 nanostructures with enhanced electrocatalytic activity for oxygen reduction, J. Phys. Chem. C 114 (2010) 1694-1700.
13. F.H.B. Lima, M.L. Calegaro, E.A. Ticianelli, Electrocatalytic activity of manganese oxides prepared by thermal decomposition for oxygen reduction, Electrochim. Acta 52 (2007) 3732-8.
14. P. Ruetschi, R. Giovanoli, Cation vacancies in MnO_2 and their influence on electrochemical reactivity, J. Electrochem. Soc. 135 (1988) 2663-9.
15. P. Ruetschi, Cation-vacancy model for MnO_2, J. Electrochem. Soc. 131 (1984) 2737-44.
16. C. Zhang, F.-R.F. Fan, A.J. Bard, Electrochemistry of oxygen in concentrated NaOH solutions: solubility, diffusion coefficients, and superoxide formation, J. Am. Chem. Soc 131 (2008) 177-81.
17. W.-Y. Yan, S.-L. Zheng, W. Jin, Z. Peng, S.-N. Wang, H. Du, Y. Zhang, The influence of KOH concentration, oxygen partial pressure and temperature on the oxygen reduction reaction at Pt electrodes, J. Electroanal. Chem. 741 (2015) 100-8.
18. W. Jin, H. Du, S. Zheng, H. Xu, Y. Zhang, Comparison of the oxygen reduction reaction between NaOH and KOH solutions on a Pt electrode: the electrolyte-dependent effect, J. Phys. Chem. B 114 (2010) 6542-8.

Chapter 6 Selection of Catalyst for Oxygen Evolution Reaction

A review of the literature on oxides and hydroxides of transition metals indicates that the trend in reactivity for OER follows Ni > Co > Fe. In addition to being highly active for OER, nickel is also commonly used in practical alkaline water electrolysis, demonstrating good resistance to corrosion (refer to Section 2.2.1.2 in Chapter 2). Since the mechanical stability of the OER catalyst layer is crucial due to the evolution of O_2 bubbles which can cause the degradation of the catalyst from the electrode over time, in this chapter, spinel oxides Co_3O_4 and $NiCo_2O_4$ were directly coated onto a stainless steel mesh electrode using a dip-coating process whilst the Ni and Ni-Fe hydroxides were directly grown on the mesh electrode via an electrodeposition method. The stability of selected catalysts were later assessed in a zero-gap alkaline water electrolyser.

6.1. Experimental section

6.1.1 Synthesis of catalysts on electrode substrates

Nickel mesh (DeXmet Corporation, 4Ni 6-040, 0.004″ nominal thickness, 0.006″ strand width, 0.040″ long diagonal of the diamond) and stainless steel mesh (DeXmet Corporation, 4SS 5-050, 0.004″ nominal thickness, 0.005″ strand width, 0.050″ long diagonal of the diamond) were selected as electrode substrates. These were cleaned by ultrasonication in isopropanol for 15 mins followed by ultrasonication in deionised H_2O for another 15 mins. The mesh was then rinsed thoroughly in deionised H_2O and dried before use.

Spinel cobalt oxide, Co_3O_4, and nickel cobaltite, $NiCo_2O_4$, catalysts were synthesised by thermal decomposition of nitrates on stainless steel mesh substrate. A 100 mL solution of 0.5 M nickel (II) nitrate hexahydrate and 1 M cobalt (II) nitrate hexahydrate were prepared with a 1:1 H_2O/ IPA solvent solution. Pre-cleaned stainless steel mesh pieces were fully immersed in this solution for 6 mins before being removed and dried at room temperature for 10 mins. Compressed air was used to remove any excess solution from the mesh. This was followed by heat treatment in air

at 648 K [1] for 10 mins. This coating procedure was repeated 4 more times before the samples were calcined in air at 648 K for 2 h. The stainless steel mesh pieces were weighed before and after the coating process to determine the catalyst loading per unit surface area.

$Ni(OH)_2$ and $Ni\text{-}Fe(OH)_2$ coated stainless steel mesh electrodes were synthesised using a cathodic electrodeposition method. This was carried out in a small undivided glass cell (~20 cm^3) equipped with a water jacket and polymer lid and Pt mesh and Hg/HgO in 1 M NaOH were used as counter and reference electrodes respectively. Deposition solutions of 18 mM metal sulphate + 25 mM ammonium sulphate were prepared with nickel (II) sulfate hexahydrate, $NiSO_4.6H_2O$ (Sigma-Aldrich, ≥98%), iron (II) sulfate heptahydrate, $FeSO_4.7H_2O$ (Sigma Aldrich, ≥99.0%) and ammonium sulfate, $(NH_4)_2SO_4$ (Sigma Aldrich, ≥99.%) using different percentages of metal salts: 100% Ni and 75%Ni 25%Fe for $Ni(OH)_2$ and $Ni\text{-}Fe(OH)_2$ respectively. The depositions were carried out at a cathodic current of 200 mA cm^{-2} for 120 s. The catalyst loading per unit surface area was determined assuming 100% coulombic efficiency.

Preparation of $Ni(OH)_2$ and $Ni\text{-}Fe(OH)_2$ coated SS mesh samples for stability testing in an electrolyser was done using two pieces of Pt mesh counter electrodes arranged on either side of the working electrode (**Figure 6.1**), 34 by 34 mm, to assist in the even distribution of current during electrodeposition and reference electrode of Hg/ HgO in 1 M NaOH.

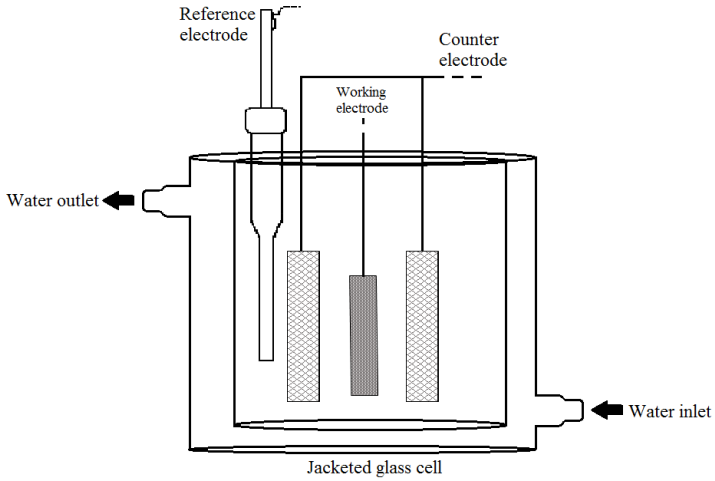

Figure 6.1 Labelled cross-section of jacketed glass cell showing arrangement of electrodes for cathodic electrodeposition of catalyst onto a SS mesh working electrode.

6.1.2 Structural and morphological characterisation

The morphology of the catalyst samples were characterised using an SEM-EDS (FEI Quanta 650 FEG) operated at 5 kV accelerating voltage. X-ray diffraction measurements of the catalyst coated stainless steel mesh were collected on a Siemens D5000 X-ray diffractometer with a Cu tube source ((λ= 1.5418 Å) between 20 and 80 degrees at a step rate of 0.02, 4 s per step and analysed with Bruker Diffraction Suite EVA software.

6.1.3 Electrochemical characterisation

Electrochemical measurements were carried out with a Bio-logic potentiostat and EC-lab software. To regulate the size of the active surface area, a hole-punch was used to punch a 2 mm diameter hole a piece of polyimide tape which was then taped over the mesh samples to give an active area of ~0.0314 cm^2. Air bubbles trapped under the tape were carefully removed before testing. The samples were tested in a standard three-electrode cell constructed of glass with an inbuilt water jacket and polymer lid at ambient temperature. Pt mesh was used as a counter electrode and Hg/ HgO in 1 M NaOH was used as a reference electrode.

Cyclic voltammograms were obtained in potential range of 0.1 to 0.7 V at various scan rates and slow scan linear sweep voltammograms were recorded between anodic potentials of 0.45 to 0.8 V at scan rate of 1 mV s^{-1}. All reported results were obtained after several scans when a stable response was recorded. The current densities are reported as a function of the geometric surface area of the electrode as well as the mass of catalyst coated on the electrode. Overpotential values were calculated as described in Section 3.4.1.2, E_{rev} is the potential at which OER is expected to take place at and this is taken to be 0.303 V vs Hg/ HgO in 1 M NaOH [2]. Selected catalyst coated mesh samples were further tested in a zero-gap alkaline water electrolyser to demonstrate preliminary OER performance.

6.1.4

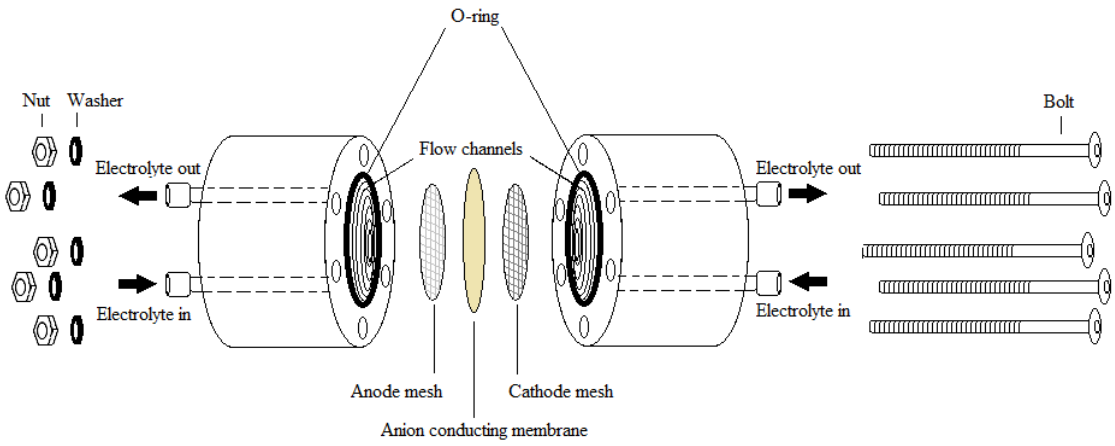

Figure 6.2 Schematic of assembly of custom-designed water electrolyser unit cell. Electrolyte inlet and outlets were connected to an electrolyte reservoir by Marprene tubing and circulated by peristaltic pump.

The electrolyser in **Figure 6.2** was assembled with two metal mesh electrodes of working area ~9 cm^2 on either side of an anion exchange membrane. 4 M NaOH electrolyte solution was continuously pumped through the cell from an electrolyte reservoir at a flowrate of 250 mL min^{-1} by peristaltic pump (300 series, Watson Marlow, UK) via Marprene tubing (i.d. 1.4 mm; Watson Marlow, UK) to remove any build-up of gas bubbles at the surface of the electrodes. The electrolyte reservoir was maintained at a temperature of 333 K by a recirculating water bath (TC120, Grant). The membrane was a commercial anion exchange membrane A201, supplied by Tokuyama Corp, pre-treated initially in deionised H_2O for a period of 24 h at room temperature, followed by soaking in 1 M NaOH overnight for ~ 18 h at room temperature. Finally the membrane was immersed in 4 M NaOH at 333 K for 2 h before being assembled into the electrolyser cell.

Expanded Ni mesh and SS mesh electrode substrates were used for the cathode and anode respectively. The metal substrates were cleaned and dried before use. The selected anode catalysts were coated onto the mesh either via a dip-coating method or by cathodic electrodeposition onto pre-treated SS mesh as described in Section 6.1.1.

6.2. Results and discussion

6.2.1. Physical characterisation of catalyst samples

The morphology of the catalysts and the homogeneity of the catalyst coatings on the stainless steel substrate as described in Section 6.1.1 were observed with SEM. SEM micrographs of uncoated SS mesh at high and low magnification are shown in **Figure 6.3** as a benchmark. The uncoated SS mesh appears to have a relatively even texture as is characteristic of an uncoated metal surface.

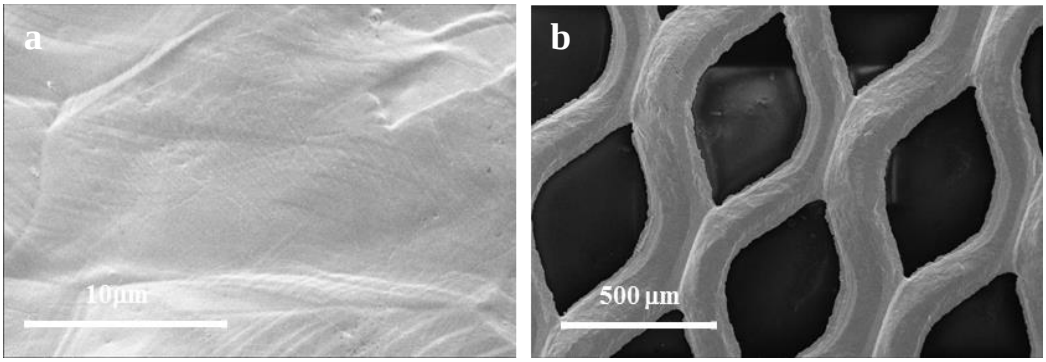

Figure 6.3 SEM micrographs of uncoated SS mesh at **a)** high and **b)** low magnification.

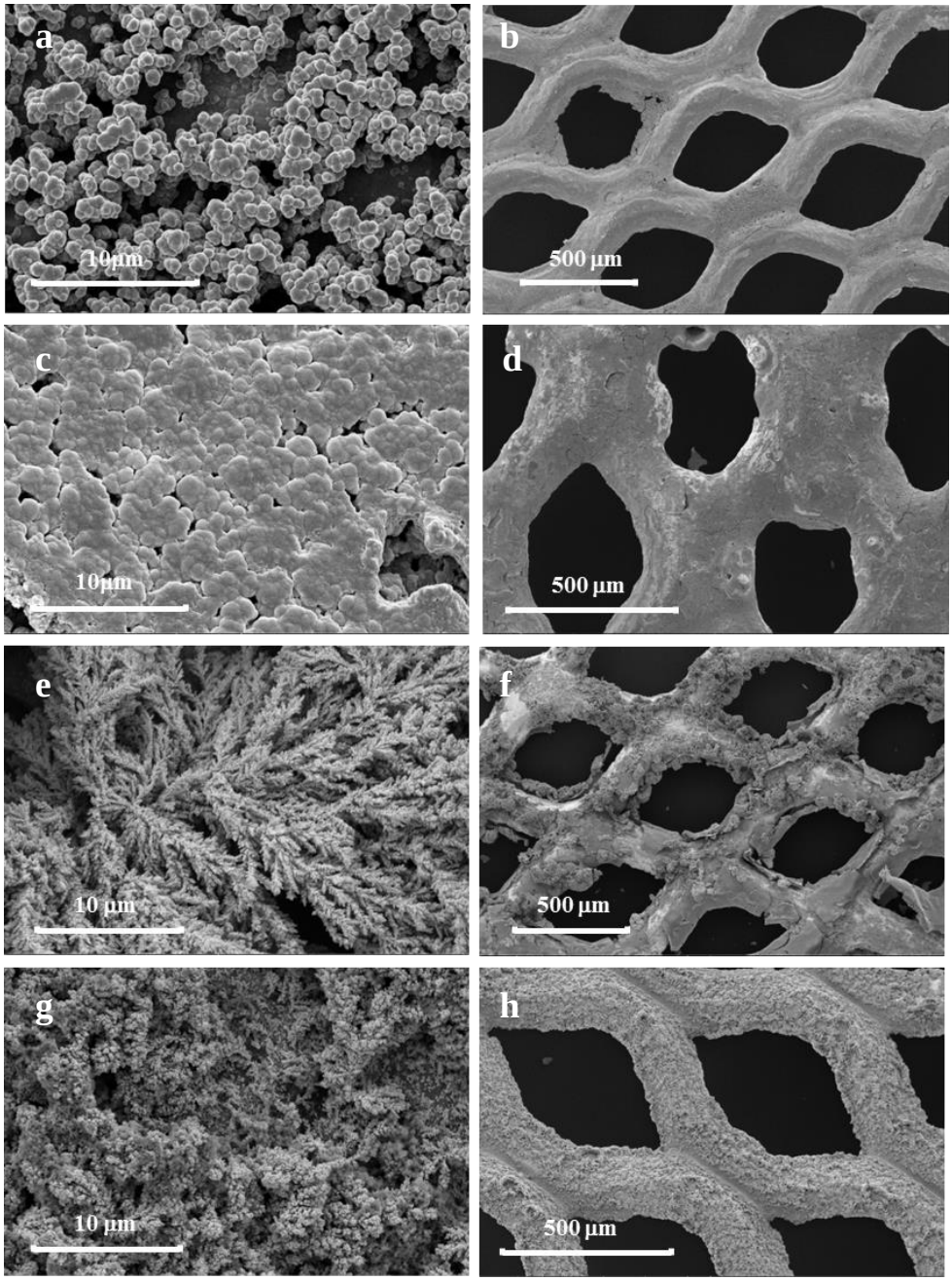

Figure 6.4 SEM micrographs of SS mesh coated with **(a, b)** Co_3O_4; **(c, d)** $NiCo_2O_4$; **(e, f)** $Ni(OH)_2$; **(g,h)** Ni-$Fe(OH)_2$ at high and low magnifications respectively.

The Co_3O_4 catalyst coating on the surface of the SS mesh in **Figure 6.4 a & b** is composed of loosely packed clusters of small spherical particles of average diameter ~0.8 μm. Larger clusters of the spinel oxide appear to be more present at the edges of the apertures of the SS mesh and at the bonds where the strands intersect. In contrast, the $NiCo_2O_4$ catalyst coating in **Figure 6.4 c** consists of tightly packed layers of particles with uniform coverage of the SS mesh surface. Lower magnification

micrographs in **Figure 6.4 d** of the mesh indicate that some of the apertures of the SS mesh are considerably reduced in size due to the thickness of the $NiCo_2O_4$ catalyst layer. The $Ni(OH)_2$ catalyst layer is observed to be dendritic (**Figure 6.4 e**) with branches as long as 10 µm and the overall coating of catalyst on the SS mesh in **Figure 6.4 f** is uneven as some areas of the mesh are covered in thicker layers of catalyst. Several fragments of the catalyst layer also appear to be flaking off the SS substrate indicating poor adhesion. The Ni-$Fe(OH)_2$ catalyst layer in **Figure 6.4 h** appears to be constructed of shorter branches of dendritic $Ni(OH)_2$ mixed with spherical particles of a different morphology most likely an Fe based oxide or hydroxide which was simultaneously electrodeposited. The addition of Fe into the electrodeposition solution appears to control the thickness of the catalyst layer across the SS substrate and help improve the distribution of catalyst across the surface such that the apertures of the mesh are not reduced in size.

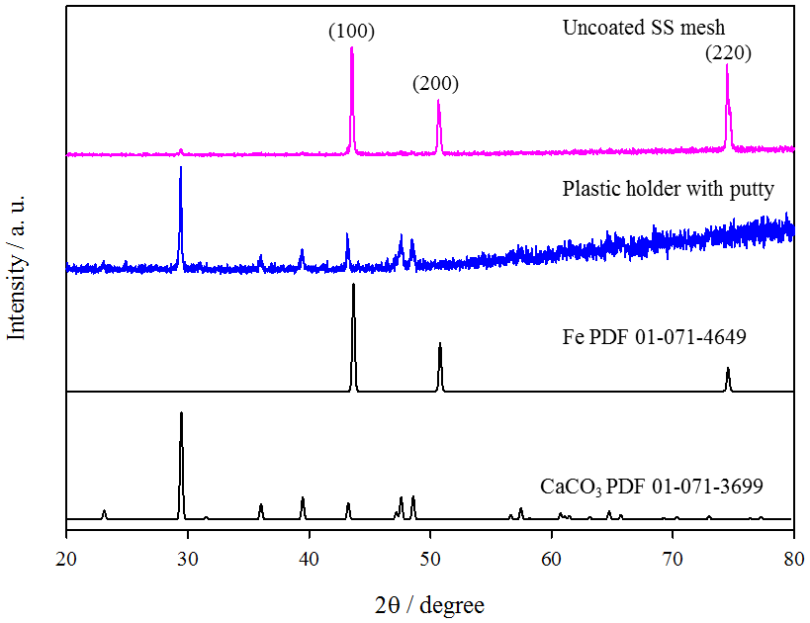

Figure 6.5 XRD diffractograms of uncoated SS mesh and the plastic sample holder with putty.

The crystal structures and chemical compositions of the various catalyst coated electrodes are obtained via X-ray diffraction as displayed in **Figure 6.5 and 6.6**. The structural parameters of the diffractograms are summarised in **Table 6.1**. Since the samples were secured in the sample holder with a small amount of putty, a diffractogram of the plastic holder with putty was obtained for comparison. From the graph in **Figure 6.5**, trigonal $CaCO_3$ (PDF 01-071-3699) was identified to be present

as a particulate filler in the putty and the most intense peak at 29.5 º is seen in the diffractogram of uncoated stainless steel mesh. The peaks in the diffractogram of uncoated stainless steel mesh match the standard pattern of cubic Fe (PDF 01-071-4649) and the (100), (200) and (220) peaks are observed in all subsequent diffractograms. These peaks can therefore be disregarded in the following diffractograms.

Table 6.1 Summary of XRD structures of the diffractograms in Figure 6.5 and 6.6.

Sample	**Crystal system**	**Space group**	**Lattice constant / Å**	**Cell volume / Å^3**
$CaCo_3$	Trigonal	R-3cH	a=b=4.99, c =17.1	368.07
Fe metal	Cubic	Fm-3m	a=b=c=3.61	47.05
Co_3O_4	Cubic	Fd-3m S	a=b=c=8.07	525.56
$NiCo_2O_4$	Cubic	Fd-3m Z	a=b=c=8.11	533.41
Ni metal	Cubic	Fm-3m	a=b=c=3.54	44.36

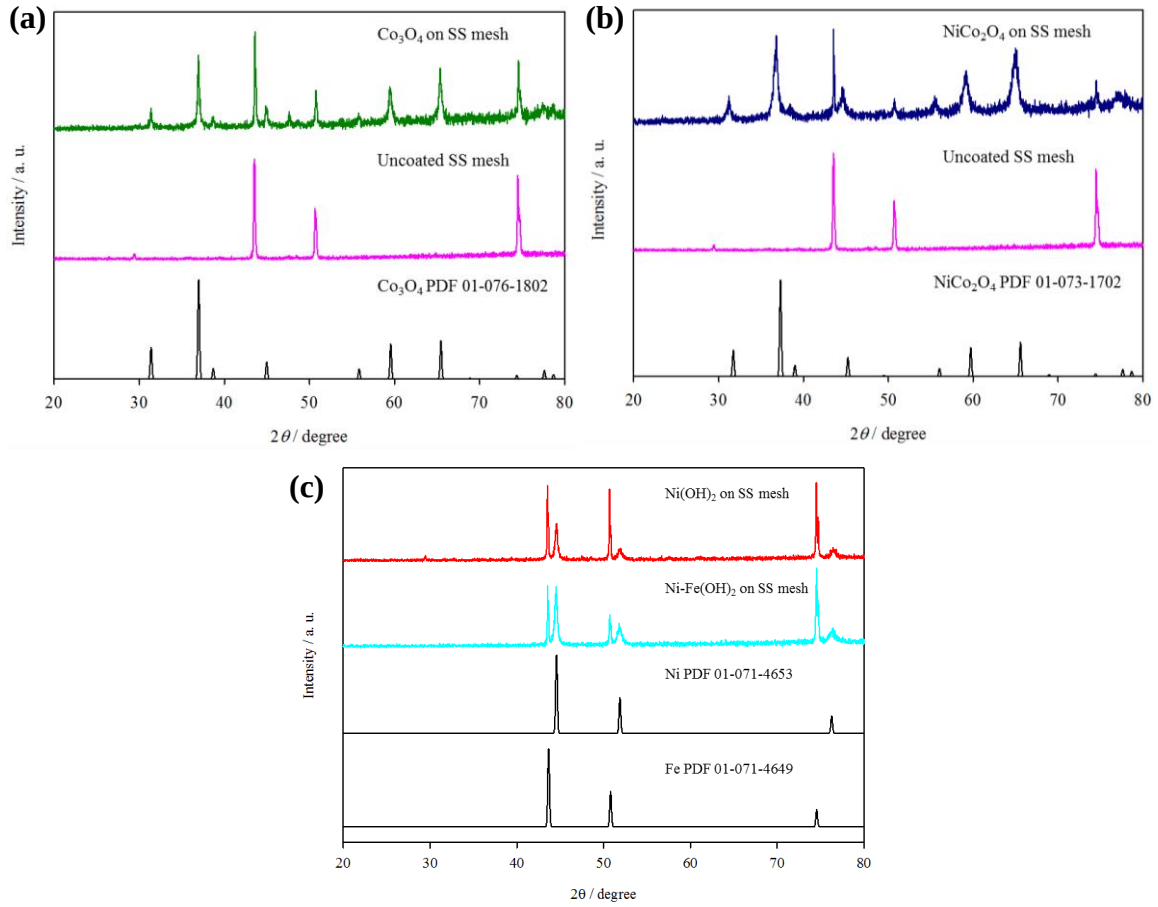

Figure 6.6 XRD diffractograms of SS mesh coated with **a)** Co_3O_4, **b)** $NiCo_2O_4$, **c)** $Ni(OH)_2$ and $Ni\text{-}Fe(OH)_2$.

From the diffractogram of spinels Co_3O_4 and $NiCo_2O_4$ coated on stainless steel mesh, it can be seen clearly that the peaks are sharp and intense indicating the crystallinity of these materials. The peaks of these diffractograms match standard patterns for cubic Co_3O_4 (PDF 01-076-1802) and cubic $NiCo_2O_4$ (PDF 01-073-1702) as illustrated. In the diffractograms of $Ni(OH)_2$ and Ni-$Fe(OH)_2$, both have peaks which match the standard pattern for cubic Ni metal (PDF 01-071-4653), but the lack of appearance of other peaks is likely due to the amorphous nature of the Fe hydroxide and this has been investigated further and discussed in Chapter 7. The greater intensity of the Ni peaks in the diffractogram of Ni-$Fe(OH)_2$ compared to the same peaks in the diffractogram of $Ni(OH)_2$, can be attributed to the better coverage of the SS mesh by the deposited Ni-$Fe(OH)_2$ catalyst layer.

6.2.2. Electrochemical characterisation of catalyst samples

The interconversion of Ni ion species was introduced by Bode [3] for nickel oxy/ hydroxide electrodes. All species or phases are non-stoichoimetric with different ranges of oxidation states and one phase can be easily converted to another by charging or discharging at different potentials. The presence of certain Ni oxide phases indicate more active species are available for oxygen evolution reaction which has been shown by more than one study to be true. A labelled voltammogram of Ni-based oxidation is presented in **Figure 6.7** and a brief description of each stage is given below.

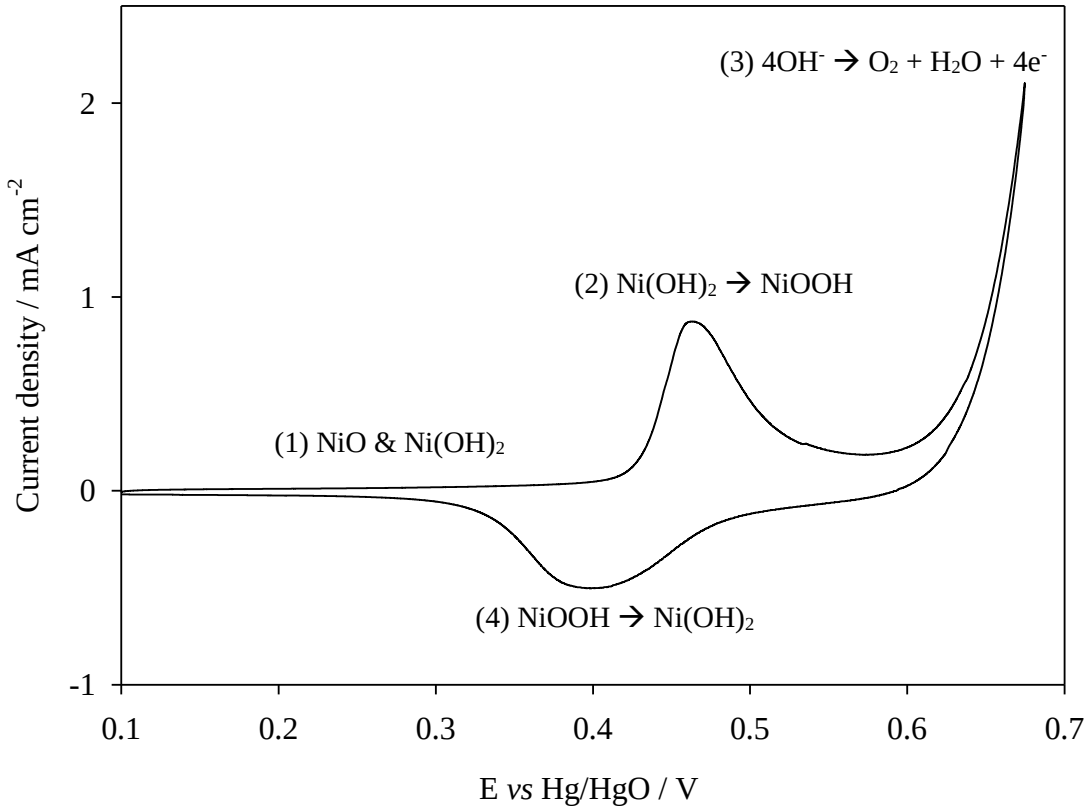

Figure 6.7 Labelled cyclic voltammogram of Ni mesh cycled at scan rate of 50 mV s^{-1} between 0.1 and 0.675 V (*vs* Hg/HgO) in 1 M NaOH at 295 K.

(1) The Ni electrode upon contact with alkaline solution forms NiO or mildly soluble $Ni(OH)_2$ phase, since the two reactions take place at roughly the same potentials, they are both favourable thermodynamically [4]. Some studies mention the spontaneous passivation of nickel forms an NiO layer and then $Ni(OH)_2$ layers are formed on top of this layer [5, 6]. These layers give the Ni electrode an open circuit potential of ~0.3 V.

(2) Upon cycling in an anodic direction, the first anodic peak at ~0.47 V indicates the oxidation of Ni^{2+} surface species to Ni^{3+}. This species of NiOOH is referred to as β-NiOOH [7-9] and is suggested to be the desired species for oxygen evolution, providing active sites for the reaction to occur at.

(3) The second anodic peak is found between 0.6 and 0.7 V and indicates the evolution of oxygen. It is suggested that the Ni species at this stage consists of a mixture of NiO_2 and NiOOH compounds and the composition of this mixture is dependent on the electrolyte used. The Ni^{4+} species is inactive for the oxygen evolution reaction.

(4) On the return sweep in the cathodic direction, the reduction of NiOOH to $Ni(OH)_2$ takes place leading up to the cathodic peak at ~0.4 V. Further reduction continues past 0.4 V until only $Ni(OH)_2$ is present again.

Cyclic voltammograms of the various catalyst coated SS mesh were carried out at 100 mV s^{-1} between oxidising potentials of 0.1 and 0.7 V. The current values recorded were normalised against both geometrical electrode area (**Figure 6.8 a**) as well as catalyst mass or loading (**Figure 6.8 b**) as the electrodes were not evenly coated with the same amount of catalyst due to the different methods of preparation. This was to ensure a better representation of the catalysts performance since normalising the current value solely against electrode geometrical area is not likely to be accurate enough especially for three dimensional electrodes [10].

From the results, all catalyst coated SS mesh appear to be more active for OER compared to uncoated SS mesh. In both graphs, the Ni-$Fe(OH)_2$ catalyst displayed the earliest onset potential for OER even though the OER peak currents of the plots differed in magnitude. This was followed by spinel oxide $NiCo_2O_4$, $Ni(OH)_2$ and lastly Co_3O_4. The OER activity of Ni-$Fe(OH)_2$ and $NiCo_2O_4$ appear unchanged regardless of whether the current was normalised against geometric surface area or catalyst mass which indicates that the better performance for OER of Ni-$Fe(OH)_2$ was due to the catalyst's intrinsic activity for the reaction and unlikely a result from a greater surface area or mass of catalyst.

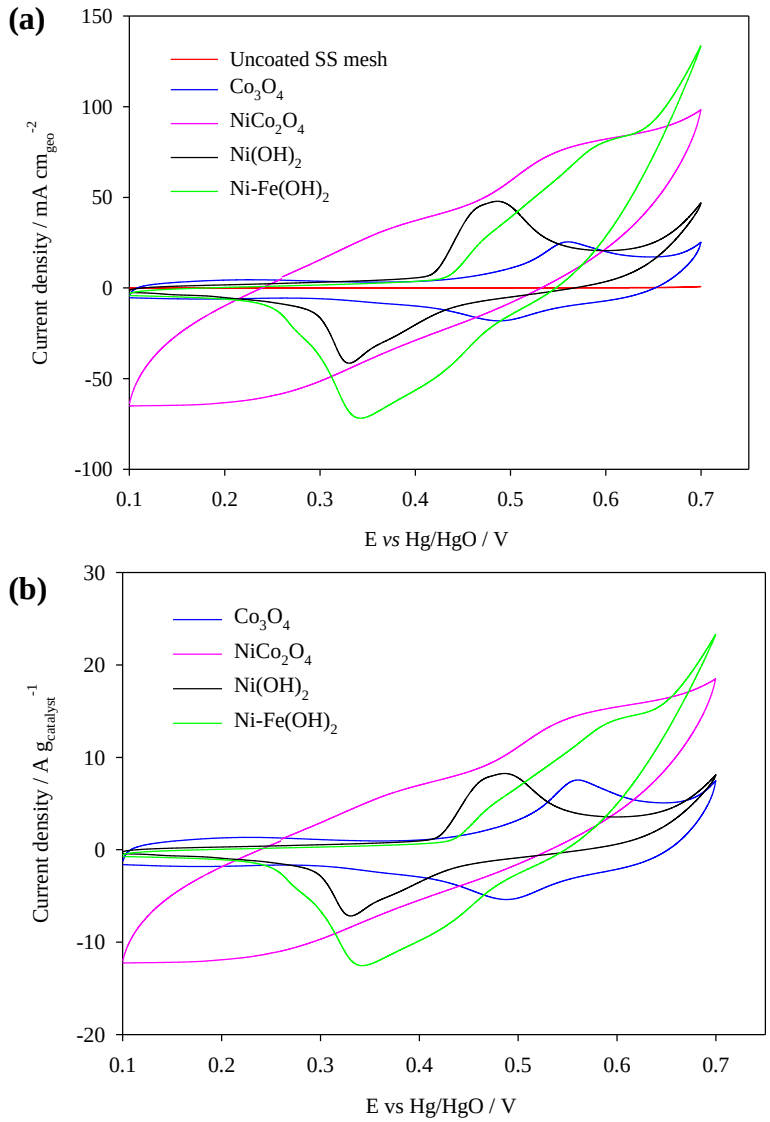

Figure 6.8 Cyclic voltammograms of various catalyst coated SS mesh cycled between 0.1 V and 0.7 V vs Hg/HgO at 100 mV s^{-1} in 1 M NaOH at 295 K plotted against current per **a)** electrode geometric surface area and **b)** mass of catalyst.

From the voltammogram of the Co_3O_4 catalyst film (— blue curve), the anodic peak at 0.56 V and cathodic peak at 0.49 V are related to the $Co^{3+/4+}$ redox couple [11, 12] given in equation (6.3). The broad anodic and cathodic peaks around 0.2 V are expected to be due to the small number of Co^{2+} cations present in tetrahedral sites being oxidised to Co^{3+} [12, 13] as represented by equation (6.4) and the low intensity of these peaks is a result of the higher bonding energy required for oxidation and reduction of $Co^{2+/3+}$ [14].

$$CoOOH + OH^- \leftrightarrow CoO_2 + H_2O + e^- \qquad 0.56\ V\ vs\ Hg/HgO \qquad (6.3)$$

$$CoOOH + e - \leftrightarrow Co_3O_4 + OH^- + H_2O \qquad 0.22\ V\ vs\ Hg/HgO \qquad (6.4)$$

The voltammogram for $NiCo_2O_4$ (— pink curve) in this study is consistent with that of $NiCo_2O_4$ prepared in a similar manner on a Ni substrate by thermal decomposition of nitrates dissolved in ethanol [15]. The broad anodic peaks at 0.37 V can be assigned to the $Co^{2+/3+}$ and $Ni^{2+/3+}$ couples based on equations (6.4) and (6.5). The second anodic peak at 0.54 V can be related to $Co^{3+/4+}$ and $Ni^{3+/4+}$ redox couples [16, 17] represented by equations (6.3) and (6.6) respectively whilst the broad cathodic peak at 0.3 V is due to the reduction of Ni^{4+} and Co^{4+}.

$$2Ni_3O_4 + 2OH^- \leftrightarrow 3Ni_2O_3 + H_2O + 2e^- \quad 0.37\ V\ vs\ Hg/HgO \quad (6.5)$$

$$NiOOH + OH^- \leftrightarrow NiO_2 + H_2O + e^- \quad 0.50\ V\ vs\ Hg/HgO \quad (6.6)$$

The shape of the voltammogram for $Ni(OH)_2$ (— black curve) is similar to the voltammogram for Ni mesh described in **Figure 6.7**. However, the broad anodic peak seen at 0.48 V is likely to consist of two forms of $Ni(OH)_2$, the hydrated α-phase and the unhydrated β-phase [3]. From literature, the β-phase is observed to be more active for the oxygen evolution reaction compared to the α-phase as the β/β oxidation cycle occurs at more positive potentials than the α/γ cycle. The Bode plot in **Figure 6.9** illustrates the transition of Ni^{2+} to Ni^{3+} seen in equation (6.7) and indicates that aging or dehydration of the α-phase gives the desirable stable β-phase. This reaction occurs around the same oxidative potentials as the oxygen evolution reaction given in equation (6.2) [18].

$$Ni(OH)_2 + OH^- \rightarrow NiOOH + H_2O + e^- \quad 0.39\ V\ vs\ Hg/HgO \quad (6.7)$$

The presence of two phases of NiOOH is more obvious in the overlapping cathodic peaks at 0.33 V and 0.37 V which are typically related to the β/β cycle and α/γ cycle respectively.

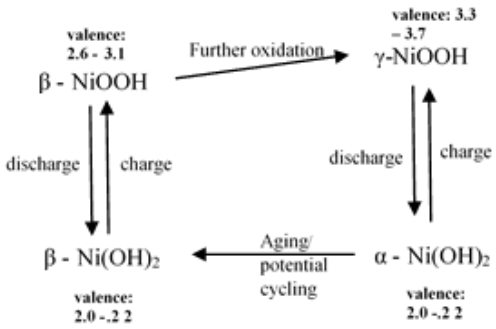

Figure 6.9 Bode plot for Ni^{2+} to Ni^{3+} redox transition [18].

Finally, in the voltammogram of Ni-Fe(OH)$_2$ (— green curve) the addition of Fe appears to cause a shift in the anodic peak for redox couple $Ni^{2+}/^{3+}$ to more positive potentials of ~0.59 V, likely due to the oxidation of Fe^{3+}, and a decrease in OER onset potential is observed to coincide with this peak [19]. This decrease in OER overpotential is suggested to be a result of the stabilisation of an intermediate in the rate determining step from the substitution of Ni^{3+} with Fe^{3+} in NiOOH [20, 21]

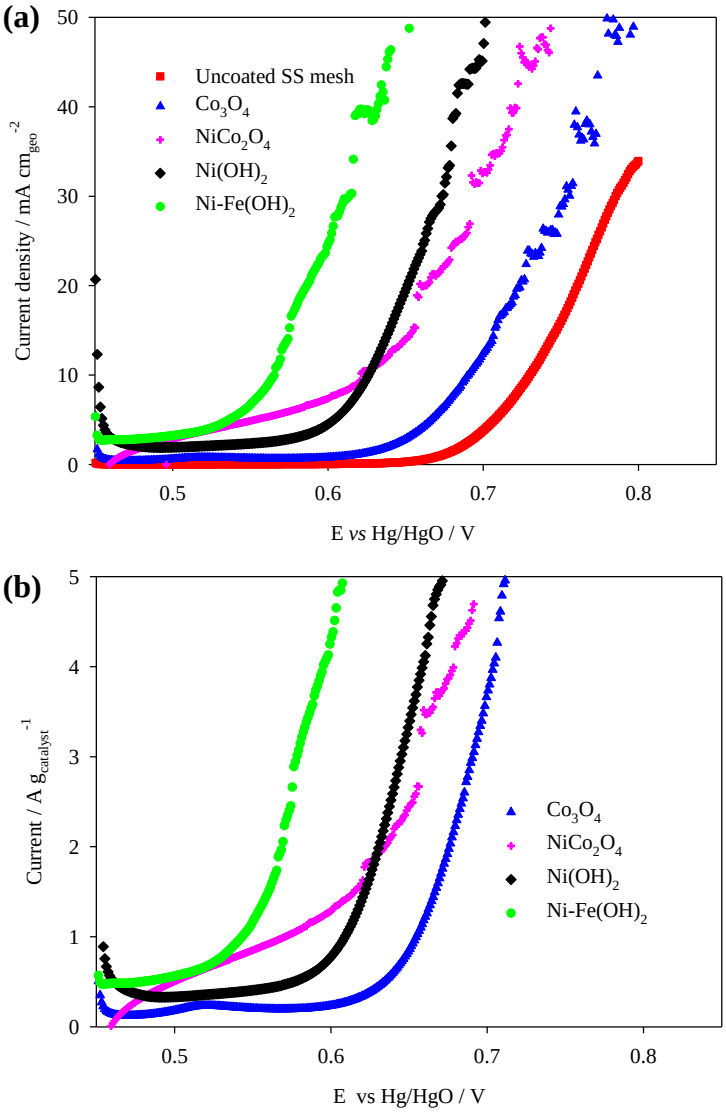

Figure 6.10 Slow scan voltammograms of various OER catalysts swept between 0.45 and 0.8 V vs Hg/HgO at 1 mV s^{-1} in 1 M NaOH at 295 K plotted against current per **a)** electrode geometric surface area and **b)** mass of catalyst.

Additional slow scan anodic polarisations at 1 mV s^{-1} (**Figure 6.10**) were carried out on the catalyst films under the same conditions and plotted against current normalised against geometric surface area and mass of catalyst. A low scan rate was selected to increase accuracy as holding the potentials for a slightly longer period of

time helps to ensure that steady current values can be obtained. Overall, the results of the slow scan voltammograms match that of the cyclic voltammograms with Ni-$Fe(OH)_2$ displaying the lowest overpotential for OER of 262 mV at 10 mA cm_{geo}^{-2} and 265 mV at 2 A $g_{catalyst}^{-1}$ (**Table 6.2**). At low current densities, the spinel $NiCo_2O_4$ initially displays a lower onset potential for OER than $Ni(OH)_2$ however at higher current densities, the overpotential for OER is greater for $NiCo_2O_4$ than $Ni(OH)_2$. The noise observed at higher overpotentials is due to the evolution of oxygen gas bubbles on the surface of the electrodes, masking the active area available. The growth of bubbles at the surface of the electrode affects the voltage of the cell by increasing ohmic resistance and hence overpotential of the reaction, and the release of bubbles from the electrode surface also creates turbulence in the electrode boundary layer which affects heat and mass transfer [22].

Table 6.2 Comparison of catalyst composition on OER activity in 1 M NaOH, 295 K.

Sample	**Overpotential at 10 mA cm_{geo}^{-2} / mV**	**Tafel slope/ mV dec^{-1}**	**Overpotential at 2 A $g_{catalyst}^{-1}$ / mV**	**Tafel slope/ mV dec^{-1}**
Uncoated SS mesh	430	45	-	-
Co_3O_4	391	68	371	69
$NiCo_2O_4$	323	-	331	-
$Ni(OH)_2$	325	71	328	74
Ni-$Fe(OH)_2$	262	64	265	69

The overpotentials from the slow scan voltammograms and corresponding Tafel slope values are summarised in **Table 6.2**. In both log *j* vs potential graphs presented in **Figure 6.11** there is no linear region in the plots for $NiCo_2O_4$ catalyst layer for the Tafel equation to be fitted against possibly because a charge transfer process does not control the reaction rate of OER [23]. The Tafel slope value of uncoated SS mesh is in agreement with previously recorded Tafel slope values 45- 48 mV dec^{-1} for Fe electrode [24]. This value of ca. 40 mV dec^{-1} suggests that the second electron transfer step is the rate determining step.

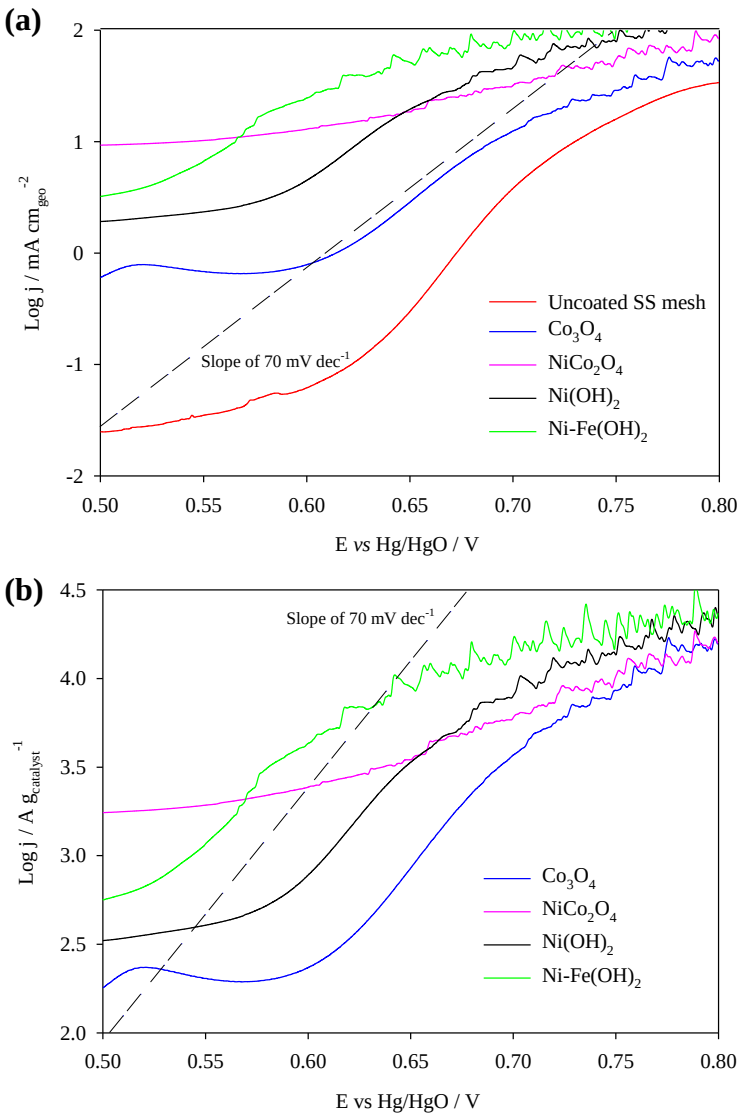

Figure 6.11 Tafel slope plots of various OER catalysts at low overpotentials in 1 M NaOH at 295 K for current per **a)** electrode geometric surface area and **b)** mass of catalyst.

The Tafel slope values of Co_3O_4, $Ni(OH)_2$ and Ni-Fe$(OH)_2$ presented in **Table 6.2** are in the range of 60 to 75 mV dec^{-1}. Tafel slope values of ca. 60 mV dec^{-1} indicate that a chemical step, for instance the chemical decomposition of OH^- radicals which are adsorbed to the surface, is the rate determining step. However these slope values are greater than values reported elsewhere for these catalysts, which is suggested to be due to greater resistances at the electrolyte/ electrode interface. The Tafel equation normally only takes into account the overpotential from charge transfer and assumes that the cation is able to move away from the reaction interface once dissolved [25]. However mass transfer and double layer effects which are normally assumed to be

negligible for the Tafel equation are more significant in this case especially for catalyst layers coated on a three dimensional electrode substrate.

6.2.3. Electrode stability test

The stability of spinel oxide $NiCo_2O_4$ and Ni-$Fe(OH)_2$ on SS mesh were evaluated for OER performance at 500 mA cm^{-2} over a period of 3.5 h (**Figure 6.12**). An uncoated Ni mesh was used as the cathode in the experiments.

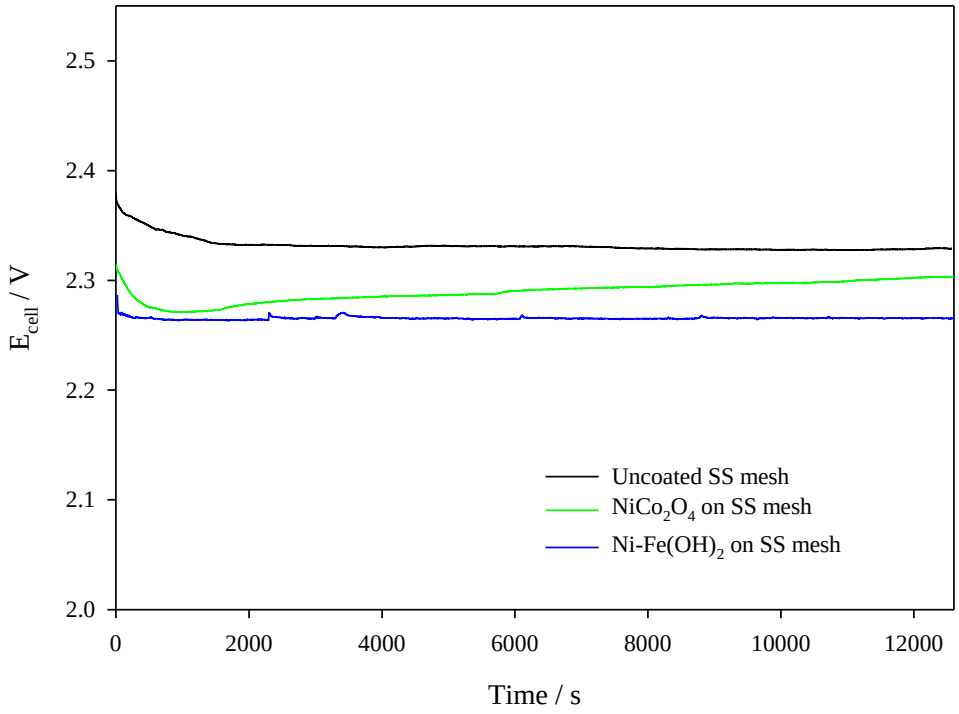

Figure 6.12 Cell voltage of alkaline water electrolyser over a period of 3.5 h at 0.5 A cm^{-2} of different catalyst coated SS mesh anodes and expanded Ni mesh as cathode pressed up against Tokuyama A201 hydroxide anion exchange membrane in 4 M NaOH at 333 K, 250 mL min^{-1} pump rate.

Over the duration of the experiment, both catalyst coated electrodes presented lower overpotentials compared to that of uncoated SS. The performance of the $NiCo_2O_4$ catalyst was observed to improve over the first half an hour before gradually degrading as seen from the increase in cell voltage over time. This was perhaps due to the weaker attachment of the catalyst to the SS mesh as catalyst particles were observed to collect in the electrolyte reservoir over time. The recirculation of electrolyte through the electrolyser and evolution of oxygen could have removed the catalyst from the surface of the mesh, which will be examined in the future by weighing the mass of

the mesh, and/ or collecting SEM micrographs, before and after testing. In contrast, the electrodeposited Ni-Fe$(OH)_2$ catalyst on SS mesh displayed consistent performance and high activity for OER over the same period of time indicating its stability and potential for further optimisation.

6.3. Conclusion

In this chapter, spinel oxide catalysts were prepared with a thermal decomposition method and coated onto stainless steel mesh via a dip-coating process; and hydroxide catalysts were synthesised via an electrodeposition method directly onto stainless steel mesh. SEM characterisation revealed the microstructures of the catalyst layers and coverage of the mesh samples. XRD characterisation confirmed the presence of cubic Co_3O_4 and $NiCo_2O_4$ catalyst layers whilst the shape of the cyclic voltammograms confirmed the presence of $Ni(OH)_2$ and Ni-Fe$(OH)_2$ catalyst layers.

The activity of these electrodes for oxygen evolution were compared and evaluated with slow scan anodic polarisation under similar conditions. The Ni-Fe$(OH)_2$ catalyst coated SS mesh displayed the highest OER activity with lowest overpotentials for both current normalised against geometric surface area and current normalised against mass of catalyst plots. Due to the higher resistance at the electrolyte/ electrode interfaces of the catalyst coated SS mesh, the Tafel slope values for Co_3O_4, $Ni(OH)_2$ and Ni-Fe$(OH)_2$ were greater than expected. Preliminary stability tests in a water electrolyser set-up verified the Ni-Fe hydroxide catalyst's durability when held at anodic potentials over an extended period of time and potential for further optimisation.

6.4. References

1. D.P. Lapham, A.C.C. Tseung, The effect of firing temperature, preparation technique and composition on the electrical properties of the nickel cobalt oxide series $Ni_xCo_{1-x}O_y$, J. Mater. Chem. Sci. 39 (2004) 251-64.
2. M.E.G. Lyons, M.P. Brandon, The oxygen evolution reaction on passive oxide covered transition metal electrodes in aqueous alkaline solution. Part 1-Nickel Int. J. Electrochem. Sci. 3 (2008) 1386-424.
3. H. Bode, K. Dehmelt, J. Witte, Zur kenntnis der nickelhydroxidelektrode—I.Über das nickel (II)-hydroxidhydrat, Electrochim. Acta 11 (1966) 1079-87.
4. K. Juodkazis, J. Juodkazytė, R. Vilkauskaitė, V. Jasulaitienė, Nickel surface anodic oxidation and electrocatalysis of oxygen evolution, Journal of Solid State Electrochemistry 12 (2008) 1469-479.
5. S.L.Medway, C.A.Lucas, A.Kowal, R.J.Nichols, D.Johnson, In situ studies of the oxidation of nickel electrodes in alkaline solution, J. Electroanal. Chem. 587 (2006) 172-81.
6. L.M.M.d. Souza, F.P. Kong, F.R. McLarnon, R.H. Muller, Spectroscopic ellipsometry study of nickel oxidation in alkaline solution Electrochim. Acta 42 (1997) 1253-67.
7. C. Bocca, A. Barbucci, G. Cerisola, The influence of surface finishing on the electrocatalytic properties of nickel for the oxygen evolution reaction (OER) in alkaline solution, Int. J. Hydrogen Energy 23 (1998) 247-52.
8. M.E.G. Lyons, M.P. Brandon, The oxygen evolution reaction on passive oxide covered transition metal electrodes in aqueous alkaline solution. Part 1-Nickel, Inter. J. Electrochem. Sci 3 (2008) 1386-424.
9. M.H. Miles, G. Kissel, P.W.T. Lu, S. Srinivasan, Effect of temperature on electrode kinetic parameters for hydrogen and oxygen evolution reactions on nickel electrodes in alkaline solutions, J. Electrochem. Soc. 123 (1976) 332-36.
10. E. Fabbri, A. Habereder, K. Waltar, R. Kötz, T.J. Schmidt, Developments and perspectives of oxide-based catalysts for the oxygen evolution reaction, Catalysis Science and Technology 4 (2014) 3800-3821.
11. I. Barauskienė, E. Valatka, Synthesis, structure and capacitive properties of cobalt hydroxide films on stainless steel substrates, Cent. Eur. J. Chem. 12 (2014) 1206-11.
12. P. Nkeng, G. Poillerat, J.F. Koenig, P. Charfier, B. Lefez, J. Lopitaux, M. Lenglet, Characterization of spinel-type cobalt and nickel oxide thin films by x-ray near grazing diffraction, transmission and reflectance spectroscopies, and cyclic voltammetry, J. Electrochem. Soc. 142 (1995) 1777-83.
13. E. Zhang, Y. Xie, S. Cia, J. Jia, Z. Wen, Porous Co_3O_4 hollow nanododecahedra for nonenzymatic glucose biosensor and biofuel cell, Biosensors and Bioelectronics 81 (2016) 46-53.
14. I.D. Belova, Y.E. Roginskaya, R.R. Shifrina, S.G. Gagarin, Y.V. Plekhanov, Y.N. Venevtsev, Co (III) ions high-spin configuration in nonstoichiometric Co_3O_4 films, Solid State Commun. 47 (1983) 577-84.
15. E.B. Castro, C.A. Gervasi, Electrodeposited Ni–Co-oxide electrodes: characterization and kinetics of the oxygen evolution reaction, Int. J. Hydrogen Energy 25 (2000) 1163-70.
16. D. Baronetto, I.M. Kodintsev, S. Trasatti, Origin of ohmic losses at Co_3O_4/Ti electrodes, J. Appl. Electrochem. 24 (1994) 189-94.
17. P. Rasiyah, A.C.C. Tseung, D.B. Hibbert, A mechanistic study of oxygen evolution on $NiCo_2O_4$, J. Electrochem. Soc. 129 (1982) 1724-7.
18. A.J. Bard, R. Parsons, J. Jordan, Standard Potentials in Aqueous Solutions, ed. M. Dekker. 1985, New York
19. D.A. Corrigan, R.M. Bendert, Effect of coprecipitated metal ions on the electrochemistry of nickel hydroxide thin films: cyclic voltammetry in 1M KOH J. Electrochem. Soc. 136 (1989) 723-728.

20. H. Shin, H. Xiao, I. William A. Goddard, In silico discovery of new dopants for Fe-doped Ni oxyhydroxide ($Ni_{1-x}Fe_xOOH$) catalysts for oxygen evolution reaction, J. Am. Chem. Soc. 140 (2018) 6745-48.
21. D. Friebel, M.W. Louie, M. Bajdich, K.E. Sanwald, Y. Cai, A.M. Wise, M.-J. Cheng, D. Sokaras, T.-C. Weng, R. Alonso-Mori, R.C. Davis, J.R. Bargar, J.K. Nørskov, A. Nilsson, A.T. Bell, Identification of highly active Fe sites in (Ni,Fe)OOH for electrocatalytic water splitting, J. Am. Chem. Soc. 137 (2015) 1305-13.
22. J. Eigeldinger, H. Vogt, The bubble coverage of gas-evolving electrodes in a flowing electrolyte, Electrochim. Acta 45 (2000) 4449-56.
23. G. Kear, F.C. Walsh, The characteristics of a true tafel slope, Corro. Mater. 30 (2005) 51-5.
24. M.E.G. Lyons, M.P. Brandon, A comparative study of the oxygen evolution reaction on oxidised nickel, cobalt and iron electrodes in base, J. Electroanal. Chem. 641 (2010) 119-30.
25. R.L. Doyle, M.E.G. Lyons, Photoelectrochemical Solar Fuel Production: From Basic Principles to Advanced Devices,S. Giménez, J. Bisquert (ed), Springer, 2016

Chapter 7 Optimisation and Characterisation of Selected OER Catalyst

Based on the results of the previous chapter, this chapter focuses on the characterisation and optimisation of various transition metal hydroxide catalysts for OER performance. The synergism of multiple first row transition metals with various oxidation states is proposed to enhance the catalyst's OER activity. In this chapter, a unique microelectrode set-up was used to prepare different compositions of unary, binary and ternary metal hydroxide catalysts by cathodic electrodeposition and test their performance at high current densities > 1 A cm^{-2}. In addition, the effects of changing the electrodeposition parameters on the OER catalytic performance, was investigated and discussed in detail. Lastly, the stability of the optimal Ni-Fe-Co hydroxide catalyst was assessed in a zero-gap alkaline water electrolyser.

7.1. Experimental section

7.1.1 Synthesis of metal hydroxide catalysts

Table 7.1 Table of chemicals, and their respective suppliers, used for the synthesis of catalysts.

Material	Supplier
Nickel (II) sulfate hexahydrate, $NiSO_4.6H_2O$ (≥98%)	Sigma-Aldrich
Iron (II) sulfate heptahydrate, $FeSO_4.7H_2O$ (≥99%)	Sigma Aldrich
Chromium (III) sulfate hydrate $Cr(SO_4)_3.xH_2O$	Sigma Aldrich
Cobalt (II) sulfate heptahydrate, $CoSO_4.7H_2O$ (98%)	Alfa Aesar
Ammonium molybdate tetrahydrate, $(NH_4)_6Mo_7O_{24}.4H_2O$ (99%)	Alfa Aesar
Ammonium sulfate, $(NH_4)_2SO_4$ (≥99%)	Sigma Aldrich

The chemicals listed in **Table 7.1** were used to prepare aqueous electrodeposition solutions of 18 mM binary (i.e. Ni-Fe, Ni-Co, Ni-Cr, Ni-Mo) and ternary (i.e. Ni-Fe-Co, Ni-Fe-Cr and Ni-Fe-Mo) metal salts for catalyst synthesis. The cathodic deposition of the various metal hydroxides was conducted under galvanostatic control using current densities of 100-500 mA cm^{-2} for deposition times

of 60 to 300 s at pH between 2 and 6 and temperatures of 22-70 ºC. Standard deposition parameters used were cathodic current density of 200 mA cm^{-2} for 120 s at ambient temperature unless otherwise mentioned. The stainless steel microdisc electrode was fabricated by sealing a stainless steel wire (Goodfellow, purity 99.0 %, ⌀ = 25 µm) in glass to give an exposed area of ≈ 5 x 10^{-6} cm^2. The microelectrode tip was polished with 1.0 µm and 0.05 µm alumina slurry (MicroPolish, Buehlar) consecutively on Microcloth (Buehlar) followed by sonicating in deionised H_2O for ~15 mins between each run.

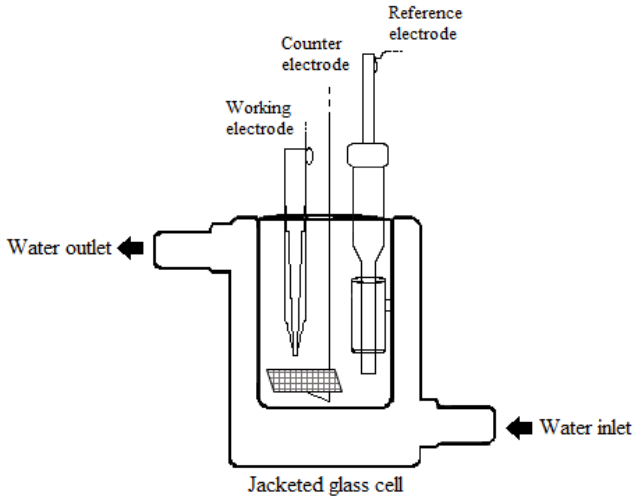

Figure 7.1 Labelled cross section of custom-made jacketed glass cell for rapid catalyst synthesis via cathodic electrodeposition.

The glass cell (~20 cm^3) used for catalyst synthesis via three electrode cathodic electrodeposition is shown in **Figure 7.1**. An inbuilt water jacket allowed the temperature of the cell environment to be controlled using a recirculating water bath (TC120, Grant) and the volume and shape of the cell were designed to minimise material waste and permit quick electrolyte changeover for rapid catalyst synthesis. A polymer lid (not pictured here) and inbuilt glass holder held the working, counter and reference electrodes at a fixed distance from each other. Pt mesh and in-house manufactured Hg/ HgO in 1 M NaOH were used as counter and reference electrodes respectively. The working electrode was positioned at a distance of 3 mm from the counter electrode whilst the reference electrode was kept at a distance of 18 mm from the working electrode.

7.1.2. Physical characterisation

The surface morphology of the catalyst samples were characterised with a SEM-EDX (FEI Quanta 650 FEG) operated at accelerating voltage 5 kV. TEM analysis was conducted with a JEM-2100 LaB6 at an accelerating voltage of 200 kV and catalyst samples were directly deposited onto 3.05 mm diameter Cu grid of 100 square mesh (AGG2100C, Agar Scientific) for characterisation. The composition of transition metals in the catalyst layers were determined with EDX from samples that were deposited on carbon polymer plate (BMA5, Eisenhuth) with a controlled working area of ~0.126 cm^2. Carbon polymer plate was selected as the electrode substrate material, to allow the composition of the deposit to be determined more accurately. In the same manner, samples were prepared on carbon polymer plate for X-ray photoelectron spectroscopy (XPS, Thermo Fisher, ESCALAB 250Xi) measurements carried out with a monochromatic Al Kα source over energy range of 0 to 1350 eV with pass energy of 30.0 eV, step size of 0.05 eV and X-ray spot size of 500 μm. All spectra were analysed with XPSPEAK 4.1 software and NIST XPS database [1].

7.1.3. Electrochemical characterisation

Electrochemical measurements were carried out with a Bio-logic potentiostat using EC-lab software. After catalyst was deposited on the surface of the microdisc, the microelectrode was removed from the glass cell pictured in **Figure 7.1** and the tip was rinsed several times with deionised H_2O. The microelectrode was then inserted into the bottom of another custom-made glass cell (**Figure 7.2**) of ~25 cm^3 with a screw cap and an O-ring to prevent any leakages.

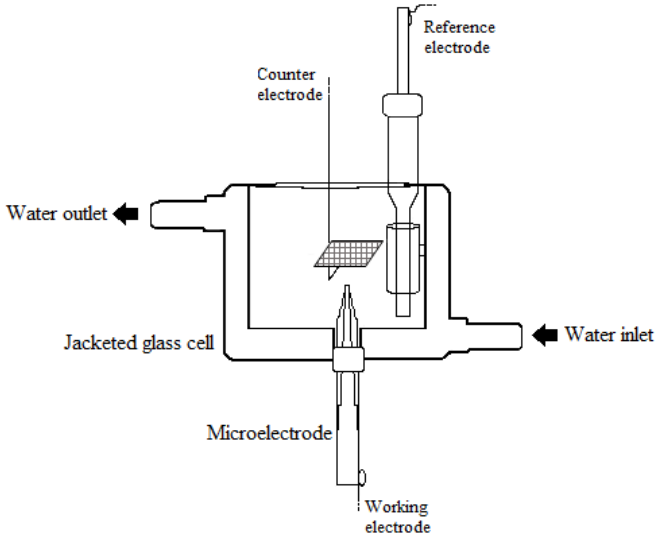

Figure 7.2 Labelled cross section of jacketed glass cell used for screening of catalyst performance.

The microdisc was orientated facing upwards in the cell to help facilitate the release of O_2 bubbles and prevent the build-up of bubbles on the electrode surface. The inbuilt cell jacket was connected to a recirculating water bath which maintained the cell environment at 333 K. A polymer lid (not pictured here) and an in-built glass holder held the Pt mesh counter electrode and in-house manufactured Hg/ HgO in 1 M NaOH reference electrodes in place at a fixed distance from each other and the working electrode. The working electrode a distance of 5 mm from the counter electrode and 7 mm from the reference electrode.

Cyclic voltammograms were obtained in potential range of 0.1 to 0.7 V at scan rate of 100 mV s^{-1} and slow scan linear sweep voltammograms were carried out at anodic potentials of 0.45 to 0.8 V at scan rate of 1 mV s^{-1}. Overpotential values were calculated as described in Section 3.4.1.2, E_{rev} was taken to be 0.303 V vs Hg/ HgO in 1 M NaOH [2]. All experiments were carried out in a static alkaline electrolyte and results were obtained after several scans when a stable response was recorded. The current densities are reported as a function of the geometric surface area of the microelectrode tip.

The optimised catalyst samples were electrodeposited onto SS mesh for further tests in a zero-gap alkaline water electrolyser as described in Chapter 6 to demonstrate preliminary stability for OER. The cell was constructed with an expanded Ni mesh cathode and a catalyst coated expanded SS mesh on either side of a

hydroxide membrane a peristaltic pump helped to pump 4 M NaOH electrolyte at a flow rate of 250 mL min^{-1} through the system and across the face of the mesh electrodes to remove H_2 and O_2 bubbles produced. The cell was run at current density of 0.5 A cm^{-2} over 3.5 h.

7.2. Results and discussion

7.2.1. Cathodic electrodeposition of metal hydroxides

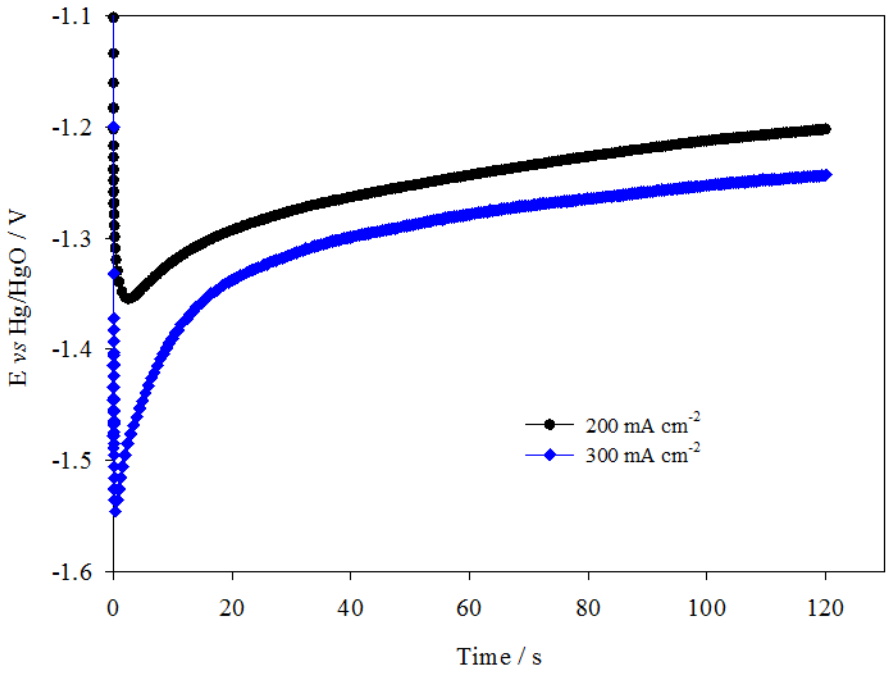

Figure 7.3 Potential versus time plot for the chronopotentiometric electrodeposition from 18 mM nickel sulphate + 25 mM ammonium sulphate at cathodic current densities of 200 mA cm^{-2} and 300 mA cm^{-2} on SS microelectrode over 120 s at room temperature.

Figure 7.3 shows the potential versus time plots for the chronopotentiometric cathodic deposition of 18 mM nickel sulphate + 25 mM ammonium sulphate at 200 mA cm^{-2} and 300 mA cm^{-2} on SS microelectrode over 120 s. This causes the precipitation of insoluble transition metal hydroxides out onto the microdisc surface [3] as described by equation (7.1). Since in this case very high current densities are used, the potential response is usually more negative than the standard reduction potential of water represented by equation (7.2) therefore a small percentage of the current efficiency is lost to the production of H_2.

$$Ni^{2+} + 2OH^- \rightarrow Ni(OH)_2 \quad (7.1)$$

$$2H_2O + 2e^- \rightarrow H_2 + 2OH^- \quad -0.73\ V\ vs\ Hg/HgO \quad (7.2)$$

From the plot of cathodic deposition at 200 mA cm^{-2} in **Figure 7.3**, the potential is observed to dip initially indicating the onset of the reduction reaction and the overpotential observed is due to the nucleation of the nickel hydroxide deposits at the surface of the microdisc. This is then followed by a gradual decrease in the magnitude of potential over time as the surface area increases from the growth in the catalyst layer therefore the current applied per area decreases over time. Since the thickness of the deposit over the microdisc is dependent on the current density at each point on the surface, a uniformly thick deposit is difficult to achieve due to various irregularities across the surface of the microdisc hence polishing of the microdisc between experiments was carried out to reduce this effect. At 300 mA cm^{-2}, the plot has a similar shape to the plot at 200 mA cm^{-2}, however, dip at the beginning is sharper and overpotential is much greater in comparison. This is due to the greater current applied to the conductive microdisc and indicates that the rate of nucleation of the hydroxide deposits increases as well. The effect of changing this parameter on OER performance is discussed in Section 7.2.6.1.

7.2.2. Oxygen evolution on Ni hydroxide catalyst

Cyclic voltammograms of polished stainless steel microelectrode and $Ni(OH)_2$ layer deposited on the SS microelectrode cycled between 0.1 and 0.7 V at 100 mV s^{-1} in 1 M NaOH at 333 K are compared in **Figure 7.4**. On the current density scale of the figure, the features of the voltammogram of uncoated SS microelectrode are indistinct. Whilst in the voltammogram of $Ni(OH)_2$ catalyst layer, a well-formed symmetrical anodic peak at 0.49 V and corresponding cathodic peak at 0.42 V are seen which relates to the surface conversion between $Ni(OH)_2$ and NiOOH [4]. The reaction is described previously by equation (6.7).

The anodic peak at ≥ 0.6 V in both voltammograms indicates the evolution of oxygen. The oxidation of $Ni(OH)_2$ and evolution of O_2 theoretically occur around the same potentials, however, due to the sluggish kinetics of the oxygen evolution reaction, the experimental onset of this reaction usually takes place at more positive potentials. Overall, the presence of $Ni(OH)_2$ catalyst layer on the surface of the microelectrode clearly helps to decrease the overpotential of the oxygen evolution reaction by ~65 mV at 0.1 A cm^{-2} compared to the bare SS microdisc surface.

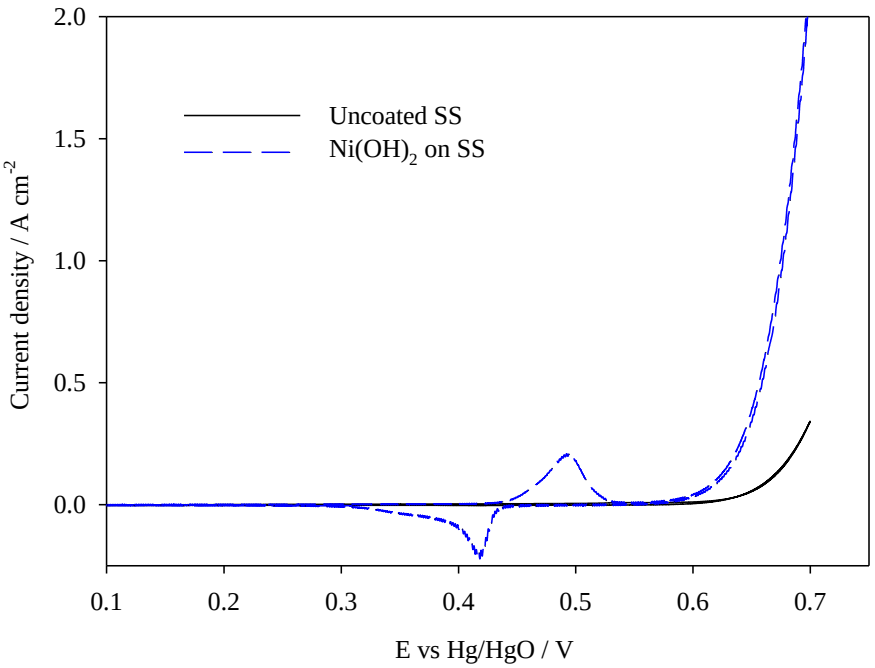

Figure 7.4 Cyclic voltammograms of uncoated stainless steel microelectrode and stainless steel microelectrode with $Ni(OH)_2$ cathodically electrodeposited at 200 mA cm^{-2} for 120 s from 18 mM nickel sulfate solution onto the surface. Cycled between 0.1 and 0.7 V vs Hg/HgO in 1 M NaOH, 333 K at scan rate of 100 mV s^{-1}.

7.2.3. Comparison of unary metal hydroxide catalysts

The linear sweep voltammograms of unary hydroxide catalysts are displayed in **Figure 7.5 a**. From the voltammograms, Ni and Co unary hydroxide are observed to demonstrate the best overall OER performance with lowest overpotentials. At lower current densities, unary Cr hydroxide demonstrates better catalytic performance than Fe and Mo unary hydroxides. However, at current densities greater than 1 A cm^{-2}, the catalytic performance of Fe unary hydroxide surpasses that of Cr unary hydroxide.

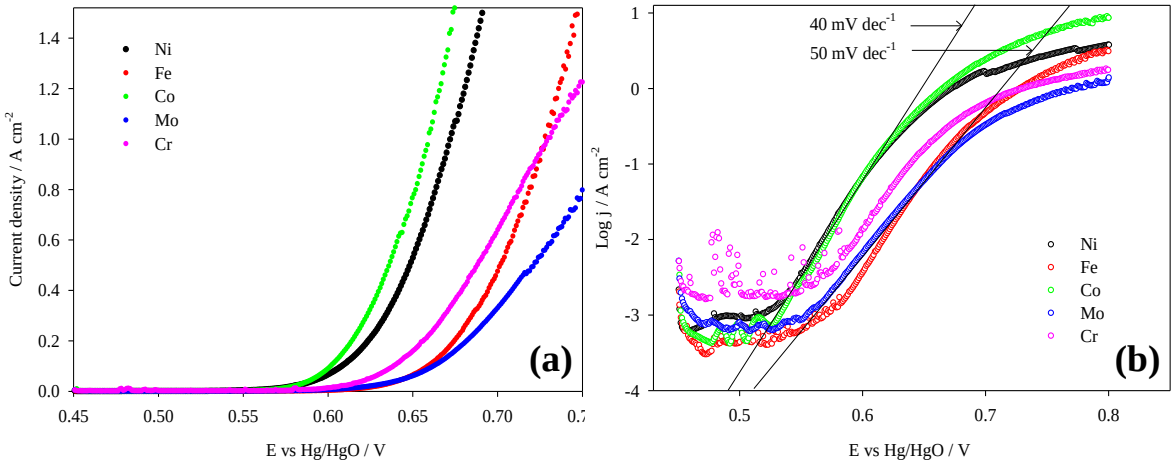

Figure 7.5 a) Linear sweep voltammograms swept at scan rate 1 mV s^{-1} from 0.45 to 0.75 V **b)** Tafel slope plots of unary hydroxide catalysts tested in 1M NaOH, 333 K. All catalysts were cathodically electrodeposited at 200 mA cm^{-2} for 120s on the surface of the stainless steel microelectrode from their respective 18 mM metal sulfate + 25 mM $(NH_4)_2SO_4$ solutions.

From **Figure 7.5 b** the Tafel slopes of unary hydroxides of Ni, Co, Fe and Cr were in the range of 38 to 43 mV dec^{-1} at low overpotentials (**Table 7.2**) which agree well with reported values [5, 6]. Since these values are close to slope value of ~ 39 mV dec^{-1}, this corresponds to an OER mechanism where the second electron transfer step is rate determining. On the contrary, the Tafel slope of Mo unary hydroxide was found to be 50 mV dec^{-1} indicating that the rate determining step for OER at this catalyst is a chemical step[7].

Table 7.2 Overpotentials and Tafel slope values for unary hydroxide catalysts extracted from Figure 7.6.

Unary hydroxide	Overpotential, $\eta_{0.5\ A\ cm^{-2}}$ / mV	Overpotential, $\eta_{0.1\ A\ cm^{-2}}$ / mV	Tafel slope, b / mV dec^{-1}
Ni	348	307	40
Co	335	301	38
Fe	400	357	42
Cr	387	337	43
Mo	420	361	50

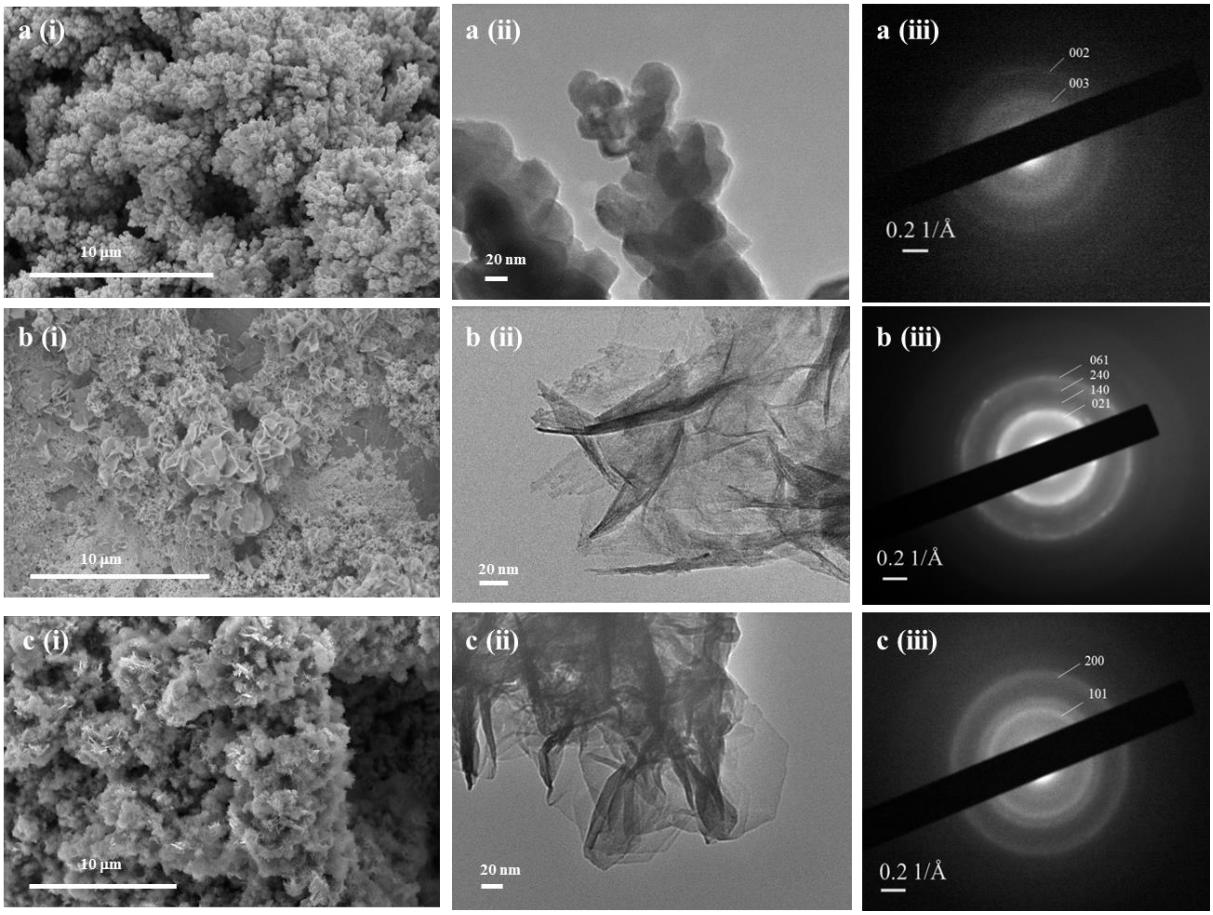

Figure 7.6 i) SEM micrographs (left), **ii)** TEM and **iii)** corresponding diffraction patterns (right) of cathodic depositions from solutions of 18 mM **a)** Ni **b)** Fe and **c)** Co metal sulfate +25 mM $(NH_4)_2SO_4$.

Depositions from unary metal sulfate solutions of Ni, Fe and Co were characterised with SEM and TEM to determine the morphology of the films at micro and nano-scale. XPS was carried out to confirm the presence of metal hydroxides in the films. SEM and TEM micrographs presented in **Figure 7.6 a i** and **ii** reveal the morphology of the sample deposited from Ni sulphate solution to be composed of

interconnected crystals forming clumps of dendritic structures. In **Figure 7.6 b i** and **ii**, micrographs of the deposit from Fe sulphate solution shows densely packed crumpled layers of nanosheets which form flake-like structures on a micro-scale. Finally in **Figure 7.6 c i and ii** of sample deposited from Co sulphate solution, the TEM micrograph displays a nanoflower-like architecture which translates into layers of aggregated nanoflowers at micro-scale The diffraction patterns of these samples are composed of concentric circles which suggest that all three deposits are polycrystalline. However, the diffused rings in diffraction patterns of all samples also indicate the low crystallinity of the deposits. The ring diameters of diffraction pattern **Figure 7.6 a iii** are indexed to the lattice planes of hexagonal $Ni(OH)_2$ (JCPDS 00-002-1112, space group: P-3m1 (164) with lattice constants a = 3.11 and c = 4.66) and rings in **Figure 7.6 b iii** and **c iii** are similarly found to correspond to standard d_{hkl} patterns for orthorhombic FeOOH (COD 9003076, space group: Pbnm (62) with lattice constants a = 4.63, b = 9.99, c = 3.04, a/b =0.463 and c/b =0.304) and hexagonal $Co(OH)_2$ (JCPDS 00-030-0443, space group: P-3m1 (164) with lattice constants a = 3.18 and c = 4.65) respectively.

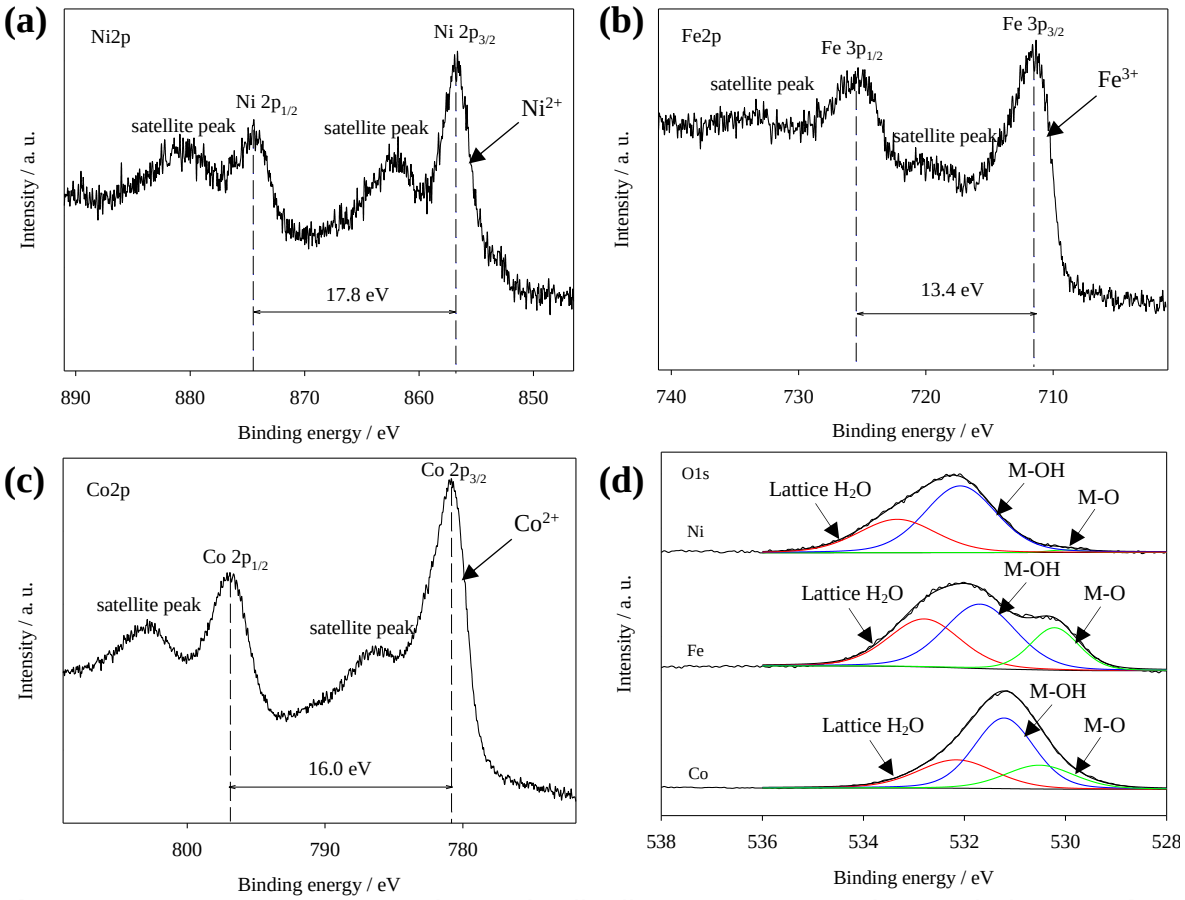

Figure 7.7 XPS M-2p for samples cathodically from 18 mM sulfate solutions of **a)** 100% Ni, **b)** 100% Fe and **c)** 100% Co and **d)** O1s spectra for the various samples. All sulfate solutions contained 25 mM $(NH_4)_2SO_4$.

XPS analysis give further insight into the elements present in these samples as well as their oxidation states. **Figure 7.7 a** shows the spectra for Ni 2p with peaks for p orbitals $2p_{3/2}$ and $2p_{1/2}$ centred at 856.7 eV and 874.5 eV respectively. The spin orbit separation of these two peaks is 17.8 eV which is characteristic of $Ni(OH)_2$ [8]. The O1s spectrum of this sample (**Figure 7.7 d**) was fitted with peaks for lattice H_2O, M-O and M-OH bonds. The peak at binding energy 532 eV is characteristic of the OH^- bound hydroxide group for $Ni(OH)_2$ and peak at ~530 eV is characteristic of O^{2-} of M-O bond for NiO. Overall, the shapes and positions of the Ni 2p and O1s peaks match those of standard XPS spectra for Ni^{2+} [9-12]. The signal areas of M-O and M-OH peaks in the O1s spectra also correspond well to that of NiO and $Ni(OH)_2$ in the Ni2p spectrum confirming that the sample is largely composed of $Ni(OH)_2$.

The Fe 2p spectrum (**Figure 7.7 b**) shows peaks for $Fe2p_{3/2}$ and $Fe2p_{1/2}$ at 711.5 eV and 724.9 eV giving a spin separation of 13.4 eV characteristic of both FeOOH and Fe_2O_3 [13]. The broad satellite peak at ~720 eV in this spectra indicates

that the Fe has an oxidation state of 3 [14] and $BE_{O1s} - BE_{Fe2p3/2}$ = 181.1 eV gives further evidence of the presence of Fe^{3+} [15]. The accompanying O1s spectra (**Figure 7.7 d**) has a peak at 531.6 eV from M-OH of FeOOH and a shoulder peak at 530.2 eV for M-O of Fe_2O_3, consistent for metal oxyhydroxide of Fe^{3+}. Overall, the Fe2p and O1s spectra matches that of FeOOH in the literature [15-18].

The Co 2p spectrum (**Figure 7.7 c**) shows peaks for $Co2p_{3/2}$ and $Co2p_{1/2}$ at binding energies of 781.0 eV and 797.0 eV giving a spin separation of 16.0 eV which is characteristic of $Co(OH)_2$ [19]. The prominent satellite peaks which accompany the Co 2p peaks further indicate that high-spin Co^{2+} species is dominant in the deposit as these satellite peaks are usually weak or absent for low-spin Co^{3+} species [20, 21]. The accompanying O1s spectrum (**Figure 7.7 d**) has a peak at 531.2 eV which is characteristic of the M-OH bond in $Co(OH)_2$ [22, 23]. The signal areas of M-O and M-OH in O1s spectrum correspond well to that of Co2p spectrum confirming that Co^{2+} species is present and the sample is largely composed of $Co(OH)_2$.

7.2.4. Comparison of binary metal hydroxide catalysts

Binary hydroxides of Ni-Fe, Ni-Co, Ni-Mo and Ni-Cr were investigated in the same manner and their overpotentials and Tafel slope values are summarised in **Table 7.3.** The electrodeposition bath compositions used to prepare the catalysts as well as the atomic percentages of the elements present in selected catalyst samples are also displayed.

Table 7.3 Overpotentials and Tafel slope values for unary and binary Ni-Fe, Ni-Co, Ni-Mo and Ni-Cr hydroxides tested in 1 M NaOH, 333 K.

Binary hydroxide	Electroplating bath composition/ molar %	EDX of catalyst surface (at. %)	Overpotential, $\eta_{0.5\ A\ cm^{-2}}$ / mV	Overpotential, $\eta_{0.1\ A\ cm^{-2}}$ / mV	Tafel slope, b / mV dec^{-1}
Ni-Fe	75:25	76:24	323	292	48
	50:50	-	341	304	39
	25:75	-	354	320	42
Ni-Co	75:25	-	332	299	36
	50:50	-	326	298	34
	25:75	34:66	322	295	36
Ni-Mo	75:25	-	357	312	41
	50:50	75:25	335	298	42
	25:75	-	339	300	42
Ni-Cr	75:25	83:17	329	293	38
	50:50	-	354	309	43
	25:75	-	379	333	44

The cyclic voltammograms of catalyst hydroxide films deposited from solutions of varying molar percentages between Ni and Fe are given in **Figure 7.8 a**. The anodic peak potential representative of the $Ni^{2+/3+}$ redox couple shifts to more positive potentials in response to increases in molar percentage of Fe in the deposition solution. The sample deposited from solution containing 25% Fe gives the lowest overpotential of 292 mV at 0.1 Acm^{-2} (**Figure 7.8 b**), which has also been reported by several other studies [24-26]. Compared to the Tafel slope values of unary Ni and Fe hydroxides, the Tafel slope of catalyst deposited from deposition solution containing 25% Fe is determined to be 48 mV dec^{-1} indicating a change in OER mechanism to one where the formation of a superoxy intermediate –OOH is the rate determining step [5].

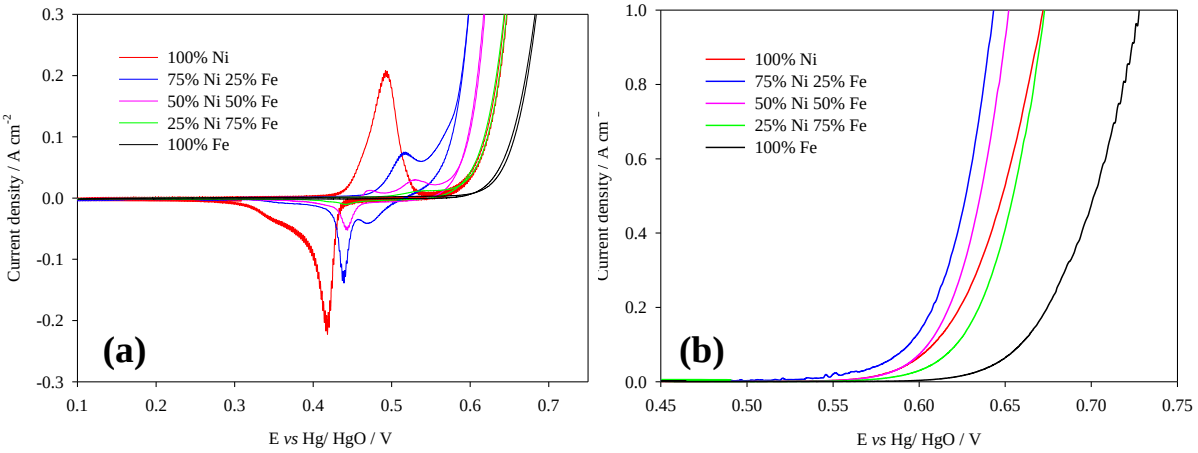

Figure 7.8 a) Cyclic voltammograms cycled between 0.1 and 0.7 V vs Hg/HgO at scan rate of 100 mV s^{-1} and **b)** linear sweep voltammogram swept at scan rate 1 mV s^{-1} tested in 1M NaOH, 333 K. All catalysts were cathodically electrodeposited from their respective 18 mM metal sulfate solutions of various molar percentages + 25 mM $(NH_4)_2SO_4$.

Among the Ni-Co binary hydroxides, the overpotential for the oxygen evolution reaction is lowest at 295 mV at 0.1 A cm^{-2} for the catalyst from deposition solution containing 75% Co. The OER overpotential is observed to increase gradually with the Ni content in the deposition solution. Tafel slope values for the mixed Ni-Co based binary hydroxide catalysts are found to be between 34 and 36 mV dec^{-1} which suggests that the OER reaction pathway is similar to that of Co unary hydroxide.

Mixed hydroxides of Ni-Mo are observed to be more active OER catalysts than unary Mo hydroxide. Electroplating solutions with 50% and 75% Mo content produced catalysts with lower OER overpotentials compared to unary Ni hydroxide, with the sample prepared from a deposition solution of 50% Mo content exhibiting the lowest overpotential for OER. EDX analysis of the sample's surface showed that it was actually composed of 75% Ni and 25% Mo indicating that Ni is deposited preferentially to Mo.

Compared to other binary Ni-Cr hydroxides and their respective unary hydroxides, the presence of 25% Cr in the deposition solution gives a catalyst with the lowest overpotential for OER. Catalysts from electroplating solutions with 50 - 100% Cr content however, have much higher overpotentials for OER. This result is supported by Diaz-Morales et al.'s computational study [27] of doped Ni oxyhydroxides which proposed that Ni is the active site on Cr-doped Ni oxyhydroxide hence a catalyst

prepared from a solution with a larger percentage of Ni is likely to have more OER sites. The Tafel slope of the Ni-Cr binary hydroxide sample from 25% Cr 75% Ni deposition solution was determined to be 38 mV dec^{-1} which is very close to that of the sample from 100 % Ni deposition solution (40 mV dec^{-1}). It is therefore likely that the presence of ~ 20 % Cr in the $Ni(OH)_2$ catalyst does not change the OER pathway, but instead increases the rate of the rate determining step.

Overall, the optimal Ni-based binary metal hydroxides ranked according to their overpotential values are Ni-Fe < Ni-Cr < Ni-Co < Ni-Mo at 0.1 A cm^{-2} and Ni-Fe ≈ Ni-Co < Ni-Cr < Ni-Mo at 0.5 A cm^{-2}. These trends are generally similar to those obtained from benchmarking studies of Ni-based metal oxides [28], hydroxides [26] and oxyhydroxides [27].

7.2.5. Comparison of ternary metal hydroxide catalysts

The optimisation of the ternary metal hydroxide catalyst composition is complicated by the preferential order of unary hydroxide deposition [29-31]. In order to account for the interactions between binary metal hydroxides, the experimentally obtained optimal compositions of binary metal hydroxides of Ni-Fe, Ni-Co, Ni-Cr and Ni-Mo were initially used to determine electroplating solution compositions of the Ni-Fe based hydroxide of Ni-Fe-Co, Ni-Fe-Mo and Ni-Fe-Cr although other plating compositions were also tested. The overpotentials and corresponding Tafel slope values of these ternary metal hydroxides are shown in **Table 7.4.** From the table, the optimal ternary hydroxides of Ni-Fe-Cr, Ni-Fe-Mo and Ni-Fe-Co were found to be closely associated to the molar percentages of the optimal binary hydroxides. For example, the optimal Ni-Fe-Mo catalyst was synthesised from a bath composition of Ni 44.5: Fe 11: Mo 44.5 metal sulphate solution since the optimal molar percentage of Ni:Fe is 75:25 and Ni:Mo is 50:50.

Table 7.4 Overpotentials and Tafel slope values for Ni-Fe based ternary metal hydroxide catalysts tested in 1 M NaOH, 333 K.

Ternary hydroxide	Electroplating bath composition/ molar %	Overpotential, $\eta_{0.5\ A\ cm^{-2}}$ / mV	Overpotential, $\eta_{0.1\ A\ cm^{-2}}$ / mV	Tafel slope, b / mV dec^{-1}
Ni-Fe-Cr	75:12.5:12.5	322	287	48
	70:20:10	339	301	53
	66:17:17	335	299	46
Ni-Fe-Mo	44.5:11:44.5	300	270	40
	62.5:12.5:25	319	282	44
	40:10:50	309	279	37
Ni-Fe-Co	62.5:12.5:25	326	296	40
	44.5:11:44.5	316	290	31
	23:8:69	296	265	37

The voltammograms of unary Ni and binary Ni-Fe metal hydroxide as well as the optimal ternary metal hydroxides of Ni-Fe-Co, Ni-Fe-Mo and Ni-Fe-Cr are displayed in **Figure 7.9**. The lowest overpotential at 0.1 A cm^{-2} and 0.5 A cm^{-2}, was obtained from Ni-Fe-Co ternary metal hydroxide followed by Ni-Fe-Mo < Ni-Fe-Cr < Ni-Fe < Ni. This implies that the combination of ternary transition metals in the metal hydroxide catalyst versus binary or unary metals has a greater effect on the OER catalytic activity.

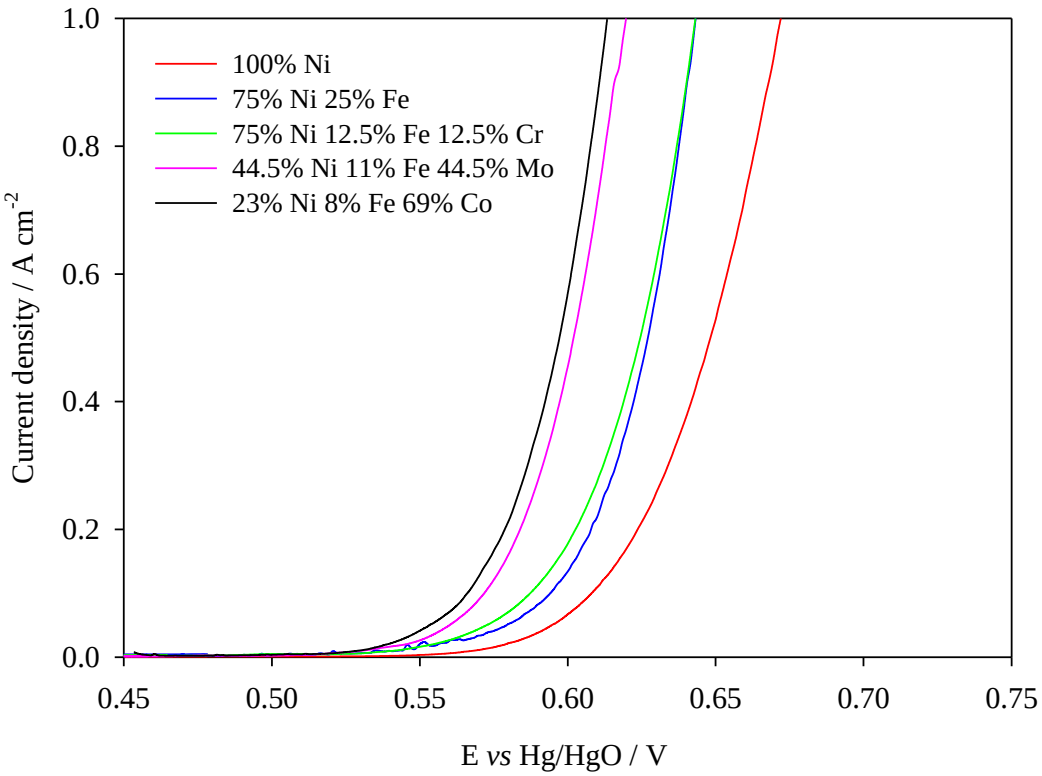

Figure 7.9 Steady state polarisation curves swept at scan rate of 1 mV s^{-1} in 1 M NaOH, 333 K of various catalysts cathodically deposited from various 18 mM metal sulfate solutions at 200 mA cm^{-2} for 120 s on SS microelectrode.

The morphological effect of co-depositing more than one transition metal hydroxide in binary and ternary hydroxides of Ni-Fe, Ni-Co and Ni-Fe-Co was observed with TEM. The TEM micrograph of Ni-Fe binary hydroxide in **Figure 7.10 a** displays a morphology of unary Ni hydroxide crystals encased by nanosheets of unary Fe hydroxide. It is likely that during electrodeposition, unary Fe hydroxide coats the dendritic structure of unary Ni hydroxide.

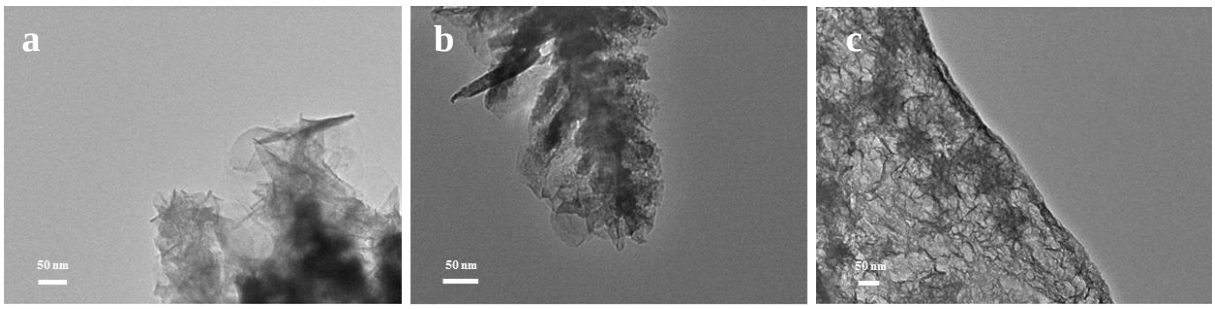

Figure 7.10 TEM micrographs of cathodic depositions at 200 mA cm^{-2} for 120 s from 18 mM metal sulfate solutions of **a)** 75%Ni-25%Fe **b**) 25%Ni-75%Co and **c**) 23%Ni-8%Fe-69%Co. All sulfate solutions contained 25 mM $(NH_4)_2SO_4$.

In **Figure 7.10 b**, the Ni-Co binary hydroxide reveals a dendrite of unary Ni hydroxide with unary Co hydroxide nanoflowers interwoven within it. This suggests that the Ni hydroxide provides a platform for the smaller discs of Co hydroxide to attach to. The TEM micrograph of ternary Ni-Fe-Co hydroxide in **Figure 7.10 c** shows an interwoven network of Co hydroxide nanoflowers with Ni hydroxide platelets dispersed throughout. The Fe hydroxide nanosheets present are difficult to discern from the Co hydroxide nanoflowers as they closely resemble each other. The Ni hydroxide therefore, likely serves as a scaffold for the Co hydroxide to deposit onto and the Fe hydroxide is deposited at the edges of the structure.

7.2.6. Optimisation of ternary metal hydroxide catalysts

As the Ni-Fe-Co ternary metal hydroxide catalyst demonstrated lowest overpotential at both 0.1 and 0.5 A cm^{-2}, it was selected for further study of the effects of electrodeposition conditions on catalytic performance. The parameters investigated were cathodic current density, pH, electroplating time and temperature.

7.2.6.1. Electrodeposition current density

Comparing the effect of cathodic current density, the SEM micrograph of deposit at 100 mA cm^{-2} (**Figure 7.11 a**) shows deposit particles which are relatively uniform in size and approximately 20-40 µm in characteristic length. Increasing the deposition current density to 200 or 300 mA cm^{-2} causes the nucleation rate of the deposit to speed up due, to the higher overpotential of the deposition reaction.

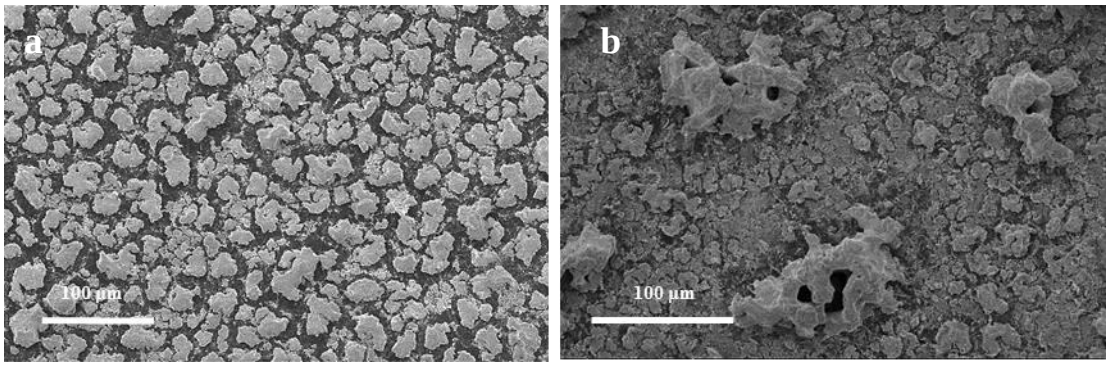

Figure 7.11 SEM micrographs of Ni-Fe-Co ternary hydroxide catalyst prepared at **a)** 100 and **b)** 500 mA cm^{-2} electrodeposition current density.

At very high current densities of 500 mA cm^{-2} (**Figure 7.11 b**), the rate of growth of the deposit becomes mass-transfer controlled [32] resulting in much larger clusters

of deposit and the influence of other electrochemical reactions such as the evolution of hydrogen which becomes more prominent.

At these higher current densities, not only are the deposit particles larger because of increasing nucleation rate, voids in the particles which are created by the competing hydrogen evolution reaction also appear to increase in number and size. Based on the slow scan voltammogram results, a deposition current density of 300 mA cm^{-2} gives the best OER catalytic activity for Ni-Fe-Co hydroxide catalyst (**Figure 7.12**) at both low and high current densities. This reduction in overpotential at 300 mA cm^{-2} is likely to be due to increased electrocatalytically active surface area from the mixture of large and small deposit particles and increase in number and size of voids caused by hydrogen evolution, which exposes more surface area for the catalysis of oxygen evolution.

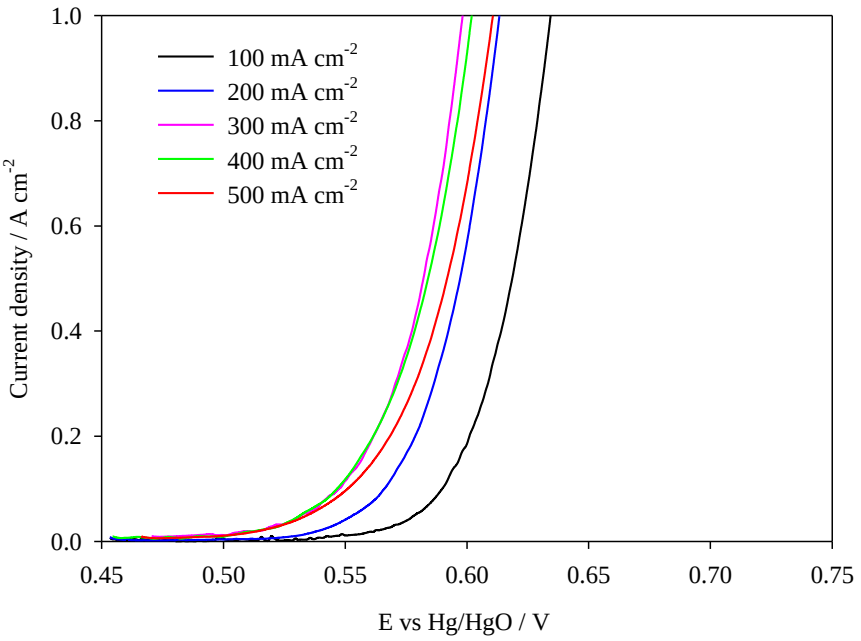

Figure 7.12 Linear sweep voltammograms of Ni-Fe-Co ternary hydroxide catalyst prepared from 18 mM metal sulfate solution of 23%Ni-8%Fe-69%Co electrodeposited at different cathodic current densities.

7.2.6.2. pH of electroplating bath

The effect of the deposition solution pH on deposits were investigated by adjusting the solution pH with diluted H_2SO_4 and NaOH to acidic and alkaline pH respectively. The pH of the unadjusted plating solution of Ni-Fe-Co hydroxide was ~5.5. This was adjusted to values between pH 2.5 to 6.6; the reason being that at pH values

greater than 7.0, Fe^{2+} present in the solutions oxidised and precipitated out as insoluble Fe^{3+}. From the slow scan voltammograms (**Figure 7.13**), a low pH of 2.5 is observed to produce catalyst which is less active for OER. Conversely, at higher pH values of 3.9 and 5.5 the catalyst deposit is more active for OER.

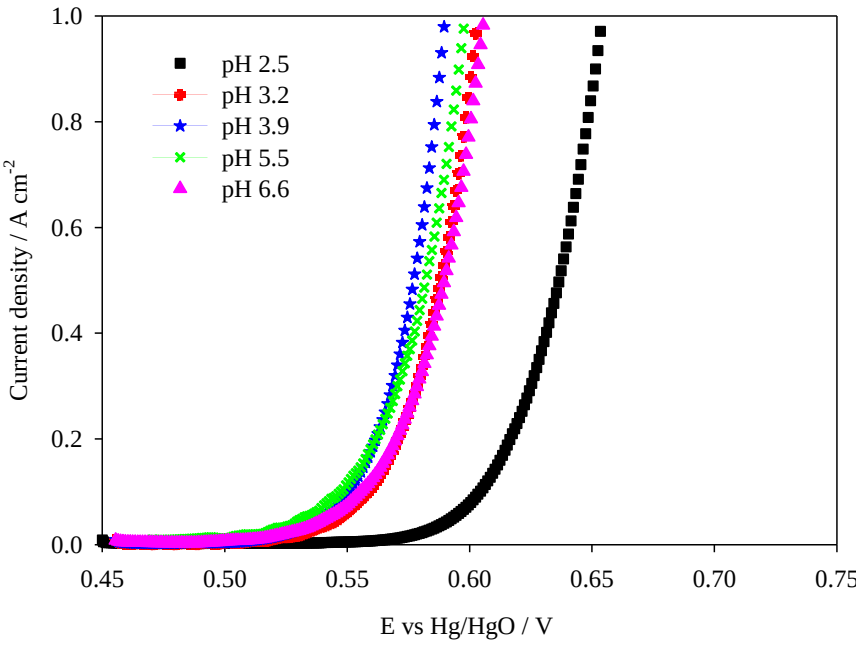

Figure 7.13 Linear sweep voltammograms of Ni-Fe-Co ternary hydroxide catalyst prepared from 18 mM metal sulfate solution of 23%Ni-8%Fe-69%Co adjusted to different pH at cathodic current density of 300 mA cm^{-2}.

Comparing the surface morphology of the deposits at pH 2.5 and 3.9 from SEM micrographs (**Figure 7.14 a & b** respectively), the surface of the deposit from pH 3.9 displays clusters of nanoflower-like structures representative of Co hydroxide which are not seen on the surface of the deposit from pH 2.5. The deposition solution pH therefore affects the surface composition of the deposits. At a much lower pH, the competing hydrogen evolution reaction is also enhanced [33, 34] resulting in weak and unstable deposits which appear to negatively affect catalytic activity for OER. When adjusting to higher pH values, the deposition of metal hydroxides are favoured due to the higher concentration of hydroxyl ions near the electrode surface. As shown the overpotential for OER is lowest for Ni-Fe-Co hydroxide deposits at pH 3.9 and pH 5.5,

this suggests that electrodeposition solutions in this pH range are able to produce stable and catalytically active deposits for oxygen evolution.

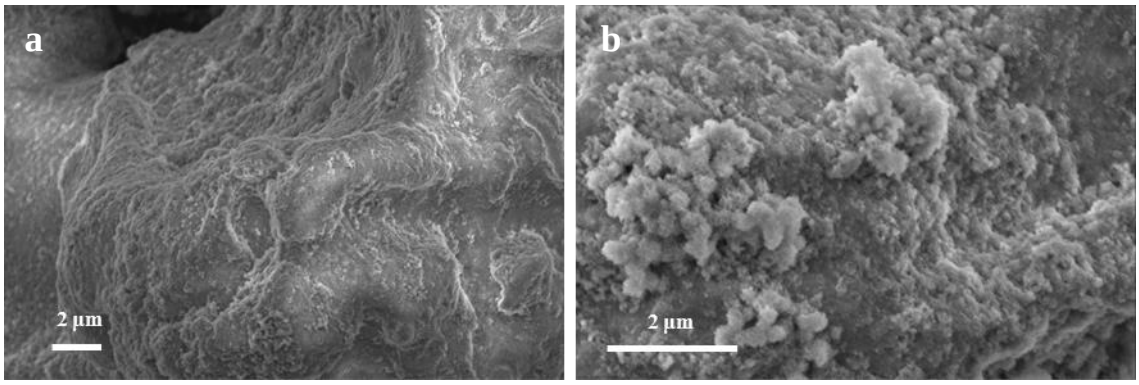

Figure 7.14 SEM micrographs of Ni-Fe-Co ternary hydroxide catalyst prepared from electrodeposition solution of pH **a)** 2.5 and **b)** 3.9.

7.2.6.3. Electrodeposition time

While keeping deposition current density constant at 300 mA cm^{-2}, the mass of the deposits will be increased by increasing electrodeposition time. This ensured that the nucleation rate of the deposits remained constant therefore the size of the deposits did not appear to be hugely affected.

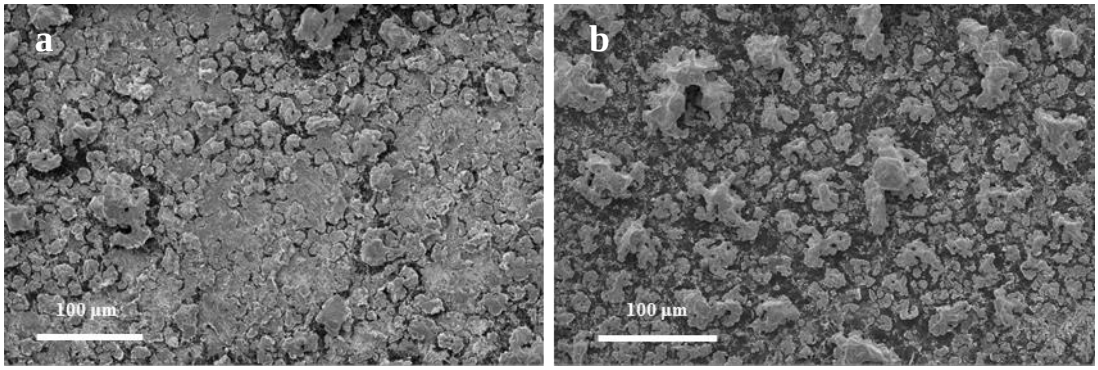

Figure 7.15 SEM micrographs of Ni-Fe-Co ternary hydroxide catalyst prepared with **a)** 60 s and **b)** 180 s electrodeposition time.

As seen in **Figure 7.15 a**, at a plating time of 60 s, the surface of the electrode was evenly covered by the deposit. Owing to the high nucleation rate, a mixture of large clusters and smaller fragments are seen on the surface of the electrode. With increasing electrodeposition time, the large clusters remained similar in size but some appeared more distorted due to the greater number of voids created by the consistent

production of hydrogen bubbles over this longer period of time [35-37], which also contributed to the surface of the electrode being less well covered (**Figure 7.15 b**).

The decrease in overpotential of catalyst performance of catalyst prepared with 180 s electrodeposition time correlates to the increase in voids and three dimensional features observed in the deposit clusters on the electrode support, indicating an increase in electrocatalytically active surface area for oxygen evolution. This was considered a strategic way of using the competing hydrogen evolution reaction to increase the porosity of the deposits. A plating time of 240 s was found to give the lowest overpotential value of 235 mV at 0.1 Acm^{-2} and 262 mV at 0.5 A cm^{-2} for the Ni-Fe-Co hydroxide catalyst (**Figure 7.16**). In addition, the Tafel slope value for this catalyst was found to be 36.3 mV dec^{-1} which is the lowest value obtained of all the tested Ni-Fe based ternary metal hydroxides. Since Tafel slope is a measure of the change in rate of OER to potential applied for the reaction, a lower Tafel slope value typically indicates a more efficient catalyst for the reaction.

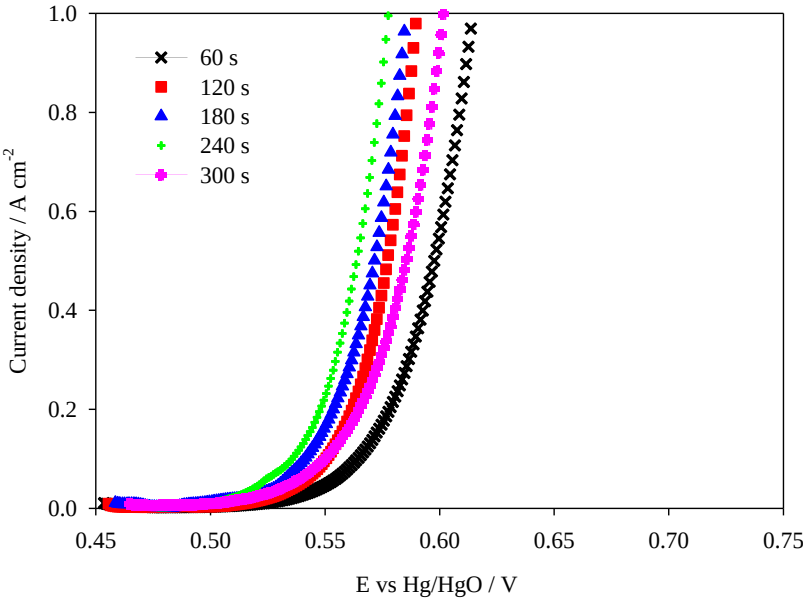

Figure 7.16 Linear sweep voltammograms of Ni-Fe-Co ternary hydroxide catalyst prepared from 18 mM metal sulfate solution of 23%Ni-8%Fe-69%Co adjusted to pH 3.9 at cathodic current density of 300 mA cm^{-2} at varying lengths of electrodeposition time.

7.2.6.4. Electrodeposition temperature

Distinct morphological changes are observed in deposit when the electrodeposition temperature increase. Initially increasing the temperature from 22

ºC to 35 ºC causes the rate of deposition to speed up due to the quicker diffusion of ions and lower nucleation activation energy resulting in the formation of larger deposits on the surface of the electrode. At temperatures ≥ 50 ºC however, the effect of increasing electrodeposition temperature changes abruptly and structure of the deposits become thinner, weaker and less compact.

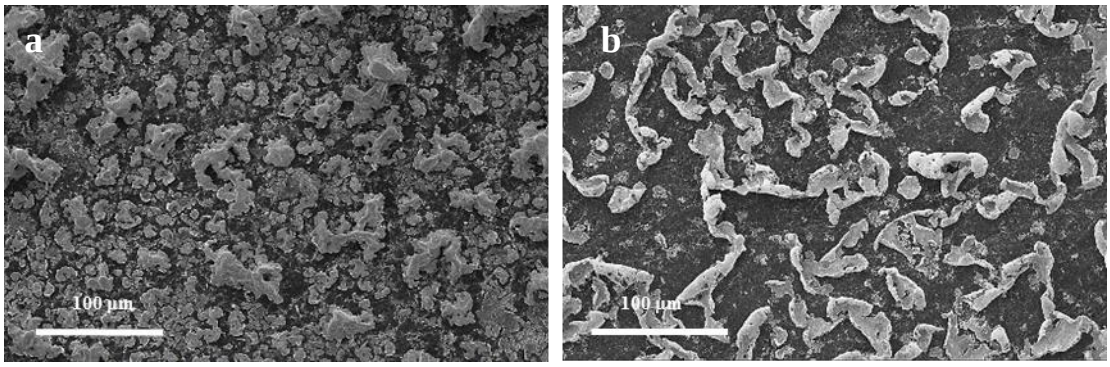

Figure 7.17 SEM micrographs of Ni-Fe-Co ternary hydroxide catalyst prepared from deposition solutions adjusted to **a)** 22 ºC and **b)** 70 ºC.

At a high temperature of 70ºC, the deposits curl up to expose more uncovered electrode surface (**Figure 7.17 b**). This could be partially attributed to the greater enhancement of the rate of hydrogen evolution at the electrode surface. Increasing the temperature also led to observable chemical changes in the electrodeposition sulfate solution which could have affected the electrodeposition reactions. For example, at ≥ 35 ºC insoluble reddish-brown $Fe(OH)_3$ was observed to precipitate out of the Ni-Fe-Co sulfate solution after electrodeposition. It is clear from the linear sweep voltammograms of catalyst produced from deposition solutions of different temperatures that overpotential increases with temperature (**Figure 7.18**) and the catalyst prepared at 22 ºC displayed the lowest overpotential for OER.

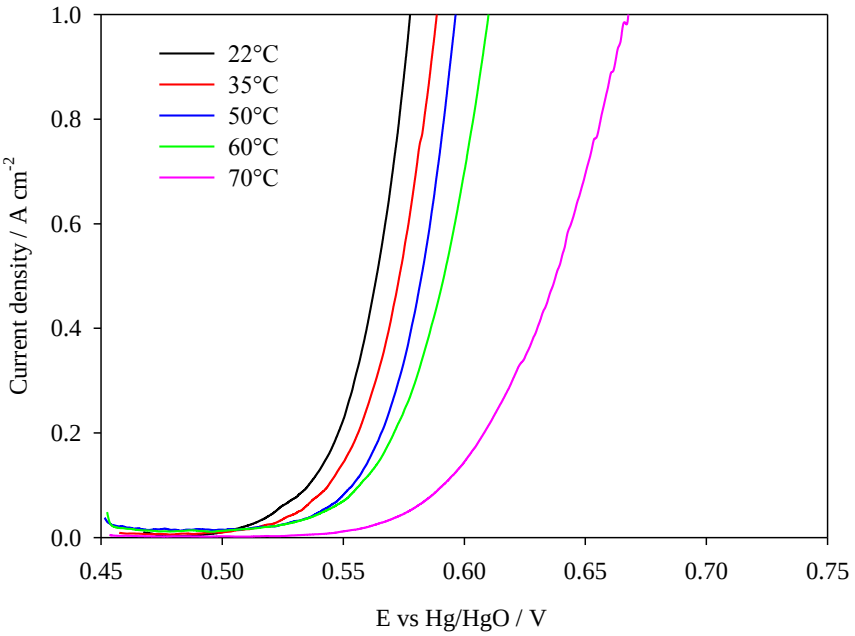

Figure 7.18 Linear sweep voltammograms of Ni-Fe-Co ternary hydroxide catalyst prepared from 18 mM metal sulfate solution of 23%Ni-8%Fe-69%Co adjusted to pH 3.9 at cathodic current density of 300 mA cm^{-2} for 240s at varying temperatures.

7.2.7. Characterisation of optimised ternary hydroxide catalyst

The optimised Ni-Fe-Co ternary hydroxide catalyst was deposited onto carbon polymer plate and examined with SEM, EDX and XPS before and after undergoing anodic polarisation at high current density of 100 mA cm^{-2} for 15 mins. From SEM micrographs in **Figure 7.19**, the catalyst layer did not undergo any size or shape changes after oxidation, however the most noticeable difference was the growth of clusters of nanoflowers from all exposed surfaces of the deposit in **Figure 7.19 b**. Similar nanoflower-like structures were seen on the deposit surface before evolving oxygen (**Figure 7.19 a**) but these were only present on small areas of the deposit surface. It is therefore apparent that this morphological change is linked to the evolution of oxygen which occurs at the surface of the particles. EDX analysis showed that the atomic composition of the deposit remained fairly constant across the electrode before and after oxygen evolution, confirming sample homogeneity.

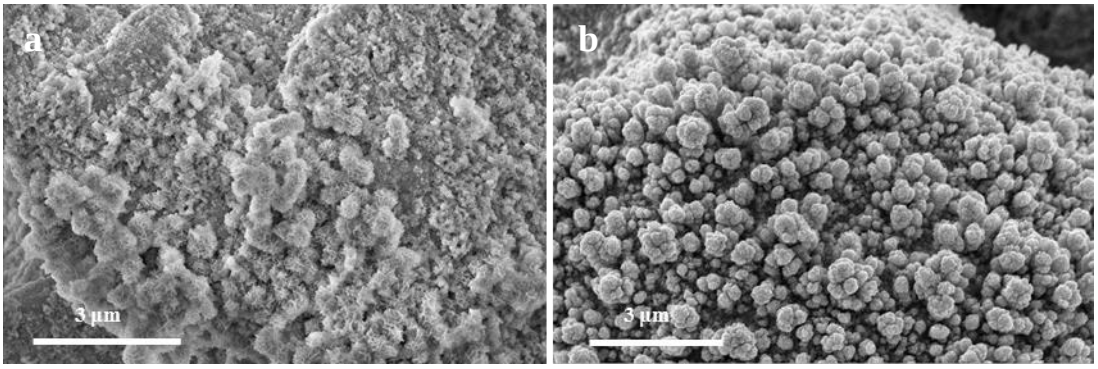

Figure 7.19 SEM micrographs of optimised Ni-Fe-Co ternary hydroxide catalyst **a)** before and **b)** after anodic polarisation at 100 mA cm^{-2}.

XPS spectra of the ternary Ni-Fe-Co hydroxide before and after anodic polarisation reveal that changes occur during the surface chemical reactions. From the Co 2p spectra (**Figure 7.20 a**) of the sample before evolving oxygen, a peak at 781.3 eV with accompanying satellite peak at 786.2 eV confirms the presence of $Co(OH)_2$. After being subjected to oxidising conditions, the spectra displays a $Co2p_{3/2}$ peak at binding energy 780.4 eV which is characteristic of $Co^{3+/4+}$ in both CoOOH and Co_3O_4 due to their slightly overlapping binding energies. Given the absence of the accompanying satellite peak of the $Co2p_{3/2}$ peak at 786.2 eV as well, it is apparent that Co^{3+} species is present predominantly as CoOOH [20, 23]. Additionally, the difference in binding energy of multiplet peaks $2p_{3/2}$ and $2p_{1/2}$ peaks before evolving oxygen is ~16 eV which is characteristic of $Co(OH)_2$ and after evolving oxygen it is reduced to ~15 eV which is characteristic of CoOOH [38] (**Figure 7.20 b**). It is therefore evident that during the evolution of oxygen, reaction (7.3) takes place.

$$Co(OH)_2 + OH^- \rightarrow CoOOH + H_2O + e^- \quad (7.3)$$

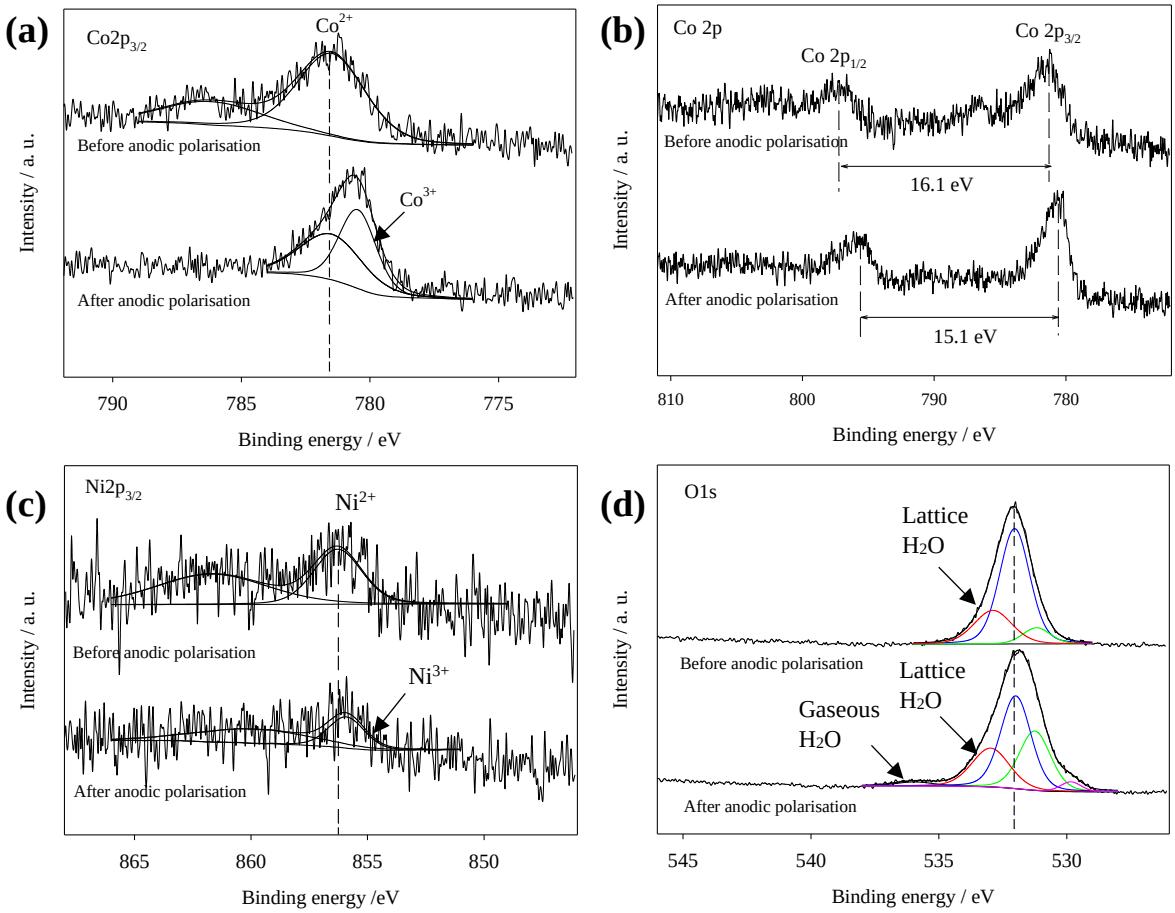

Figure 7.20 XPS **a)** $Co2p_{3/2}$ **b)** Co2p **c)** Ni2p **d)** O1s spectra of optimised Ni-Fe-Co ternary hydroxide catalyst before and after anodic polarisation at 100 mA cm^{-2} for 15 mins.

The $Ni2p_{3/2}$ spectra (**Figure 7.20 c**) for the sample before anodic polarisation displays peaks at 856.4 eV and corresponding satellite peak at 861.2 eV characteristic of $Ni(OH)_2$. However, after evolving oxygen the binding energies of the $2p_{3/2}$ and $2p_{1/2}$ peaks are shifted to slightly lower values which are characteristic of Ni^{3+} in NiOOH and the corresponding satellite peaks also appear broader and flattened [10, 39]. This suggests that under OER conditions the $Ni(OH)_2$ present undergoes oxidation to form NiOOH as presented in reaction (7.4).

$$Ni(OH)_2 + OH^- \rightarrow NiOOH + H_2O + e^- \qquad (7.4)$$

Due to the extremely low quantity of Fe species present in the surface of the deposit, the Fe $2p_{3/2}$ and $2p_{1/2}$ peaks are not well defined and appear merged in the spectra (not shown). Comparing the electron binding energies before and after anodic polarisation, the $Fe2p_{3/2}$ peak at 712.7 eV which is characteristic of Fe^{3+} did not change

significantly. The observation that Fe remains at 3+ oxidation state during anodic polarisation was also seen in several detailed studies on Fe-incorporated oxide and oxyhydroxide catalysts [24, 40, 41]. For a similar ternary Ni-Fe-Co metal oxide catalyst [40], it was proposed that the presence of Ni and Co activated the Fe active sites for binding to OER intermediates –OH and –OOH leading to enhanced OER activity compared to the binary Ni-Fe oxide.

Before anodic polarisation, the O1s spectra of the Ni-Fe-Co ternary metal hydroxide (**Figure 7.20 d**) displays a peak at 532.0 eV which is characteristic of the M-OH bond in $Ni(OH)_2$ and $Co(OH)_2$, and a peak at 531.2 eV which can be assigned to the O^{2-} and OH^- oxygen atoms in FeOOH [13]. After evolving oxygen, the O1s spectra reveals a decrease in signal area for the peak at 532.0 eV by ~23% likely due to the oxidation of $Ni(OH)_2$ and $Co(OH)_2$ to NiOOH and CoOOH respectively. The peak at 531.2 eV correspondingly increases in signal area by ~20% after anodic polarisation and the increase is attributed to the presence of M-OH bond for CoOOH [23] and M-O bond for NiOOH [42]. A small peak at 529.8 eV of ~3% signal area in the O1s spectra after anodic polarisation is assigned to the M-O bond in CoOOH [23]. A minor peak at 535.9 eV was observed in the O1s spectra after anodic polarisation and assigned to gaseous phase H_2O [43]. Since the increase in signal area of the peak for H_2O (g) matches the decrease in signal area of the peak at 533.0 eV for lattice H_2O (l), it is likely that lattice H_2O (l) was converted to H_2O (g) due to changes in the catalyst morphology during anodic polarisation. These changes observed in the O1s spectra correspond well to the changes observed in the M2p spectra that the catalyst undergoes under OER conditions.

7.2.8. Stability test in a zero-gap alkaline water electrolyser

Preliminary stability tests of the optimised ternary metal hydroxide were carried out in an alkaline zero gap water electrolyser with working area of 9 cm^2 (Section 6.1.4.). The current density was held at 0.5 A cm^{-2} for a period of 3.5 h and the cell voltage was recorded during this time. Binary Ni-Fe hydroxide catalyst and ternary Ni-Fe-Co hydroxide catalyst on SS expanded mesh were prepared by cathodic electrodeposition using the optimised deposition solution and parameters. As the difference in current density distribution across a planar versus mesh working

electrode must be taken into account, two pieces of Pt mesh counter electrodes were placed on either side of the SS mesh to facilitate a well-distributed electric field for electrodeposition and the deposition time was extended to ensure that the meshes were sufficiently coated with catalyst. In addition to this since H_2 gas is evolved as a side reaction during electrodeposition, the area and rate of mass transfer [44] becomes more significant over a larger electrode area. To ensure more uniformly coated SS meshes, the deposition solution was stirred at a slow stir rate of 100 rpm to prevent H_2 bubbles from obstructing the surface to be coated.

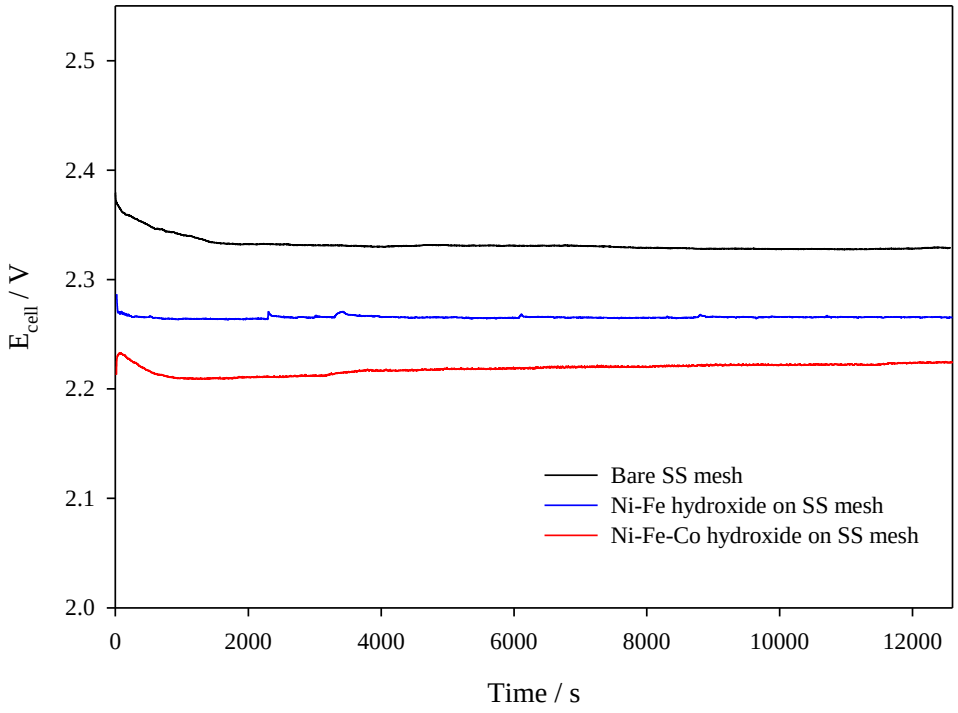

Figure 7.21 Cell voltage of alkaline water electrolyser over 3.5 h at 0.5 A cm^{-2} of different anodes and expanded Ni mesh as cathode pressed up against Tokuyama A201 hydroxide ion exchange membrane in 4 M NaOH at 333 K, 250 mL min^{-1} pump rate.

Figure 7.21 shows the E_{cell} against time plot for the uncoated and coated SS anodes tested. The E_{cell} of electrolyser with anode of uncoated SS mesh was found to be 2.33 V. This was compared to the E_{cell} of the cells assembled with anodes of Ni-Fe binary hydroxide catalyst and Ni-Fe-Co ternary hydroxide catalyst coated onto SS mesh which gave a 70 mV reduction and 110 mV reduction in E_{cell} respectively. This demonstrates that the catalyst coatings help to reduce the potential required for the same reaction rate. The potentials of these cells were maintained for the whole

duration of the tests indicating the stability of the various anodes. Overall, the ternary Ni-Fe-Co hydroxide catalyst demonstrated better performance for OER than the binary Ni-Fe hydroxide catalyst and uncoated SS mesh.

7.3. Conclusion

A unique microelectrode set-up was employed for screening the performance of unary and Ni-based binary and ternary metal hydroxide catalysts synthesised with a cathodic electrodeposition method from transition metal sulfate solutions. A clear reduction in the OER overpotential by ~65 mV at 0.1 A cm^{-2} was observed with the coating of a $Ni(OH)_2$ catalyst layer on the SS microelectrode surface compared to the uncoated SS microelectrode surface.

Of the unary hydroxides tested, hydroxides of Ni and Co displayed the lowest overpotentials for OER. SEM and TEM were used to study the morphology of the deposits from unary metal sulfate solutions of Ni, Fe and Co, whilst XPS analysis confirmed the presence of transition metal hydroxides in the films. Binary hydroxides of Ni-Fe, Ni-Co, Ni-Mo and Ni-Cr were investigated in the same manner and ordered according to their overpotential values Ni-Fe < Ni-Cr < Ni-Co < Ni-Mo at 0.1 A cm^{-2} and Ni-Fe ≈ Ni-Co < Ni-Cr < Ni-Mo at 0.5 A cm^{-2}. The Ni-Fe-Co ternary metal hydroxide displayed lowest overpotential values at 0.1 A cm^{-2} and 0.5 A cm^{-2} followed by Ni-Fe-Mo < Ni-Fe-Cr < Ni-Fe < Ni. The ternary metal hydroxide catalysts showed considerably lower oxygen evolution overpotentials compared to their binary and unary counterparts.

The influence of electrodeposition parameters on the crystallisation of ternary Ni-Fe-Co hydroxide catalysts as well as their effect on the catalytic performance were investigated using SEM and slow scan anodic polarisation. It was found that the catalyst cathodically deposited at 300 mA cm^{-2} for 240 s at 22 ºC in electrodeposition solution pH 3.9 produced the most active catalyst with an overpotential of 235 mV at 0.1 A cm^{-2} tested in 1 M NaOH, 333 K.

The catalytic activity of the optimal Ni-Fe-Co ternary hydroxide catalyst was proven to be consistently better than Ni-Fe binary hydroxide and uncoated SS mesh

when tested in an alkaline zero gap electrolyser at 0.5 A cm^{-2} for 3.5 h giving a potential of ~2.22 V which was maintained throughout.

7.4. References

1. A.V. Naumkin, A. Kraut-Vass, S.W. Gaarenstroom, C.J. Powell. *NIST X-ray Photoelectron Spectroscopy Database* 2012 15/09/2012 [cited 2018; Version 4.1 [Available from: http://srdata.nist.gov/xps/.
2. M.E.G. Lyons, M.P. Brandon, The oxygen evolution reaction on passive oxide covered transition metal electrodes in aqueous alkaline solution. Part 1-Nickel Int. J. Electrochem. Sci. 3 (2008) 1386-1424.
3. D.S. Hall, D.J. Lockwood, C. Bock, B.R. MacDougall, Nickel hydroxides and related materials: a review of their structures, synthesis and properties, Pro. R. Soc. A 471 (2014) 1-65.
4. Debabrata Chanda, Jaromir Hnat, Martin Paidar, K. Bouzek, Evolution of physicochemical and electrocatalytic properties of $NiCo_2O_4$ (AB_2O_4) spinel oxide with the effect of Fe substitution at the A site leading to efficient anodic O_2 evolution in an alkaline environment, Int. J. Hydrogen Energy 39 (2014) 5713-22.
5. M.E.G. Lyons, M.P. Brandon, A comparative study of the oxygen evolution reaction on oxidised nickel, cobalt and iron electrodes in base, J. Electroanal. Chem. 641 (2010) 119-30.
6. M.E.G. Lyons, M.P. Brandon, The oxygen evolution reaction on passive oxide covered transition metal electrodes in alkaline solution. Part II - Cobalt, Int. J. Electrochem. Sci. 3 (2008) 1425-62.
7. S. Trasatti, G. Lodi, Electrodes of Conductive Metallic Oxides Part B,S. Trasatti (ed), Elsevier, Amsterdam, 1981
8. A.M. Venezia, R. Bertoncello, G. Deganello, X-ray photoelectron spectroscopy investigation of pumice-supported nickel catalysts Surf. Interface Anal. 23 (1995) 239-47.
9. B.P. Payne, M.C. Biesinger, N.S. McIntyre, Use of oxygen/nickel ratios in the XPS characterisation of oxide phases on nickel metal and nickel alloy surfaces, J. Electron. Spectrosc. Relat. Phenom. 185 (2012) 159-66.
10. A.P. Grosvenor, M.C. Biesinger, R.S.C. Smart, N.S. McIntyre, New interpretations of XPS spectra of nickel metal and oxides, Surf. Sci. 600 (2006) 1771-9.
11. M.C. Biesinger, B.P. Payne, L.W.M. Lau, A. Gerson, R.S.C. Smart, X-ray photoelectron spectroscopic chemical state quantification of mixed nickel metal, oxide and hydroxide systems, Surf. Interface Anal. 41 (2008) 324-32.
12. H.W. Nesbitt, D. Legrand, G.M. Bancroft, Interpretation of Ni2p XPS spectra of Ni conductors and Ni insulators, Phys. Chem. Min. 27 (2000) 357-66.
13. G.C. Allen, M.T. Curtis, A.J. Hooper, P.M. Tucker, X-ray photoelectron spectroscopy of iron-oxygen systems JCS. Dalton 14 (1974) 1525-30.
14. P.C.J. Graat, M.A.J. Somers, Simultaneous determination of composition and thickness of thin iron-oxide films from XPS Fe 2p spectra Appl. Surf. Sci. 100 (1996) 36-40.
15. M. Descostes, F. Mercier, N. Thromat, C.Beaucairea, M.Gautier-Soyer, Use of XPS in the determination of chemical environment and oxidation state of iron and sulfur samples: constitution of a data basis in binding energies for Fe and S reference compounds and applications to the evidence of surface species of an oxidized pyrite in a carbonate medium, Appl. Surf. Sci. 165 (2000) 288-302.
16. T. Yamashita, P. Hayes, Analysis of XPS spectra of Fe^{2+} and Fe^{3+} ions in oxide materials, Appl. Surf. Sci. 254 (2008) 2441-9.
17. N.S. McIntyre, D.G. Zetaruk, X-ray photoelectron spectroscopic studies of iron oxides, Anal. Chem. 49 (1977) 1521-9.
18. A.P. Grosvenor, B.A. Kobe, M.C. Biesinger, N.S. McIntyre, Investigation of multiplet splitting of Fe 2p XPS spectra and bonding in iron compounds, Surf. Interface Anal. 36 (2004) 1564-74.

19. D.C. Frost, C.A. McDowell, L.S. Woolsey, Evidence for multiplet splitting of 2p photoelectron lines of transition metal complexes, Chem. Phys. Lett. 17 (1972) 320-3.
20. N.S. McIntyre, M.G. Cook, X-ray photoelectron studies on some oxides and hydroxides of cobalt, nickel, and copper, Anal. Chem. 47 (1975) 2208-13.
21. D.C. Frost, C.A. McDowell, I.S. Woolsey, X-ray photoelectron spectra of cobalt compounds, Mol. Phys. 27 (1974) 1473-89.
22. M.C. Biesinger, B.P. Payne, A.P. Grosvenor, L.W.M. Lau, A.R. Gerson, R.S.C. Smart, Resolving surface chemical states in XPS analysis of first row transition metals, oxides and hydroxides: Cr, Mn, Fe, Co and Ni, Appl. Surf. Sci. 257 (2011) 2717-30.
23. J. Yang, H. Liu, W.N. Martens, R.L. Frost, Synthesis and characterization of cobalt hydroxide, cobalt oxyhydroxide, and cobalt oxide nanodiscs, J. Phys. Chem. C 114 (2010) 111-19.
24. D. Friebel, M.W. Louie, M. Bajdich, K.E. Sanwald, Y. Cai, A.M. Wise, M.-J. Cheng, D. Sokaras, T.-C. Weng, R. Alonso-Mori, R.C. Davis, J.R. Bargar, J.K. Nørskov, A. Nilsson, A.T. Bell, Identification of highly active Fe sites in (Ni,Fe)OOH for electrocatalytic water splitting, J. Am. Chem. Soc. 137 (2015) 1305-13.
25. Lena Trotochaud, Samantha L. Young, James K. Ranney, S.W. Boettcher, Nickel−iron oxyhydroxide oxygen-evolution electrocatalysts: the role of intentional and incidental iron incorporation, J. Am. Chem. Soc. 136 (2014) 6744-53.
26. Xiaohong Li, Frank C. Walsh, D. Pletcher, Nickel based electrocatalysts for oxygen evolution in high current density, alkaline water electrolysers, Phys. Chem. Chem. Phys. 13 (2010) 1162-7.
27. O. Diaz-Morales, I. Ledezma-Yanez, M.T.M. Koper, F. Calle-Vallejo, Guidelines for the rational design of Ni-based double hydroxide electrocatalysts for the oxygen evolution reaction, ACS Catalysis 5 (2015) 5380-7.
28. S.J. Charles C. L. McCrory, Jonas C. Peters and Thomas F. Jaramillo, Benchmarking heterogeneous electrocatalysts for the oxygen evolution reaction, J. Am. Chem. Soc. 135 (2013) 16977−87.
29. K.Y. Sasaki, J.B. Talbot, Electrodeposition of iron-group metals and binary alloys from sulfate baths II. Modelling, J. Electrochem. Soc. 147 (2000) 189-97.
30. K.Y. Sasaki, J.B. Talbot, Electrodeposition of iron-group metals and binary alloys from sulfate baths I. Experimental study, J. Electrochem. Soc. 145 (1998) 981-90.
31. K.Y. Sasaki, J.B. Talbot, Electrodeposition of binary iron-group alloys, J. Electrochem. Soc. 142 (1995) 775-82.
32. A.M. Rashidi, A. Amadeh, The effect of current density on the grain size of electrodeposited nanocrystalline nickel coatings, Surf. Coat. Technol. 202 (2008) 3772-76.
33. Y. Yang, Preparation of Fe-Co-Ni ternary alloys with electrodeposition, Int. J. Electrochem. Sci. 10 (2015) 5164-75.
34. J.B. O'Sullivan, Studies in the electro-deposition of nickel. Part I. The effect of pH and of various buffering agents; the presence of oxygen in the deposits, Trans. Faraday Soc. 26 (1930) 89-93.
35. F. Ebrahimi, Z. Ahmed, The effect of current density on properties of electrodeposited nanocrystalline nickel, J. Appl. Electrochem. 33 (2003) 733-9.
36. N.A. Resali, K.M. Hyie, M.N.Berhan, Z. Salleh, S. Kasolang, Cobalt-nickel-iron nanoparticles coated on stainless steel substrate, Procedia Eng. 68 (2013) 30-6.
37. K.-Q. Zhang, M. Wang, R.-W. Peng, Y. Xiao, N.-b. Ming, H_3O^+-dependent morphological change in the electrochemical deposition of iron, Phys. Lett. A 278 (2001) 286-92.
38. C.V. Schenck, J.G. Dillard, J.W. Murray, Surface analysis and the adsorption of Co(ll) on goethite J. Colloid Interface Sci. 95 (1983) 398-409.
39. H. Sambe, T.M. Nabi, D.E. Ramaker, A.N. Mansour, W.E. O'Grady, *The oxidation state of Ni in the nickel oxide electrode and related nickel oxide compounds: 1. Spectroscopic evidence*. 1997, Office of Naval Research: Arlington, VA.

40. M.K. Bates, H.D. Qingying Jia, Wentao Liang, S. Mukerjee, Charge-transfer effects in Ni−Fe and Ni−Fe−Co mixed-metal oxides for the alkaline oxygen evolution reaction, ACS Catal. 6 (2016) 155-61.
41. M. Gong, Y. Li, H. Wang, Y. Liang, J.Z. Wu, J. Zhou, J. Wang, T. Regier, F. Wei, H. Dai, An advanced Ni−Fe layered double hydroxide electrocatalyst for water oxidation, J. Am. Chem. Soc. 135 (2013) 8452-5.
42. I.G. Casella, M.R. Guascito, M.G. Sannazzaro, Voltammetric and XPS investigations of nickel hydroxide electrochemically dispersed on gold surface electrodes, J. Electroanal. Chem. 462 (1999) 202-10.
43. H. Ali-Löytty, M.W. Louie, M.R. Singh, L. Li, H.G.S. Casalongue, H. Ogasawara, E.J. Crumlin, Z. Liu, A.T. Bell, A. Nilsson, D. Friebel, Ambient-pressure XPS study of a Ni−Fe electrocatalyst for the oxygen evolution reaction, J. Phys. Chem. C 120 (2016) 2247-53.
44. J. Eigeldinger, H. Vogt, The bubble coverage of gas-evolving electrodes in a flowing electrolyte, Electrochim. Acta 45 (2000) 4449-56.

Chapter 8 Design and Testing of a Secondary Tri-electrode Zinc-Air Set-up

Bifunctional ORR and OER catalyst electrodes currently dominate the literature of the research field. In theory, the “bifunctional” properties can simplify the electrode construction and help with cost reduction. In reality, however, it is not always the case that a catalyst which is optimal for ORR is optimal for OER and vice versa. Based on the advantages and disadvantages of the proposed secondary oxygen electrode designs (Chapter 2, Table 2.7), the tri-electrode configuration was found to be most suitable in this research because the ORR and OER electrodes can be optimised separately. In this chapter, the optimised ORR and OER electrodes from Chapters 5 and 7 were incorporated into a secondary tri-electrode Zn-air set-up. Details of the construction of the secondary cycling set-up are provided; and the effects of varying operational parameters on the performance as well as the long-term durability of the oxygen electrodes are assessed with the set-up.

8.1. Experimental section

8.1.1. Synthesis of oxygen electrocatalysts

ORR catalysts amorphous MnO_x and $MnCo_2O_4$ were prepared as outlined in Section 4.1.1. Amorphous MnO_x was prepared via a chemical redox method as previously reported [1]. 200 mL of 0.04 M $KMnO_4$ (Fisher Scientific, 99%) was added to 100 mL of 0.03 M $Mn(CH_3COO)_2$ (Fisher Scientific, 98%) with continuous stirring. The pH of the mixture was then adjusted to pH 12 with sodium hydroxide (Fisher Scientific, 98%). Following this, the mixture was centrifuged for 20 mins at a speed of 2500 rpm. This was repeated 3 to 5 times with rinsing in between with deionised H_2O. The brown precipitate collected was dried overnight in an oven at 333 K in air before being ground into a powder.

$MnCo_2O_4$ was synthesised by a thermal decomposition method. The precursor solution was made by adding methanol (Fisher Scientific, 99.9%) to 0.5 M (12.6 g) manganese (II) nitrate tetrahydrate $Mn(NO_3)_2.4H_2O$ (Sigma Aldrich, ≥ 97%) and 1 M (29.1 g) cobalt (II) nitrate hexahydrate, $Co(NO_3)_2.6H_2O$ (Fisher Scientific, 98+%, ACS

reagent) in a 100 mL dilution flask. The mixture was stirred well to ensure homogeneity and then heated in a crucible over a hot plate until dryness. The leftover dark red solid was then calcined in a furnace at 648 K for 20 h before finally being ground into a fine powder.

OER catalysts, Ni-Fe based hydroxides, were prepared as described in Section 7.1.1. Briefly, electroplating solutions comprising of 18 mM transition metal sulfate salt + 25 mM ammonium sulfate (Sigma Aldrich, ≥99%) were made from different ratios of transition metal salts nickel (II) sulfate hexahydrate, $NiSO_4.6H_2O$ (Sigma-Aldrich, ≥98%), iron (II) sulfate heptahydrate, $FeSO_4.7H_2O$ (Sigma Aldrich, ≥99.0%), cobalt (II) sulfate heptahydrate, $CoSO_4.7H_2O$ (Alfa Aesar, 98%) and ammonium molybdate tetrahydrate, $(NH_4)_6Mo_7O_{24}.4H_2O$ (Alfa Aesar, 99%). Cathodic deposition was carried out in ambient temperature at a current density of 200 mA cm^{-2} for 120s for the Ni-Fe and Ni-Fe-Mo hydroxide and at a current density of 300 mA cm^{-2} for 240s for the ternary Ni-Fe-Co hydroxide catalyst. The electroplating metal sulfate solution of Ni-Fe-Co hydroxide was adjusted to a pH of 3.9 with dilute sulfuric acid (AnalaR NORMAPUR®, ≥95%) before electrodeposition.

8.1.2. Electrode fabrication

ORR catalyst ink was prepared and then coated onto carbon paper to make gas diffusion electrodes following the previously reported protocol in Section 4.1.3. OER electrodes were fabricated by direct electrodeposition of catalyst onto pieces of 15 mm by 15 mm expanded SS mesh (DeXmet Corp, 4SS 5-050). The catalyst coated SS mesh was left to dry in air before an active area of ~ 0.8 cm^2 was cut out of it with a 10 mm carbon steel die.

Commercial ORR and OER electrodes were used as received and tested under the same conditions for comparison. The commercial ORR electrode (QSI-Nano® Gas Diffusion Electrodes, Quantum Sphere, 0.35 mm thick) was composed of manganese oxide and carbon coated onto a nickel mesh current collector, whilst the commercial OER electrode (Type 1.7, Magneto special anodes, B.V.) was an expanded Ti mesh 1.3 to 1.6 mm thick, coated with Ru-Ir mixed metal oxides.

8.1.3. Electrochemical characterisation

Electrochemical measurements were carried out with a Biologic SP-150 potentiostat and EC-lab software. The performances of the fabricated ORR and OER electrodes were evaluated in a jacketed glass cell (200 cm^3) with a PTFE insert similar to the GDE cell described in Section 4.1.3. **Figure 8.1** presents a schematic of the jacketed glass cell with electrodes connected to a relay module and microcontroller. The electrodes in the cell were connected as in a three electrode system. The working electrode connector of the potentiostat was attached to the relay module, the counter electrode connector was connected to the Zn anode and the reference electrode connector was connected to the reference electrode.

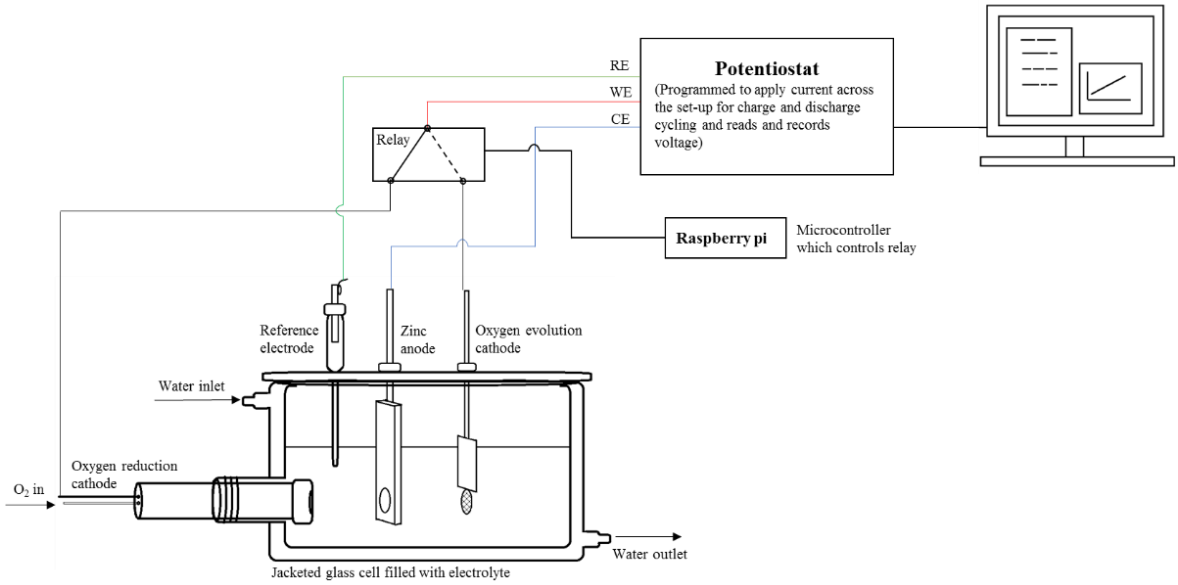

Figure 8.1 Schematic of electrodes in jacketed glass cell used for galvanostatic cycling connected to Raspberry Pi microcontroller set-up.

As seen in **Figure 8.2 a**, the cell was modified to accommodate a Zn foil (Goodfellow, 1 mm thick, 99.95%) anode and the use of a polymer lid allowed the electrodes to be positioned at a fixed distance of 4 mm in parallel to each other unless otherwise stated. Stoppers were made from nitrile rubber to hold the electrodes in position in the lid and nickel wire (Alfa Aesar, 0.5 mm dia, annealed, 99.5%) was used for electrical contact of the electrodes. The Zn foil anode was cleaned in isopropanol followed by deionised water before use. The surface of the Zn foil was then masked off with polypropylene tape (Avon, 25 µm thick) to expose an active area of ~ 0.8 cm^2.

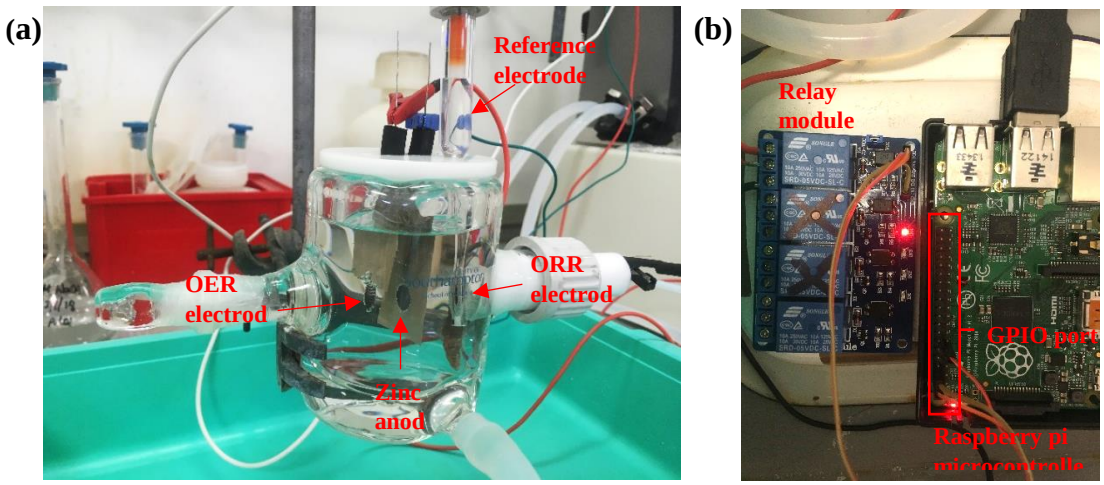

Figure 8.2 Labelled photographs of the **a)** glass cell and **b)** relay module with Raspberry Pi microcontroller in the cycling set-up.

The microcontroller (**Figure 8.2 b**) used in this set-up is a Raspberry Pi model B+ V1. 2 (Raspberry Pi 2014 ©) which uses General Purpose Input/ Output (GPIO) pins to control input and output devices etc. These digital IO pins are either in an on or off state. The relay (Songle relay, maximum output of AC 250 V, 10 A and DC 30V, 10 A) used in this set-up was part of a four-relay module which required 15-20 mA of current and was controlled by a DC 5 V input voltage. The module was connected to the Raspberry Pi and supplied with power via the VCC pin and ground via the GND pin whilst the relays were initiated by low inputs to the IN1, IN2 etc. pins. Apart from sharing the power and ground pin, each of the four relays in the module operated as a separate circuit isolated from each other. Each relay had a common, normally open (NO) and normally closed (NC) terminal which are marked clearly on the relay board. The ORR electrode was connected to the normally closed terminal and the OER electrode was connected to the normally open terminal.

The relay board consisted of an opto-coupler which uses light to transfer electrical signals between two circuits, this allowed for isolation from the high voltage inputs ensuring safety when using the board. LEDS embedded in the board acted as a visual indication of the position of the relay switch. The interface of the relay board was also directly compatible with several microcontrollers including the Raspberry Pi. In this instance, Python programming language was used and the script written to control the relay board is given in Appendix C. Variables ‘SleepTimeL’ and

'SleepTimeS' refer to the period of cycle time (e.g. 15 min) and rest time (e.g. 1 min at OCV) in between cycles.

All experiments were carried out in electrolyte of 4 M NaOH + 0.3 M ZnO at 333 K unless otherwise stated and potentials were measured against an Hg/ HgO reference electrode in 4 M NaOH held at a distance of ~3 mm from the anode. Oxygen or compressed air was supplied at a constant flow rate of 200 cm^3 min^{-1} to the back of the oxygen reduction electrode. The cycling stability and performance of the electrodes was investigated at a current density of 20 mA cm^{-2} for a cycle period of 30 mins with 1 min rest period at OCV between each half cycle. Each test was run for at least 10 cycles and data was extracted from cycles 1, 5 and 10 in order to establish the state of the electrodes over time. Energy efficiency was calculated as described in equation (8.1)

$$Energy\ efficiency\ (\%) = \frac{Discharge\ capacity,Ah\ x\ Discharge\ voltage,V}{Charge\ capacity,Ah\ x\ Charge\ voltage,V}\ x\ 100\% \qquad (8.1)$$

8.2. Results and discussion

8.2.1. Selection of ORR and OER electrodes

The performances of the Ni-Fe based hydroxide electrodes were initially assessed against the commercial OER electrode in the cycling set-up. Commercial ORR electrodes were used for these tests, the voltage versus time plots of cycle 1, 5 and 10 are given in **Figure 8.3**.

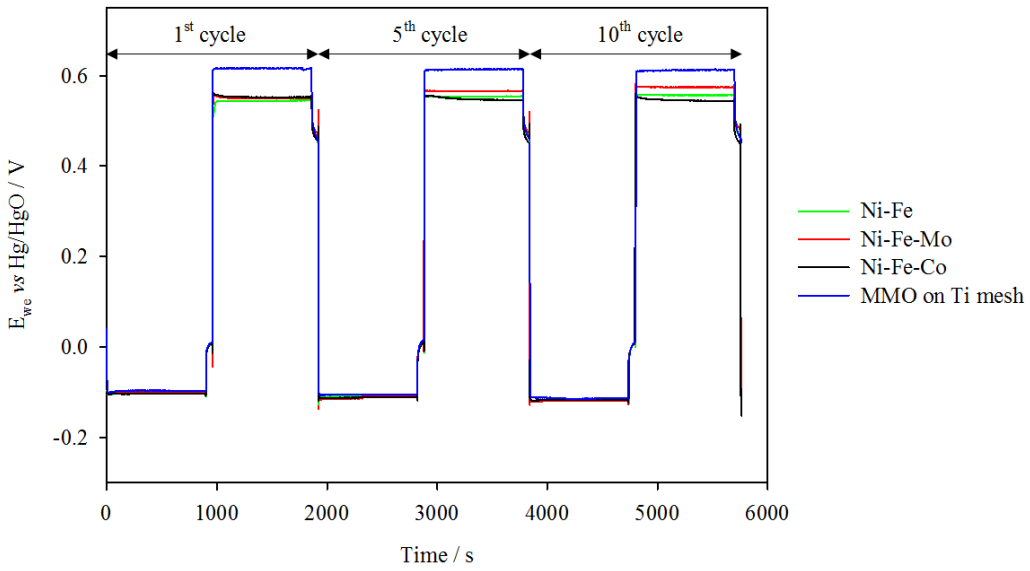

Figure 8.3 Comparison of OER electrodes at 20 mA cm^{-2} alternating between oxygen reduction and evolution in static electrolyte 4 M NaOH + 0.3 M ZnO at 333 K, O_2 was supplied at a constant flow rate of 200 cm^3 min^{-1}.

Table 8.1 summarises the potentials of the OER electrodes at cycles 1, 5 and 10 as well as the polarisation, ΔE, between ORR and OER. A smaller potential window between ORR and OER marks a higher voltage efficiency for the system, therefore it is a good indicator of performance for both the forward and backward reactions of the electrode. It can be seen clearly that all Ni-Fe hydroxide based catalysts had between 40 to 70 mV less OER overpotential than the precious metal benchmark electrode. In cycle 1, the OER activity of both Ni-Fe$(OH)_2$ and Ni-Fe-Mo$(OH)_2$ coated SS mesh electrodes surpasses that of Ni-Fe-Co$(OH)_2$ coated SS mesh. However, the Ni-Fe-Co$(OH)_2$ coated SS mesh electrode displayed a gradual decrease in OER overpotential over 10 cycles whilst the performance of both Ni-Fe$(OH)_2$ and Ni-Fe-Mo$(OH)_2$ coated SS mesh electrodes degraded rapidly after the first 5 cycles with increases of up to 22 mV in overpotential over the course of the experiment. This indicates that the Ni-Fe-Co$(OH)_2$ coated SS mesh electrode is more stable than the Ni-Fe$(OH)_2$ and Ni-Fe-Mo$(OH)_2$ hydroxide coated SS mesh electrodes.

Table 8.1 Results from Figure 8.3 of cycling data comparing various OER electrodes.

Cycle number	OER electrode	E_{we} (Charge) *vs* Hg/HgO / mV	Δ E between ORR and OER/ mV
1	Ni-Fe$(OH)_2$ on SS mesh	544	646
	Ni-Fe-Mo$(OH)_2$ on SS mesh	550	649
	Ni-Fe-Co$(OH)_2$ on SS mesh	553	657
	MMO on Ti mesh	615	712
5	Ni-Fe$(OH)_2$ on SS mesh	554	664
	Ni-Fe-Mo$(OH)_2$ on SS mesh	566	675
	Ni-Fe-Co$(OH)_2$ on SS mesh	547	658
	MMO on Ti mesh	614	719
10	Ni-Fe$(OH)_2$ on SS mesh	556	674
	Ni-Fe-Mo$(OH)_2$ on SS mesh	572	691
	Ni-Fe-Co$(OH)_2$ on SS mesh	545	660
	MMO on Ti mesh	613	728

As the performance of the ORR commercial electrode was observed to degrade at a constant rate across these experiments, the activities of prepared ORR catalysts $MnCo_2O_4$ and MnO_x were compared against the commercial QSI-Nano® ORR electrode in the cycling set-up. Ni-Fe-Co$(OH)_2$ was employed as the OER electrode for these tests and results are shown in **Figure 8.4.**

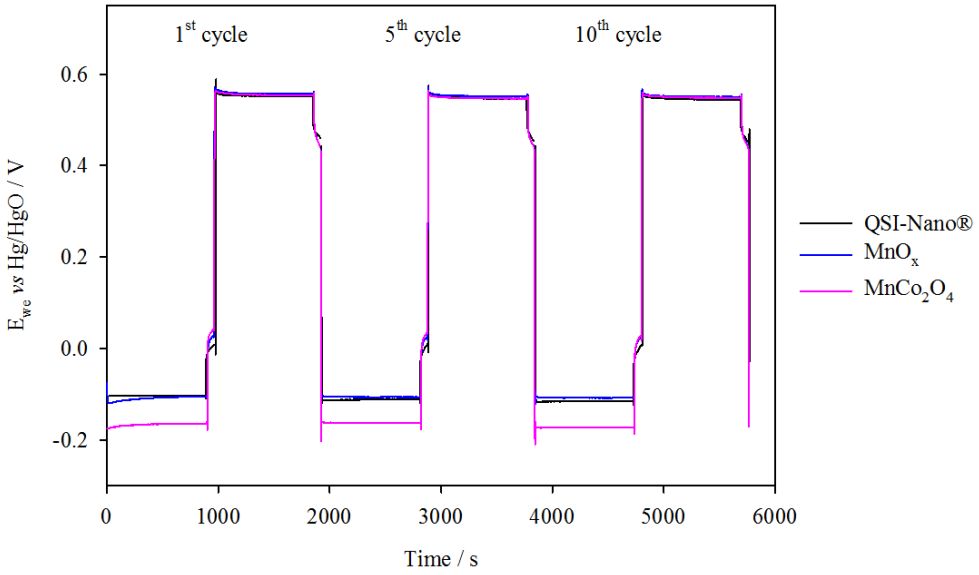

Figure 8.4 Comparison of ORR electrodes at 20 mA cm^{-2} alternating between oxygen reduction and evolution in static electrolyte 4 M NaOH + 0.3 M ZnO at 333 K, O_2 was supplied at a constant flow rate of 200 cm^3 min^{-1}.

The working potentials for these ORR electrodes are given in **Table 8.2**. Across all cycles, the ORR overpotential of the $MnCo_2O_4$ catalyst coated electrode was 51−64 mV greater than that of the commercial ORR electrode and amorphous MnO_x catalyst coated electrode and therefore not used for further cycling experiments. The initial performance of the commercial ORR electrode and amorphous MnO_x appears to be quite similar however the ORR overpotential of the commercial ORR electrode increased more rapidly over 10 cycles due to electrode degradation or instability. Additionally, the mass of the commercial electrode was nearly four times that of the amorphous MnO_x on carbon paper indicating that amorphous MnO_x has a greater activity per gram of catalyst.

Table 8.2 Results from Figure 8.4 of cycling data comparing various ORR electrodes.

Cycle number	ORR electrode	E_{we} (Discharge) *vs* Hg/HgO / mV	Δ E between ORR and OER/ mV
1	QSI-Nano®	-0.104	657
	Amorphous MnO_x on C paper	-0.106	663
	$MnCo_2O_4$ on C paper	-0.165	720
5	QSI-Nano®	-0.111	658
	Amorphous MnO_x on C paper	-0.106	659
	$MnCo_2O_4$ on C paper	-0.163	711
10	QSI-Nano®	-0.115	660
	Amorphous MnO_x on C paper	-0.108	659
	$MnCo_2O_4$ on C paper	-0.172	721

The amorphous MnO_x coated electrode and Ni-Fe-Co hydroxide coated SS mesh which displayed good performance and stability over the duration of the experiment were selected for further cycling experiments. **Figure 8.5** shows consecutive charge and discharge cycling data at 20 mA cm^{-2} of the tri-electrode system with MnO_x on carbon paper (ORR) and Ni-Fe-Co hydroxide on stainless steel mesh (OER) oxygen electrodes. As the overall shape of the E_{cell} plot resembles that of the oxygen electrode (E_{we}) plot, it is clear that the oxygen electrode has a much greater contribution to the

overall overpotential of the reaction compared to the Zn electrode (E_{ce}). The voltage efficiency of the system was calculated to be approximately 64%. The coulombic efficiency of the system is approximately 100% due to the utilisation of Zn foil, this resulted in an energy efficiency of the same value, 64%. This indicates a strong link between the reduction of oxygen overpotential and increase in the energy efficiency.

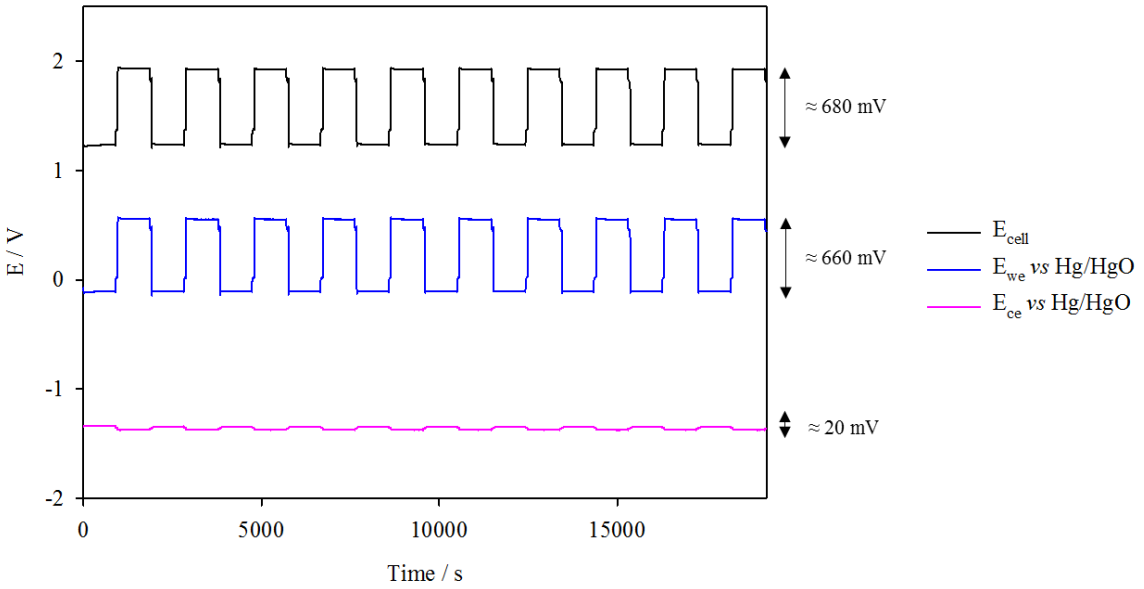

Figure 8.5 Galvanostatic cycling data at 20 mA cm^{-2} for 15 min charging period cycles with 1 min OCV after each charge/ discharge step. Oxygen electrodes of amorphous MnO_x on C paper (ORR) and Ni-Fe-Co hydroxide on SS mesh (OER) were positioned on either side of a Zn foil anode in static electrolyte 4 M NaOH + 0.3 M ZnO at 333 K. O_2 was supplied at a constant flow rate of 200 cm^3 min^{-1}.

8.2.2. Effect of testing parameters

8.2.2.1. Inter-electrode gap

As an important design consideration, the effect of the distance of the inter-electrode gaps on the voltage drop across the electrodes needs to be investigated. Considering Ohm's law, the additional iR drop through the system given in equation (8.2) is seen to be directly proportional to the current applied, *i* as well as the resistance through the conductor, R.

$$E = iR \qquad (8.2)$$

The resistance, R of a conductor is a function of *l*, ρ and A as expressed by equation (8.3).

$$R = \frac{l}{\sigma A} = \frac{\rho l}{A} \qquad (8.3)$$

Where *l* is the length or distance through which the external electric field is applied

σ is the conductivity of the material

ρ is the resistivity of the material $(\rho = \frac{1}{\sigma})$

A is the cross sectional area of the conductor

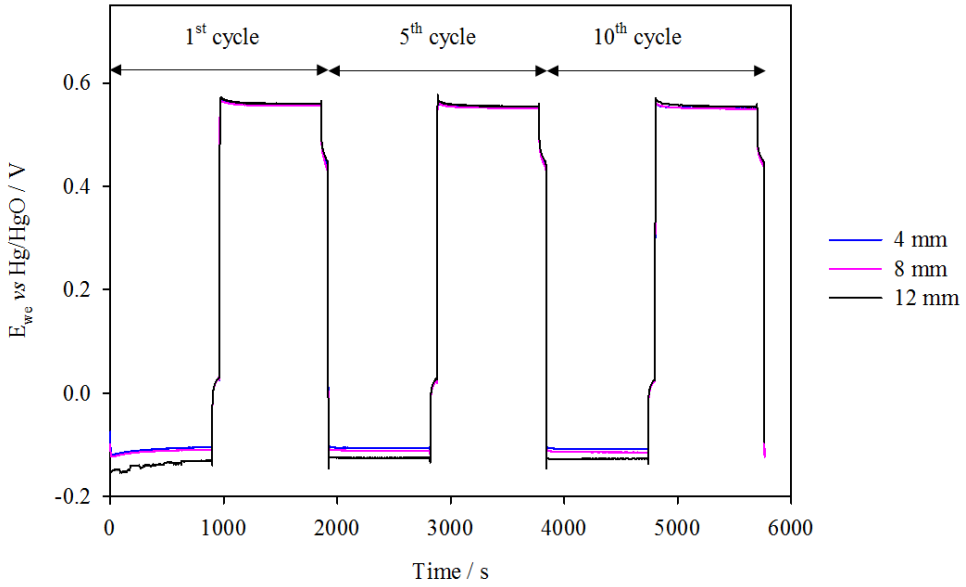

Figure 8.6 Effect of different inter-electrode gaps at 20 mA cm^{-2} alternating between oxygen reduction and evolution in static electrolyte 4 M NaOH + 0.3 M ZnO at 333 K, O_2 was supplied at a constant flow rate of 200 cm^3 min^{-1}.

Table 8.3 Performance data extracted from the 10th cycle of Figures 8.6.

j/ mA cm^{-2}	Gap / mm	Charge / V			Discharge / V			Δ E / mV		Energy efficiency / %
		E_{cell}	E_{we} *vs* Hg/HgO	E_{ce} *vs* Hg/HgO	E_{cell}	E_{we} *vs* Hg/HgO	E_{ce} *vs* Hg/HgO	ORR and OER	Zn	
20	4	1.926	0.551	1.375	1.238	-0.108	1.346	659	29	64
	8	1.929	0.550	1.379	1.231	-0.114	1.345	664	34	64
	12	1.931	0.555	1.376	1.213	-0.128	1.341	683	35	63

In this study, the effect of three different distances i.e. 4 mm, 8 mm and 12 mm, between the oxygen electrodes and the Zn electrode, were reported in **Figure 8.6**. The performance and efficiency data from **Figure 8.6** is extracted and tabulated in **Table 8.3**. At a lower current density of 20 mA cm^{-2}, the potential window between ORR and OER was observed to increase with inter-electrode gap from 659 mV at 4

mm to 683 mV at 12 mm. This was mainly due to increases in overpotential at the ORR electrode and suggested to be because of the tortuosity of the ORR catalyst layer, which increases the distance, l, affects the current distribution across the surface and flux of reactants reaching the three phase boundary layer. On the other hand, no significant increase in OER overpotential was observed with increases in inter-electrode gap up to 12 mm indicating that the OER electrode's performance is independent of inter-electrode gap at 20 mA cm^{-2}.

The voltage window between Zn potentials is observed to follow an increasing trend with inter-electrode gap 4 mm < 8 mm < 12 mm. The energy efficiency, however, was not visibly affected by the increases in electrode gap at 20 mA cm^{-2} as the electrolyte was perhaps sufficiently conductive to prevent large voltage drops across the electrodes.

8.2.2.2. Current density

The performance of the oxygen electrodes was monitored using constant chronopotentiometry at 10 mA cm^{-2}, 20 mA cm^{-2}, 50 mA cm^{-2} and 100 mA cm^{-2} as shown in **Figure 8.7**. As defined in equations (8.2) and (8.3), the overpotential at the electrodes is a function of current density. At higher current densities, the overpotentials of both oxygen electrodes are seen to increase although the rise in overpotentials at the ORR electrode was three to five times greater than the OER electrode. This indicates that the performance of the ORR electrode is more sensitive to changes in current than the OER electrode.

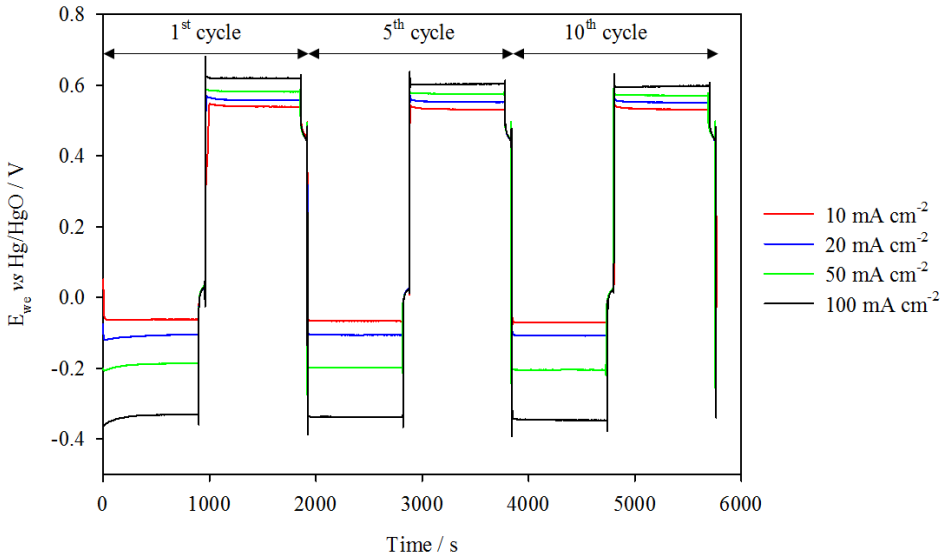

Figure 8.7 Effect of various current densities on oxygen electrode performance in static electrolyte 4 M NaOH + 0.3 M ZnO at 333 K, O_2 was supplied at a constant flow rate of 200 cm^3 min^{-1}.

Table 8.4 Performance data extracted from the 10th cycle of Figure 8.7.

j/ mA cm^{-2}	Capacity/ mAh	Charge / V			Discharge / V			Δ E / mV		Energy efficiency / %
		E_{cell}	E_{we} *vs* Hg/HgO	E_{ce} *vs* Hg/HgO	E_{cell}	E_{we} *vs* Hg/HgO	E_{ce} *vs* Hg/HgO	ORR and OER	Zn	
10	2	1.903	0.532	1.371	1.281	-0.070	1.351	606	20	67
20	4	1.926	0.551	1.375	1.238	-0.108	1.346	659	29	64
50	10	1.956	0.571	1.385	1.140	-0.204	1.344	775	41	58
100	20	2.011	0.596	1.415	0.978	-0.346	1.324	942	91	49

The ORR electrode potential increased by ~ 40 mV following the first 10 mA cm^{-2} increase in current density from 10 to 20 mA cm^{-2}. Every subsequent 10 mA cm^{-2} increase up to 100 mA cm^{-2} resulted in a further ~30 mV increase in overpotential signifying a strong dependence of ORR overpotential on current density. Similarly, the OER electrode potential was observed to increase at a decreasing rate with current density. The first 10 mA cm^{-2} increase in current density resulted in a ~ 20 mV increase in overpotential, followed by an increase of only ~ 7 mV per 10 mA cm^{-2} increase between 20 and 50 mA cm^{-2}. This was further reduced to just ~5 mV per 10 mA cm^{-2} increase between 50 and 100 mA cm^{-2}. As the increases in overpotential, at the OER

electrode in particular, were not directly proportional to increases in current density it implies that the OER overpotential is much less dependent on this parameter.

On the contrary, the potential window between charge and discharge potentials for the Zn electrode increased at a consistent rate of ~10 mV for every 10 mA cm^{-2} increase in current density indicating a strong dependence of the overpotential on current. The contribution of the Zn electrode overpotential to the overall overpotential of the system over the range of current densities tested however, was still significantly lower than the oxygen electrodes. The voltage efficiency and hence the energy efficiency of the whole system saw a decrease of ~ 3% per 10 mA cm^{-2} increase in current density.

8.2.2.3. Electrolyte concentration

The molarity of the NaOH electrolyte was varied from 2 M to 8 M and the electrolyte conductivity was measured with a benchtop conductivity meter (Jenway, 4310) at 333 K as shown in **Table 8.5**. The conductivity does not increase linearly with molarity with the largest increase in conductivity of 89 mS cm^{-1} recorded between 2 M and 4 M NaOH. Further increasing the molarity of the NaOH electrolyte from 4 M to 6 M only produced a rise of 9 mS cm^{-1} and an increase of just 7 mS $^{-1}$ was seen between 6 M and 8 M.

Table 8.5 Conductivity of different molarities of electrolyte at 333 K.

Electrolyte	**Conductivity / mS cm^{-1}**
2 M NaOH + 0.3 M ZnO	266
4 M NaOH + 0.3 M ZnO	353
6 M NaOH + 0.3 M ZnO	362
8 M NaOH + 0.3 M ZnO	369

The NaOH electrolyte concentration was observed to affect the Zn and oxygen electrodes in different ways. As the electrolyte concentration increased, the oxidation and reduction potentials of the Zn anode shifted to more negative values whilst retaining the same potential separation of ~30 mV as seen in **Figure 8.8**. The Zn anode half reaction is given as

Charge: $Zn(OH)_4^{2-} + 2e^- \leftrightarrow Zn + 4OH^-$ E^θ = -1.25 V vs SHE (8.4)

The overall cathodic reaction, as proposed by Bockris [2], involves the reduction of Zn^{2+} to Zn^+ and then Zn, through two electron transfer steps. The rate determining step is the same regardless of the direction in which the reaction proceeds.

$$Zn(OH)_4^{2-} \rightarrow Zn(OH)_3^- + OH^- \quad (8.5)$$

$$Zn(OH)_3^- + e^- \xrightarrow{rds} Zn(OH)_2^- + OH^- \quad (8.6)$$

$$Zn(OH)_2^- \rightarrow ZnOH + OH^- \quad (8.7)$$

$$ZnOH + e^- \rightarrow Zn + OH^- \quad (8.8)$$

The gradual shift in observed potentials towards more negative values for the charge and discharge reaction of Zn anode agrees well with observations by Bockris of the Zn rest potential, which was affected by the pH of the alkaline zincate solution that it is placed in.

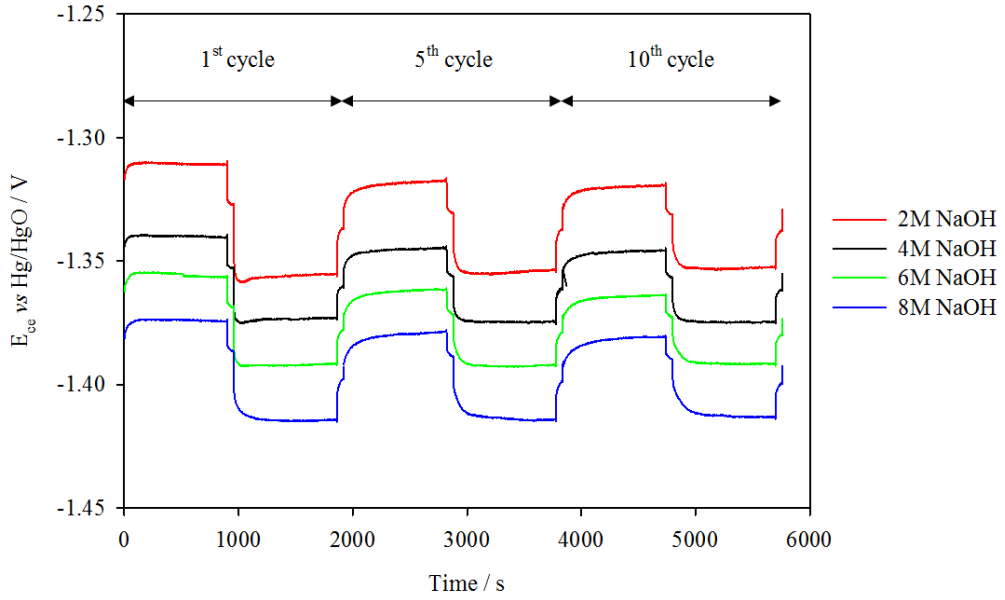

Figure 8.8 Effect of electrolyte concentration on Zn electrode performance in static electrolyte 4 M NaOH + 0.3 M ZnO at 333 K, O_2 was supplied at a constant flow rate of 200 $cm^3\ min^{-1}$.

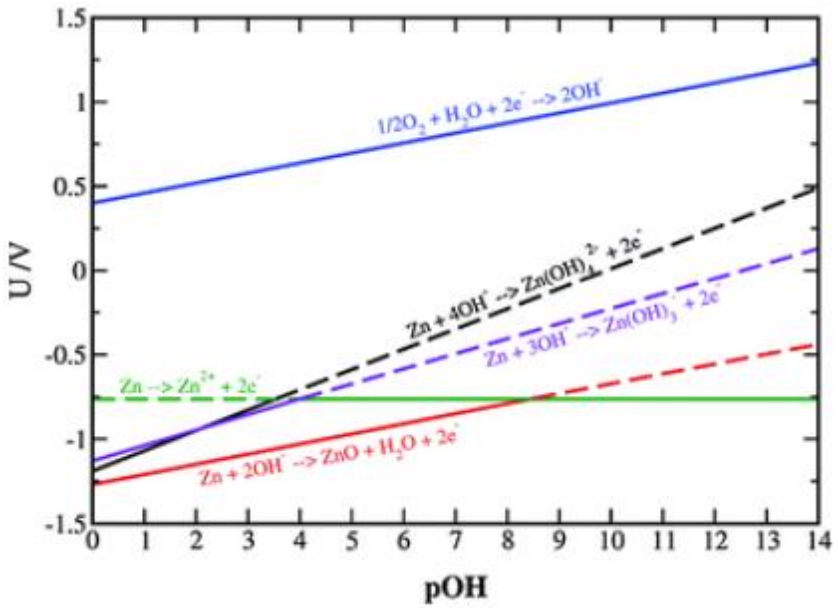

Figure 8.9 Standard electrode potential versus pOH plot for the anodic and cathodic reactions in a Zn-air cell [3].

Although the dissolution of Zn is an electrochemical process, the formation of aqueous $Zn(OH)_4^{2-}$ is a chemical step which is dependent on the presence of OH^- ions in the solution. From the standard electrode potential plot versus pOH of the cathodic and anodic reactions in a Zn-air cell in **Figure 8.9** from Rossmeisl *et al.* [3], at higher pH or lower pOH values the standard electrode potentials for the dissolution of zinc are seen to decrease to more negative values. At lower pOH values, the energy levels for $Zn(OH)_3^-$ and $Zn(OH)_4^{2-}$ converge suggesting that the zinc dissolution reaction takes place more rapidly. This is reflected in the negative shift in potential of the discharge reaction of zinc. On the other hand, the $Zn(OH)_3^-$ and $Zn(OH)_4^{2-}$ ions are more stable at higher pH or lower pOH values resulting in a greater equilibrium cell potential for the reverse reaction or deposition of Zn as well. Since the two reactions take place at different faces of the Zn anode in this secondary cell set-up, the reaction potentials for both charge and discharge are shifted to the same extent resulting in a similar potential gap for the Zn anode regardless of the electrolyte concentration.

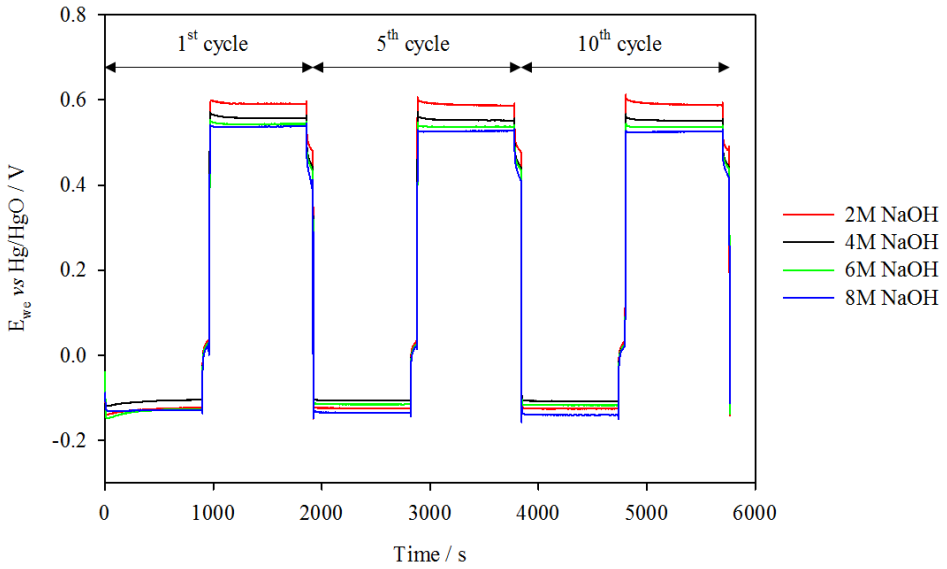

Figure 8.10 Effect of electrolyte concentration on oxygen electrode performance at 20 mA cm^{-2} in static electrolyte 4 M NaOH + 0.3 M ZnO at 333 K, O_2 was supplied at a constant flow rate of 200 cm^3 min^{-1}.

The response of the ORR electrode at different electrolyte concentrations is given in **Figure 8.10**. It is noted that in cycle 1, the ORR overpotentials for the electrodes in 6 M and 8 M electrolyte concentration are slightly greater. This was likely because of the greater viscosities of the electrolyte. The system equilibrated by cycle 5 as the ORR overpotentials remained quite consistent up to cycle 10.

The ORR electrode tested in 2 M NaOH electrolyte concentration displayed the highest overpotential due to the low conductivity of the reaction environment. Increasing the concentration of electrolyte to 4 M reduced the overpotential for ORR significantly by ~20 mV which can be attributed to the large increase in conductivity. However, further increasing the NaOH concentration to 6 M and 8 M resulted in subsequent increases in overpotential for ORR. This suggests that at electrolyte concentrations of ≥ 6 M, the increase in conductivity is outweighed by detrimental effects of greater viscosity and decreasing oxygen solubility and diffusivity [4], all of which contribute to a lower concentration of oxygen at the three phase boundary. On top of this, since the ORR results in the production of OH^- ions, a high concentration of OH^- in the electrolyte can hinder the rate of protonation of O_2^- to HO_2^- thereby increasing the overpotential of the reaction.

The OER electrode performance was observed to improve with increasing electrolyte concentration as presented in **Table 8.6**. This can be related to the changes in adsorption energy of intermediates in the OER reaction pathway which has been shown to be influenced by pH [5, 6]. In an electrolyte concentration of 4 M, the overpotential of the OER electrode was ~30 mV less than that of the OER electrode in 2 M. The OER electrode overpotential was decreased further in an electrolyte concentration of 6 M by ~ 20 mV and by another 10 mV in an electrolyte concentration of 8 M.

Table 8.6 Performance data extracted from the 10th cycle of Figures 8.8 and 8.10.

Electrolyte molarity / M	**Charge / V**			**Discharge / V**			**Δ E / mV**		**Energy efficiency / %**
	E_{cell}	E_{we} *vs* Hg/HgO	E_{ce} *vs* Hg/HgO	E_{cell}	E_{we} *vs* Hg/HgO	E_{ce} *vs* Hg/HgO	ORR and OER	Zn	
2	1.944	0.590	1.354	1.195	-0.126	1.321	716	33	62
4	1.926	0.551	1.375	1.238	-0.108	1.346	659	29	64
6	1.927	0.535	1.392	1.247	-0.117	1.364	652	28	65
8	1.939	0.525	1.414	1.241	-0.140	1.381	665	33	64

Interestingly the polarisation, ΔE, between ORR and OER was comparable in 4 M and 6 M NaOH electrolyte concentration as the improvement in OER performance offsets the reduction in ORR performance. Overall from **Table 8.6**, the voltage and energy efficiencies of the system in both 4 M and 6 M electrolyte concentration were fairly similar as well. Therefore, either 4 M or 6 M NaOH electrolyte concentration is suitable for further tests.

8.2.2.4. Temperature

As reaction rates are dependent on temperature as seen from the Arrhenius equation [7-9] given below, the effect of temperature on the performances of the electrodes are examined.

$$k\,(T) = Ae^{-\frac{E_a}{RT}} \qquad (8.9)$$

Where k is the reaction rate constant

R is the universal gas constant, 8.314 J mol^{-1} K^{-1}

E_a is the activation energy
A is a pre-exponential factor
T is the temperature in Kelvin, K

The temperature of the NaOH electrolyte was varied from 25 ºC to 80 ºC. A lower limit of 25 ºC was selected to mimic room temperature conditions and an upper limit of 80 ºC was selected as temperatures higher than this could be hazardous and loss of water from the electrolyte through evaporation occurs more rapidly. From the plots in **Figure 8.11**, it is clear that as the temperature increases the overpotential of both oxygen reactions decreases.

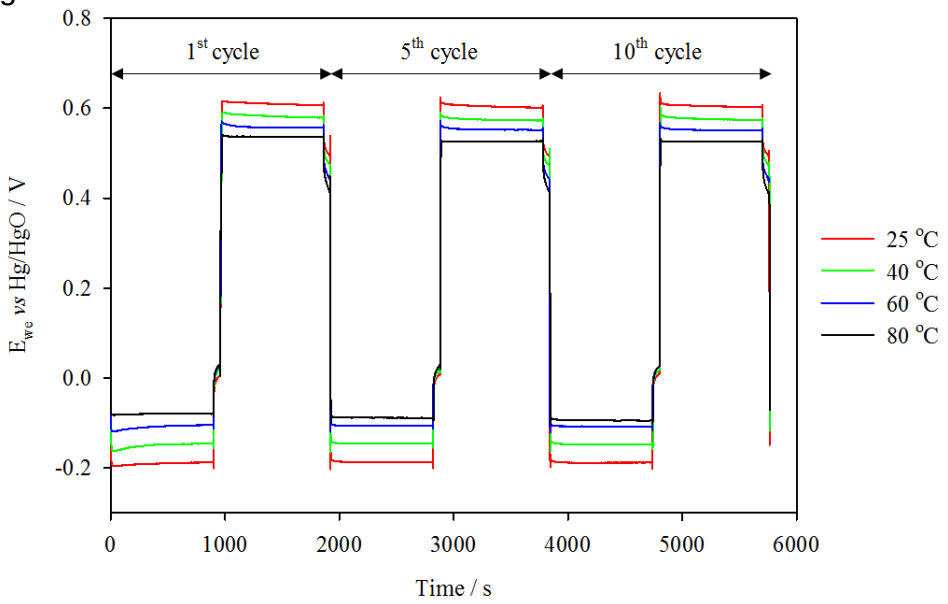

Figure 8.11 Effect of temperature on oxygen electrode performance at 20 mA cm^{-2} in static electrolyte 4 M NaOH + 0.3 M ZnO at 333 K, O_2 was supplied at a constant flow rate of 200 cm^3 min^{-1}.

Table 8.7 Performance data extracted from cycle 10 of Figure 8.11**.**

Temperature / ºC	**Charge / V**			**Discharge / V**			**Δ E / mV**		**Energy efficiency / %**
	E_{cell}	E_{we} *vs* Hg/HgO	E_{ce} *vs* Hg/HgO	E_{cell}	E_{we} *vs* Hg/HgO	E_{ce} *vs* Hg/HgO	ORR and OER	Zn	
25	1.993	0.604	1.389	1.159	-0.189	1.348	793	42	58
40	1.955	0.575	1.380	1.200	-0.147	1.347	722	33	61
60	1.926	0.551	1.375	1.238	-0.108	1.346	659	29	64
80	1.904	0.526	1.378	1.260	-0.094	1.354	620	24	66

The reduction in the potential window between ORR and OER was observed to occur at a decreasing rate with increases in temperature (**Table 8.7**). This can be explained by the Arrhenius equation which describes the reaction rate as increasing exponentially with temperature. Between temperatures of 25 ºC and 40 ºC a decrease in overpotential of ~ 50 mV per 10 ºC increase was observed. Subsequently between 40 ºC and 60 ºC, the overpotential was reduced by ~ 30 mV per 10 ºC rise in temperature and further increases in temperature from 60 ºC to 80 ºC resulted in a ~ 20 mV reduction in overpotential per 10 ºC increase in temperature. The potential window between the zinc deposition/ dissolution was greater at lower temperatures as well. The reduction in the polarisation for the zinc deposition/ dissolution was 6 mV per 10 ºC increase in temperature between 25 ºC and 40 ºC. However at higher temperatures between 60 ºC and 80 ºC, the potential gap was reduced by only ~2 mV per 10 ºC increase in temperature signifying that the Zn electrode reactions are less sensitive to changes in temperature compared to the oxygen electrode reactions. Overall, as the voltage and energy efficiency is mainly influenced by the potential window between ORR and OER, the efficiency values are also observed to increase at a decreasing rate accordingly with rises in temperature.

At a lower temperature of 25 ºC to 40 ºC the effect of temperature is initially more significant at the ORR electrode than the OER electrode whereby a ~ 30 mV decrease in ORR overpotential was observed per 10 ºC increase compared to a ~ 20 mV reduction in overpotential at the OER electrode. However between 60 ºC and 80 ºC, the effect of temperature on either of the oxygen electrodes becomes more comparable with a ~10 mV reduction in overpotential per 10 ºC increase at either electrode.

8.2.2.5. Compressed air versus O_2

For large-scale applications, it would be challenging and impractical to supply large volumes of pure oxygen to the system. It is therefore essential to understand how the electrodes, especially the ORR electrode, responds to the use of air in place of pure O_2. A major challenge associated with the use of air instead of O_2, however, is the formation of carbonates of low solubility from the interaction of atmospheric CO_2 with the alkaline electrolyte [10], leading to clogging of the pores in the gas diffusion

layer of the ORR electrode which contributes to the premature failure of the system. Filters and continuous CO_2 scrubbers such as soda lime or amines [11] have been shown to manage the concentration of CO_2 in the compressed air before it enters the system. In this work, the compressed air supplied to the oxygen reduction electrode was not scrubbed as the formation of carbonates over this timescale was not expected to be significant as seen from the relatively consistent discharge potentials of the ORR electrode in **Figure 8.12**.

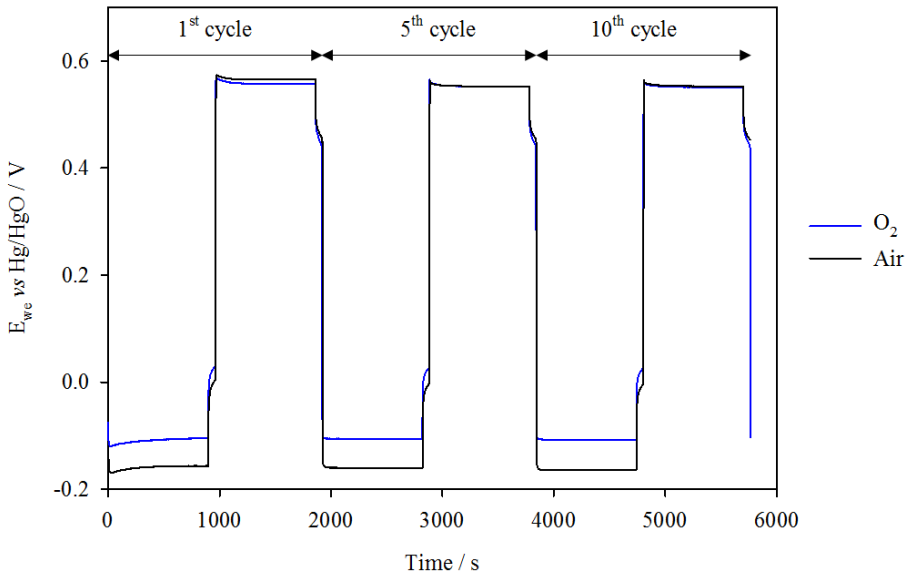

Figure 8.12 Effect of supply of O_2 on oxygen electrode performance at 20 mA cm^{-2} in static electrolyte 4 M NaOH + 0.3 M ZnO at 333 K, O_2 or compressed air was supplied at a constant flow rate of 200 cm^3 min^{-1}.

From the plots, the overpotential of the OER electrode appears unaffected by the use of compressed air, as expected, but the ORR electrode overpotential is seen to be ~ 56 mV greater. The voltage window of the Zn electrode given in **Table 8.8**, remains unaffected by the use of compressed air as well. Therefore the decrease in voltage and energy efficiency of the system is affected solely by the increase in the polarisation between ORR and OER. As air is typically composed of only ~21% oxygen, the use of compressed air is seen to cause ~3% reduction in energy and voltage efficiency of the system.

Table 8.8 Performance data extracted from cycle 10 of Figure 8.12.

Source of O_2	Charge / V			Discharge / V			Δ E / mV		Energy efficiency / %
	E_{cell}	E_{we} *vs* Hg/HgO	E_{ce} *vs* Hg/HgO	E_{cell}	E_{we} *vs* Hg/HgO	E_{ce} *vs* Hg/HgO	ORR and OER	Zn	
Compressed air	1.925	0.553	1.372	1.180	-0.164	1.344	718	28	61
Bottled O_2	1.926	0.551	1.375	1.238	-0.108	1.346	659	29	64

8.2.2.6. Sensitivity of electrodes to test parameters

To determine the sensitivity of the oxygen electrodes to the parameters tested, the changes in overpotential at the ORR and OER electrodes were plotted against these parameters in **Figure 8.13**. The effect of compressed air versus O_2 was omitted as it is clear that this parameter only affects the ORR electrode.

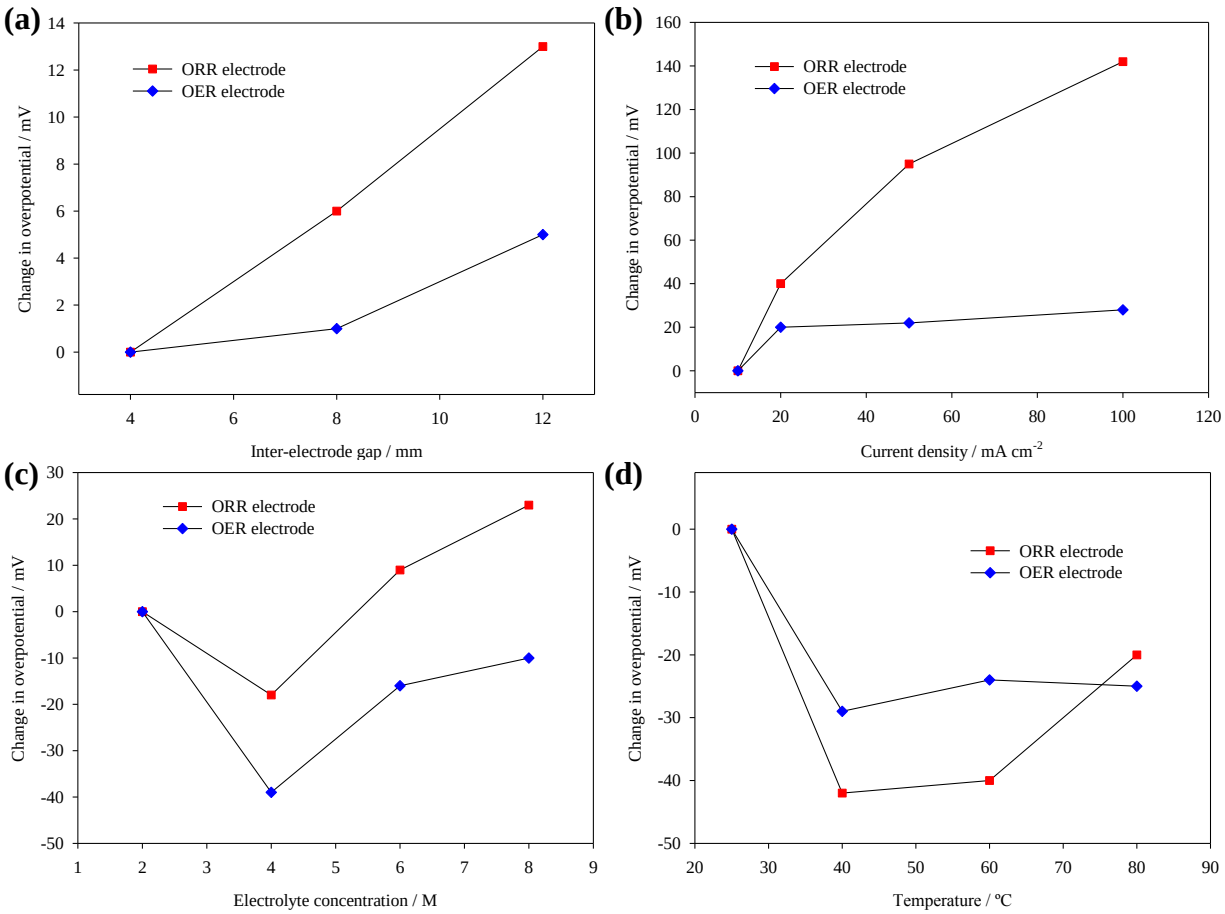

Figure 8.13 Change in overpotential at the ORR and OER electrode versus **a)** inter-electrode gap, **b)** current density, **c)** electrolyte concentration and **d)** temperature.

The performance of the ORR electrode compared to the OER electrode is more sensitive to changes in inter-electrode distance as well as temperature and current density. This suggests that a clear current path is vital for ensuring good ORR performance hence the catalyst layer and electrode structure are of particular importance for the ORR electrode. The transport of reactants to the three-phase boundary within the ORR electrode catalyst layer is equally important as electrolyte temperature, which alters the electrolyte viscosity and solubility of oxygen in the electrolyte, producing a more noticeable effect on the rate of change of ORR overpotential as well. In contrast, the OER electrode appears to be influenced by electrolyte concentration to a greater extent compared to the ORR electrode. This is because the OER requires OH^- ions for the evolution of O_2. Thus, a greater concentration of OH^- ions in the reaction environment brings about a greater decrease in overpotential at the OER electrode.

8.2.3. Electrode durability

The overall performance and stability of the oxygen electrodes was assessed over a longer period of time by cycling at 20 mA cm^{-2} for 50 hours with compressed air. The OER electrode was placed between the Zn electrode and ORR electrode for these cycling tests (**Figure 8.14**) as this configuration is considered to be more practical for applications since the same face of the Zn electrode is used for both discharge and charge reactions. The growth of zinc dendrites over the extended cycling period was also able to be better managed in this configuration to prevent short circuits.

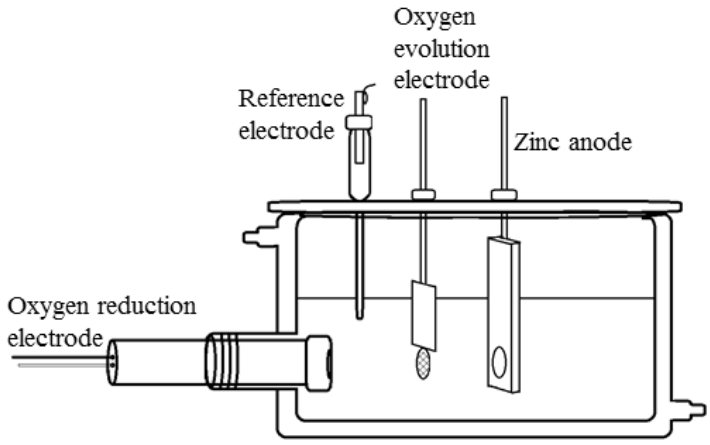

Figure 8.14 Schematic of electrode arrangement for durability tests.

From the results in **Figure 8.15**, the oxygen potentials were not hugely affected by the arrangement of electrodes. However the potential window, ΔE, between the Zn potentials appears to be ~ 20 mV greater in this arrangement most likely due to the increased distance between the ORR electrode and the Zn anode and possibly the presence of the OER electrode in between. The polarisation, ΔE, between ORR and OER at 20 mA cm^{-2} was maintained at ~700 mV for the first 30 cycles, and the cell exhibited an energy efficiency of ~61%. Subsequently, the ΔE between ORR and OER increased by ~20 mV for every 10 cycles giving energy efficiencies of 58-60% between cycle 31 and 75. These energy efficiencies seem reasonable as they are in the same range as reported energy efficiencies (~58-65%) in the literature (Chapter 2, Table 2.8) for secondary oxygen electrodes cycled at 20 mA cm^{-2} in the tri-electrode configuration. The increase in polarisation observed was mainly due to the increase of ORR overpotential as the OER electrode potential was maintained between 0.556 and 0.565 V *vs* Hg/HgO throughout the duration of the test. The ORR potential eventually reached -0.663 V *vs* Hg/HgO by cycle 90 whereby the test was discontinued.

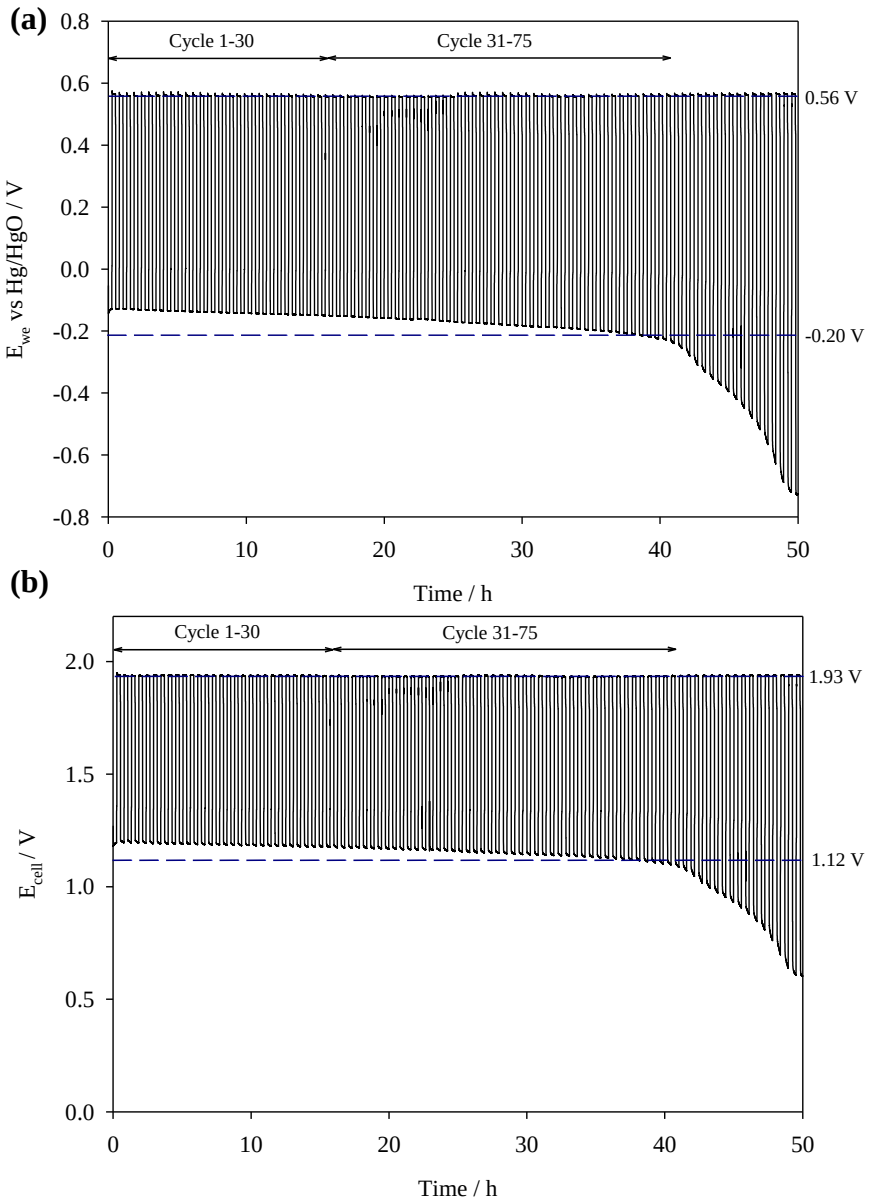

Figure 8.15 Galvanostatic cycling performance of **a)** oxygen electrode potential and **b)** full cell potential versus time in a tri-electrode Zn-air set-up of MnO_x + Ni-Fe-$Co(OH)_2$ over a duration of 50 h at 20 mA cm^{-2} with 30 min cycle period in static electrolyte of 4 M NaOH + 0.3 M ZnO at 333 K. Compressed air was supplied at a constant flow rate of 200 cm^3 min^{-1}.

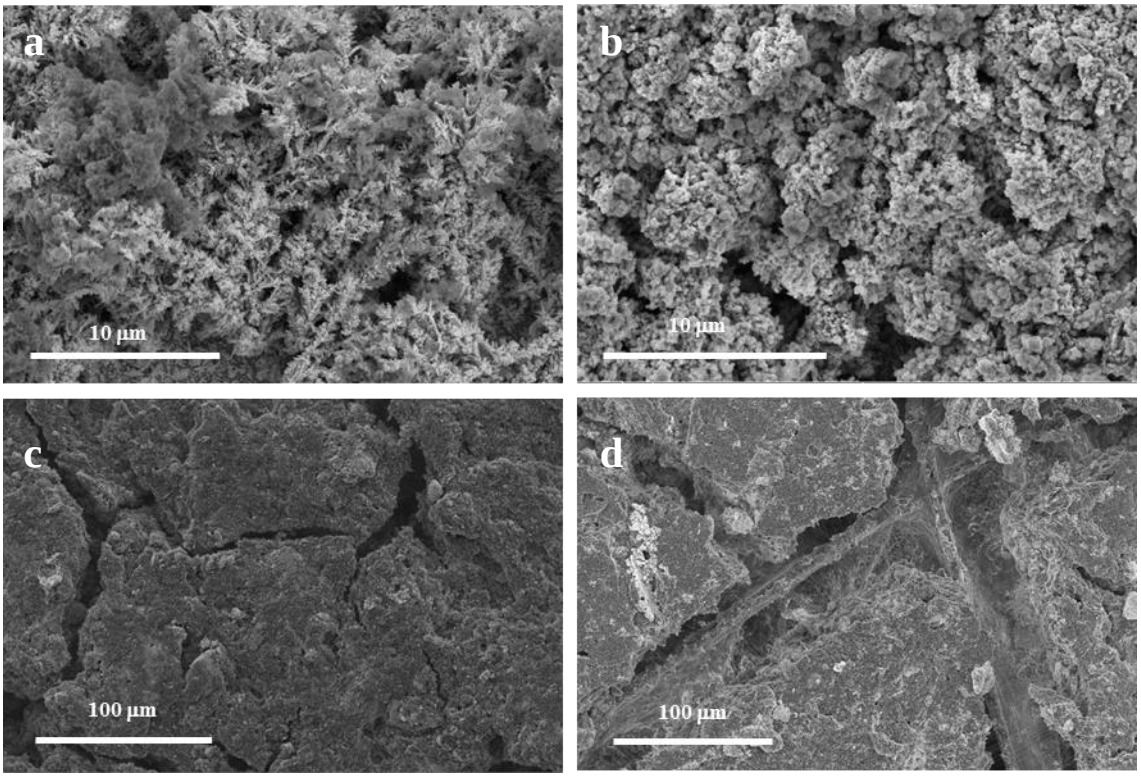

Figure 8.16 SEM micrographs of Ni-Fe-Co(OH)$_2$ coated SS mesh OER electrode **a)** before cycling and **b)** after cycling and the amorphous MnO_x catalyst layer on carbon paper electrode **c)** before cycling, **d)** after cycling.

Both the amorphous MnO_x on C paper and Ni-Fe-Co(OH)$_2$ on SS mesh electrodes were examined with SEM before and after cycling. The SEM micrographs of the OER electrode before and after cycling in **Figure 8.16 a & b** respectively show no observable loss of catalyst layer however there is an obvious change in morphology of the Ni-Fe-Co(OH)$_2$ similar to that seen in Section 7.2.7 which is suggested to be related to the oxidation of both Ni^{2+} and Co^{2+} to Ni^{3+} and Co^{3+} respectively. Contrary to this, there is a noticeable difference in the amorphous MnO_x catalyst layer on the carbon paper after cycling. Compared to the SEM micrograph of the ORR electrode before cycling in **Figure 8.16 c**, the fibres of the carbon paper are more visible under the catalyst layer after cycling (**Figure 8.16 d**), which suggests that parts of the catalyst layer were washed off or removed in the electrolyte during the long-term cycling test. The SEM micrographs of the back of the ORR electrode which was facing the supply of O_2 did not display any apparent differences before and after cycling. It is therefore likely that the increase in ORR overpotential was due to the loss of catalyst layer over

time as well as a possible loss of hydrophobicity from PTFE degradation, especially after 75 cycles, resulting in flooding of the electrode which reduced the number of active sites for ORR.

Overall, the Ni-Fe-Co$(OH)_2$ on SS mesh OER electrode demonstrated excellent stability over the entire testing period whilst the amorphous MnO_x on C paper ORR electrode demonstrated adequate stability over 70 cycles in compressed air due to the composition and structure of the catalyst layer which helped to delay the onset of flooding.

8.3. Conclusion

A secondary tri-electrode Zn-air cycling set-up was constructed with a relay module and Raspberry Pi as microcontroller to test the performance and stability of the optimised oxygen electrodes. Initially, the performance of various ORR and OER electrodes were compared in the set-up at 20 mA cm^{-2} alternating between reduction and oxidation in static electrode of 4 M NaOH + 0.3 M ZnO at 333 K.

The effects of operational parameters including inter-electrode gap, current density, electrolyte concentration, temperature and source of O_2 have been investigated. The amorphous MnO_x on C paper ORR electrode was revealed to be more sensitive to changes in inter-electrode gap, temperature and current density whilst the Ni-Fe-Co$(OH)_2$ on SS mesh OER electrode was regarded to be more prone to changes in electrolyte concentration. The use of compressed air instead of bottled O_2 resulted in a 3% decrease in energy and voltage efficiency of the system which was solely due to the increase in overpotential at the ORR electrode.

The constructed cell was cycled at 20 mA cm^{-2} for a period of 50 h in compressed air in order to demonstrate the overall performance and durability of these electrodes. The ORR and OER electrodes displayed good performance and reasonable energy efficiencies between 58-61% for up to 40 h. The loss in energy efficiency from cycle 75 onwards was mainly caused by degradation of the ORR electrode performance, which was observed from the SEM micrographs. The degradation of the ORR electrode performance was linked to the loss of catalyst layer as well as hydrophobicity leading to premature flooding of gas diffusion pathways.

8.4. References

1. A. Loh, K. Xu, X. Li, B. Wang, Influence of synthesis parameters on amorphous manganese dioxide catalyst electrocatalytic performance, Electrochim. Acta 245 (2017) 615-24.
2. J.O.M. Bockris, Z. Nagy, A. Damjanovic, On the deposition and dissolution of zinc in alkaline solutions, J. Electrochem. Soc. 119 (1972) 285-95.
3. S. Siahrostami, V. Tripkovic, K.T. Lundgaard, K.E. Jensen, H.A. Hansen, J.S. Hummelshøj, J.S.G. Myrdal, T. Vegge, J.K. Nørskov, J. Rossmeisl, First principles investigation of zinc-anode dissolution in zinc–air batteries, Phys. Chem. Chem. Phys 15 (2013) 6416.
4. W. Jin, H. Du, S. Zheng, H. Xu, Y. Zhang, Comparison of the oxygen reduction reaction between NaOH and KOH solutions on a Pt electrode: The electrolyte-dependent effect, J. Phys. Chem. B 114 (2010) 6542-8.
5. D.-Y. Kuo, J.K. Kawasaki, J.N. Nelson, J. Kloppenburg, G. Hautier, K.M. Shen, D.G. Schlom, J. Suntivich, Influence of surface adsorption on the oxygen evolution reaction on IrO_2(110), J. Am. Chem. Soc. 139 (2017) 3473-9.
6. K. A.Stoerzinger, R. R.Rao, X.R. Wang, W. T.Hong, C. M.Rouleau, Y. Shao-Horn, The role of Ru redox in pH-dependent oxygen evolution on rutile ruthenium dioxide surfaces, Chem. 2 (2017) 668-75.
7. K.J. Laidler, The development of the Arrhenius equation, J. Chem. Educ. 61 (1984) 494-8.
8. S. R.Logan, The origin and status of the Arrhenius equation, J. Chem. Educ. 59 (1982) 279-81.
9. I.W.M. Smith, The temperature-dependence of elementary reaction rates: beyond Arrhenius, Chem. Soc. Rev 37 (2007) 812-26.
10. F.Bidault, D.J.L.Brett, P.H.Middleton, N.P.Brandon, Review of gas diffusion cathodes for alkaline fuel cells, J. Power Sources 187 (2009) 39-48.
11. M. Cifrain, K. Kordesch, Handbook of Fuel Cells – Fundamentals, Technology and Applications,W. Vielstich, A. Lamm, H.A. Gasteiger (ed), Chichester, 2003

Chapter 9 Conclusions and Suggestions for Future Work

9.1. Conclusions

The main aim of this research project was to improve the performance of ORR and OER electrodes by developing low-cost, high activity and stability transition metal-based electrocatalysts. The designed experiments were carried out systematically according to the research plan. Key findings from the research work can be summarised as follows:

Regarding ORR catalyst selection and optimisation, the comparison of single and mixed transition metal oxide catalysts as well as non-metal catalysts against Pt/C benchmark catalyst showed that catalysts in the same category shared similar ORR onset potentials, where non-precious metal oxides displayed the most negative onset potentials which were strongly believed to be dictated by the simultaneous electroreduction of the transition metal species at the catalyst surface. This was followed by carbonaceous materials and then precious metals which had the least negative onset potentials.

The addition of a carbon support, Vulcan XC-72R, was noticeably electrochemically beneficial for all catalysts apart from graphene. More importantly, significant changes in ORR pathway were observed at single metal oxides, such as amorphous MnO_x and Co_3O_4, after the introduction of Vulcan XC-72R to the catalyst layer. When combined with Vulcan XC-72R in a gas diffusion electrode, amorphous MnO_x out-performed all of the other ORR catalysts demonstrating lowest ORR overpotentials over a range of current densities from 10 to 100 mA cm^{-2}.

Systematic examination of the influence of synthesis parameters on the resultant amorphous MnO_x as well as its catalytic activity revealed that an optimal amorphous MnO_x catalyst can be synthesised with a molar ratio of MnO_4^-/ Mn^{2+} of 2.67, by adding $KMnO_4$ to $Mn(CH_3COO)_2$ in a basic solution of pH 12 at 295 K. The optimal GDE is prepared with MnO_x to Vulcan XC-72R in a weight ratio of 1:1, catalyst MnO_x to PTFE in a weight ratio of 10:2, and catalyst loading of 2 mg cm^{-2}. The resulting GDE shows

lower overpotentials for oxygen reduction reaction than a commercial MnO_2-based GDE with the same catalyst loading.

Regarding OER catalyst selection and optimisation, single and mixed transition metal oxides and hydroxides coated directly onto stainless steel metal mesh were tested for their OER activity. Screening of electrodeposited unary, binary and ternary transition metal hydroxides in a unique microelectrode set-up revealed that ternary Ni-Fe based metal hydroxides of Ni-Fe-Cr, Ni-Fe-Mo and Ni-Fe-Co displayed lower OER overpotentials compared to their binary and unary counterparts as well. Among the optimised ternary metal hydroxides, Ni-Fe-Co hydroxide presented the highest activity for OER. The interaction between the transition metals Ni, Fe and Co in the hydroxide is not yet fully understood however XPS measurements and SEM micrographs showed that the Ni and Co hydroxide are involved in OER.

An investigation of the effect of electrodeposition parameters on the OER activity of the Ni-Fe-Co hydroxide found that catalyst nucleation rate was dependent on cathodic current density whilst catalyst surface morphology and composition was affected by synthesis pH. Following this, the mass of catalyst deposited and electrochemically active surface area in the catalyst layer could be strategically altered using deposition time. The synthesis temperature was equally influential on OER performance as the structure of the catalyst layer was less compact at higher temperatures. Ni-Fe-Co hydroxide cathodically deposited at 300 mA cm^{-2} for 240 s at 22 ºC, pH 3.9 was found to demonstrate best OER performance and was also capable of stable operation for 3.5 h at 0.5 A cm^{-2} in a zero-gap alkaline membrane electrolyser.

Lastly, regarding the evaluation of performance in a laboratory cell, the activity and stability of the two optimal electrodes, amorphous MnO_x on carbon paper and Ni-Fe-Co hydroxide on stainless steel mesh as ORR and OER electrodes respectively, were assessed in a tri-electrode Zn-air secondary cell set-up. The results showed that the inefficiency of the cell was dominated by the oxygen electrode, which had a potential window of 659 mV at 20 mA cm^{-2} as opposed to the Zn electrode's 30 mV dissolution/ deposition potential window, giving a combined energy efficiency of 64%.

The experiments showed that operating parameters such as current density, temperature and inter-electrode distance have a greater influence on the overpotential at the ORR electrode. On the other hand, the overpotential at the OER electrode was

more dependent on variations in electrolyte concentration. The use of compressed air instead of bottled O_2, was observed to exclusively affect the ORR overpotential, causing a 3% reduction in energy efficiency. The results of the durability experiment showed that the electrodes were capable of being cycled with overall energy efficiencies of 58-61 % at 20 mA cm^{-2} for up to 40 h in static electrolyte of 4 M NaOH + 0.3 M ZnO, 333 K. The eventual loss in performance was a result of the degradation of the ORR electrode.

9.2. Suggestions for future work

- The use of carbon paper with two different microporous layer compositions as an electrode support for the catalyst layer was seen to substantially affect the ORR overpotential especially at high current densities (see Appendix B). The composition of the microporous layer on the carbon paper GDE can be optimised to further enhance the ORR performance.

- Further characterisation of the amorphous MnO_x can be performed using complementary characterisation techniques such as X-ray Absorption Spectroscopy (XAS) to investigate the chemical and structural changes of the elements at the surface of the catalyst and ascertain the reactions which are occurring during ORR.

- XPS analysis and SEM micrographs in Chapter 7 have revealed changes in Ni and Co- hydroxide species at the surface of the Ni-Fe-Co hydroxide catalyst before and after anodic polarisation. Detailed ex- or in-situ chracterisation of the catalyst surface during anodic polarisation can be performed to monitor the interaction between the co-deposited transition metal hydroxides in the catalyst and possibly determine the OER mechanism.

- Based on the thorough investigation of composition and optimal deposition conditions of Ni-Fe-Co hydroxide in Chapter 7, a beneficial extension of this work could be to use a three dimensional electrode support such as a metal foam to increase the catalyst loading, and therefore electrochemically active surface area to enhance OER activity. Alternatively, the growth of stable

nanostructures on the electrode support for the catalyst to be deposited onto can be attempted. Issues of mass transport will have to be taken into consideration for these three dimensional electrode structures.

Appendix A: SEM Micrographs of MnO_x Catalysts

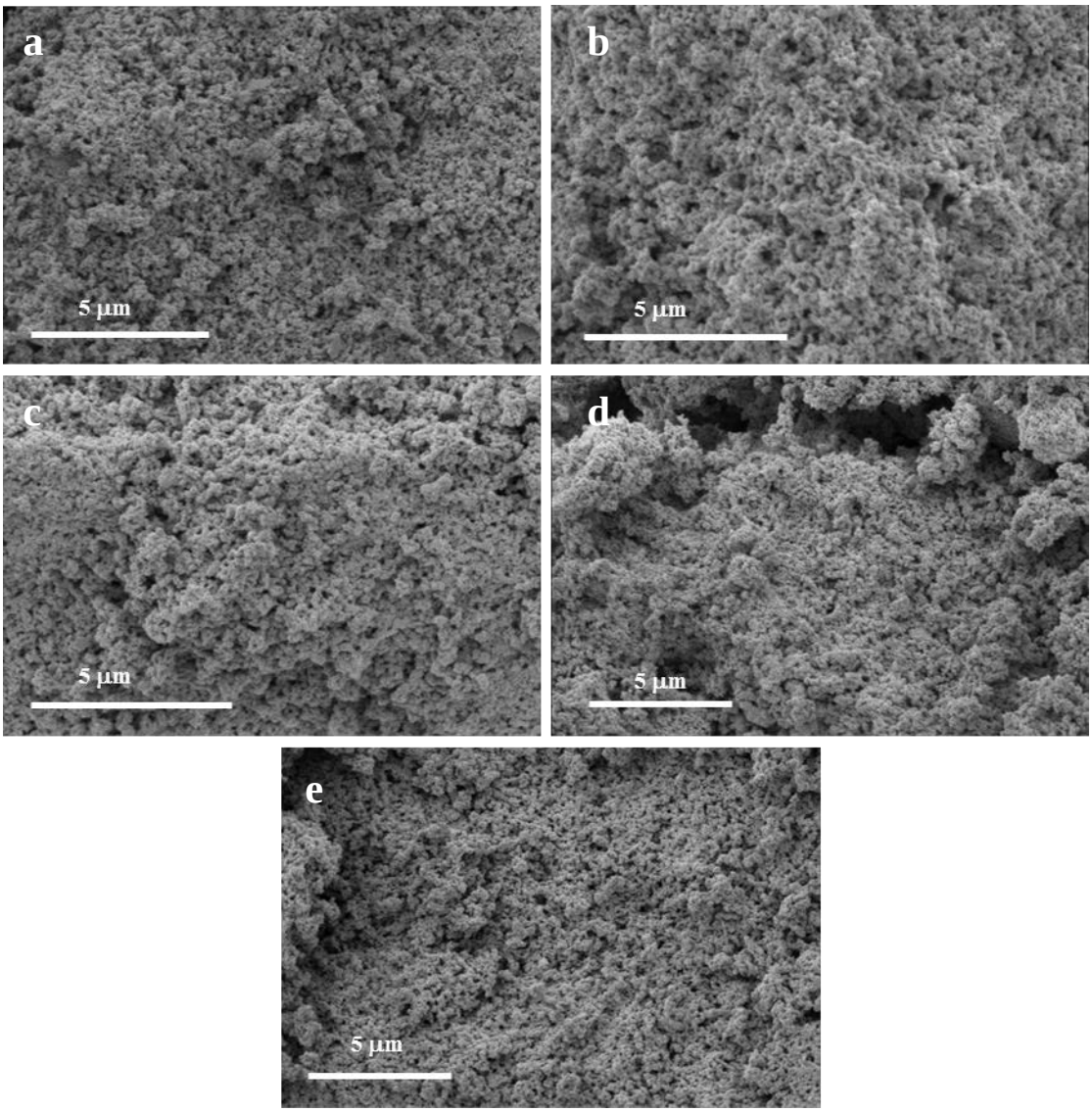

Figure A1 SEM micrographs of catalysts **a)** M1 **b)** M2 **c)** M3 **d)** M4 and **e)** M5 synthesised at 295 K by order A, with basic pH adjustment to pH 12.

The SEM micrographs of MnO_x catalysts M1, M2, M3, M4 and M5 in **Figure A1** indicate that altering the synthesis molar ratio of MnO_4^-:Mn^{2+} did not cause any noticeable changes in the surface morphology of the catalysts.

Appendix B: Comparison of Carbon Fibre Paper

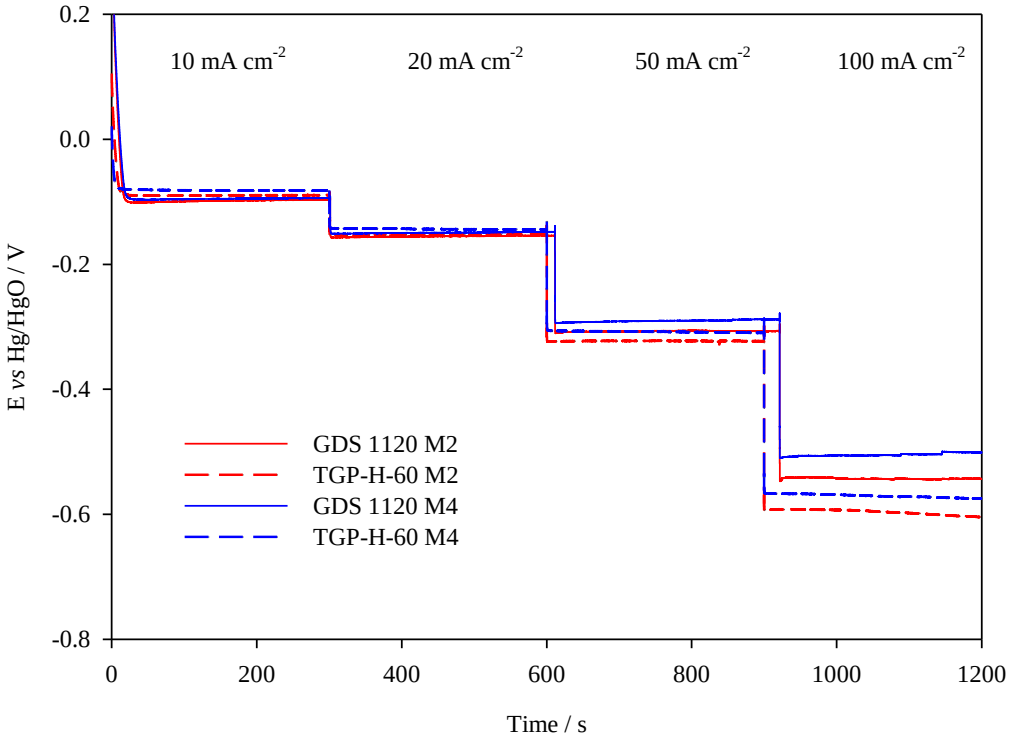

Figure B1 Chronopotentiometric measurements at 10, 20, 50 and 100 mA cm^{-2} of M2 and M4 MnO_x catalyst coated GDE (loading 2 mg cm^{-2}) on either GDS 1120 or TGP-H-60 carbon fibre paper in 1 M NaOH, 333 K, O_2 feed rate of 200 cm^3 min^{-1} to the back of the electrode.

The carbon fibre paper appears to have a significant impact on the GDE performance as seen from the plot above. As seen in Figure B1, with either an M2 or M4 MnO_x catalyst layer, the TGP-H-60 electrodes yield better performance at low current densities of 10 and 20 mA cm^{-2} compared to the GDS 1120 electrodes. At higher current densities, however, the GDS 1120 electrodes exhibits considerably lower overpotentials. Since the TGP-H-60 paper has a greater average PTFE content than GDS 1120 paper, this ensures good mass transfer of the gaseous reactants to the catalyst layer, especially at low current densities. Whilst at higher current densities of 50 and 100 mA cm^{-2}, the lower conductivity or higher resistance through the TGP-H-60 paper likely contributes to its worse performance compared to the GDS 1120 paper.

Appendix C: Python Script for Raspberry Pi-Relay System

```
#Script for controlling relay system
#This section sets the Pi up

import RPi.GPIO as GPIO
import time
GPIO.setmode (GPIO.BCM)

#Initial list with pin numbers (i.e. pin used was number 17)
pinList = [17]

#Loop through set mode and state to 'high'
for i in pinList:
        GPIO.setup(i, GPIO.OUT)
        GPIO.output(i, GPIO.HIGH)

#Length of time between operations in the main loop
#Held at oxidative or reduction current for 15 mins
SleepTimeL = 900
#Held at OCV for 60s
SleepTimeS = 60

#Main loop
#To set a countdown for the number of cycles the loop is repeated
try:
    count = 20
    while (count > 0)
          print 'The count is', count
```

```
#for i in pinList
        GPIO.output(17, GPIO.HIGH)
        print "DISCHARGE"
        time.sleep (SleepTimeL)

        print "OCV"
        time.sleep (SleepTimeS)

        GPIO.output(17, GPIO.LOW)
        print "CHARGE"
        time.sleep (SleepTimeL);

        print "OCV"
        time.sleep (SleepTimeS)

        count = count - 1

    GPIO.cleanup()
    print "Goodbye"

#End programme cleanly with keyboard
Except KeyboardInterrupt:
    print "Quit"

#Reset GPIO settings
    GPIO.cleanup()
```